

Experimentele en numerieke modellering van stroming
en massatransport in een biokunstlever

Experimental and Numerical Modeling of Flow
and Mass Transport in a Bioartificial Liver

Guy Mareels

Promotor: prof. dr. ir. P. Verdonck
Proefschrift ingediend tot het behalen van de graad van
Doctor in de Ingenieurswetenschappen

Vakgroep Civiele Techniek
Voorzitter: prof. dr. ir. J. De Rouck
Faculteit Ingenieurswetenschappen
Academiejaar 2007 - 2008



ISBN 978-90-8578-167-7
NUR 954
Wettelijk depot: D/2007/10.500/41

Supervisor:

Prof. dr. ir. Pascal Verdonck
Hydraulics Laboratory
Department of Civil Engineering (IR15)
Faculty of Engineering
Ghent University
De Pintelaan 185
B-9000 Gent

Members of the exam committee:

Prof. dr. ir. Ronny Verhoeven	(chairman, Faculty of Engineering, UGent)
Prof. dr. ir. Jan Vierendeels	(secretary, Faculty of Engineering, UGent)
Prof. dr. Robert Chamuleau	(Faculty of Medicine, University of Amsterdam, The Netherlands)
Prof. dr. ir. Cécile Legallais	(Faculty of Engineering, Université de Technologie de Compiègne, France)
Prof. dr. Raymond Vanholder	(Faculty of Medicine, UGent)
Prof. dr ir. Peter Van Ransbeeck	(Faculty of applied engineering sciences, HoGent)
dr. ir. Sunny Eloot	(Faculty of Engineering, UGent)
Prof. dr. ir. Patrick Segers	(Faculty of Engineering, UGent)
Prof. dr. ir. Pascal Verdonck	(supervisor, Faculty of Engineering, UGent)

This research was funded by a grant from the Special Research Council from Ghent University, Belgium (**BOF – 011D09503**).

Acknowledgements

Four years ago, I was a little hesitant to start a PhD in biomedical engineering as I doubted if it would provide added value for my future career. Now, four years later, I am not only convinced my professional skills have greatly improved, but I have also learned a great deal on a personal level. I have many people to thank who made this past journey the interesting and challenging experience that it was.

I want to thank my promotor, prof. Pascal Verdonck, for the opportunity to perform research in his lab and to attend many interesting conferences (both on scientific and social level), and for his guidance in the expanding field of biomedical engineering. I also want to thank dr. Dirk De Wachter for introducing me to biomedical research, and for his critical mind and challenging discussions which always helped me one step ahead when I was stuck. Unfortunately (for me), your career guided you away from the lab, but your place was very well filled by dr. Sunny Eloot. She deserves special credit for her endless support and invaluable advice and for always being available as a listening ear in times of need. Also prof. Patrick Segers is thanked for the many interesting discussions. I will miss our *mini-BIO's* on the train.

I am thankful to prof. Jan Vierendeels for his advice in computational fluid dynamics and to Prof. Robert Chamuleau for the interesting discussions on liver support systems; I wish you and the *BAL* the very best in the future. I also want to thank the other members of my exam committee: prof. Ronny Verhoeven, prof. Cécile Legallais, prof. Raymond Vanholder and prof. Peter Van Ransbeeck for the time they spent on reviewing my manuscript and for their insightful questions and comments.

A significant part of my dissertation could not have been completed without the invaluable input of dr. Paul Poyck. Paul, I would like to thank you for the many interesting (and often entertaining) discussions over the phone and at conferences, and for your friendship and support. Good luck with your future training, I am sure you will make an excellent surgeon! Another part of my research has been successful thanks to the cooperation with Rado Kaminsky. I learnt a lot from his excellent experimental skills. Rado, thanks for your friendship and for the many much needed drinks we had together when it was time to unwind.

I would also like to thank my former colleagues (in random order) Ilse, Koen, Kris, Stijn, Wim, and Fadi, and my current colleagues Lieve, Sebastian, Jan, Koen, Tom, Frederic, Abigail, Benjamin, Peter, Dries, Matthieu, Mirko and Denis for their companionship and the fun times in the lab. I am also grateful to Manuella and Eva for helping me out with the administrative tasks. The experimental work was possible thanks to the excellent constructions of Jurgen, Marcel, Martin, and Stefaan.

Of course I am also indebted to my parents for their support in my endeavours. My girlfriend Jessie deserves special thanks for her continuous love and encouragements, and for her patience when my work consumed me too much.

Finally, also thanks to everybody – friends, family and others – who were not directly involved in this work, but were curious about the developments. Thanks for the support.

Guy Mareels

September 2007

List of abbreviations and symbols

Abbreviations

(m)RNA	(messenger) ribonucleic acid
(q)RT-PCR	(quantitative) reverse transcription polymerase chain reaction
2D	two-dimensional
3D	three-dimensional
AAT	α -1-antitrypsin
AFP	α -fetoprotein
AHS-BAL	Alginate-entrapped Hepatocyte Spheroid Bioartificial Liver
ALAT	alanine aminotransaminase
ALF	acute liver failure
AMC-BAL	Academic Medical Center - Bioartificial Liver
AoCLF	acute-on-chronic liver failure
ASAT	aspartate aminotransferase
AST	aspartate transaminase
AVF	arteriovenous fistula
BAL	bioartificial liver
Bax- α	Bcl2-associated X protein
BCE	blood constitutive equation
Bcl-XL	Bcl-XL protein
BLSS	Bioartificial Liver Support System
CCL	capillary cell layer
CFD	computational fluid dynamics
CLF	chronic liver failure
CPS	carbamoyl-phosphate synthetase
CVC	central venous catheter
CYP3A29	cytochrome P450 3A29
DOQI	Dialysis Outcomes Quality Initiative
ECM	extracellular matrix
ECS	extracapillary space
ELAD	Extracorporeal Liver Assist Device
FHF	fulminant liver failure
FMB	flat membrane bioreactor
FP	flat plate
FPSA	Fractionated Plasma Separation and Adsorption
GGT	gamma glutamyl transpeptidase
GS	glutamine synthetase
GST π	π class glutathione S transferase
Hb	hemoglobin
HBAL	Hybrid Bioartificial Liver
HCC	hepatocellular carcinoma
HE	hepatic encephalopathy
HE	hematoxylin and eosin
HF	hollow fiber

HGF	hepatic growth factor
IJV	internal jugular vein
IL	interleukin
IVC	inferior vena cava
LDH	lactate dehydrogenase
LLS-HALSS	Liver Lobule-like structure Hybrid Artificial Liver Support System
MARS	Molecular Adsorbent Recycling System
MDS	Microspheres-based Detoxification System
MELD	model for end-stage liver disease
MELS	Modular Extracorporeal Liver Support
MOF	multi organ failure
MT	mat thickness
MW	molecular weight
NAFLD	non-alcoholic fatty liver disease
NASH	non-alcoholic steatohepatitis
NKF	National Kidney Foundation
OCR	oxygen consumption rate
OCT	oxygen consumption test
OLT	orthotopic liver transplantation
PBC	primary biliary cirrhosis
Pepck1	cytosolic phosphoenolpyruvate carboxykinase 1
PERV	porcine endogenous retrovirus
Pfkfb1	6-phosphofructo -2-kinase/fructose-2,6-biphosphatase 1
PIV	particle image velocimetry
PLI	platelet lysis index
PMMA	polymethyl methacrylate
PSC	primary sclerosing cholangitis
PTFE	polytetrafluoroethylene
PUF-HALSS	Polyurethane Foam Hybrid Artificial Liver Support System
RBC	red blood cell
RES	Reticuloendothelial system
RFB	radial flow bioreactor
RI	refractive index
ROS	reactive oxygen species
RT	residence time
SEPET	Selective Plasma Filtration Therapy
SHBG	sexual hormone binding globulin
SOD1	[Cu/Zn] superoxide dismutase 1
SOD2	[Mn] superoxide dismutase 2
SPAD	Single-Pass Albumin Dialysis
SPF	specific pathogen free
SS	shear stress
SSR	Sorbent Suspension Reactor
SVC	superior vena cava

TNF	tumor necrosis factor
UCP-2	uncoupling protein 2
UNOS	United Network for Organ Sharing

Symbols

α	oxygen solubility
α_γ	shear strain scale factor
α_L	length scale factor
α_V	velocity scale factor
C	concentration
D	diameter
D_o	free diffusion coefficient
D_{cell}	intracellular diffusion coefficient
D_{eff}	effective diffusion coefficient
D_{ij}	strain rate tensor
K	dialyzer clearance
K_M	michaelis-menten constant
L	length
ν	kinematic viscosity
p, P	pressure
pO_2	oxygen partial pressure
Q	flow rate
R	hydraulic resistance
ρ	density
ρ_{cell}	cell density
Re	Reynolds number
t	time
τ	shear stress
u_i	i-th component of the velocity vector
μ	dynamic viscosity
V	velocity magnitude
V_M	maximum oxygen consumption rate
V_{ratio}	effective hepatocyte utilization ratio
x_i	i-th component of the location vector

Table of Contents

Samenvatting	i
Summary	xiii

Part A: Central venous catheters A vascular access for extracorporeal therapy

CHAPTER I: INTRODUCTION TO CENTRAL VENOUS CATHETERS.. 1

1	VASCULAR ACCESS FOR EXTRACORPOREAL THERAPY	3
2	CENTRAL VENOUS CATHETERS	5
2.1	<i>Classification and use</i>	5
2.2	<i>Existing catheter designs</i>	6
2.3	<i>Insertion site and tip location</i>	10
2.4	<i>Clinical performance: complications</i>	11
2.4.1	Immediate complications	11
2.4.2	Delayed complications	12
2.5	<i>Hemodynamic performance</i>	14
2.5.1	Catheter blood flow rate and pressure drop	14
2.5.2	Internal flow and shear stress distribution	15
2.5.3	Access recirculation	15
3	DETERMINANTS OF CVC PERFORMANCE	17
3.1	<i>Insertion site</i>	17
3.2	<i>Tip location</i>	17
3.3	<i>Catheter design</i>	18
3.3.1	Cuff	18
3.3.2	Material type	18
3.3.3	Side holes and catheter tip design	18
4	RATIONALE AND RESEARCH OUTLINE	21

CHAPTER II: IMPACT OF SIDE HOLES AND TIP LOCATION ON FLOW FIELD, SHEAR STRESS DISTRIBUTION AND ACCESS RECIRCULATION IN A CENTRAL VENOUS CATHETER 23

1	INTRODUCTION	25
2	MATERIALS AND METHODS	26
2.1	<i>Catheter model</i>	26
2.2	<i>Blood model</i>	26
2.3	<i>Validation of the calculation grid and the numerical method</i>	27
2.4	<i>Numerical simulation of the catheter in a tube model</i>	27
2.4.1	Boundary conditions	28
2.4.2	Hemodynamic effect of side holes	28
2.4.3	Hemodynamic effect of the size of catheter side holes	28
2.4.4	Recirculation percentage: normal use vs. reversed catheter lines	29

2.5	<i>Numerical simulation of the catheter in an anatomically realistic model</i>	29
3	RESULTS	30
3.1	<i>Validation of the calculation grid and the numerical method.....</i>	30
3.2	<i>Numerical simulation of the catheter in a hollow tube.....</i>	30
3.3	<i>Numerical simulation of the catheter in an anatomically realistic model</i>	34
4	DISCUSSION	36
4.1	<i>Numerical simulation of the catheter in a hollow tube.....</i>	36
4.2	<i>Numerical simulation of the catheter in an anatomically realistic model</i>	39
5	ACKNOWLEDGEMENTS	41

CHAPTER III: PIV VALIDATED CFD BASED DESIGN TO REDUCE SHEAR STRESS AND RESIDENCE TIME IN CENTRAL VENOUS HEMODIALYSIS CATHETERS43

1	INTRODUCTION	45
2	MATERIALS AND METHODS.....	46
2.1	<i>Catheter designs</i>	46
2.1.1	Three catheter designs studied by PIV and CFD	46
2.1.2	Four additional catheter designs studied by CFD only	47
2.2	<i>PIV analysis.....</i>	47
2.2.1	Catheter prototypes.....	47
2.2.2	Experimental setup	47
2.2.3	Measurement protocol	49
2.3	<i>CFD analysis</i>	50
2.3.1	Comparison with PIV	50
2.3.2	Assessment of shear stress levels and blood residence time	51
2.3.3	Influence of a realistic SVC flow.....	53
3	RESULTS	54
3.1	<i>CFD validation by PIV measurements for three catheter designs.....</i>	54
3.2	<i>CFD assessment of shear stress and residence time in the tip of 7 catheter designs.....</i>	56
4	DISCUSSION	58
5	CONCLUSIONS.....	62
6	ACKNOWLEDGMENTS	62

Part B: Bioartificial liver support
Improving the efficiency of the AMC Bioartificial Liver

CHAPTER IV: LIVER SUPPORT SYSTEMS – A REVIEW FROM ANATOMY TO ZOONOSIS.....65

1	THE HUMAN LIVER.....	67
1.1	<i>Anatomy</i>	67
1.1.1	Gross anatomy	67
1.1.2	Macrocirculation.....	68
1.1.3	Microcirculation	68
1.1.4	Histology	69
1.2	<i>Physiology</i>	75
1.2.1	Functions of the hepatic vasculature system	75
1.2.2	Metabolic functions of the liver	76
1.2.3	Formation of Bile.....	79
1.2.4	Liver regeneration.....	80
1.3	<i>Pathology of the liver</i>	80
1.3.1	Hepatocellular diseases	81
1.3.2	Cholestatic diseases	83
2	LIVER FAILURE	84
2.1	<i>Definition and classification</i>	84
2.2	<i>Symptoms</i>	84
2.3	<i>A problem on world scale</i>	86
2.4	<i>Current treatment of liver failure</i>	86
2.4.1	Standard medical care.....	86
2.4.2	Orthotopic liver transplantation (OLT).....	86
2.5	<i>The need for liver support systems</i>	90
3	ARTIFICIAL LIVER SUPPORT	91
3.1	<i>Conventional systems</i>	91
3.1.1	Hemodialysis	91
3.1.2	Hemofiltration.....	91
3.1.3	Hemodiafiltration.....	91
3.1.4	Hemo- and plasmapheresis: adsorption therapy.....	91
3.2	<i>Advanced artificial support systems</i>	92
3.2.1	Molecular Adsorbent Recirculating System (MARS).....	93
3.2.2	Fractionated Plasma Separation and Adsorption (FPSA – Prometheus).....	94
3.2.3	Single-pass albumin dialysis (SPAD)	96
3.2.4	Selective Plasma Filtration Therapy (SEPET).....	96
3.2.5	Hemodiafiltration: BioLogic-DT (a.k.a. ‘Liver Dialysis Unit’).....	98
3.2.6	Sorbent Suspension Reactor (SSR).....	100
3.2.7	Push-Pull Pheresis: Biologic-DTPF / PF-Liver Dialysis Unit.....	101
3.2.8	Microspheres-based Detoxification System (MDS).....	102
3.3	<i>Conclusion</i>	102
4	BIOLOGIC LIVER SUPPORT	104
4.1	<i>Blood / tissue xeno cross-hemodialysis</i>	104
4.2	<i>Human cross-circulation</i>	104

4.3	<i>Human or xenogeneic extracorporeal liver perfusion</i>	104
4.4	<i>Exchange transfusion or high volume plasmapheresis</i>	105
4.5	<i>Heterotopic hepatocyte transplantation</i>	105
4.6	<i>Orthotopic liver transplantation</i>	105
5	BIOARTIFICIAL LIVER SUPPORT	106
5.1	<i>Biological component: Necessary mass and optimal source of hepatocytes?</i>	106
5.1.1	Necessary mass of hepatocytes.....	106
5.1.2	Optimal type and source of hepatocytes.....	107
5.1.3	Conclusion.....	109
5.2	<i>Mechanical component: Design of a hepatocyte bioreactor system</i>	109
5.2.1	Essential requirements and challenges.....	109
5.2.2	Classification of bioreactor designs.....	115
5.2.3	Additional challenges in bioartificial liver system design.....	119
5.3	<i>Overview of Bioartificial Liver systems in in vitro or preclinical tests</i>	121
5.3.1	FMB-BAL.....	121
5.3.2	LIVERx2000.....	122
5.3.3	LIVERaid.....	123
5.3.4	LLS-HALSS.....	124
5.3.5	PUF-HALSS.....	125
5.3.6	UCLA-BAL.....	126
5.3.7	AHS-BAL.....	126
5.3.8	Fluidized bed BAL.....	126
5.3.9	Oxy-HFB.....	127
5.4	<i>Overview of clinically applied BAL systems</i>	128
5.4.1	Extracorporeal Liver Assist Device (ELAD).....	128
5.4.2	HepatAssist.....	129
5.4.3	TECA-HALSS.....	130
5.4.4	Bioartificial Liver Support System (BLSS).....	131
5.4.5	Hybrid Bioartificial Liver (HBAL).....	131
5.4.6	Hybrid Liver Support System (LSS) – Modular Extracorporeal Liver Support System.....	132
5.4.7	Radial Flow Bioreactor (RFB).....	133
5.4.8	AMC Bioartificial Liver (AMC-BAL).....	134
5.5	<i>Conclusions and motivation of research</i>	135
5.6	<i>Overview of prior numerical research on perfusion and mass transfer in BAL systems</i>	136
5.7	<i>Research outline</i>	143

CHAPTER V: THREE-DIMENSIONAL NUMERICAL MODELING AND COMPUTATIONAL FLUID DYNAMICS SIMULATIONS TO ANALYZE AND IMPROVE OXYGEN AVAILABILITY IN THE AMC

BIOARTIFICIAL LIVER.	145
1 INTRODUCTION.....	147
2 MATERIALS AND METHODS.....	148
2.1 <i>Computer model</i>	149
2.2 <i>Modeling fluid flow</i>	150

2.2.1	Theoretical model	150
2.2.2	Resistance to flow of the non-woven polyester mat.....	150
2.2.3	Boundary conditions	150
2.3	<i>Modeling oxygen transport and consumption.....</i>	<i>151</i>
2.3.1	Theoretical model	151
2.3.2	Hepatocyte distribution in the micro models	152
2.3.3	O ₂ diffusion constant through non-woven matrix	152
2.3.4	O ₂ diffusion constant through zones containing hepatocytes	153
2.3.5	Boundary conditions	155
2.4	<i>Grid dependency.....</i>	<i>155</i>
2.5	<i>Simulations overview and assessment.....</i>	<i>155</i>
3	RESULTS	158
3.1	<i>Fluid flow and shear stress distribution</i>	<i>158</i>
3.2	<i>Oxygen transport and consumption</i>	<i>160</i>
3.2.1	Reference case simulations (case 1).....	162
3.2.2	The effect of the internal oxygenator (case 2,3).....	163
3.2.3	Increasing oxygen availability (case 4-11).....	163
3.2.4	Clinical vs. experimental setting (case 12,13).....	164
3.2.5	Changes in hepatocyte O ₂ consumption in time (case 14,15)	164
4	DISCUSSION	165
4.1	<i>Fluid flow and shear stress distribution</i>	<i>165</i>
4.2	<i>Oxygen transport and consumption</i>	<i>166</i>
4.2.1	Reference case simulations (case 1).....	166
4.2.2	The effect of the internal oxygenator (case 2,3).....	167
4.2.3	Increasing oxygen availability (case 4-11).....	168
4.2.4	Clinical vs. experimental setting (case 12,13).....	170
4.2.5	Changes in hepatocyte O ₂ consumption in time (case 14,15)	170
5	CONCLUSIONS.....	171
6	ACKNOWLEDGMENTS	171
7	ADDENDUM	172
7.1	<i>Modeling methodology and limitations.....</i>	<i>172</i>
7.1.1	Resistance to flow of the non-woven polyester mat.....	172
7.1.2	Resistance to flow of hepatocytes	172
7.1.3	O ₂ diffusion constant through zones containing hepatocytes	172
7.1.4	O ₂ supply by the hydrophobic gas capillaries	173
7.1.5	Hepatocyte oxygen consumption parameters.....	173
7.2	<i>Future work</i>	<i>174</i>

CHAPTER VI: ENHANCED OXYGEN AVAILABILITY IMPROVES LIVER-SPECIFIC FUNCTIONS OF THE AMC BIOARTIFICIAL LIVER175

1	INTRODUCTION	177
2	MATERIALS AND METHODS.....	178
2.1	<i>Bioreactor configurations.....</i>	<i>178</i>
2.2	<i>Experimental set-up.....</i>	<i>178</i>
2.3	<i>Hepatocyte isolation</i>	<i>179</i>
2.4	<i>Hepatocyte culture.....</i>	<i>179</i>
2.5	<i>Hepatocyte function test.....</i>	<i>180</i>

2.6	<i>Quantitative reverse transcription-PCR (qRT-PCR)</i>	180
2.7	<i>Histological analysis</i>	181
2.8	<i>Statistical analysis</i>	181
3	RESULTS.....	182
3.1	<i>Bioreactor configurations</i>	182
3.2	<i>Isolation outcome and loading</i>	182
3.3	<i>Medium pO₂ and pH</i>	182
3.4	<i>Carbohydrate metabolism and oxygen consumption</i>	183
3.5	<i>Hepatocyte function test</i>	184
3.6	<i>AST and LDH release</i>	186
3.7	<i>qRT-PCR</i>	186
3.8	<i>Histological analysis</i>	187
4	DISCUSSION.....	188
5	ACKNOWLEDGEMENTS.....	191

CHAPTER VII: A FULL-SCALE NUMERICAL MODEL OF THE AMC BIOARTIFICIAL LIVER CORRELATED WITH *IN VITRO*

EXPERIMENTAL DATA. 193

1	INTRODUCTION.....	195
2	MATERIALS AND METHODS.....	197
2.1	<i>Full scale computer model of the AMC BAL</i>	197
2.2	<i>Mesh independency</i>	198
2.3	<i>In vitro hepatocyte distribution in the AMC BAL</i>	200
2.4	<i>Modeling fluid flow</i>	202
2.5	<i>Modeling O₂ transport and consumption</i>	202
2.6	<i>Simulation overview</i>	203
3	RESULTS.....	204
3.1	<i>In vitro hepatocyte distribution in the AMC-BAL</i>	204
3.2	<i>Fluid flow in a full scale model of the original and new design AMC-BAL</i> 207	
3.3	<i>Oxygen availability and medium outlet pO₂ in the AMC-BAL</i>	208
4	DISCUSSION.....	211
4.1	<i>In vitro hepatocyte distribution in the AMC BAL</i>	211
4.2	<i>Fluid flow and oxygen availability in the original design AMC-BAL</i> ... 211	
4.3	<i>Strategies to improve O₂ availability in the AMC-BAL</i>	212
4.4	<i>Influence of imposed O₂ consumption rates</i>	213
4.5	<i>Estimating in vitro hepatocyte oxygen consumption rates based on experimental data</i>	213
4.6	<i>Relation between simulated O₂ availability, estimated OCR and in vitro functionality</i>	214
5	CONCLUSIONS.....	215
6	ACKNOWLEDGEMENTS.....	216
7	ADDENDUM: MICRO VS. MACRO MODEL.....	216
7.1	<i>Introduction</i>	216
7.2	<i>Methods</i>	216
7.3	<i>Results</i>	217
7.4	<i>Discussion</i>	218

7.5	<i>Conclusions</i>	218
CHAPTER VIII: CONCLUSIONS AND FUTURE PROSPECTS.....		221
1	CENTRAL VENOUS CATHETERS	223
1.1	<i>Conclusions</i>	223
1.2	<i>Future prospects</i>	225
2	AMC BIOARTIFICIAL LIVER	226
2.1	<i>Conclusions</i>	226
2.2	<i>Future prospects</i>	227
APPENDIX A – MODELING CELLULAR GROWTH AND METABOLISM		229
References.....		245

Samenvatting

Een mogelijke therapie om in de toekomst patiënten met ernstig leverfalen te overbruggen naar transplantatie of naar regeneratie van het eigen orgaan, is het gebruik van een biokunstlever. Dit is een extracorporele bioreactor bezaaid met levende, functioneel actieve levercellen. In een klinische omgeving wordt plasma of bloed aan de circulatie van de patiënt onttrokken en vervolgens doorheen de biokunstlever gecirculeerd waar de hepatocyten er hun leverspecifieke functies op uitvoeren. Het behandelde bloed wordt dan teruggestuurd naar de patiënt. Om dit extracorporeel leverondersteunend systeem te kunnen toepassen, zijn dus zowel een performante vaattoegang als een klinisch toepasbare biokunstlever nodig. In dit proefschrift worden experimentele en numerieke technieken gecombineerd om een beter inzicht te verkrijgen in de transportverschijnselen in de vaattoegang én de biokunstlever. Bovendien wordt telkens een poging ondernomen om de performantie en de klinische toepasbaarheid van beide deelsystemen te verbeteren. Het proefschrift is dan ook opgedeeld in twee grote delen.

Deel A: Centraal veneuze katheters: Een vaattoegang voor extracorporele therapie.

Hoofdstuk I

Inleiding tot centraal veneuze katheters

Een centraal veneuze katheter is een cilindervormig buisje met één of meerdere holtes of lumens langs waar men bloed enerzijds kan onttrekken en anderzijds kan terugvoeren naar de patiënt. Als dit buisje wordt ingebracht in één van de grote aders die leiden naar het rechter atrium, spreekt men van een centraal veneuze katheter. Hoewel zijn doel simpel is, zijn er toch vele verschillende katheterontwerpen op de markt. In dit hoofdstuk worden de meest voorkomende ontwerpen besproken. Om een onderscheid te kunnen maken tussen de verschillende katheterontwerpen is het nodig de performantiecriteriën te bepalen. Deze criteria zijn enerzijds klinisch en anderzijds hemodynamisch van aard.

Klinische performantiecriteriën omvatten de verschillende complicaties die gepaard gaan met het inbrengen en het gebruik van een centraal veneuze katheter. In de tekst wordt een overzicht gegeven van de mogelijk 'vroeg' en zogenaamde 'vertraagde' complicaties. Een voorafgaande, gedetailleerde evaluatie van de patiënt, rekening houdend met de gekende risicofactoren, en het laten uitvoeren van de inbrengprocedure door een getraind staflid kan het risico op de 'vroeg' complicaties minimaliseren. De 'vertraagde' complicaties zijn echter minder gemakkelijk te controleren. Zij omvatten infecties, bloedklontervorming (trombose) in de katheter zelf of in de ader en een vernauwing (stenose) van de ader. Deze complicaties kunnen de klinische toepassing van deze vaattoegang sterk belemmeren. Hierbij zijn vooral het kathetermateriaal, de plaats van inbreng en het katheterontwerp van belang.

Hemodynamische performantiecriteriën omvatten het bloeddebiet en de drukval over de katheter, het stromingsprofiel en de afschuifspanningsverdeling binnenin de katheter en de zogenaamde toegangsrecirculatie. Er moet gestreefd worden naar een bloeddebiet van minstens 300 mL/min terwijl de drukval over de katheter moet

beperkt worden. Deze is immers beperkt tot wat de bloedpomp (i.e. rollerpomp) kan leveren zonder teveel bloedbeschadiging te veroorzaken. Bovendien kan een hoge drukval over de katheter erop wijzen dat het bloed lokaal door erg nauwe segmenten in de katheter moet stromen. Hier zal bloedstroming aan hoge snelheid gepaard gaan met hoge afschuifkrachten op het bloed. Deze kunnen de rode bloedcellen beschadigen (hemolyse) en leiden tot een activatie van de bloedplaatjes, wat dan weer bloedstolling in de hand werkt. Bloedstolling is dan weer een van de belangrijke klinische performantiecriteria. De stromingsverdeling in het lumen van de katheter is ook van belang: zones met stagnerend bloed kunnen trombus-vorming in de hand werken. Ten slotte is ook het vermijden van toegangsrecirculatie erg belangrijk. Dit is namelijk het effect waarbij bloed dat de katheter verlaat onmiddellijk terug wordt aangezogen door het bloedaanzuigende ('arteriële') lumen van de katheter, in plaats van verder door de ader te stromen. Zo wordt reeds behandeld bloed opnieuw door het extracorporeel circuit gestuurd en daalt de efficiëntie van de behandeling.

Zoals reeds gezegd zijn er vele katheterontwerpen op de markt, elk met hun specifieke kenmerken. Uit een gedetailleerde literatuurstudie verder in dit hoofdstuk blijkt dat de katheterontwerpen die de laatste 10 jaar in gebruik zijn, onderling weinig of niet significant verschillen wat betreft hun performantiecriteria. Toch blijft elke fabrikant maar nieuwe modellen op de markt brengen met de meest exotische ontwerpen, zonder enig bewijs van toegevoegde waarde. In de volgende twee hoofdstukken van dit proefschrift worden door middel van numerieke simulaties en experimentele visualisatietechnieken verschillende basiskennmerken van katheterontwerpen beoordeeld om inzicht te krijgen in welk ontwerp de sleutel heeft tot een meer performante vaattoegang. Deze informatie kan dan gebruikt worden om in de nabije toekomst een nieuw katheterontwerp te ontwikkelen.

Hoofdstuk II

Impact van de aanwezigheid en grootte van zijgaatjes, en van de locatie van de kathertip op stroming, schuifspanningsverdeling en toegangsrecirculatie van centraal veneuze katheters

Zijgaatjes zijn zijdelingse openingen aan de tip van de katheter. Volgens katheterfabrikanten zouden die de bloedaanzuiging in de katheter moeten verbeteren. Door middel van numerieke simulaties ('Computational Fluid Dynamics' – CFD) worden in dit hoofdstuk de stroming doorheen drie step-tip kathetermodellen gesimuleerd. De drie modellen verschillen slechts op één punt: ofwel zijn er géén zijgaatjes, ofwel zijn er wél zijgaatjes volgens de specificaties van de fabrikant, ofwel zijn er zijgaatjes met een diameter van maar de helft van het origineel. Deze kathetermodellen worden elk in een holle buis, die de vaatwand voorstelt, gemodelleerd. Telkens wordt er gekeken naar de hemodynamische performantiecriteria zoals die in hoofdstuk 1 werden voorgesteld. Het blijkt dat de aanwezigheid en de grootte van de zijgaatjes een belangrijke rol spelen in hoe de stromings- en schuifspanningsverdeling in het katheterlumen eruit zien. De aanwezigheid van de zijgaatjes beïnvloedt vooral de locatie van de verhoogde schuifspanningen. Kleinere zijgaatjes veroorzaken een groter gebied met verhoogde schuifspanning. Niettemin is een eenduidige classificatie van de kathetermodellen,

gebaseerd op het niveau van aanwezige schuifspanningen, niet zo eenvoudig op te stellen. Toegangsrecirculatie wordt slechts verwaarloosbaar beïnvloed door zowel de aanwezigheid als de grootte van de zijgaatjes. Wel is toegangsrecirculatie licht afhankelijk van het bloeddebiet doorheen katheter en ader.

Om na te gaan of deze resultaten geldig zijn in de klinische situatie werden de simulaties herhaald waarbij het kathetermodel nu in een anatomisch realistische omgeving werd ingebracht. Hiervoor werden doorsneden van een rechter atrium via medische beeldvorming gesegmenteerd en gereconstrueerd naar een drie-dimensionaal model. In dit model werd het kathetermodel geplaatst met zijn tip aan de scheiding tussen het rechter atrium en de bovenste holle ader. Het blijkt dat de locatie van de kathetertip de stromings- en schuifspanningsverdeling in de katheter niet beïnvloedt, maar wel de waarden van toegangsrecirculatie. Een anatomisch realistisch model is bijgevolg enkel nodig om de toegangsrecirculatie bij centraal veneuze katheters correct te kunnen simuleren.

Hoofdstuk III

PIV gevalideerd, CFD gebaseerd ontwerp om afschuifspanning en verblijftijd in centraal veneuze katheters te minimaliseren.

De afschuifspanningsverdeling en de aanwezigheid van zones met lage bloedsnelheden zijn cruciale factoren in de vorming van bloedklonters. Daarom wordt in deze studie een gecombineerde numerieke en experimentele aanpak gebruikt om deze factoren in verschillende ontwerpen van een kathetertip te bestuderen. Numerieke stromingsmechanica is een tijd- en kosteffectieve methode om de hemodynamica in virtuele kathetertipontwerpen te bestuderen. Omdat hiervoor echter zeer gedetailleerde schuifspanningsverdelingen nodig zijn en deze niet eenvoudig en slechts bij hoge lokale meshdichtheden worden bereikt, is validatie van de numerieke resultaten nodig. Ter validatie werd gekozen voor Particle Image Velocimetry (PIV) als een uitdagende methode om hoge resolutie snelheids- en schuifspanningsverdelingen te bekomen binnenin de lumens van drie verschillende katheterontwerpen. Volgende katheterontwerpen werden bestudeerd: een step-tip katheter met cilindrische lumens en een arteriële tip die (1) loodrecht op zijn as werd afgesneden, (2) schuin werd afgesneden, en (3) loodrecht werd afgesneden en een sleufvormige zijopening heeft. Voor deze studie werd de PIV techniek aangepast om hem toepasbaar te maken op deze kleine schaal. Dit resulteerde in de eerste experimentele metingen van de stroming en schuifspanningsverdeling in een katheterlumen. De bekomen snelheids- en afschuifspanningsverdelingen in telkens twee orthogonale vlakken doorheen het arteriële katheterlumen werden vergeleken met numerieke simulaties. De kwalitatieve en kwantitatieve overeenkomst was bevredigend. Na deze validatie werden nog vier bijkomende (zeven in totaal) kathetertipontwerpen numeriek gesimuleerd: een cilindrisch lumen met twee zijgaatjes en de tip (4) loodrecht of (5) schuin afgesneden; (6) een katheter met concentrische lumina en (7) een Ash Split gebaseerd ontwerp. Zes parameters waaronder de gemiddelde afschuifspanning, de verblijftijd van het bloed in de tip en de zogenaamde Platelet Lysis Index werden voor elk van de ontwerpen berekend. Deze laatste parameter houdt rekening met het feit dat activatie van bloedplaatjes

niet alleen afhankelijk is van het niveau van de afschuifspanning, maar ook van de duur van de blootstelling. Uit deze analyse wordt aanbevolen dat de eindopening van een kathetertip best loodrecht op zijn as wordt afgesneden. De aanwezigheid van zijgaatjes wordt in deze analyse enkel aangeraden indien de kathetertip onder een schuine hoek wordt afgesneden. Katheters met concentrische lumens worden sterk afgeraden vanwege hun hoge afschuifspanningen en verblijfstijden. Een Ash Split gebaseerd ontwerp vertoont lagere schuifspanningswaarden dan een step-tip katheter. Dit wordt echter teniet gedaan door de verhoogde gemiddelde verblijftijd van bloed in de kathetertip doordat het meeste bloed de katheter binnenstroomt via de meest proximale zijgaatjes waardoor de bloedstroming in de distale tipzone erg laag is. Deze data kan leiden tot een meer performant katheterontwerp in de toekomst.

<p style="text-align: center;">Deel B: Biokunstlevers: Naar de verbetering van de klinische efficiëntie van de AMC-Bioartificiële Lever.</p>
--

Hoofdstuk IV

Leverondersteunende apparaten: overzicht van Anatomie tot Zoonose

In dit hoofdstuk wordt een bespreking gegeven van de rationale voor extracorporele leverondersteunende systemen en de uitdagingen die gepaard gaan met het ontwerp ervan. Eerst wordt een overzicht gegeven van de anatomie, bloedcirculatie, histologie, fysiologie en de pathologie van de lever. Uit dit overzicht blijkt dat de lever een uiterst vitaal orgaan is. Het falen van dit orgaan, hetzij acuut, hetzij chronisch, is een levensbedreigende situatie die enkel verholpen kan worden met een levertransplantatie. Deze ingreep verhoogt sterk de overlevingskansen van de patiënt, maar heeft niettemin een reeks onopgeloste problemen: de complexiteit van de chirurgische ingreep, de levenslange immunotherapie en de bijhorende kost aan de gezondheidszorg, de kans op afstoting van het getransplanteerde orgaan en vooral de grote schaarste aan geschikte donorlevers. Het is dus niet te verwonderen dat er voor een zeker aantal patiënten niet tijdig een donororgaan kan gevonden worden. De mortaliteit op de wachtlijst is dan ook gemiddeld 8%, sterk afhankelijk van de onderliggende medische oorzaak. Voorafgaande maakt duidelijk dat er dringende nood is aan een alternatieve leverondersteunende therapie. Deze zou een ondersteunende functie kunnen hebben voor een getransplanteerde lever tot deze volledig functioneel is, of een overbruggende functie waarbij de patiënt in leven wordt gehouden totdat zijn eigen lever voldoende hersteld is of een geschikt donororgaan wordt gevonden.

Leverondersteunende apparaten kunnen ingedeeld worden als volgt: (1) artificiële leverondersteuning: hierbij wordt enkel de bloed-filterende werking van de lever vervangen, (2) biologische leverondersteuning: hierbij worden bijvoorbeeld hele dierenlevers gebruikt; en (3) bioartificiële leverondersteuning (biokunstlevers):

hierbij wordt een mechanische component (de bioreactor) en een biologische component (levercellen) op zulke wijze gecombineerd dat ze de taak van de falende lever kunnen overnemen. Verder omvat de tekst een uitgebreide literatuurstudie van verschillende bestaande leverondersteunende systemen. De nadruk in dit proefschrift ligt op de biokunstleversystemen die reeds veelbelovende resultaten hebben geboekt in *in vitro*, dieren- en klinische studies op patiënten. Eén van de grootste voordelen van bioartificiële levers ten opzichte van artificiële leverondersteuning is dat ze de mogelijkheid hebben om alle leverspecifieke functies te leveren die nodig zijn om de complexe metabole verstoringen van leverfalen te compenseren. Er wordt in de tekst dieper ingegaan op de ontwerpcriteria van biokunstlevers en de bijhorende uitdagingen. Vooral het voorzien van voldoende zuurstof voor de levercellen in de bioreactor wordt aanzien als de grootste beperking in de klinische toepasbaarheid van de biokunstlever.

Eén van de biokunstlevers die het stadium van klinische toepasbaarheid bereikt heeft, is de AMC Bioartificial Liver (AMC-BAL; Academisch Medisch Centrum, Amsterdam, Nederland, patent nr. WO 97/12960). Dit apparaat bevat functioneel actieve hepatocyten, gezaaid in een niet-geweven polyester mat die spiraalvormig rond een centrale massieve kern gewikkeld is. Tussen de windingen van de mat lopen gascapillairen over de hele lengte van de bioreactor als een intern oxygenatiesysteem. In de klinische toepassing wordt de bioreactor bezaaid met één miljard levercellen en doorstroomd met het plasma van de leverpatiënt om verwerkt te worden door de actieve hepatocyten. De AMC-BAL laat veelbelovende resultaten zien in *in vitro* opstellingen, heeft reeds significant de overlevingstijd verlengd in kleine- en grotere dierenstudies en heeft de veiligheid in zijn klinische toepassing bewezen in een fase I klinische studie. Niettemin wezen *in vitro* studies op een verhoogd anaeroob glycolytisch metabolisme in de AMC-BAL over een vierdaagse kweekperiode. Dit zou kunnen wijzen op een lokaal zuurstoftekort in de bioreactor. In de volgende hoofdstukken zal de perfusie en de zuurstofbeschikbaarheid van de hepatocyten in de AMC-BAL bestudeerd worden met numerieke modellen. Ook zullen wijzigingen aan het ontwerp en de werkingscondities voorgesteld worden om de zuurstofbeschikbaarheid te verhogen en zullen deze bevindingen *in vitro* getest worden. Aangezien in de volgende hoofdstukken het numeriek modelleren van zuurstoftransport in dit deel van het proefschrift centraal staat, bevat dit overzichtshoofdstuk tot slot nog een literatuurstudie van bestaande numerieke studies op biokunstleversystemen.

Hoofdstuk V

Numerieke modellering om de zuurstofbeschikbaarheid in de AMC-BAL te analyseren en te verbeteren

In dit hoofdstuk werd een computermodel ontwikkeld waarmee de stroming en het zuurstoftransport en -consumptie in de AMC-biokunstlever (Academisch Medisch Centrum, Amsterdam, Nederland) kan worden gesimuleerd. Deze bioreactor bestaat uit een cilindrische behuizing waarin twee stukken niet-geweven polyester mat spiraalsgewijze afzonderlijk achter elkaar gewikkeld zijn rond een massieve inwendige kern. In de twee stukken hydrofiele mat is een dense cultuur van

hepatocyten mogelijk. Tussen de windingen van de matrix lopen 300 hydrofobe gaspermeabele capillairen parallel over de gehele lengte van de bioreactor. Door deze capillairen stroomt kweekgas (95% lucht, 5% CO₂). Zo vormen ze een inwendig oxygenatiesysteem om bijkomende O₂ toe te voeren aan de hepatocyten.

Twee eenheidsvolumes (micromodellen) werden uit de bioreactorgeometrie geïsoleerd. Elk model bestaat uit een stuk niet-geweven mat en de omgevende vloeistofzones en gascapillairen. De twee micromodellen verschillen enkel in de oriëntatie van de gascapillairen (ofwel in een 'in-lijn' of 'triangulaire' schikking). Ook werden twee hypothetische celverdelingen voorgesteld: verdeling (1) waarbij alle levercellen zich in de mat bevinden, en verdeling (2) waarbij 50% van de cellen in de mat zitten en de overige 50% in een 122 µm dikke cellaag rond de gascapillairen. Deze celverdelingen werden toegepast op elk van de twee micromodellen. Op deze vier micromodelconfiguraties werd de stroming en zuurstofbeschikbaarheid in de biokunstlever gesimuleerd onder standaard werkingscondities. Zuurstofbeschikbaarheid werd gekwantificeerd als het percentage cellen dat over voldoende zuurstof beschikt om aan minimaal 90% van zijn maximale zuurstofconsumptiesnelheid zuurstof op te nemen ($V_{ratio} > 0.9$). Tevens liet het model toe het effect van verschillende aanpassingen aan de werkingscondities en het ontwerp van de biokunstlever te testen, om zo de beste strategie te bepalen om de zuurstofbeschikbaarheid in de AMC-biokunstlever zo maximaal en optimaal mogelijk te verhogen. Volgende werkingscondities werden getest: externe oxygenatie van het kweekmedium, verhogen van het kweekmediumdebiet, verhoging van de zuurstofconcentratie van het gas dat door de zuurstofcapillairen stroomt en van het aantal zuurstofcapillairen. Bijkomend werd het belang van het intern oxygenatiesysteem onderzocht, het effect van de verandering van de zuurstofconsumptie van levercellen in de tijd en de impact van de verandering van de *in vitro* naar een *in vivo* omgeving.

Onder standaard werkingscondities kan de AMC-BAL niet alle cellen in voldoende zuurstof voorzien om aan minimaal 90% van hun maximale zuurstofopname te komen. De simulatieresultaten verschilden echter significant naargelang de gebruikte celverdeling: slechts 16% van de levercellen in celverdeling 1 en 29% in celverdeling 2 werden geacht over voldoende zuurstof te beschikken. De verschillende schikkingen van de gascapillairen hadden geen invloed op de zuurstofbeschikbaarheid. De drukval over de AMC-BAL en de maximale schuifspanningen waren laag en worden niet beschouwd als mogelijk schadelijk voor de celcultuur. Het inwendig oxygenatiesysteem blijkt een onmisbaar onderdeel van de bioreactor te zijn: zonder dit systeem zakt de zuurstofbeschikbaarheid voor de levercellen tot bijna nul. Een verdubbeling in debiet van het kweekmedium verhoogt het aantal levercellen met voldoende zuurstof slechts met 14%. Het verdubbelen van de zuurstofconcentratie (pO₂) van het oxygenatiegas dat door de gascapillairen stroomt (van 150 mmHg naar 300 mmHg) verdubbelt het ' $V_{ratio} > 0.9$ ' percentage in vergelijking met de standaard werkingscondities. Het kweekmediumdebiet zou in vergelijking met meer dan een factor 10 moeten verhoogd worden om dezelfde winst te boeken. De zuurstofbeschikbaarheid kan echter ook verhoogd worden door de pO₂ van het kweekmedium tot carbogene concentraties (95% O₂) te brengen of door het aantal capillairen te verdubbelen. Deze twee technieken leiden tot een verdubbeling van de

zuurstofbeschikbaarheid in de AMC-BAL. Een verhoging van het aantal capillairen wordt echter verkozen boven perfusie van carbogeen medium aangezien het carbogene zuurstofniveau mogelijk schadelijk is voor levercellen en bovendien een uitgebreid uitwendig oxygenatiesysteem vereist. De zuurstofbeschikbaarheid wordt maximaal verhoogd door de $pO_{2\text{-gas}}$ van het oxygenatiegas op carbogeen niveau te brengen of door een combinatie van een dubbel aantal capillairen en een dubbele pO_2 van het gas. $V_{\text{ratio}} > 0.9$ percentages zijn nu verviervoudigd voor celverdeling 1 en verdrievoudigd voor celverdeling 2 in vergelijking met het referentiegeval. Aangezien men liever niet kiest voor carbogene zuurstofniveaus, is een verbeterd bioreactorontwerp dat bestaat uit een dubbel aantal capillairen gecombineerd met een verdubbeling van de pO_2 van het oxygenatiegas, de optimale manier om de zuurstofbeschikbaarheid in de AMC-BAL te maximaliseren.

Hoofdstuk VI

Verbeterde zuurstofbeschikbaarheid verhoogt de lever-specifieke functie in de AMC-BAL

In dit hoofdstuk wordt het verbeterde bioreactorontwerp dat op basis van de numerieke simulaties in het vorige hoofdstuk werd voorgesteld, ook effectief *in vitro* getest. Vier configuraties van AMC-BAL worden met elkaar vergeleken: (G1) het originele ontwerp, (G2) origineel ontwerp met verdubbelde zuurstofconcentratie van het gas doorheen de capillairen ($pO_{2\text{-gas}}$), (G3) nieuw bioreactorontwerp met 2.2-maal dunnere mat en dubbel aantal zuurstofcapillairen en (G4) nieuw bioreactorontwerp met een verdubbelde $pO_{2\text{-gas}}$ (analoog G2 \rightarrow G1). Na een kweekperiode van 6 dagen met varkenslevercellen wordt besloten dat het nieuwe bioreactorontwerp met verhoogde oxygenatie (G4) significant verminderde anaerobe glycolyse vertoont, 60% hogere leverspecifieke functies en verhoogde transcriptieniveaus van vijf lever-specifieke genen in vergelijking met het originele bioreactorontwerp met standaard oxygenatie. De verandering in bioreactordesign en de verhoging van de $pO_{2\text{-gas}}$ droegen elk evenveel bij tot deze verbetering. Histologisch onderzoek bracht kleine verschillen in celorganisatie tussen de verschillende culturen naar boven. Er werd een hogere, stabielere metabole activiteit en lever-specifieke functionaliteit bereikt door een verbeterde zuurstofbeschikbaarheid. Voor de eerste keer in het onderzoek naar biokunstleversystemen werd een significant beter bioreactorontwerp bekomen door middel van voorafgaande numerieke simulaties.

Hoofdstuk VII

Een full-scale model van de AMC-BAL gecorreleerd met experimentele in-vitro data

De winst in zuurstofbeschikbaarheid tussen het *originele* en *nieuwe* bioreactorontwerp die op basis van de simulaties op de micromodellen bekomen werd, is echter persistent groter dan de winst in functionaliteit die in de *in vitro* studie gevonden werd. Dit wordt geïllustreerd door het feit dat, ondanks de verdubbeling in zuurstofbeschikbaarheid gesimuleerd met de micromodellen, het nieuwe bioreactorontwerp geen significante verbetering van de leverspecifieke

functies toonde ten opzichte van het originele ontwerp, onder standaard oxygenatie. Deze discrepantie kan nog steeds te wijten zijn aan een gelimiteerde zuurstofbeschikbaarheid of aan een inhomogene perfusie van de levercellen in de AMC-BAL omdat de micromodellen een aantal limitaties hebben die de extrapolatie van de resultaten naar de *in vitro* situatie kunnen verhinderen. Belangrijke beperkingen zijn: (1) het verschil tussen de werkelijke *in vitro* celverdeling in de AMC-BAL en de twee hypothetische celverdelingen voorgesteld in de micromodellen; (2) de onregelmatige locatie van de capillairen tussen de matwindingen in de AMC-BAL ten opzichte van de vaste, equidistante plaatsing in de micromodellen; (3) de aanwezigheid van inlaat- en uitlaatzones in de AMC-BAL, die bovendien het verlengde van de oxygenatiecapillairen bevatten, wat geen deel uitmaakte van de micromodellen en (4) de opgelegde zuurstofconsumptiewaarden (OCR) van de levercellen.

In dit hoofdstuk wordt een full-scale numeriek model van de AMC-BAL ontwikkeld om deze beperkingen te omzeilen. Dit macromodel is dus geen eenheidsmodel, maar een volledig drie-dimensionaal model van de AMC-BAL bioreactor. Daarenboven wordt een realistische *in vitro* celverdeling bepaald door middel van analyse van histologische coupes van geparafiniseerde bioreactoren. Deze realistische celverdeling werd vervolgens toegepast op full-scale computermodellen van het *originele* en *nieuwe* bioreactorontwerp. Op deze modellen werd dan de stroming en het zuurstoftransport gesimuleerd onder zowel standaard als dubbele zuurstofoxygenatie, in overeenstemming met de G1-4 bioreactorconfiguraties uit de vorige *in vitro* studie. Verder werd de invloed van de opgelegde zuurstofconsumptiewaarde van de hepatocyten nagegaan door twee waarden op te leggen (een veeleisende die ook gebruikt werd in de micromodellen, en een minder hoge waarde). Als mogelijke validatie wordt de gesimuleerde zuurstofconcentratie van het kweekmedium ($pO_{2\text{-med}}$) dat de bioreactor verlaat, vergeleken met *in vitro* opgemeten waarden.

Er werd een belangrijke preferentiële stroombaan geobserveerd nabij de massieve kern van de originele bioreactor. Deze preferentiële stroming was echter niet aanwezig in het nieuwe ontwerp met dubbel aantal gascapillairen en een 2.2-maal dunnere mat. Deze nieuwe configuratie zorgde voor een homogener perfusie en een hogere zuurstofbeschikbaarheid voor de hepatocyten. Een verdubbeling van de pO_2 van het oxygenatiegas verhoogde de zuurstofbeschikbaarheid nog meer.

De waarde van de gesimuleerde zuurstofbeschikbaarheid en van de zuurstofconcentratie van het medium aan de uitlaat van de bioreactor ($pO_{2\text{-med}}$) waren sterk afhankelijk van de opgelegde zuurstofconsumptiewaarde. Daarom werd de *in vitro* zuurstofconsumptie van de levercellen geschat door de numerieke en experimentele waarde van de $pO_{2\text{-med}}$ te fitten. Zo werd de invloed van de verschillende AMC-BAL configuraties (G1-4) op de *in vitro* zuurstofconsumptie van de levercellen bepaald. Er wordt geconcludeerd dat de zuurstofconsumptie van de levercellen in de originele en nieuwe bioreactor ongeveer gelijk zijn onder standaard oxygenatie. De bekomen waarden stemmen zeer goed overeen met waarden die in de literatuur beschikbaar zijn. Het verdubbelen van de $pO_{2\text{-gas}}$ resulteerde in een verdrie- (G2) tot een verzevenvoudiging (G4) van de zuurstofconsumptie van de hepatocyten.

Ten slotte werd het model nog gebruikt om dieper in te gaan op de relatie tussen de gesimuleerde zuurstofbeschikbaarheid, de geschatte zuurstofconsumptie, en de *in vitro* functionaliteit van de levercellen. Wanneer de strenge zuurstofconsumptiewaarden gebruikt worden, stemt de classificatie van de vier AMC-BAL configuraties volgens gesimuleerde zuurstofbeschikbaarheid overeen met de functionele resultaten uit de *in vitro* studie. Echter, de uitlaat-pO₂ van het kweekmedium komt in dit geval niet overeen met de experimentele waarde. Wanneer de geschatte zuurstofconsumptiewaarden gebruikt worden, tonen de simulaties een bijna maximale zuurstofbeschikbaarheid in alle configuraties. Analyse van deze geschatte zuurstofconsumptiewaarden doet vermoeden dat de hepatocyten hun zuurstofconsumptieniveau aanpassen aan de lokale omstandigheden in de AMC-BAL terwijl ze een maximale zuurstofbeschikbaarheid handhaven. Aangezien het nieuwe bioreactorontwerp echter in staat is om cellen met hogere zuurstofconsumptieniveaus in voldoende zuurstof te voorzien, wordt de zuurstofconsumptie van de levercellen in de nieuwe bioreactor dus niet gelimiteerd door een tekort aan zuurstof en spelen andere omgevingsfactoren een belangrijke rol in de regeling van zuurstofconsumptie.

Met de geschatte zuurstofconsumptiewaarden beschikken alle configuraties van de AMC-BAL over een maximale zuurstofbeschikbaarheid, daar waar duidelijke verschillen in anaeroob glycolytisch metabolisme en leverfuncties aangetoond zijn in de *in vitro* studie. Dit laat vermoeden dat de zuurstofbeschikbaarheid zoals gedefinieerd in deze studies (% cellen met $V_{ratio} > 0.9$) niet kan gebruikt worden als een indicator voor *in vitro* verbeteringen. Ook de geschatte zuurstofconsumptie van de levercellen kan niet direct gecorreleerd worden met de verhoogde *in vitro* functionele activiteit. Niettegenstaande de bioreactor met de hoogste functie ook het meeste zuurstof consumeerde, toonden G2 en G3 heel gelijkaardige *in vitro* activiteit, terwijl hun geschatte zuurstofconsumptiewaarden sterk verschilden. Dit toont aan dat andere factoren dan zuurstofbeschikbaarheid (vb. absoluut zuurstofniveau, verhoogd cel-cel of cel-matrix contact) een doorslaggevende rol spelen in het anaeroob glycolytisch metabolisme en de leverspecifieke functionaliteit in de verschillende AMC-BAL configuraties, zoals ook reeds werd voorspeld voor de regulatie van de zuurstofconsumptie van de levercellen. Toekomstige modellen zouden een spatiale variatie van de zuurstofconsumptiewaarde kunnen incorporeren, gebaseerd op de lokale celdichtheid en het absolute zuurstofniveau. Simulaties met zulke modellen zouden kunnen leiden tot een betere correlatie tussen vb. lokale zuurstofbeschikbaarheid en een gereduceerd anaeroob glycolytisch metabolisme in de verschillende AMC-BAL configuraties en tegelijkertijd toch gepaard gaan met een gevalideerde uitlaat pO₂ van het medium. Er is echter meer *in vitro* onderzoek nodig om de parameters voor zo een model te bepalen.

Part C: Conclusies en toekomstperspectieven

Hoofdstuk VIII

Conclusies en toekomstperspectieven

In dit hoofdstuk worden de belangrijkste conclusies van beide delen van dit proefschrift opgesomd. Voor de eerste keer werd de hemodynamische performantie van centraal veneuze katheters bestudeerd, gebruikmakend van geavanceerde numerieke technieken. Het was eveneens voor de eerste keer dat de standaard PIV techniek aangepast werd om het visualiseren van de stroming toe te laten en om de afschuifspanningsverdeling binnenin een katheterlumen te berekenen. Deze experimentele resultaten werden succesvol gebruikt voor de validatie van de numerieke modellen. Ten slotte, werden waardevolle richtlijnen voor het katheterontwerp geïdentificeerd. Deze kunnen leiden tot een meer doeltreffende vaattoegang in de toekomst. Verder worden enkele toekomstperspectieven voorgesteld: de in dit proefschrift bekomen conclusies zouden verder moeten onderzocht worden in *in vivo* experimenten. De gebruikte numerieke modellen kunnen ook verder geoptimaliseerd worden door toevoeging van tijdafhankelijke randvoorwaarden of een geavanceerd vloeistof-structuur interactiemodel. Ook is de studie van het verlies aan slotvloeistof uit de katheter tussen de behandelingen in door middel van numerieke technieken een uitdagend toekomstig onderzoeksgebied.

Numerieke modellen werden ook gebruikt om de zuurstofbeschikbaarheid in de BAL Bioartificiële Lever succesvol te beoordelen en te verbeteren. Het nieuwe bioreactormodel en de werkingscondities die voorgesteld werden in het numerieke werk, werden met succes getest in een *in vitro* studie. De voorgestelde verbeteringen leidden tot een verhoogde stabiliteit en functionele activiteit van de varkenslevercellen in de AMC-BAL. Verder werd een meer realistisch full-scale model van de AMC-BAL ontwikkeld. Hiervoor werd een nieuwe strategie ontwikkeld om de *in vitro* verdeling van de hepatocyten te kwantificeren. De combinatie van de *in vitro* hepatocytenverdeling toegepast op het full-scale computermodel van de AMC-BAL liet een meer accurate analyse toe van de perfusie en de zuurstofbeschikbaarheid voor de levercellen. Bovendien liet het *in vitro* gebaseerde model een dieptestudie toe van relatie tussen de zuurstofbeschikbaarheid voor de levercellen, hun zuurstofconsumptie en hun *in vitro* functionaliteit. Verder onderzoek naar de AMC-BAL zou zich moeten richten op het vinden van een nieuwe cellijn die de prestaties van varkenslevercellen overtreft om zo de efficiëntie en de klinische toepasbaarheid van de AMC-BAL verder te verbeteren. Daarnaast worden in dit hoofdstuk enkele voorlopig studies naar het modelleren van celgroei en metabolisme in de AMC-BAL gepresenteerd. Bij deze modellen wordt gebruik gemaakt van de numerieke en experimentele resultaten van de voorgaande studies.

De informatie in dit proefschrift kan de cyclustijd naar de klinische toepasbaarheid van dit extracorporeel, bioartificieel leversysteem verkorten. Dit zowel voor de vaattoegang als voor het klinisch apparaat zelf. Zo zou het systeem uiteindelijk hulp kunnen bieden aan de talloze patiënten met ernstig leverfalen.

Summary

A possible future therapy to bridge patients with severe liver failure to transplantation or regeneration of their own organ, is the use of a bioartificial liver. This is an extracorporeal bioreactor which is seeded with living, functionally active liver cells. In a clinical setting, plasma or blood is drawn from the patient's circulation and perfused through the bioreactor in which the active hepatocytes perform their liver-specific functions. The treated blood is then returned to the patient. To apply this extracorporeal liver support system, both a performant vascular access and a clinical applicable bioartificial liver are necessary. In this dissertation, experimental and numerical techniques are combined to gain a better insight in the transport phenomena in both the vascular access and the bioartificial liver. Also, an attempt is made to improve the performance and clinical applicability of both systems. This dissertation is thus divided in two major parts.

Part A: Central venous catheters: A vascular access for extracorporeal therapy.

Chapter I

Introduction to central venous catheters

A central venous catheter is a cylindrical tube with one or more cavities called lumina through which blood is withdrawn from the circulation, and/or returned to the patient. When this tube is inserted in one of the major veins leading to the right atrium, it is called a central venous catheter. Although it serves a simple purpose, many different catheter designs are marketed. In this chapter the most common types are discussed. To be able to make a classification between the different catheter designs, performance criteria are determined. These criteria can either be of a clinical or hemodynamical nature.

Clinical performance criteria concern all complications that accompany the insertion and subsequent use of central venous catheters. In the text, an overview is given of the possible early and late complications. A prior, in-depth evaluation of the patient, taking into account the known risk factors, and letting a trained member of staff perform the insertion, can minimize the risk of early complications. However, the late complications are more difficult to control. These include infection, thrombosis of the catheter itself or the vein in which it is inserted, and stenosis of the vein. These complications can severely limit the clinical functionality of the vascular access. Major impact factors are the catheter material, the catheter insertion site, and the catheter design.

Hemodynamic performance criteria include catheter blood flow, pressure drop over the lumen, the flow field and shear stress distribution inside the catheter lumens, and so-called access recirculation. A recommended catheter blood flow rate is 300 mL/min, while the pressure drop over the catheter must be minimized as it is limited by the maximum driving force of the blood roller pump. Moreover, an elevated pressure drop may indicate that inside the catheter, blood must flow through very narrow gaps, which lead to large blood velocities and induce highly elevated shear

forces on the blood. The latter can damage red blood cells (hemolysis) and lead to an activation of platelets, which in its turn leads to blood clotting (thrombus formation): one of the clinical performance criteria. The flow distribution in the catheter lumen is also important as stagnating blood zones may promote thrombus formation. Finally, also access recirculation must be avoided. This is the phenomenon where treated blood that leaves the catheter is immediately sucked back into the other lumen of the catheter, instead of continuing its path in the vein. As such, already treated blood is sent back to the extracorporeal circuit, reducing the efficiency of the extracorporeal treatment.

As mentioned above, numerous catheter designs are marketed, each with their specific design features. Further in the chapter, a detailed literature review is performed from which it is concluded that no significant differences exist between the most recent catheter designs, concerning the performance criteria. And yet, each manufacturer of catheter keeps throwing new catheter designs into the market with the most exotic design features, without any proof of added benefit. In the following two chapters of this dissertation, numerical simulations and experimental visualization techniques are used to assess various catheter design features. This may give us a clue which design has the key to a more performant vascular access. This information may then be used to design a more performant catheter in the future.

Chapter II

Impact of the side holes and tip location on flow, shear stress distribution and access recirculation in central venous catheters

Side holes are additional side-way entry or exit openings placed near the catheter tip. Catheter manufacturers claim they improve blood flow in the catheter lumen. By using numerical simulations ('Computational Fluid Dynamics' – CFD) blood flow through three step-tip catheter models are simulated in this chapter. The three models only differ in one aspect: either the catheter has no side holes, normal size holes according to manufacturer's specifications, or side holes with only half of the original diameter. These catheter models are each placed into a hollow tube, which models the vein in which it is inserted *in vivo*. During the simulations, special attention is paid to the hemodynamic performance criteria as defined in Chapter I. Simulation results show that the presence and size of the side holes are a major determinant of the flow and shear stress distribution in the catheter lumen. Especially the location of elevated shear stresses is influenced by the side holes, whereas the smaller side holes lead to a more extended area of elevated shear stress levels. Nevertheless, a distinct classification of the simulated catheter models based on the level of apparent shear stress is not a straight-forward task. Access recirculation is only marginally influenced by both presence and size of the side holes. There is also only a minor dependence of access recirculation on the flow rate through the catheter or the vein.

To assess whether the simulation results can be translated to the clinical setting, simulations are repeated with the catheter model now inserted in an anatomically realistic environment. For this purpose, cross-sectional slices of the right atrium, obtained via medical imaging, are segmented and three-dimensionally reconstructed.

In this model, the catheter model is inserted with its tip at the junction of the right atrium and the upper caval vein. Simulation results show that the internal flow and shear stress distribution are not affected by the change in simulation environment (*i.e.* tip location). However, access recirculation percentages differ between the catheter inserted in the vein model or in the right atrium model. Consequently, an anatomically realistic model is only necessary to accurately assess access recirculation in central venous catheters.

Chapter III

PIV validated, CFD based design to reduce shear stress and residence time in central venous catheters.

Shear stress on blood cells and the presence of zones with low blood velocities are crucial factors in the formation of blood clots. In this chapter, a combined numerical and experimental approach is used to assess these factors in different catheter tip designs. Computational Fluid Dynamics is a time and cost effective method for studying the hemodynamics in virtual catheter designs. However, as this catheter performance study requires very detailed and accurate shear stress distributions, the validation of CFD results is necessary, as mesh-independent shear stress fields –in contrast to flow fields– are difficult to achieve and are only obtained at very high (local) mesh density. Particle Image Velocimetry (PIV) was chosen as a challenging approach to obtain both high resolution flow fields and shear stress distributions inside the lumens of three different catheter models for validation purposes. A step-tip catheter with cylindrical lumens and an ‘arterial’ tip cut straight (1), cut at an angle (2) or cut straight with a sleeve entrance (3) were studied. For this, standard PIV was adapted for use in this small scale setting. This resulted in the first time ever experimental measurement of flow velocities and shear stress distribution inside a catheter lumen. The experimental results of flow and shear strain distribution in two orthogonal planes through the arterial lumen were compared to the numerical simulations. Qualitative and quantitative agreement was satisfactory. After this validation, four additional catheter tip designs were numerically simulated (seven in total): cylindrical lumen with two side holes and tip cut straight (4) or at an angle (5); concentric lumens (6) and Ash Split based design (7). Six parameters including shear stress, blood residence time, and the Platelet Lysis Index were calculated for each of the seven catheter tip designs. The latter parameter takes into account that platelet activation, an important factor in blood clot formation, does not only depend on the level of shear stress that acts on the platelets, but also on the exposure time. From the numerical analysis, it is concluded that the end-opening of a step-tip catheter is best cut orthogonally to its axis. Side holes are only recommended when the catheter tip is cut at an angle. Catheters with concentric lumina are discarded due to the highly elevated shear stress levels and blood residence time in the lumen. An Ash-Split based design has low average shear stresses as compared to the step-tip catheter, but this is offset by the elevated blood residence times as the major inflow occurs through the most proximal side holes, leaving low velocities in the distal tip zone. The information derived from these studies can lead to more patent catheters in the near future.

Part B: Bioartificial livers: Improving the efficiency of the AMC Bioartificial Liver.

Chapter IV

Liver support systems: review from Anatomy to Zoonosis

In this chapter, a comprehensive review is presented of the rationale for extracorporeal liver support systems and the challenges encountered in their design. First, an overview is given of liver anatomy, circulation, histology, physiology and pathology. From this overview, it is clear that the liver is an extremely vital organ. Failure of this organ, albeit acute or chronic, is a life-threatening situation which can only be relieved with an orthotopic liver transplantation. This procedure greatly increases survival of the patient, but nevertheless has some drawbacks: the complexity of the surgical procedure, the life-long immunosuppressive therapy and the cost for health care, the risk of organ rejection and foremost, the huge shortage of suitable donor livers. It will not surprise that the mortality on the waiting list for liver transplantation is significant: 8% on average, but strongly depending on etiology. As such, there is a large need for an alternative liver support therapy. This therapy could have a bridging function until transplantation or regeneration of the diseased liver, or a supportive function for the transplanted organs until it regains its full capacity.

Liver support systems can be divided as follows: (1) artificial systems: here only the detoxifying function of the liver is replaced; (2) biologic systems, in which only liver tissues are used extracorporeally; and (3) bioartificial liver (BAL) support systems: in these systems, a mechanical component (the bioreactor) and a biological component (liver cells) are combined in such a way that the device can substitute the full range of liver specific tasks. Further in the text, an extended literature review is given in which these different forms of liver support are described and illustrated. Focus in this dissertation is on the bioartificial liver systems as they have shown promising results in *in vitro*, animal and clinical studies. A major advantage of BAL systems, as compared to other non-biological liver support systems, is the capacity to provide a full range of metabolic functions to compensate for the complex metabolic disorders seen in ALF. In this review, special attention is paid to the design criteria of these bioartificial livers, and to the challenges encountered in the development of such a system. In particular, a lack of oxygen availability for the hepatocytes in the bioartificial liver system is generally considered as the main limitation in the clinical applicability of bioartificial liver systems.

One of the clinically applied BAL devices is the AMC Bioartificial Liver (AMC-BAL; Academic Medical Center, Amsterdam, The Netherlands, patent No: WO 97/12960). This device contains functionally active hepatocytes seeded in a non-woven mat which is spirally wound around an inner core. Gas capillaries run between the mat windings as an internal oxygenator. In the clinical setting, one billion hepatocytes are seeded in the bioreactor and the toxic plasma of liver failure patients is perfused through the system to be processed by the viable hepatocytes. The AMC-BAL has shown promising results in *in vitro* set-ups, significantly improved survival time in small and large animal acute liver failure models, and proven safety in a phase I

clinical study with ALF patients. However, *in vitro* studies showed an increased anaerobic glycolytic metabolism in the AMC Bioartificial Liver after a 4-day culture period. This may indicate local oxygen shortage in the bioreactor. In the following chapters, the perfusion and oxygen availability of hepatocytes in the AMC-BAL will be assessed using numerical modeling. Also, modifications to the design and operating conditions will be proposed to increase oxygen availability, and these findings will be tested experimentally. As numerical modeling plays an essential role in this part of the dissertation, a literature review of prior numerical work regarding oxygen transport in bioartificial liver systems is given at the end of this chapter.

Chapter V

Three-dimensional numerical modeling and computational fluid dynamics simulations to assess and improve oxygen availability in the AMC-Bioartificial liver.

In this chapter, a numerical model was developed which allows the simulation of fluid flow and oxygen transport and consumption in a hepatocyte bioreactor system. This model was subsequently applied to the AMC-bioartificial liver (Academic Medical Center, Amsterdam, The Netherlands). This bioreactor consists of a cylindrical housing in which two pieces of non-woven mat are spirally wound in series around a massive inner core. In these two pieces of hydrophilic matrix, a dense hepatocyte culture is possible. Between the windings of the mat, 300 hydrophobic gas capillaries run parallel over the entire length of the bioreactor. Through them flows culture gas (95% air, 5% CO₂). They form the bioreactor's internal oxygenating system to supply additional oxygen to the hepatocytes. Two unit volumes (micro models) were isolated from the bioreactor geometry; each consisting of a piece of non-woven mat, and surrounding fluid zones and gas capillaries. The two micro models differed only in their gas capillaries' position (either in an 'inline' or 'triangular' pattern). Also, two possible hepatocyte distributions were hypothesized: distribution (1) in which all hepatocytes are located in the non-woven mat, and distribution (2) with 50% of the cells in the mat and the other 50% in a 122 μm cell layer around the gas capillaries. These hepatocyte distributions were applied to each of the two micro models. On these four micro model configurations, flow and oxygen availability in the bioartificial liver were simulated under standard operating conditions. Oxygen availability was calculated as the percentage of cells which are able to consume oxygen at minimally 90% of their maximal O₂ uptake rate, the so-called effective hepatocyte utilization ratio ($V_{ratio} > 0.9$). Additionally, the model allowed changing the operating conditions and the bioreactor design to assess their influence on oxygen availability. As such, the optimal strategy to maximize oxygen availability in the AMC-BAL can be identified. Following operating conditions were tested: external oxygenation of the culture medium, increase in culture medium flow rate, increase of the oxygen content of the gas running through the gas capillaries, and increase of the number of gas capillaries. In addition, the importance of the internal oxygenator, the effect of the change of hepatocyte oxygen consumption in time, and the effect of the change from an experimental to a clinical setting were assessed.

Under standard boundary conditions, numerical simulations showed that the AMC-BAL cannot supply all hepatocytes with sufficient oxygen to consume oxygen at at least 90% of their maximal oxygen uptake rate. Simulations results, however, significantly differed depending on the proposed hepatocyte distribution: only 16% of the hepatocytes in distribution (1), and 29% in distribution (2) were considered to have sufficient oxygen available. The different capillary patterns of the two micro models did not influence oxygen availability. Pressure drop over the AMC-BAL and maximal shear stresses were low and not considered to be harmful. The internal oxygenator proved to be an essential part of the bioreactor as oxygen availability dropped to virtually zero if discarded. A two-fold increase in flow rate resulted in an increase in regions with $V_{\text{ratio}} > 0.9$ of only 14%. Doubling the pO_2 of the oxygenation gas ($pO_{2\text{-gas}} = 300$ mmHg vs. 150 mmHg) increased the “ $V_{\text{ratio}} > 0.9$ ” percentage significantly to almost a doubled level as compared to standard operating conditions. In comparison, culture medium flow rate had to be increased more than 10-fold to achieve similar results as with a 2-fold increase in pO_2 of the oxygenation gas. The effective hepatocyte utilization ratio could also be improved by elevating the culture medium pO_2 to carbogen level (95% O_2) or by doubling the number of capillaries. On average and for both hepatocyte distributions, these two methods led to a 2-fold increase in the amount of hepatocytes consuming oxygen at $V_{\text{ratio}} > 0.9$ as compared to the reference case. An increase in the number of capillaries was preferred over carbogen medium perfusion, since carbogen oxygen levels are considered possibly toxic. Carbogen medium perfusion also requires an additional external oxygenator. Therefore, increasing the number of capillaries by two-fold is a more easy and safe method to increase the effective hepatocyte utilization ratio. The ultimate results in improving cellular oxygen availability and effective hepatocyte utilization ratio was found when oxygenation gas $pO_{2\text{-gas}}$ was set to carbogen level or when a double number of capillaries is used in combination with a doubled $pO_{2\text{-gas}}$. $V_{\text{ratio}} > 0.9$ percentages have now quadrupled for cell distribution (1) and tripled for cell distribution (2) as compared to the reference case for both approaches. As carbogen oxygen levels are not preferred, an improved bioreactor design with double number of gas capillaries combined with a doubled oxygen concentration of the oxygenation gas was considered to be the most optimal way to maximize oxygen availability in the AMC Bioartificial Liver.

Chapter VI

Enhanced oxygen availability improves liver-specific functions of the AMC bioartificial liver

In this chapter, the improved bioreactor design and the guidelines to improve oxygen availability in the AMC-BAL, following from the numerical simulations in the previous chapter, were effectively tested in an *in vitro* study. Four configurations of the AMC-BAL were compared: (G1) *original* design, (G2) *original* design with doubled oxygen concentration of the oxygenation gas ($pO_{2\text{-gas}}$), (G3) *new* bioreactor design with 2.2-fold thinner mat and 2-fold number of gas capillaries, and (G4) the *new* bioreactor design combined with a doubled $pO_{2\text{-gas}}$. After 6 days culturing, the *new* configuration bioreactor with increased oxygenation (G4) showed significantly reduced anaerobic glycolysis, 60% higher liver-specific functions, and increased

transcript levels of five liver-specific genes compared to the standard bioreactor cultures. Changed bioreactor configuration and increasing pO_2 of the culture medium contributed equally to these improvements. Histological examination demonstrated small differences in cell organization. In conclusion, higher metabolic stability and liver-specific functionality was achieved by enhanced oxygen availability. For the first time in the research of bioartificial liver systems, this was achieved through prior numerical modeling.

Chapter VII

A full-scale model of the AMC-BAL correlated with experimental *in vitro* data.

The increase in O_2 availability between the *original* and *new* bioreactor design, simulated using the micro model approach, was persistently larger than the increase in functionality found in the *in vitro* study. This was illustrated by the fact that although a 2-fold increase in O_2 availability was predicted in the micro model study, the *new* design bioreactor with standard oxygenation did not show a significantly improved hepatic function as compared to the *original* design under standard oxygenation. This discrepancy could still be due to local limited O_2 availability or to inhomogeneous perfusion in the AMC-BAL, as the micro model approach has several limitations which preclude extrapolating results to the *in vitro* situation. Important limitations are (1) the difference between the *in vitro* cell distribution of the AMC-BAL vs. the two proposed -hypothetical- cell distributions in the micro model; (2) the observed irregular placement of gas capillaries inside the AMC-BAL vs. the equidistant location in the micro model; (3) the presence of an inlet and outflow zone in the AMC-BAL containing oxygenation gas capillaries, which was not constructed in the micro model, and (4) the imposed hepatocyte O_2 consumption rate (OCR).

A full-scale realistic model of the AMC-BAL was developed to avoid these limitations. For this, the *in vitro* hepatocyte distribution in the AMC-BAL was quantified experimentally by analyzing histological coupes of a fixed bioreactor specimen. This realistic hepatocyte distribution was subsequently applied to full-scale computer models (macro models) of the *original* and *new* design AMC-BAL. On these macro models, flow and oxygen transport and consumption simulations were performed under both standard and increased oxygenation gas pO_2 , corresponding to the G1-4 bioreactor configurations of the previous *in vitro* study. Furthermore, the influence of the imposed hepatocyte O_2 consumption parameters was studied by using two sets of values in the numerical analysis (one stringent which was used in the micro model study, and one less stringent). As possible validation, simulated culture medium outlet pO_2 (pO_{2-med}) was compared to *in vitro* measured pO_{2-med} values.

We observed a large preferential flow near the inner core in the original design bioreactor. This preferential flow, however, was absent in the new design bioreactor with a double number of gas capillaries and 2.2-fold thinner mat. This configuration also leads to a more homogenous perfusion and higher O_2 availability for the hepatocytes. Doubling the oxygenation gas pO_2 further increased O_2 availability.

Simulated O_2 availability and outlet culture medium pO_{2-med} were strongly dependent on the imposed O_2 consumption rate. Subsequently, *in vitro* hepatocyte O_2

consumption parameters were estimated by matching in numero and *in vitro* outlet $pO_{2\text{-med}}$ for different bioreactor configurations. As such, the influence of different AMC-BAL configurations on the *in vitro* hepatocyte oxygen consumption rate in the AMC-BAL was assessed. It was concluded that the hepatocyte OCR in the original and new design bioreactors under standard oxygenation (G1 and G3) is very similar, with values corresponding to literature data for high density, porcine hepatocyte culture. Doubling of the $pO_{2\text{-gas}}$ resulted in 3- (G2) to 7-fold (G4) higher hepatocyte oxygen consumption values.

Finally, the model is used to elaborate on the relation between simulated O_2 availability, estimated O_2 consumption and *in vitro* functionality. Using the stringent O_2 consumption parameters, the classification of the four AMC-BAL configurations according to simulated O_2 availability corresponded to the functional results observed in the *in vitro* study. However, culture medium outlet pO_2 under this hepatocyte OCR did not match with *in vitro* results. Using the estimated OCR, obtained by fitting numerical and *in vitro* outlet medium pO_2 values, simulation results show almost maximal hepatocyte O_2 availability in all cases. This OCR estimation analysis suggests that hepatocytes adapt their OCR to the local environment in the AMC-BAL while maintaining maximal local hepatic O_2 availability. However, as the new design bioreactor (i.e. G3) is able to sustain higher OCR values with almost maximal O_2 availability, OCR is not limited by a lack of oxygen and other factors besides absolute O_2 level and local O_2 availability must also play an important role in the regulation of hepatocyte OCR.

Using estimated OCR, all bioreactor configurations maintain maximal oxygen availability, whereas clearly differences in anaerobic glycolytic metabolism and liver-specific functionality have been shown *in vitro*. This suggests that O_2 availability (as defined in this study: % cells with $V_{\text{ratio}} > 0.9$) may not be used as an indicator of *in vitro* improvement. Similarly, the estimated OCR itself cannot be directly correlated to the increase in functional activity found *in vitro*. Although the bioreactor with highest functionality found in the *in vitro* study (i.e. G4) was found to consume most O_2 , G2 and G3 showed highly similar *in vitro* functionality, but their estimated OCR differed greatly. This proves that other factors than O_2 availability (e.g. pO_2 level, increased cell-to-cell and cell-to-matrix contact) play a determining role in anaerobic glycolytic metabolism and hepatocyte functionality between bioreactor configurations, as was already suggested for the regulation of hepatocyte OCR. Future models could include a spatial variation of V_M value in the AMC-BAL model, based on local absolute pO_2 and hepatocyte density. Subsequent simulations may show a better correlation between e.g. local O_2 availability and reduced anaerobic glycolytic metabolism in the different AMC-BAL configurations, while maintaining a validated $pO_{2\text{-med}}$. However, *in vitro* research is necessary to quantify the parameters of this model.

Part C: Conclusions and Future Prospects

Chapter VIII

Conclusions and Future Prospects

In this chapter, the major conclusions of both parts of this dissertation are summarized. For the first time, the hemodynamic performance of central venous catheters was studied using advanced numerical techniques. Also for the first time, standard Particle Image Velocimetry was adapted to allow visualizing the flow and calculate strain rate distribution inside a catheter lumen. These experimental results were successfully used for validation of the numerical models. Finally, valuable guidelines for catheter design were identified, which may lead to a more performant vascular access. Additionally, some future prospects are presented. The conclusions from the numerical studies should be investigated further in *in vivo* studies. The numerical models used can be enhanced by adding transient boundary conditions, or advanced fluid-structure-interaction to model catheter movement. Also the study of the loss of inter-dialytic locking solution by numerical techniques is a challenging future research area.

Numerical modeling was also applied to successfully assess and improve the oxygen availability in the AMC Bioartificial Liver. The new bioreactor design and operating conditions proposed in the numerical study were successfully tested in an *in vitro* study. The proposed enhancements led to an increased stability and functional activity of porcine hepatocytes in the AMC-BAL. Further, a more realistic full-scale model of the AMC-BAL was developed. For this, a novel strategy to quantify the *in vitro* hepatocyte distribution was developed. The combination of the *in vitro* hepatocyte distribution applied to the full-scale computer model of the AMC-BAL allowed a more accurate analysis of perfusion and hepatocyte oxygen availability. Additionally, the *in vitro* based model allowed an in-depth study of the relation between hepatocyte oxygen availability, consumption, and *in vitro* functionality. Future research on the AMC-BAL should focus on finding a new cell-line which outperforms the porcine hepatocytes in order to further increase the efficiency and clinical applicability of the AMC-BAL. In addition, some early research and feasibility studies on the modeling of cell growth and metabolism in the AMC-BAL are presented. In the application of these preliminary models to the AMC-BAL, data obtained in the aforementioned numerical and *in vitro* studies was used.

The information from this dissertation can reduce the cycle time towards the clinical applicability of this extracorporeal bioartificial liver system, both in terms of the vascular access and the clinical device itself. As such, it may finally offer relief for the countless patients with end-stage liver failure.

Part A: Central venous catheters
A vascular access for
extracorporeal therapy

Chapter I: Introduction to central venous catheters

1 Vascular access for extracorporeal therapy

The definition of an extracorporeal therapy, such as an artificial kidney or liver support system, is a procedure in which blood is taken from a patient's circulation to have a process applied to it in a circuit outside the body (*extra corpus*) before it is returned to the patient's circulation. As such, a means to extract and return blood from the patient – a vascular access – has to be introduced. This access should be easily available for connection to the extracorporeal circuit and should provide adequate blood flow of 200-500 ml/min [1]. After treatment, disconnecting should be possible relatively rapid. In addition, complication rates like bleeding, thrombosis and infection should be low and discomfort for the patient minimal. At present, different types of vascular access are available.

An important *first* type of vascular access are the arteriovenous fistulas (AVF). In an AVF, an artificial connection is made between the arterial and venous circulation. AVF's can be classified in autogenous and non-autogenous. When a connection between the local vein and artery is made using only native material, an **autogenous** vascular access is constructed. On one hand, this may concern a direct connection between the two local blood vessels, such as between the brachial artery and the cephalic vein (Fig. I-1). This access type is only possible if the feeding arteries are still compliant and have diameters above 2 mm. On the other hand, another option in the autogenous AVF group is via an autologous vein as a graft. The latter are also called secondary autogenous fistulas. For this, the greater saphenous vein, the basilic or brachial vein are mostly used as an autograft. If the patient has inadequate or unavailable veins to construct an autogenous vascular access, surgeons rely on grafts and consequently a **non-autogenous** fistula is placed. In this case, synthetic materials like polytetrafluoroethylene (PTFE), silicone as well as xenogeneic biologic materials like bovine and sheep vessels are used as grafts to construct the arteriovenous connection.

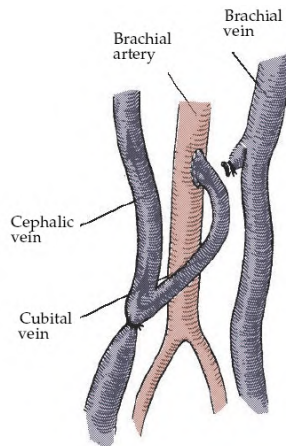


Fig. I-1: Arteriovenous fistula in the elbow region between artery brachialis and cephalic vein

Fistulas can be placed over the whole body, but by preference in the upper extremity because of the lower complication rates [2]. Surgeons choose the most distal available site to preserve more proximal vessels for possible future accesses in the case the first access fails. When all possibilities in the upper extremities are exhausted and no adequate vessels are available there, a vascular access is installed in the lower extremity.

After a period of maturation of about 6 weeks, the connecting vein in the autogenous AVF becomes more prominent and thick-walled. This process is called ‘arterialisation’. Now an easy repetitive access to the circulation can be obtained by puncturing the dilated veins. Unfortunately, an arteriovenous fistula is not always possible because of insufficient diameter or maturation of the veins. Alternatively, a non-autogenous arteriovenous connection with a synthetic arteriovenous graft can be used. These have the advantage that maturation is not needed and that they are available for puncturing after 2 to 4 weeks. However, arteriovenous grafts have a substantially higher risk for thrombosis and infection than arteriovenous fistulas and are considered second best [3]. As such, autogenous AVF have the lowest infection rates and have the smallest risk for thrombosis.

However, some patients develop a very acute need for extracorporeal therapy, such as patients with acute liver failure or end-stage renal disease. This patients often cannot rely on an AVF as a means of vascular access due to slow maturation of their fistula, combined the sometimes late referral of these patient to extracorporeal treatment [4,5,6]. Additionally, it may be impossible to create a suitable arteriovenous shunt in a patient. The latter is mostly a problem in the elderly population due to peripheral vascular diseases and diabetes mellitus [7]. This makes the **central venous catheter (CVC)** a prominent *second* type of vascular access.

A catheter is generally a cylindrical tube with one or more lumens, that can be inserted into a blood vessel. A catheter inserted into the large veins leading to the right atrium (Superior Vena Cava – SVC; Inferior Vena Cava – IVC) is called a central venous catheter. The idea to use central venous catheters as a vascular access method for extracorporeal therapy stems from the successful use in chemotherapy. Cannulation of the subclavian vein for dialysis purpose was first described by Erben *et al.* in 1969 [8]. They used two single lumen catheters inserted in both vena subclavia, both in the same vena subclavia, or one in a subclavian vein and the other in the femoral vein. In the beginning of the 1980’s, double lumen catheters were introduced. Initially, this consisted simply of a blood drawing (‘arterial’) cylindrical cannula and a coaxially placed (‘venous’) cannula that returned cleansed blood to the circulation, which were replaced after each dialysis session [9]. Catheter technology further evolved towards catheters with two lumina separated by a septum, and further to double lumen catheters with two separate lumina side-by-side (Fig. I-2).

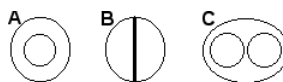


Fig. I-2: Cross-sections of the cylindrical body of different central venous catheter designs: (A) coaxial double lumen, (B) double D lumen, and (C) dual lumen catheter.

In addition to its critical role in acute vascular access, central venous catheters soon became a prominent player as a more long-term, chronic means of vascular access due to its many advantages: (1) easy insertion, removal or replacement, (2) no maturation time or venipuncture necessary, (3) universally applicable (functional in nearly 100 % of patients), (4) less hemodynamic stress to the cardiovascular system as compared to AVF. However, the use of CVC also has several disadvantages as will be discussed further in the text. As the main use of the catheter, both historically and at present, lays in the field of hemodialysis, the discussion of catheter design and performance parameters in the following text will relate to this field. Nevertheless, conclusions regarding catheter design or performance can be translated to its use in the field of (bio-)artificial liver support systems.

2 Central venous catheters

2.1 Classification and use

The use of central venous catheters as a vascular access differs significantly between Europe and the USA. The access use in 2002 for prevalent dialysis patients is 17% and 8% for the USA and Europe respectively. Also its use in incident¹ hemodialysis patients in 2002 was twice as large in USA (60%) as compared to in Europe (31%).[10]

Central venous catheters are classified into either ‘acute’ or ‘chronic’, depending on whether the catheters are expected to be used for only several days or months to years. Acute CVC (< 90 days) are designed to be placed with a minimum amount of effort. Generally, acute CVC for dialysis are relatively rigid, pointed catheters with a conically shaped tip and central lumen so that the catheter can be advanced into the vein directly over a guidewire. The guidewire is inserted through a needle placed into a vein, and the point of the catheter follows the guidewire while the catheter body itself dilates the entry site while the catheter is advanced into the vein. Chronic CVC for dialysis are soft, blunt-tipped catheters, and have a subcutaneous ‘cuff’ for tissue ingrowth or a plastic ‘grommet’² to immobilize the catheters below the skin surface. Due to their blunt shape chronic CVC have traditionally been placed through a “splitsheath,” which is a cylindrical thin walled plastic device advanced into the vein over a dilator. The dilator has a central lumen that follows the guidewire. The guidewire and dilator are then removed and the splitsheath opening is closed with a finger to prevent excessive bleeding. The catheter is then inserted through the splitsheath into the central vein. The splitsheath is split along two preformed grooves, and the halves are retracted around the catheter, leaving it in position within the central vein. More recently, techniques have been developed to allow placement of chronic CVC to be performed over a guidewire placed through a previously dilated tract, in a manner similar to acute CVC.

¹ Prevalence involves all affected individuals, regardless of the date of contraction; whereas incidence only involves individuals who have newly contracted the disease during a specified time interval

² Grommet: a plastic component connecting two separate catheter lumina

Chronic CVC have a subcutaneous tunnel leading from the vein insertion site to a distant exit site (where the catheter exits the skin). A polyester felt (Dacron™, Dupont, Wilmington, DE) cuff (or sometimes a solid plastic grommet) attached to the catheter fixes the catheter in position and prevents bacteria at the exit site from migrating around the catheter. The tunnel stops at the Dacron cuff where it melds into the fibrous tissue surrounding the cuff. Without the cuff, as in acute catheters, this subcutaneous tunnel continues all of the way to the skin exit site over time, creating potential for back-and-forth movement of the catheter and potential for pericatheter bacterial migration around the catheter.

2.2 Existing catheter designs

Fig. I-3 through Fig. I-8 represent schematic drawings of CVC used for dialysis from the 1960's to present.[11] The catheters are sometimes drawn in three separate parts displaying the external tubings and connectors, the shaft and subcutaneous components, and finally the catheter tip. Bold lines in the subcutaneous compartment delineate the aforementioned cuff. Commercial trademark names are mentioned as illustration. The design and function of these catheters is briefly described below.

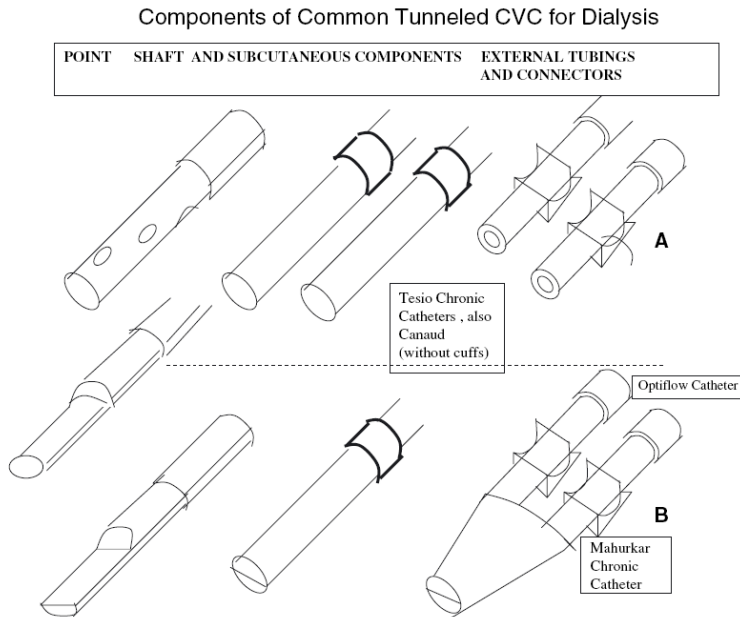


Fig. I-3: Various single body double lumen CVC designs. [11]

Canaud and Tesio catheters (Fig. I-3A) are a system of two catheters which have to be inserted side-by-side. Each catheter has a series of side holes which are arranged in a spiral pattern around the catheter tip. The largest objection to use of these

catheters came from surgeons and radiologists who did not wish to perform two separate catheter insertion procedures.

Mahurkar (Fig. I-3B) designed a CVC for chronic use out of a soft material, with a blunt tip and double-D shaped lumens. The arterial lumen is approximately 3 cm shorter than the venous lumen: the so-called 'step-tip' or 'shotgun type' catheter design. The Optiflow catheter is a variation to this design with a round shaped venous lumen and a C-shaped arterial lumen.

Fig. I-4 shows more variations of the aforementioned general design. In the Dura-Flow catheter, the arterial lumen is back-cut, creating a shape which may be less likely to be blocked by fibrosis or clot. The venous lumen also enlarges from D-shape to circular, resulting in a larger end port also making it somewhat more resistant to blockage. The Palindrome catheter is a double-D catheter with both lumens having the same length, but with oppositely angled long ports. Other variations include the LifeJet, Circle C, More-Flow and HemoGlide catheters.

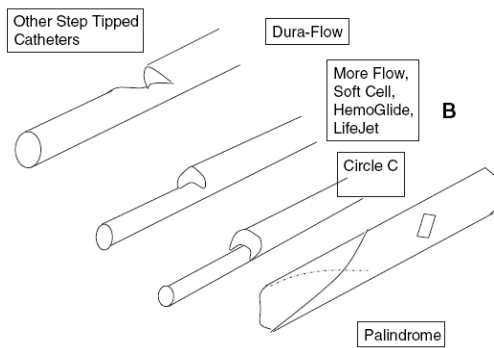


Fig. I-4: Various single body double lumen CVC designs. (cont'd) [11]

Fig. I-5 shows several dual lumen catheters. Quinton designed the PermCath dual lumen chronic catheter, an oval-shaped chronic catheter. Also using the step-tip principle, its tip was cut to create two entry ports: the shorter being the arterial and the longer being the venous return lumen. The catheter was the first chronic catheter for dialysis, and the first hemodialysis catheter to employ a subcutaneous cuff, yet it is still being placed and used. An adaptation of this shape is used in the Niagara acute catheter, having a preformed 180 degree bend to conform over the clavicle and point downward. This catheter also has two side symmetrically placed side holes near the arterial lumen tip.

Uldall created a chronic catheter with roughly the same body shape as the Quinton PermCath, but with two separate tips and a thin-wall and collapsible return lumen. The mid-body of the catheter is oval shaped.

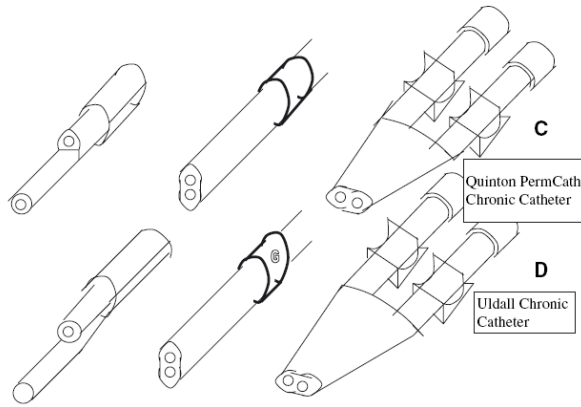


Fig. I-5: Various oval body dual lumen CVC designs. [11]

Further expanding on the concept of a single mid-body with two separate tips, the Duo Split and the Split Cath chronic catheter (Fig. I-6) have a double-D configuration in the mid-body, but separates into two separate distal tips, each with side holes in all directions. One goal of having two tips was to combine the simplicity of placement of a single-body cylindrical catheter with the low hydraulic resistance of double-D lumens and the blood flow through holes on all sides of each distal limb (similar to the Tesio catheters). These can act as a back-up flow path if the distal end-opening should get obstructed by a blood clot or fibrous sheath (see further §2.4). Another goal was to purposefully separate the limbs of the catheter, making them softer and more flexible and thus diminishing and distributing contact pressure of the catheter limbs against the wall of the vena cava. A unique feature is the step-down in diameter at the tip of the removal and return limbs. This step down is claimed to slightly increase the pressure drop at the tip, which should allow blood to enter or exit the lumen homogeneously through all of the side holes.

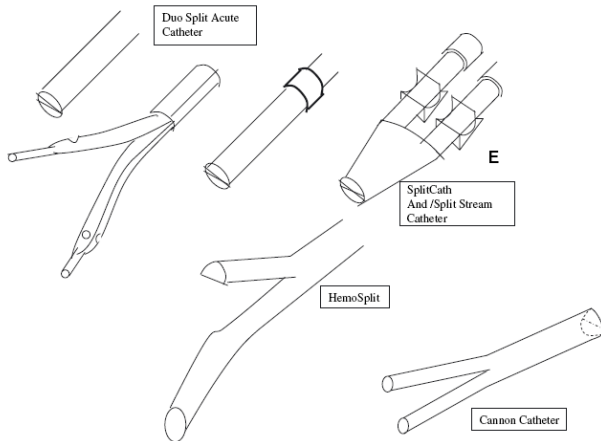


Fig. I-6: Various split-tip double lumen CVC designs. [11]

Variations on the split tip design include the Cannon catheter (Fig. I-6) which has a double shaped body ending in two separate tips, similar to the Split Cath. One major difference is that the tips are preformed to separate at an angle of about 30 degrees. This pre-set separation requires that the catheter tips be placed within the right atrium rather than “at the junction of the superior vena cava and the right atrium” (see further § Tip position). The HemoSplit catheter also has preformed split cylindrical ends leading from a double-D body, but the degree of separation of the tips is much lower, about 10 degrees.

The SchonCath (Fig. I-7) includes two catheters with intravenous and subcutaneous portions identical to the Canaud catheters and Tesio catheters (but without the subcutaneous cuffs). Instead of cuffs, there is a plastic grommet that fixes the two catheters together (delineated by bold lines in Fig. I-7). The external portions of the catheter are tunnelled independently to exit sites from the primary incisions. The Pourchez catheter also has two separate Tesio-like tips and like the Schon catheter has a cylindrical shape of the part entering the vein. However, like the Uldall or Quinton catheter the cylindrical shape continues through the subcutaneous course through the exit site.

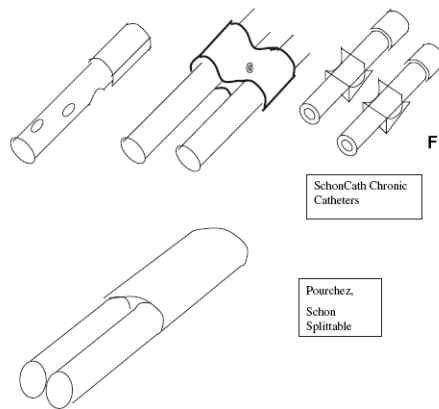


Fig. I-7: Various double lumen CVC designs. [11]

Besides the transcutane catheters discussed above, completely subcutaneous access systems have been developed.[12] These systems have multiple advantages over tunnelled catheters. The transcutane nature of the latter is considered the main cause of the large infection rate that accompanies tunnelled CVC use. Moreover, the external part of the transcutane catheter is exposed to physical damage and bacterial contamination. Completely subcutaneous systems are less prone to infection thanks to the bacteriological shield that is the human skin. Finally, they improve quality-of-life of people who desire a more discrete means of vascular access. In Fig. I-8, two such systems are presented.

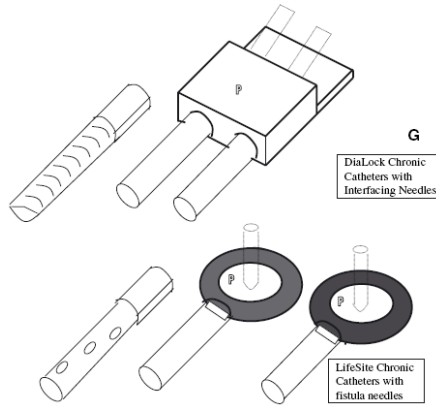


Fig. I-8: Various designs of subcutaneous access ports with dual catheters. [11]

Both have separate arterial and venous catheters, similar to Canaud catheters. The DiaLock system has a single block to receive blunted needles through the skin, connecting blood flow to wire-reinforced catheters. The LifeSite system has separate ports to receive sharp needles; catheters with side holes are used.

2.3 Insertion site and tip location

The insertion site should provide the catheter an access to a sufficient blood flow. The most common sites of insertion for transcutaneous central venous catheters are the subclavian vein (V. subclavia), the femoral vein (V. femoralis), and the internal jugular vein (IJV – V. jugularis interna).[13,14] They are illustrated in Fig. I-9.

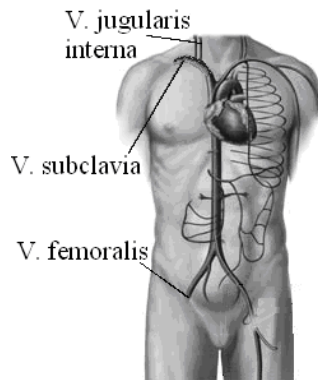


Fig. I-9: Most common insertion sites for central venous catheters.

The femoral route was first introduced in the 1960's as an alternative for peripheral arteriovenous shunts and is until present the access point by choice in case of an

emergency. This access route is particularly suitable for unmanageable or uncontrollable patients or for patients with respiratory difficulties.

The subclavian insertion, introduced in the 1970's, was the most widespread insertion site during the 1990's. Nowadays, nephrologists discourage this insertion route because it has become associated with an increased risk for stenotic and thrombotic complications (see §3). There is also a contra-indication in patients with respiratory difficulties. As such, this insertion site is the second choice for long-term vascular access.

The most recommended insertion site for chronic catheter placement is via the right internal jugular vein. Its popularity is mainly due to the many complications which plagued the subclavian route. Access via the neck is less prone to infection and to the other complications of the subclavian route. Additionally, there is no risk of compression of the catheter between rigid structures in the body, as e.g. could be the case in a catheter placed in the subclavian vein between the first rib and the clavicle. Also, the right IJV is preferred over the left IJV as the former is larger and gives a more direct route towards the right atrium.

With the body of the catheter in the superior or inferior caval vein, the catheter tip is either located in the caval vein itself, at the junction of the caval vein with the right atrium, or completely in the right atrium. It should be noted that the catheter is inserted with the patient in a supine position, but for example when the patient sits in a chair, the catheter tip may retract as much as 1 – 2 cm, depending on the patient's body habitus.

2.4 Clinical performance: complications

Catheter placement and subsequent use always involve some risks to the patient. The possibility of a complication, however, can be limited by adhering strictly to the prescribed medical guidelines and procedures. Complications associated with catheter use can be classified in two categories: immediate or early complications, versus delayed complications.[13]

2.4.1 Immediate complications

Immediate complications occur within minutes or hours of insertion of the catheter. The severity of the symptoms will distinguish minor forms from the major forms that could jeopardize the medical prognosis. Prior, detailed evaluation of the patient, taking into account the risk factors and carrying out the appropriate techniques using a trained operator, will minimize the incidence of these complications. Table I-1 lists several minor and major acute complications.

Table I-1: Early complications associated with CVC use

Minor complications
Difficulties with insertion (anatomic anomalies, previous thrombosis or stenosis in vein)
Persistent pain (head, shoulders, legs)
Hemorrhage, localized hematomas
Inflammation or infection of the skin puncture site
Early malfunction (malposition)
Major complications
Trauma (pneumo- and/or hemothorax: accumulation of air/blood in the thoracic cavity)
Anaphylactic reactions (allergy to the material or disinfectant)
Arrhythmia (extra ventricular systole, ventricular fibrillation)
Air embolism
Perforation of anatomical structure (atrium, inferior vena cava)

2.4.2 Delayed complications

The onset of delayed complications normally happens after several days' use of the catheter. The major delayed complications can be divided in three groups: (a) infection, (b) thrombosis, and (c) stenosis.

a) Infection

Any central venous catheter carries an increased risk for infection.[15,16] These infections are a result of infectious micro-organisms being introduced into the vein. It is estimated that 50% to 70% of all catheter losses are caused by infections. [15,16] Infections associated with catheter use can be classified into two categories: local infection, and generalized or systemic infections.

Localized infections of the skin puncture wound and/or the subcutaneous pathway are the most frequent. The incidence of localized infection is estimated to be between 3 and 9 episodes per 1000 patient-days. A puncture wound infection can be cleared using appropriate local treatment and a systemic antibiotic. Tunnel infections spread along the subcutaneous pathway. They require immediate removal of the catheter and systemic antibiotic treatment. These infections are frequently caused by skin bacteria moving along the subcutaneous pathway from the exit site of the catheter. As such, localized infections can act as an entry point for systemic infections.

Systemic infections, bacteremia or septicaemia present as serious and acute septic episodes. One day bacteremias usually have transient (24h to 48h) episodes with fever attacks. In this case, with suitable treatment, the catheter can be preserved. However, the catheter is often covered by a biofilm that confines the colonizing bacteria. For this reason, the lumina of the catheter need to be cleansed by fibrinolysis, and at the same time, a strong in-situ and systemic antibiotic treatment should be started. On the other hand, if a septicaemia is confirmed, the catheter must be removed immediately and an analogous double antibiotic treatment should be given.

Patient groups with increased risk for infections include patients with a history of bacteremia or with HIV infection. These patients are also at a larger risk for

endocarditis or vertebral osteomyelitis³. Other factors as age, sex or diabetes have not shown to be risk factors in catheter infections.[17]

b) *Thrombosis*

A second group of delayed complications is thrombosis. When a foreign body enters the circulation, inevitably this will lead to formation of protrombin by activation of the coagulation cascade and of the complement system, and to formation of a fibrin network which acts as a web for circulating platelets. In this way a thrombus is formed, which is potentially very dangerous. The risk for thrombus formation depends on the presence of stagnating blood zones in and around the catheter, the hemo-(in)compatibility of the catheter material, and on the prior history of the patient regarding thrombosis.

Thrombotic complications can be classified as extrinsic or intrinsic.[18] Intrinsic thrombosis is the most common form. These thrombi may be attached intraluminal, or to the outer surface of the catheter. An intraluminal thrombus may be avoided by locking the catheter with an anticoagulation solution during the intradialytic period. Traditionally, heparin is installed in the catheter lumina during non-function, but there are no studies to support this practice. Moreover, an increasing number of reports are published showing that leakage of heparin from the tip of the catheter and especially via the side holes, can cause unintentional systemic anticoagulation and clinically relevant bleeding episodes.[19] When the locking solution has leaked from the catheter tip, the stagnant blood that comes in place will clot and form a catheter tip thrombus. Intraluminal and catheter tip thrombi may completely obstruct the catheter lumen. Reopening the catheter lumen can be done mechanically (with a guidewire) or chemically (via fibrinolysis).

Another common type of intrinsic thrombus, however, is the fibrin sheath thrombus. This concerns a sleeve of fibrin that surrounds the catheter starting at the point where it enters the vein and extending further in the direction of the catheter tip. The tip can become completely surrounded and the fibrin sheath can then act as a kind of flap-valve that will allow return but prevent withdrawal of blood. This type of thrombus can also be removed by fibrinolysis. However, in extreme cases a complete removal of the catheter is warranted.

An extrinsic thrombus is a thrombus which develops completely external from the catheter. It is assumed that movement of the catheter tip causes endothelial damage, which results in the formation of a thrombus (i.e. mural thrombus) that is attached to the wall of the vessel or the atrium at the point of contact. Besides the obvious danger of a narrowing of the blood vessel (stenosis) or atrium, the tip of the catheter itself may become encased in this thrombus, interfering with catheter function. A thrombus may also be caused by the presence of a stenosis in the blood vessel, in which downstream flow patterns are created where stagnant or slowly recirculating blood velocities promote blood clotting. In any case, removal of the catheter and an anticoagulation therapy is necessary.

³ Vertebral osteomyelitis: infection of the bone or bone marrow of the spinal column.

c) Stenosis

The final group of delayed complications of catheter use is stenosis of the vein. This complication is closely coupled with the formation of extrinsic thrombi. As previously mentioned, endothelial damage originating from the catheter movement against the vessel wall could result in an ingrowth in the blood vessel, which reduces the cross-sectional flow area. This can result in swelling of the ipsilateral extremity.

2.5 Hemodynamic performance

2.5.1 Catheter blood flow rate and pressure drop

Although there is never a continuous linear correlation between blood flow through an extracorporeal artificial organ (albeit a kidney or liver replacement therapy) and solute exchange or clearance, it is clear that the achievement of a sufficient blood flow is a major requirement for a vascular access. For renal replacement therapy, the Dialysis Outcomes Quality Initiative (DOQI) project founded by the National Kidney Foundation (NKF) sets blood flow rate guideline of 300 mL/min.[1]

The blood flow through the catheter (Q_B) is linearly related to the pressure generated by the blood pump (P), and inversely related to the hydraulic resistance of the catheter (R). (Eq. I-1)

$$Q_B = \frac{\Delta P}{R} \quad \text{Eq. I-1}$$

Because of the relative small diameter of the catheter lumina, the flow through the catheter can be assumed to be laminar. Even for a 400 mL/min blood flow rate, a dynamic blood viscosity μ of 3.5 mPa.s, a blood density ρ of 1060 kg/m³, and an inner diameter D of 2.1 mm, the Reynolds number (Eq. I-2) is less than 1250 (with average velocity $v = 1.92$ m/s).

$$Re = \frac{\rho \cdot v \cdot D}{\mu} \quad \text{Eq. I-2}$$

This is well below the turbulent transition threshold of 2300. As such, the Poiseuille law for laminar flow through a cylindrical tube with circular cross-section is applicable (Eq. I-3, with L = length of tube, ΔP = pressure drop).

$$\Delta P = \frac{128 \cdot \mu \cdot L \cdot Q}{\pi \cdot D^4} \quad \text{Eq. I-3}$$

From Eq. I-1 and Eq. I-3, it is clear that the hydraulic resistance of a catheter is linearly related to its length, and related to the fourth power of its inner lumen diameter. As such, with the same pressure drop, flow can be doubled when the diameter is increased by only 19 %. A 50% increase in diameter increases flow five-fold, whereas doubling the diameter increases flow 16-fold, if the catheter is the only source of resistance and all other parameters remain constant. However, the diameter of a catheter is limited as it still has to be able to fit in the inserting vein without significant stenosis.

Nevertheless, the hydraulic resistance of a catheter should be kept as low as possible: the blood pumps which are used are roller pumps, which in principle are volumetric pumps. However, their working principle relies on the elasticity of the pump-tubing segment to expand and refill the segment on the inflow side while it is subjected to a significant negative pressure. Although the pump segment of the blood tubing is specially made from very resilient materials, refilling is less complete as the negative prepump pressure falls with increasing hydraulic resistance of the catheter. As such, effective blood flow drops below the theoretical blood flow rate should the pump be perfectly volumetric. Also, an elevated hydraulic resistance may be due to high local pressure drops in isolated parts of the catheter lumen. In this case, local elevated pressure gradients will cause high flow velocities in narrow catheter segments (tip / side holes), which subsequently induces elevated shear stresses. The latter can cause damage to white and red blood cells, and can activate platelets which is a precursor for thrombus formation (see see Chapters II and III).

2.5.2 Internal flow and shear stress distribution

A performant catheter design is characterised by a highly homogeneous inflow and outflow of blood. Zones with low blood velocity or zones where blood locally recirculates, should be avoided at any cost as this may promote blood clotting. As mentioned in the previous paragraph, also local elevated shear stresses must be avoided as much as possible as they can induce hemolysis or at least some degree of platelet activation which can also lead to thrombus formation. However, the amount of damage to blood cells is not only dependent on the level of shear stress, but also on the exposure time of the blood cells to a certain level of shear stress. In light of this, combined knowledge of both the flow and shear stress distribution is essential to assess a catheter's hemodynamic performance. (see Chapters II and III)

2.5.3 Access recirculation

Access recirculation is the phenomenon where blood, which has been processed in the extracorporeal circuit and is returned to the venous circulation via the 'venous' lumen, is re-aspirated directly by the blood withdrawing 'arterial' lumen of the catheter, instead of flowing further downstream in the vein. As such, already treated blood is again sent through the extracorporeal circuit, reducing the fraction of untreated blood in the extracorporeal system. Consequently, precious flow rate and treatment time (= patient time) is lost. Access recirculation must be avoided at all costs to maximize the efficiency of the extracorporeal treatment.

In a step-tip catheter with normal connections to the blood pump (i.e. shorter lumen draws blood; longer lumen returns blood), recirculation is virtually impossible (see dashed line in Fig. I-10A). However, recirculation is possible if the direction of blood flow in the vein reverses. This is possible if the blood flow through the vein drops below the value of the catheter flow rate (200 – 400 mL/min). In central venous catheters, this is almost never the case as the caval veins are the veins with very large flow rates (2-3 L/min). However, other factors may influence access recirculation with normal catheter connections, such as: vortices in the vein flow due to the presence of the catheter itself or due to blood clots adhered to the catheter

[20], temporary reversal of vein flow during systole; or tricuspid heart valve regurgitation. Nevertheless, access recirculation in a typical step-tip catheter with normal connections is generally negligible.

However, the situation changes when blood line connections with the blood pump are reversed. Blood now exits upstream of the blood withdrawing lumen and recirculation is virtually inevitable (see dashed line in Fig. I-10B). Access recirculation percentages, defined as the flow of cleansed blood back through the inflow port directly from the outflow port, expressed as a fraction of the inflow rate [21], can now range up to 10 – 30%. This leads to a considerably longer treatment time. Although there is no apparent need to reverse catheter connections, this technique is often used to clear out the ‘arterial lumen’ from any obstructions. Reversal of the lines can also be due to medical (mal)practice: when regular connections render no or insufficient blood flow, the dialysis technical staff often reverses the lines to improve blood flow [21].

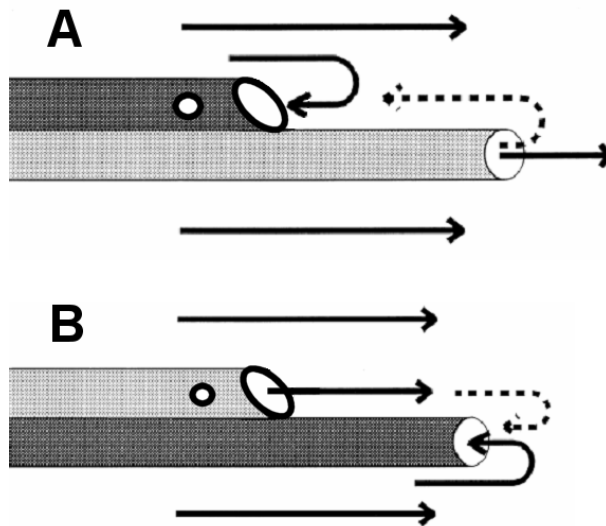


Fig. I-10: Access recirculation in a step-tip catheter with (A) normal, and (B) reversed catheter connections. Dashed line illustrates the flow path of recirculated blood. Upstream recirculation in (A) is virtually impossible, whereas recirculation in (B) seems inevitable.

3 Determinants of CVC performance

3.1 Insertion site

The choice of the catheter insertion site has a major influence on the incidence of systemic infection and bacteremia. This is illustrated in Fig. I-11.[22] This graph shows the risk for infection in function of time for acute dialysis catheters placed via the femoral or internal jugular vein. The infection risk is always larger in the femoral route, with a significant rise in infection risk after one and three weeks.

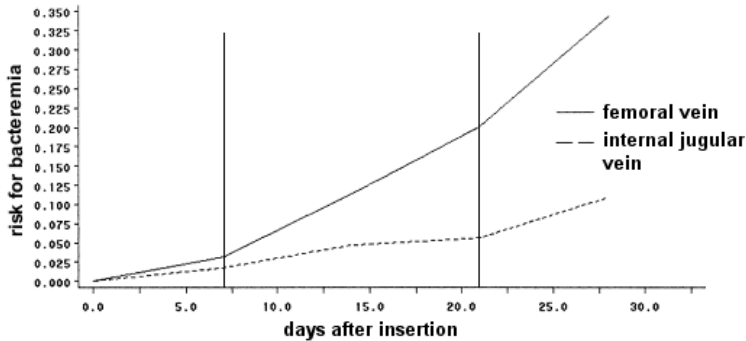


Fig. I-11: Evolution of risk for bacteremia in function of days after insertion of a CVC via the femoral or internal jugular vein. [22]

Additionally, multiple studies show that stenosis and thrombosis have a significantly higher incidence rate when the catheter is inserted via the subclavian route as compared to via the internal jugular vein.[18,23,24] Also recirculation percentages have been shown to be dependent on insertion site, with femoral catheter having significantly more recirculation.[25]

3.2 Tip location

The correct position for the tip of a central venous access catheter remains a point of continuing debate (for a thorough review: see [26]). The traditional approach has been to place the catheter tip within the vena cava. However, many researchers believe that the performance and durability of the catheter will be improved by positioning the catheter tip within the upper right atrium. To add to the confusion, manufacturer's instructions for placement of most CVC for dialysis state that the tip of the catheter should be placed 'at the junction of the superior vena cava and right atrium'. Depending on whether the arterial lumen or venous lumen tip is positioned at this junction, and taking into account the movement of the catheter tip with any change in body position, it is clear that even if there were a clear advantage of a certain catheter tip position, the exact positioning itself is a complicated procedure.

Concerning hydraulic performance, positioning the tip of a hemodialysis catheter into the SVC or higher can limit its ability to achieve this high level of performance. The catheter tip may “suck” against the adjacent vascular wall when aspiration is applied, thus reducing the aspirated blood flow rate or inducing endothelial damage to the blood vessel. This can also occur if the catheter tip is positioned too far within the right atrium. Several clinical studies have demonstrated that the performance and durability of hemodialysis catheters is improved if the tip is positioned within the right atrium. Mandolfo *et al.* [27] evaluated the performance of tunnelled hemodialysis catheters in 57 patients and reported that catheters with tips positioned in the right atrium had a statistically significant 10% and 17% higher blood flow than those with tips positioned in the SVC or inferior vena cava, respectively. Similarly, Petersen *et al.* [28] reviewed a series of 141 patients and reported that catheter malfunction (e.g. no blood return with aspiration) was minimized when the catheter tip was located within the right atrium. The investigators found that there was a significant increase in catheter malfunction when the catheter tip was located more than 4 cm superior to the SVC/atrial junction. These results indicate that malfunctions can be minimized in catheters by locating the catheter tip as close to the superior vena cava/right atrial junction as possible, or slightly inside the right atrium. To ensure proper location of the catheter tip, placement should be performed under fluoroscopy, and a radiograph should be obtained immediately following placement, with the patient in the upright position.

3.3 Catheter design

3.3.1 Cuff

As previously mentioned, the use of a catheter with a cuff or a prolonged subcutaneous tunnel provides an excellent barrier for bacteria. This is the main reason why chronic catheters are less prone to infections as compared to acute catheters.

3.3.2 Material type

Concerning intrinsic thrombosis, the catheter material type is very important. A variety of materials have been used for the construction of central venous catheters. Certain materials such as Teflon or polyethylene have been reported to be particularly thrombogenic, whereas silicone catheters are biologically inert and more resistant to thrombosis. Polyurethane, a commonly used material for catheter construction, includes a broad class of thermoplastic polymers that have an intermediate level of thrombogenicity.[11,26]

3.3.3 Side holes and catheter tip design

As illustrated in §2.2, many different catheter types are available. The design of a catheter, and more specifically of its tip, will determine the local flow pattern and shear stress distribution inside the catheter. As mentioned above, this has an impact on some of the clinical performance parameters. Also the occurrence of access

recirculation in both normal and reversed catheter connections is largely influenced by its tip design. Nevertheless, the geometry and tip design of catheters have been determined mainly by methods of trial and error.

A particular feature in a catheter tip design is the presence (or absence) of side holes. Multiple side holes were thought to be necessary to secure sufficient inflow in case of obstruction of some side holes by a blood clot or fibrous sheath, or when the catheter was placed close to the vessel wall. However, Twardowski *et al.*[29] suggested side holes at the distal catheter tip may be harmful for the following reasons:

- Loss of heparin locking solution: the heparin does not reach the catheter tip or leaches out from the side holes.
- Side holes created by drilling typically yield rough edges, as seen with electron microscopy. These rough edges may provide anchor sites for clots.
- Clots anchored in the side holes are difficult to remove or dissolve with the use of heparin.
- Clot formation on the catheter is often seen beyond the side holes. (Fig. I-12)
- Clot is formed on the outer surface, extends through the side holes into the catheter, which makes aspiration to clear the distal clot before start of the extracorporeal treatment, impossible.
- If the distal inflow bore is occluded and blood flows through the side holes, it is likely that vein intima is sucked into the catheter side holes. This causes intimal damage contributing to formation of clot and vascular stenosis.



Fig. I-12: Clot seen at the catheter tip. The clot is anchored in the distal side holes and extends into the catheter. Below, the clot is seen after extraction from the catheter. A cast of the side holes is seen on the clot. The lighter color of the distal clot indicates chronicity.

Specifically concerning side holes, few studies are available in literature. In a retrospective *in vivo* study, Tal *et al.*[30] compared flow rates, infection rate, and survival of *side hole* vs. *non side hole* hemodialysis catheters over a 16-month period. Patients were arbitrarily assigned to either a Mahurkar cuffed dual lumen tunnelled catheter with side holes or an identical catheter without side holes. No significant

difference in mean blood flow rates between the catheters was found; only a slight trend for lower flow rates in the catheter without side holes. Oddly, the only significant difference was the infection rate: per 1,000 catheter days infection rates were 2.545 with side holes and 0.254 without side holes ($p < 0.001$). Slightly improved catheter survival ($p < 0.05$) was thus recorded with the non side hole catheters. The rationale behind this is still unknown, but a possible reason for increased infection in catheters with side holes may be that a clot, which possibly occur more often when side holes are present, acts as a nest for infection.

In another experimental *in vitro* study by De Wachter *et al.* [31], pressure drop-to-flow relation of four types of catheters were measured to determine their hydraulic resistance: Tesio, Ash Split, Duo Flow (concentric catheter), and the Duo Split. It was concluded that closing the side holes did not have an impact on the hydraulic resistance of the Tesio or Ash Split catheter. However, a significant rise in pressure drop was measured when closing two side holes in the arterial lumen of the Duo Flow catheter and the Duo Split. This is understandable when looking at the catheter design: the Duo flow is a concentric catheter whose arterial lumen only has a series of side holes as entrance, and no end-opening. Closing the two most proximal side holes greatly reduces the inflow area and thus a significant increase in pressure drop is expected. Also in the Duo Split catheter (see §2.2), the closure of very large side holes as compared to the small end-opening gives a significant reduction in inflow area and thus an analogous increase in pressure drop.

More *in vivo* studies are available in literature, which generally assess and sometimes even compare in a controlled, randomized, and prospective manner, entire (i.e. not any specific design feature) catheter designs in terms of flow rates, infection rates, survival and access recirculation.

Senécal *et al.* [32] compared access recirculation rates in the Opti-Flow and High-Flow catheters. The two catheters delivered high blood flow rates without high recirculation rates (on average $\sim 1.5\%$). When connections were reversed, both catheters resulted in similar recirculation percentages ($\sim 18\% - 26\%$). Notably, recirculation did not increase significantly with rising catheter blood flow rate. Similarly, Twardowsky *et al.*[20] measured approx. 2% and 14% recirculation rates in both PermCath and Vas-Cath catheters with respectively normal and reversed connections.

Trerotola *et al.*[33] randomized 64 patients to the Ash-split catheter and 68 to the Opti-flow. Although the authors concluded that the Ash-split catheter had a better survival, the differences seemed to be caused completely by insertion problems (kinking) and manufacturing faults (broken hubs). There were no differences in catheter-related bacteremia and late flow problems despite large differences in tip construction. Opti-Flow delivered higher flow rates in some cases, but this was offset by higher recirculation.

In a prospective randomized study, O'Dwyer *et al.*[34] compared a standard step-tip hemodialysis catheter (PermCath) with a newer split-lumen catheter (Ash Split). This study revealed no significant differences in blood flow rate or catheter failure. Richard *et al.*[35] compared 38 Ash-split, 39 Opti-flow, and 36 Tesio

catheters. Tesio catheter mean insertion time (42 min) was significantly longer than that of Ash-split (29 min) or Opti-flow (30 min) catheters. There were more insertion complications related to Tesio catheters. Mean flow rates and catheter-related infections were not significantly different among the catheter groups. From these studies in tunnelled catheters, it can be concluded that double lumen catheters are preferred over two single lumen catheters and that, currently, no double lumen catheter design has shown to be superior over another.

4 Rationale and research outline

Many catheter designs are marketed nowadays. However, the geometry and tip design of catheters have been determined mainly by methods of trial and error. No real benefit of one catheter type over another has been found in studies comparing *in vivo* catheter blood flow rate, infection rate, or catheter survival.

However, very little basic research has been performed to assess the influence of specific design features of catheter tip designs (such as side holes), on the catheter's hemodynamic performance. Until present, knowledge of the internal flow and shear stress distribution inside central venous catheters, and insight in how the tip design influences these important parameters of clinical and hemodynamic performance, is non-existent. The research presented in the following chapters may lead to a better understanding of which design criteria a performant catheter should meet. Results may be used to design a new catheter type 'bottom-up', instead of drawing a *new* random design without any scientific basis.

For this purpose, the influence of the presence and size of side holes, and of the catheter tip location on the flow, shear stress and access recirculation of a step-tip central venous catheter is assessed in Chapter II. A step-tip catheter with side holes open, closed or reduced in size is simulated inserted in a vein or in an anatomically realistic three-dimensionally reconstructed right-atrium model. Qualitative and quantitative differences are discussed. This is also the first study which uses state-of-the-art Computational Fluid Dynamics simulations to address this topic.

In Chapter III, a more in-depth analysis of the possible blood clot and platelet activation risk is made. Focus of this hemodynamic study is the comparison of seven different catheter tips. The comparison is based on several calculated parameters in the catheter tip zone, such as blood residence time, shear stress, and platelet activation index. Since this analysis requires accurate shear stress calculations, special attention was paid to the validation of the numerical results. For this, an experimental flow field visualisation technique called Particle Image Velocimetry (PIV) was adapted to the small scale of the catheter lumen. As such, for the first time in literature, flow velocities and strain rates *inside* a catheter lumen were measured experimentally. The validation is provided by comparing flow and shear strain values in two measurement planes through three different catheter designs with numerical results.

Chapter II: Impact of side holes and tip location on flow field, shear stress distribution and access recirculation in a central venous catheter

Central venous catheters are widely used as a hemoaccess method for extracorporeal therapy. In this study, the performance parameters (velocities, pressure drop, shear stress, access recirculation) of a shotgun type dual lumen central venous catheter (Niagara, Bard Access Systems) are analyzed using computational fluid dynamics. Side holes are left open, closed or reduced in size to assess the influence of this design feature. Initially the catheter is inserted in a tube which represents the vena cava. In the 'arterial' luminal tip, wall shear stresses over 50 Pa are common and peaks attain 350 Pa at a 300 ml/min blood flow rate. The side holes' presence appears to affect the location but not the level of these elevated shear stresses. Halving their diameter causes elevated shear stress to appear in a more extended region. Simulated recirculation percentage is nil in normal catheter use, but attains 13 % with reversed catheter connections, varying slightly with catheter or vein blood flow rate. The results of fluid flow, shear stress distribution and access recirculation of the catheter in the tube model are compared to those in an anatomically realistic right atrium model, which was three-dimensionally reconstructed. Only access recirculation percentages differed significantly between the models and were thus dependent on catheter tip location. It is concluded that most catheter's specific hemodynamic properties can be deduced from a tube model.

The contents of this chapter were adapted from *Artif Organs* (2004); 28(7): 639-648

Computational fluid dynamics-analysis of the Niagara hemodialysis catheter in a right heart model

G. Mareels, D.S. De Wachter, and P.R. Verdonck

1 Introduction

Catheters are widely used as a hemoaccess method for safe delivery of hemodialysis therapy to both acute and end-stage renal disease patients. Central venous catheters are often the first choice access method for patients entering a dialysis program in the case of late referral [4,5,6] or when no suitable arteriovenous shunt can be created. The latter is sometimes a problem in the elderly population and more specifically for diabetics [7]. A quantification of hemodialysis performance is provided by the Kt/V -index (K = dialyzer urea clearance, t = duration of dialysis, V = distribution volume) [36,37]. The blood flow rate through the catheter, hence through the dialyzer (K), is hereby one of the main characteristics. In order to obtain an adequate Kt/V -index, higher flow rates through the dialyzer will result in shorter treatment time. Nevertheless, as no linear relation between blood flow rate and solute clearance exists [21], it is not required to strive for maximal flow rate. In addition, elevated flow rates combined with the small diameter of the catheter lumen require high pressure gradients which in their turn will induce elevated shear rates. The latter are believed to be responsible for mechanical hemolysis [38,39,40]. Yet, local flow velocities and shear rate values must not become too low as this may cause thrombus formation [41] and platelet adhesion and aggregation [42,43].

Apart from blood flow rate and shear stress, another important parameter in the performance of central venous catheters is the recirculation percentage. Access recirculation in central venous catheters is defined as the flow of cleansed blood back through the inflow port directly from the outflow port, expressed as a fraction of the inflow rate [21]. Thus the inflow concentration of solutes is diluted, which reduces the driving force for diffusion across the dialyzer membrane. Although not all solutes are equally affected by a given percentage of access recirculation [21], reducing the recirculation is a main goal in catheter use and design in order to optimize dialysis treatment time.

Many features of catheter design claim to improve its hemodynamic performance characteristics: particularly the use of catheter side holes is very popular amongst catheter manufacturers (PermCath catheter, Kendall Healthcare Products Co, Mansfield, Massachusetts, USA; Hickman, VasCath and OptiFlow catheter, BARD Access Systems, Salt Lake City, Utah, USA). Their use, however, is highly controversial. The presence of side holes could be harmful as Twardowski *et al.* [29] suggest. They observed rough side hole edges by scanning electron microscopy and clots anchored in the holes of removed catheters. The main goal of the side holes, to provide a back-up blood path when the end hole is obstructed by a fibrin sheath or a blood clot, is yet to be proven. Furthermore, in-depth research on their influence on flow dynamics and on performance parameters such as recirculation is virtually non-existent.

In this paper the local hemodynamics of the Niagara catheter are assessed by means of a computer model, to spot possible design issues. Adoption of this information by catheter manufacturers could ultimately lead to more performant catheters.

2 Materials and Methods

2.1 Catheter model

The catheter studied is the Niagara catheter (BARD Access Systems, Salt Lake City, Utah, USA), a dual lumen acute hemodialysis catheter (Fig. II-1). Its design is of a “shotgun” type. The arterial lumen, which withdraws blood from the vessel, has a round cross section with an internal diameter of 2.10 mm and is 180 mm in length. The apical end is cut at an angle of 33° and has two symmetrically placed, round side holes at 7 mm distance from the tip, each with a diameter of 1.2 mm. The venous lumen, which returns cleansed blood to the circulation, is also cylindrical with an internal diameter of 2.10 mm, but is 210 mm in length. It has no side holes. These dimensions were determined from a single specimen. From the connector to the apex, the first 97.2 mm of the catheter is eliminated from the three dimensional model to reduce CPU and memory requirements. The model is constructed with the CAD package SolidWorks 2000 (SolidWorks Corporation, Concord, Massachusetts, USA) and exported into the grid generation software Gambit 2.0 (Fluent Inc., Lebanon, New Hampshire, USA) via the Parasolid data format.

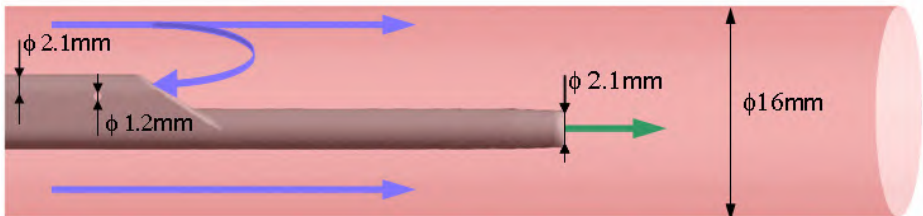


Fig. II-1: Partial three dimensional view of the central part of the simulation environment with the dual lumen Niagara catheter inserted in a hollow tube. Arrows indicate blood flow with normal blood line connections.

2.2 Blood model

The fluid representing the blood was modeled as a non-Newtonian, shear-thinning fluid with constant hematocrit and temperature. Blood density is fixed at 1053 kg/m^3 . The blood viscosity is related to the shear rate by means of the bi-exponential blood constitutive equation (BCE - Eq. II-1) provided by Zhang *et al.* [44]. This BCE can be related to red blood cell (RBC) aggregation and deformability. Considering that the apparent blood viscosity is decreasing rapidly at low shear rates with RBC aggregation and decreasing slowly at high shear rates with RBC deformability, the BCE may be represented as a bi-exponent equation containing two different exponent terms (Eq. II-1):

$$\eta = \eta_e + \eta_D \exp(-\sqrt{t_D \dot{\gamma}}) + \eta_A \exp(-\sqrt{t_A \dot{\gamma}}) \quad \text{Eq. II-1}$$

- With:
- $\eta_e = 2.7 \text{ mPa.s}$, $R_D = (\eta_D / \eta_e) - 1$: viscosity index, they may be related to RBC deformability ($\eta_D = 4.833 \text{ mPa.s}$).
 - $t_D = 0.11 \text{ s}$, $t_A = 4.93 \text{ s}$: represent the sensitivity of RBC deformability and aggregation to the shear rate.
 - $R_A = (\eta_A / \eta_e) - 1$: viscosity index, may be related to RBC aggregation ($\eta_A = 3.915 \text{ mPa.s}$).
 - $\dot{\gamma}$: strain rate, which is defined as $(2D_{ij}D_{ij})^{1/2}$ with $D_{ij}D_{ij}$ the inner product of the strain rate tensor $D_{ij} = \frac{1}{2} \left(\frac{\partial u_i}{\partial x_j} + \frac{\partial u_j}{\partial x_i} \right)$.

Importantly, the parameter values of this blood viscosity law were fitted to experimental viscosity measurements of chronic renal failure patients which underwent five hemodilution treatments.[44] However, simulation showed identical results as compared to using a constant viscosity equal to the asymptotic value of the aforementioned BCE (2.7 mPa.s). This is understandable as in the BCE, viscosity reaches this asymptotic value already at strain rates of 100 s^{-1} , and strain rates inside and surrounding the catheter model far exceed this level.

2.3 Validation of the calculation grid and the numerical method

The grid and the numerical method are validated by comparing simulation results during regular catheter use to experimental data or theoretical values. During previous experiments the pressure-flow relation of the arterial lumen of the Niagara catheter has been deducted. In the setup used [31] the catheter flows into a reservoir. To mimic this reservoir, the flow rate of the vein surrounding the catheter was set to nil. Furthermore, the omitted part of the arterial lumen was included in these simulations, equipped with a similar mesh. The flow through the simulated part of the venous lumen was validated by calculating the pressure drop with the Poiseuille law in accordance with the laminar flow in this lumen.

2.4 Numerical simulation of the catheter in a tube model

In this study, we use state-of-the-art computational fluid dynamics (CFD) [45,46] techniques to gain insight in the flow field in and around the Niagara dual lumen hemodialysis catheter and to analyze its performance characteristics such as blood flow rate, pressure drop, and shear stress distribution in different case studies to assess the influence of the presence and the size of catheter side holes. We will also take a closer look at the recirculation percentage, especially when catheter

connections are reversed. Here, cleansed blood is released back to the vessel upstream to the blood withdrawing end hole. Although recirculation seems inevitable [20], this technique is often used to clear out the 'arterial lumen' from any obstructions. Reversal of the lines can also be due to medical (mal)practice: when regular connections render no or insufficient blood flow, the dialysis technical staff often reverses the lines to improve blood flow [21].

When inserted, the tip of a central venous catheter is preferably located near the center of the right atrium [14]. This is an anatomically complex environment which is difficult to model. To avoid this problem in the CFD analysis of catheters, a simple hollow cylinder is placed concentrically around the catheter model (Fig. II-1). This tube represents the vena cava in which the catheter is placed. It has a diameter of 16 mm and a length of 150 mm. After having generated the calculation grid on the entirely fixed geometry and prescribing all initial values and boundary conditions (inlet velocities, pressure, etc.) as mentioned below, the CFD software Fluent 6.1 (Fluent Inc., Lebanon, New Hampshire, USA) will iteratively solve the continuity and momentum equations with a finite volume method to result in a steady state solution.

2.4.1 Boundary conditions

All walls in the model were set as rigid, impermeable and with no slip at the wall surfaces (Fig. II-1). The inlet surface of the tube is set as a mass flow rate inlet at a constant 3 l/min. The tube outlet is defined as a 'pressure outlet' to provide a zero reference pressure. The arterial lumen outlet and venous lumen inlet are set as a velocity outlet and – inlet respectively, with a user defined, poiseuillian profile. The distance between the arterial apical end-opening and the lumen outlet surface is sufficient to allow the flow to develop to laminar state ($Re \sim 1200$) and thus to justify the imposed poiseuillian profile. The poiseuillian boundary condition on the 'venous inlet' surface is also justified since the flow has become fully developed in the omitted part of the lumen. These conditions result in a blood flow through the lumens of 300 ml/min, following the NKF-DOQI guidelines [1]. The following simulations were performed under these conditions unless mentioned otherwise.

2.4.2 Hemodynamic effect of side holes

In this section, the effect of the side holes on the flow and shear rate distribution is studied. To evaluate the effect of the side holes, simulations are performed with either open or closed side holes. The side holes are closed by defining their surfaces as 'wall' as opposed to 'interior' and its interior volume as 'solid' instead of 'fluid'.

2.4.3 Hemodynamic effect of the size of catheter side holes

The side holes in the Niagara catheter are quite large in comparison to those in most other catheter designs (1.2 mm vs. 0.8-0.5 mm). To study their hemodynamic impact, the side hole diameter in the CAD-model was reduced from 1.2 mm to 0.6 mm, thus reducing their inlet area to one quarter of its original. This results in a total inlet area reduction of 29.6%.

2.4.4 Recirculation percentage: normal use vs. reversed catheter lines

To simulate the flow when catheter connections are switched, the boundary conditions at the lumen boundary surfaces were reversed. To quantify the recirculation percentage, the cleansed blood flowing back to the vein is labeled. The labeled blood enters the model through one of the catheter lumens: 'venous' (regular connections) or 'arterial' (reversed). By solving the convection-diffusion equation, the distribution of the local mass percentage labeled blood is obtained. The mass diffusion coefficient is set to a negligible $1 \times 10^{-18} \text{ m}^2/\text{s}$ to rule out any diffusional effect. The cup mixed concentration of labeled blood at the exit of the withdrawing lumen is taken as a measure for the recirculation percentage under these specific steady state conditions.

2.5 Numerical simulation of the catheter in an anatomically realistic model

To ascertain the validity of the simplified model and the influence of catheter tip location on the performance analysis of central venous catheters, a model of a right atrium has been three-dimensionally reconstructed from digital cryosection images from The Visible Human Project (National Library of Medicine, National Institutes of Health, Bethesda, Maryland, USA). Several simulations are repeated to compare the results to those where the catheter is inserted in a straight vein (tube model).

To reconstruct an anatomically realistic model of the right atrium, a Matlab (The Mathworks inc., Natick, Massachusetts) program was developed in house which processes axial cryosection images of a male cadaver, with an interslice distance of 1 mm. This includes a manual segmentation of the contours of the relevant anatomical structures (superior (SVC) and inferior (IVC) caval veins and the right atrium), which are then three-dimensionally stacked (interslice distance = 1 mm). After the segmentation, each contour is smoothed using a quintic smoothing spline [47] and a cubic spline interpolation to filter out any sharp edges caused by the manual segmentation. This results in a smoothed contour with a user defined number of points. Next, the sense of the contours is set identical to the sense of the first contour and all contours are subsequently aligned. Finally, the apparent surface of the geometry is smoothed by applying a cubic smoothing spline to each set of x^{th} points of all contours.

This reconstruction process is applied to two sets of data: the SVC, part of the right atrium and the IVC as well as to the entire right atrium itself. This results in two sets of data, which are separately exported and processed in Gambit. The Matlab application generates an IGES (Initial Graphical Exchange Specification, IGES/PDES Organization, National Technical Information Service, Springfield, USA) file to export the individual points into Gambit, as well as a script file ('journal file'), which is run in Gambit to transform the set of points to a meshable volume. This results in two partly overlapping volumes that are ultimately united. In this final geometry, the catheter is imported with its 'venous' tip near the junction of the SVC and the right atrium.

Catheter boundary conditions remain the same; inlet surfaces of IVC and SVC are set to a constant mass inlet flow of 3 l/min. By starting the segmentation on one side of the tricuspid valve attachment and ending it at the other, the location of the valve itself is marked by a flat, unsegmented area on the atrial surface that is defined as an outflow boundary.

In the resulting anatomical model, the total height of the atrium is 8.8 cm; the atrial major axis according to an apical 4-chamber view is 4.7 cm. The shape of the tricuspid valve diameter is somewhat rectangular (2.2 x 1.7 cm).

3 Results

3.1 Validation of the calculation grid and the numerical method

For the 'arterial' lumen, the experimentally fitted pressure drops were 14.2, 8.8 and 5.9 kPa, the simulated ones are 13.0, 7.8 and 5.5 kPa at flow rates of 300, 200 and 150 ml/min. For the 'venous' lumen the poiseuillian pressure drop at 300 ml/min is 3,2 kPa, compared to the simulated 3,3 kPa. The calculated wall shear rates are validated by comparing the values at the venous lumen wall (5630 s^{-1}) to the theoretical poiseuillian wall shear rates (5500 s^{-1}).

3.2 Numerical simulation of the catheter in a hollow tube

Simulation results are visible in Fig. II-2 where a longitudinal cross section of the catheter is shown with a colorimetric contour map of local velocity magnitudes, combined with a vector plot which shows the local flow direction in this longitudinal plane. Focus is on the arterial lumen as complex flow patterns and highest shear stresses are expected there due to the curvature of the flow path – in contrast to the blood which exits the venous lumen in a jet stream. In Fig. II-2A, Fig. II-2B, and Fig. II-2C side holes are closed, open, and reduced in size respectively. When side holes are open (Fig. II-2B), the inlet velocities at the tip are moderate (max. 1.2-1.3 m/s) and mostly situated centrally near the bottom of the lumen. Near the luminal side wall and the top of the lumen, velocities around 0.3 m/s are more common. More downstream, velocities increase to 2.2 m/s near the inflow of blood through the side holes. Inside the side holes, velocities reach 2.0 m/s at most. According to simulation results approximately 53.5% of the total arterial flow enters through the two side holes, and only 46.5% through the apical end-hole. The inflow through the side holes is visible in a transverse longitudinal cross-section through the arterial lumen in Fig. II-2B'. When the side holes are removed, flow velocities near the tip practically double up to 2.6 m/s (Fig. II-2A). The flow along the inner luminal side and top surface is now stronger: velocities reach 0.6 m/s. Fig. II-2A' shows vertical velocity

values in a perpendicular cross-section of the arterial lumen tip (dashed line in Fig. II-2A). This gives more insight in the flow pattern in the low velocity recirculation zone near the upper wall of the arterial tip. A swirl motion is visible with blood flowing upwards near the lumen side walls and coming back down in the center of the lumen. This explains the downwards velocity vectors in the low flow zone visible in Fig. II-2A.

When the side holes' diameter is halved (Fig. II-2C), the computed blood flow rate through them drops to 17.7% of the total blood flow (300 ml/min). The local flow field shows high velocities in the tip zone (app. 2.3 m/s) and even higher local velocities inside the side holes (app. 2.6 m/s). The inflow through the reduced side holes is also visible in a transverse longitudinal cross-section through the arterial lumen in Fig. II-2C'. Zones with low velocity are visible here just downstream the strong inflow of the side holes.

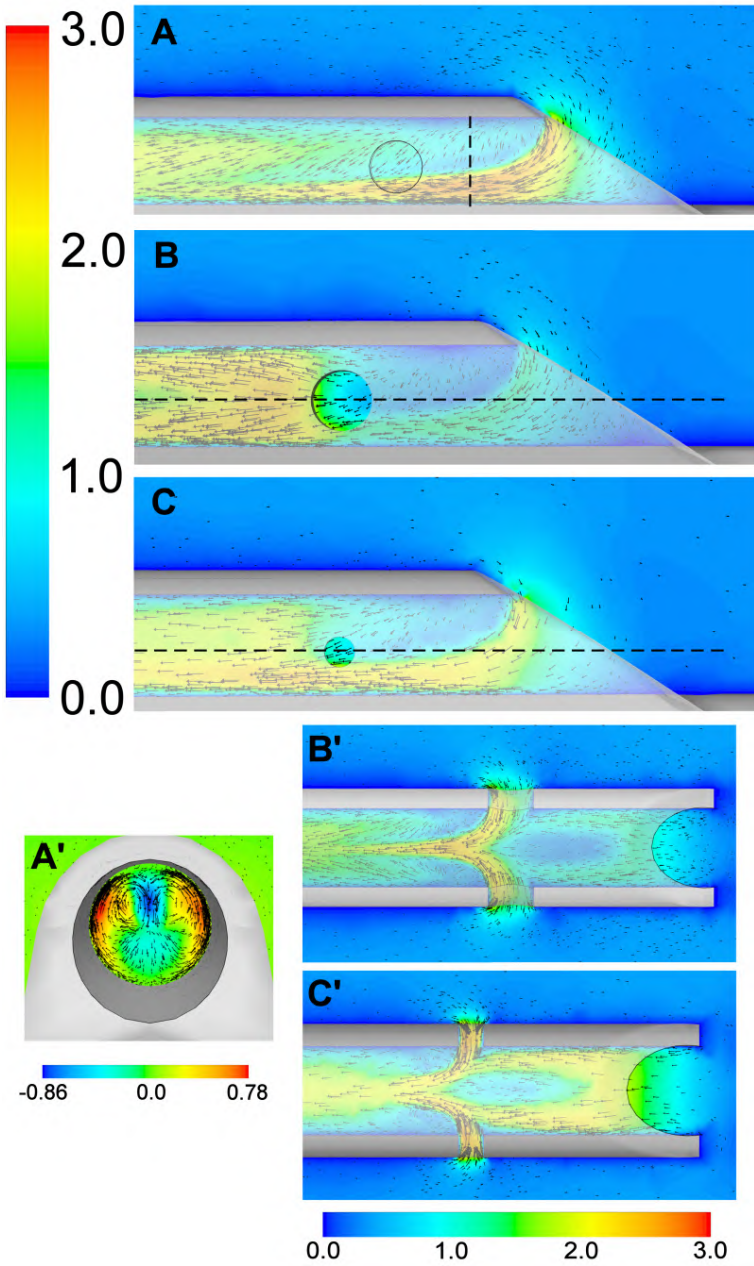


Fig. II-2: Colorimetric contour plots of velocity magnitude (m/s), combined with a vector plot which shows local flow direction, in a longitudinal plane through the catheter with side holes closed(A), open (B), or reduced in size (C). Dashed lines in (A,B,C) indicate the cross-sectional planes which are shown in (A',B',C'). (A') shows a contour plot of in-plane vertical velocities in a perpendicular cross-section of the catheter with closed side holes. (B') and (C') show velocity magnitude plots in a transverse longitudinal cross-section of the catheter with normal and reduced side holes, respectively.

The pressure drop over the simulated part of the arterial lumen is 6.3 kPa when side holes are open and 6.9 kPa when side holes are closed. When the side holes' diameter is halved, the pressure drop is 6.75 kPa.

When considering the shear stress distribution, special attention is paid to zones with highly elevated shear stress values as these may cause mechanical hemolysis. To assess the influence of catheter design on the presence of elevated shear stresses, special attention is paid to zones where values exceed 50 Pa. When side holes are open, shear stresses attain these particularly high values close near the wall of the lumen past the side holes and at the walls inside the side holes. Here shear stress over 50 Pa are common and peaks of 350 Pa are reached very locally. As an illustration, Fig. II-3 shows wall shear stresses greater than 50 Pa in the arterial lumen of the three catheter designs studied (side holes closed, open, and reduced in size). When side holes are closed, especially the side and the bottom of the lumen near the tip are subjected to elevated shear stress (Fig. II-3A). The level of common and peak values is comparable to the case of open side holes. When side holes are reduced, the zones where shear stress exceeds 50 Pa are now found in the tip zone as well as near the side hole walls and the lumen wall near the side holes (Fig. II-3C). Maximal shear stress values now reach 350 Pa both near the side holes' inlet and outlet and near the lumen end-opening.

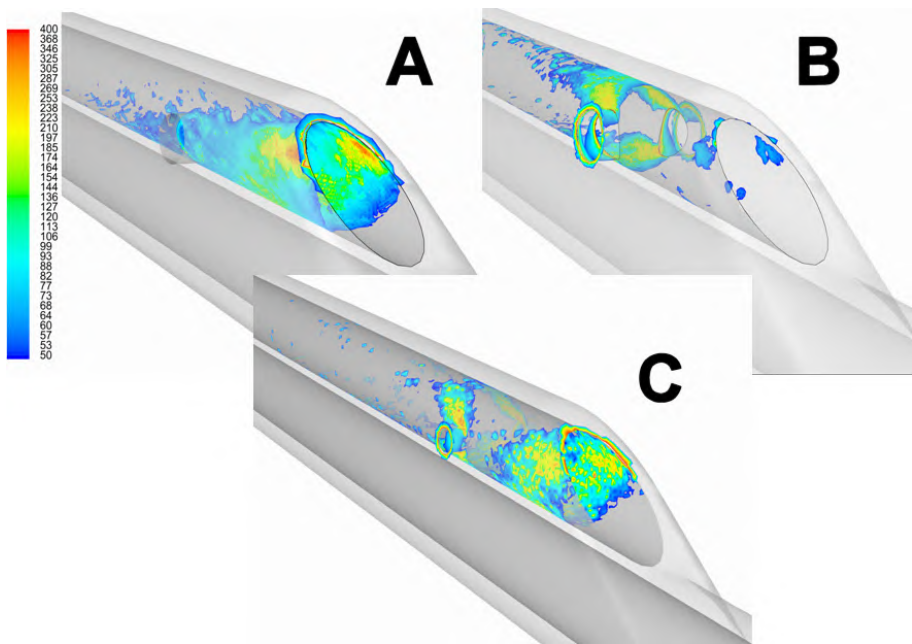


Fig. II-3: Colorimetric contour plots of wall shear stress (Pa) between 50 Pa and maximum value in the arterial lumen of the catheter with (A), side holes closed, (B) side holes open, and (C) side hole diameter halved.

As the highest shear stress values occur near the catheter walls, Table II-1 shows the average wall shear stresses of the inner side hole walls, and of the inner walls of most

distal 1.75 cm of the tip of the arterial lumen, in the three catheter designs, to give a comparable point-of-view. The average wall shear stress in the arterial lumen tip is 55.6 Pa when no side holes are present. This value decreases with about 18% when side holes are present. This is however offset by the significantly elevated wall shear stresses in the side holes, which attain on average 80.3 Pa. Reducing the size of the side holes, gives an added +10% extra average wall shear stress (from 80.3 Pa to 88.3 Pa) in the side holes, while the average shear stress value in the arterial lumen rises close to the case where no side holes are present.

Table II-1: Average wall shear stress of the 1.75 cm most distal tip of the arterial lumen, and of the side hole walls in the catheter model with side holes closed, open, or reduced in size.

	Side holes closed	Side holes open	Side holes reduced in size
Arterial lumen tip	55.6 Pa	45.8 Pa	52.6 Pa
Side hole walls	-	80.3 Pa	88.3 Pa

Considering the venous lumen, a jet exits the apical hole (max. velocity 2.8 m/s). Maximum shear rates are found at the luminal wall, according to the expected poiseuillian course.

In regular catheter use, the recirculation percentage in the simulated case is nil. When catheter connections are reversed, recirculation percentages are computed of 15.5% to 17.3% for flow rates of respectively 300 ml/min and 200 ml/min for the catheter with side holes open. When the vein flow rate is lowered from 3 L/min to 2 L/min, computed access recirculation drops from 15.5% to 12.1 % at a 300 mL/min catheter flow rate (see also Table II-2). Looking at the possible contribution of the side holes, only about 4 % of the returned blood leaves through both side holes. As for local shear stresses in the case of reversed catheter connections, the elevated shear stresses are not reached inside the ‘arterial’ lumen nor the side holes, but now in the ‘venous’ lumen tip.

3.3 Numerical simulation of the catheter in an anatomically realistic model

The reconstruction process results in a three dimensional model of the right atrium and the caval veins (Fig. II-4). In this model, the simulations of the catheter with open side holes in the tube model were repeated with the catheter inserted with its tip at the junction between the superior caval vein and the atrium. As the catheter is now not in a concentric position in a tube, it is interesting to see the impact of the venous lumen outflow in the atrium. Fig. II-5(left) illustrates this by displaying the jet exiting the ‘venous’ lumen in normal catheter use.

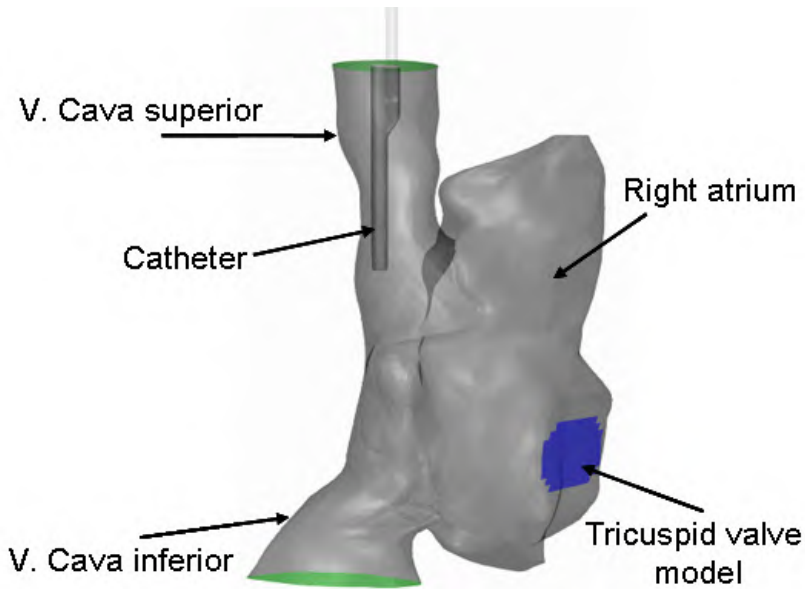


Fig. II-4: Three dimensionally reconstructed anatomically realistic model of the right atrium with catheter inserted with tip at junction of superior vena cava and atrium.

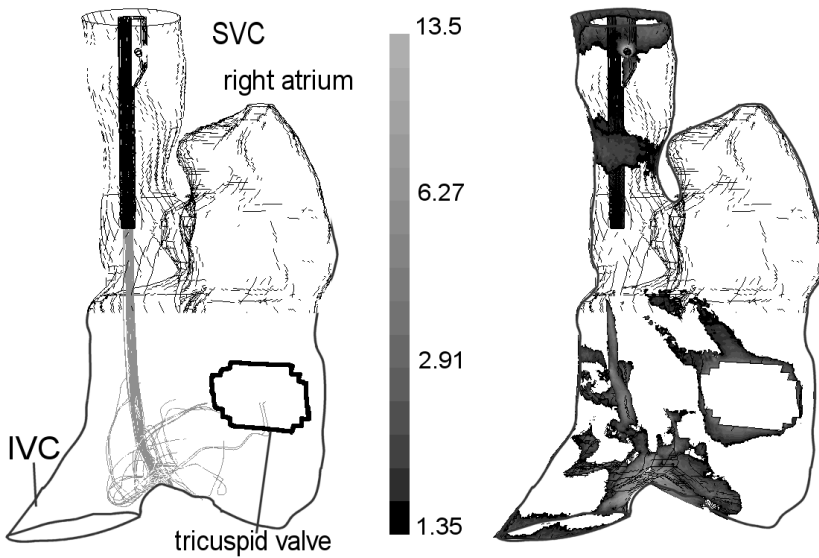


Fig. II-5: Right atrium model with superior and inferior vena cava and tricuspid valve (bold outline); Niagara catheter inserted. Path line visualization of the 'venous' lumen jet outflow (left) and colorimetric contour plot of wall shear rates ranging between 1.35 Pa and 13.5 Pa in log scale (right).

Shear stresses higher than normal artery wall shear stress ($\sim 1 - 2$ Pa) which appear inside the anatomical model are depicted in Fig. II-5(right). Where the ‘venous’ jet collides with the atrial wall, shear stress on the atrium wall reaches 13.5 Pa. Other areas with elevated wall shear rates are located around the tricuspid valve, which is possibly due to a numerical effect, and in part of the superior vena cava, due to a local diameter reduction. The highlighted zones at the caval vein inlet surfaces are due to the imposed velocity boundary condition. Blood flow and shear stress distribution inside the catheter (arterial) lumen are highly similar to the case where the catheter is inserted in the hollow tube (Fig. II-2 and Fig. II-3).

Access recirculation with normal catheter connections are also nil when the catheter is in an anatomically realistic environment. Recirculation percentages in case of reversed connections are given in Table II-2. Access recirculation in this case is about 13 % under 300 mL/min catheter blood flow and 3L/min vein flow rate. Reducing catheter blood flow rate decreases access recirculation to approx. 11 %. A reduced superior vein blood flow rate increases access recirculation to 16.5 %. These percentages and trends differ from the case with the catheter in a straight vein / tube model.

Table II-2: Access recirculation (%) for the simulated catheter with reversed connections in the tube model and in the anatomically realistic model for different combinations of catheter and vein flow rates.

Model	Catheter flow rate	Vein flow rate	Access recirculation
Tube model	200 ml/min	3.0 L/min	17.3 %
Tube model	300 ml/min	3.0 L/min	15.5 %
Tube model	300 ml/min	1.5 L/min	12.1 %
Anatomically realistic model	200 ml/min	3.0 L/min	10.9 %
Anatomically realistic model	300 ml/min	3.0 L/min	13.3 %
Anatomically realistic model	300 ml/min	1.5 L/min	16.5 %

4 Discussion

4.1 Numerical simulation of the catheter in a hollow tube

In this study, CFD – techniques were used to analyze the different flow patterns and hemodynamic performance characteristics of the Niagara catheter. While inserting the catheter in a tube representing the caval vein, its side holes were either left open,

closed or reduced in size. When inspecting the flow through the tip of the arterial lumen with open side holes, we observe that the main flow is dragged over the edge of the apical end-hole and collides with the bottom of the lumen. This swerve causes a rather large zone with low velocities near the top of the arterial lumen. The main flow additionally brings about a swirl motion of flow that originates from the lower part of the apical hole. Blood flows up along either side of the lumen and these two subflows collide somewhat downstream at the top of the lumen, hence the presence of some velocity vectors pointing downward in the low velocity zone in the arterial lumen tip. This swirl motion is present in all three catheter designs and is illustrated in Fig. II-2A' by plotting velocity vectors in a transverse plane at the location of the dotted line of Fig. II-2A. More downstream, the mix with the flow through the side holes causes a sudden velocity increase as the slow apical flow is dragged along. The high velocities of the flow exiting the side holes also create their own recirculation zones (Fig. II-2B'). When side holes are removed, the situation of a catheter design without side holes or a catheter with occluded side holes is mimicked. Now all blood must enter through the tip hole. The inflow is thus dragged more forcefully over the edge of the tip (Fig. II-2A). Also, the swirl motion along the inner luminal surface is stronger, but has a very similar flow pattern (Fig. II-2A'). This swirl can now prolong further downstream as it is not interrupted by an inflow through the side holes. This results in a smaller zone with low velocities at the tip. These occurring recirculation zones may promote thrombus formation, but simulation results show that computed shear stress never drops below 1 Pa which is considered low enough to cause red or white blood cells surface adhesion and deformation [48].

When the diameter of the side holes is halved, the local velocity field (Fig. II-2C) is best described as a combination of the flow fields of both previous cases, but with increased intensity: high velocities in the tip zone beneath a moderately sized recirculation zone, comparable to the case without side holes, and even higher local velocities inside the side holes, similar to the case with normal side holes. The previously described flow fields show that the flow rate through the side holes is definitely not negligible. The flow rate through the original sized side holes of the Niagara catheter was impressive: through them flows more than half of the total drawn blood volume. This was probably not the initial design goal. It should be noted however that these side holes are relatively large. By reducing their diameter to half their size, the resulting side holes' inflow area is cut to one quarter of its original. This diminishes the flow rate through the side holes to one third of the original flow. It is important to point out however that this contribution in flow rate is almost completely lost when catheter connections are reversed: in the case of the original sized side holes, only a small part (3.9%) is then returned to the vein through both side holes. This will further decrease with a reduction in side hole diameter.

As far as pressure drop is concerned, simulations show that neither the presence nor the size of the side holes greatly influences the pressure drop over the arterial lumen of this catheter. The addition of side holes only causes a -4.5 mmHg pressure drop decrease over the entire catheter lumen. With reduced side holes, this pressure drop is even smaller.

The influence of the side holes, however, is definitely present when considering the shear stress distribution in the arterial lumen (Fig. II-3). Generally

speaking, elevated shear stresses are located at the edge of the tip where the flow bends over and at the borderline between the low velocity zone and the tip inflow. When observing particularly high shear rates, exceeding 50 Pa, these are logically found where the highest velocities flow past or collide with a catheter wall. With open side holes, this is particularly the case inside the side holes and at the luminal wall just past the side hole outflow. When the side holes are closed, the bottom and side wall region near the tip are more significant. This is due to the higher velocities of the curved inlet flow colliding with the lumen. Common and maximal values are however comparable for both cases. In any case, apparent shear rates are at least an order of magnitude larger than normal wall shear rates found in human veins and large arteries (max. $800 \text{ s}^{-1} \sim 2 \text{ Pa}$) [49]. Very high values of 350 Pa are found very locally near the catheter walls. As only a fraction of the blood which enters the lumen comes into contact with these very isolated zones, acute hemolysis ($> 200 \text{ Pa}$) is not likely induced. However, some degree of leukocyte damage (sublytic granule release, increased adhesion and aggregation and decreased phagocytic ability) and platelet activation (granule release, GPIIb/IIIa expression and increased aggregation) is inevitable [50,51,52,53]. To which extent these processes will take place, and how the presence and size of the side holes plays an influencing role in the classification of the simulated catheter designs, cannot be readily concluded from these results. The presence of the side holes only seems to affect the location of the region with higher shear stress, and not the level itself. Also, when assessing the possible damage of the shear stress to red blood cells or platelets, not only the level of shear is important, but also the exposure time and the amount of blood that has been exposed to these shear rates. As this work does not take into account all these influences, it is not yet clear if the presence of side holes in this catheter has a beneficial or an unfavorable effect. When side holes are reduced however, the intensified flow field also leads to an intensified shear stress distribution. The area in which shear stresses are elevated is more extended than in any other case. Based on this result, downsizing the arterial side holes in the Niagara catheter seems pernicious to its performance.

Observing the venous lumen, shear stress values are higher than encountered inside the vasculature, but do not attain the extreme values found in the arterial lumen. This situation is inverted when catheter connections are reversed. Now highly elevated levels of wall shear rate are found at the entrance of the 'venous' lumen, comparable to the values previously found in the 'arterial' lumen. Reversing the connections has as a consequence no real effect on possible blood damage caused by elevated shear stress.

As an important performance parameter for limiting dialysis time, the study of access recirculation is essential in a thorough catheter performance analysis. The absence of such recirculation in the performed simulation of normal catheter use is clear, for it is impossible for cleansed blood to return to the 'arterial' holes due to the 'venous' jet outflow and the surrounding bulk flow in the vein. When catheter connections are reversed however, blood leaves the catheter upstream to the 'venous' blood-withdrawing hole and a considerable amount ($\sim 16 \%$) of cleansed blood which passes the 'venous' end hole is redrawn to the dialyzer. In an example of a patient undergoing a dialysis session of 4 hours, the treatment time would have to be extended with 46 minutes to allow the same amount of uncleansed blood to pass

through the dialyzer. The recirculation percentage slightly increases with a lower catheter flow rate, which may be explained by the fact that the jet ejects more slowly from the arterial lumen, has less momentum, and is more easily redrawn by the blood sucking venous lumen. A decrease in vein flow rate decreases access recirculation since this case is analogous to an increased catheter flow (which accordingly decreases recirculation), as the ratio of momentum between catheter and vein flow is increased. This will be further discussed when comparing the results to the case where the catheter is inserted in a more anatomically realistic environment.

4.2 Numerical simulation of the catheter in an anatomically realistic model

Since the reconstruction is based on a single specimen, the model is no representation of the average right atrium. It is foremost important that the catheter is now inserted in a model that shows a complete different flow pattern better resembling *in vivo* conditions. Velocities through the tricuspid valve range to 0.5 m/s which is a realistic value [54].

A steady-state simulation of the regular catheter use, analogous to the one conducted in the tube, revealed no substantially different flow or shear stress patterns inside the ‘venous’ and the ‘arterial’ lumen, nor in the side holes. This shows that for this type of analysis, the catheter can be modeled inside a simple hollow tube, instead of in a complex anatomical model which requires a time and resource consuming reconstruction process. This may be due to the fact that, although the tip of the catheter is located in the right atrium, the tip of the ‘arterial’ lumen still resides in the caval vein which is comparable to a tube. The surrounding caval vein, however, does influence the flow around the catheter. Due to its shape, the bulk flow in the vein is not as straightforward as it is in the tube-model. This is particularly visible in the venous lumen outflow, which is bent towards the tricuspid valve model due to the surrounding atrial flow (Fig. II-5(left)). Additionally, this realistic blood flow pattern has its effect in particular when looking at recirculation with reversed catheter connections. As is presented in Fig. II-6A, the outflow of the arterial lumen of the catheter in the tube model stays close to the catheter lumen wall. However, simulation results show that this flow, ejected from the arterial lumen in the anatomically realistic model (Fig. II-6B), drifts somewhat away from the sucking ‘venous’ lumen, due to the surrounding blood flow. As such, less blood is redrawn by the venous lumen. This is very likely the cause of the apparent reduction of recirculation when the catheter is inserted in the right-atrium model. When the catheter flow rate is reduced, the ejecting jet also has less momentum and is more easily drifted even further away from the blood withdrawing venous lumen, and towards the tricuspid valve model outflow. This further reduces access recirculation, as is presented in Table II-2. Analogously, a decrease in vein flow rate increases access recirculation as the vein flow has less momentum to divert the catheter outflow away from the blood sucking lumen.

Changes in catheter and vein flow rate influence access recirculation according to the ratio of momentum between the catheter and vein flow: e.g. the

influence of a higher catheter flow is similar to that of a decreased vein flow. Whether a change in the momentum ratio increases or decreases access recirculation differs between the two models because this is influenced by the surrounding flow field. This indicates the importance of accurately resolving the blood flow surrounding the catheter model for realistical simulations of access recirculation.

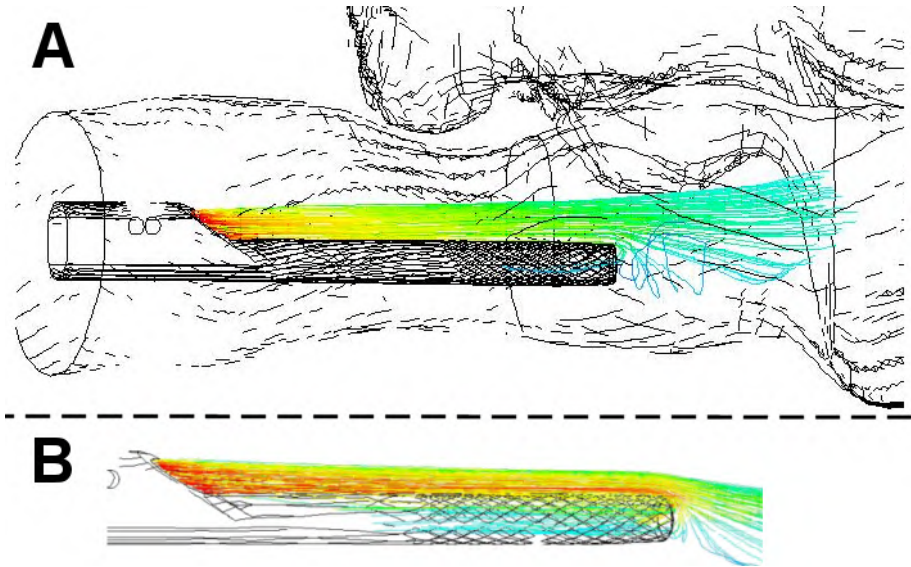


Fig. II-6: Path lines of the blood ejecting from the arterial lumen in case of reversed catheter connections with the catheter model inserted (A) in an anatomically realistic model, or (B) in a tube model. Access recirculation is visualized by path lines returning in the venous lumen.

It should be noted that the simulated recirculation percentage is only a picture at a given moment in the cardiac cycle. When the valve closes and flow stagnates, recirculation percentage is expected to rise. Due to the discrepancy between the recirculation percentages in the tube and in the anatomical model, comparison with *in vivo* results is recommended. Access recirculation percentages for the Niagara catheter are not available in literature, but in an *in vivo* study [32], a mean access recirculation percentage of 13.6 % in thirty patients with a similar catheter design with reversed connections was reported (see also Chapter I). This corresponds very well with the simulation results in the anatomically realistic model.

Another advantage of the anatomical model is that it offers the possibility to study the interaction between the ‘venous’ lumen outflow and the atrial wall (Fig. II-5 (left)). This feature cannot be studied within the simplified model: due to the concentric placement of the catheter in the vein model, the jet does not collide with an anatomical surface. This is the ideal case because the catheter is in fact not a rigid body and its position inside the vein is variable. Even a non-concentric placement of the catheter in the tube is no representation for the complex interaction of the ‘venous’ jet with the atrial wall. In the anatomical model the colliding jet causes

local atrial wall shear rates to rise from the normal arterial values (800 s^{-1}) to $5'000\text{ s}^{-1}$ ($\sim 13.5\text{ Pa}$) at the junction between the IVC and the right atrium (Fig. II-5 (right)).

It can be concluded that the catheter's specific hemodynamic properties, such as pressure drop and internal flow and shear stress distribution can be deduced from simulations where the catheter is inserted in a tube, instead of in an anatomical model. As such, the placement of the catheter tip in a straight vein or at the junction of the superior caval vein and the right atrium seems to have little impact on these parameters. Hence the time and resource consuming reconstruction of an anatomical model can be avoided. However, to better understand the interaction of the catheter with its physiological surroundings, and to realistically predict access recirculation percentages, the availability of an anatomically realistic model is indispensable. The model reconstructed in this study is a step towards the development of an even more realistic environment (improved tricuspid valve model, dynamic wall and/or catheter movement, transient caval vein flow rates) in which the assessment of central venous catheter performance can be further improved using more advanced simulation techniques (unsteady, time dependent simulations).

5 Acknowledgements

The research of Guy Mareels is supported by a BOF-grant (011D09503) of Ghent University, Belgium. Dirk De Wachter is a post-doctoral Fellow of the Fund for Scientific Research – Flanders, Belgium. The authors wish to thank our colleague Fadi Glor for his part in the reconstruction process and Marcel C Weijmer (St-Lucas Andreas Ziekenhuis, Amsterdam, The Netherlands) for the Niagara catheter specimens.

Chapter III: PIV Validated CFD Based Design to Reduce Shear Stress and Residence Time in Central Venous Hemodialysis Catheters

Central venous catheters are a common vascular access method for artificial organ therapy. As crucial factors in blood clot formation, shear stress distribution and low flow zones are assessed in different catheter tip designs using a combined numerical and experimental approach. Standard Particle Image Velocimetry (PIV) was adapted to small scale to measure velocities in the blood withdrawing 'arterial' lumen of three catheter models: catheter with cylindrical lumen and 'arterial' tip cut straight (1), cut at an angle (2) or cut straight with a sleeve entrance (3). Catheter was inserted in a superior vena cava model and was scaled according to dynamic similarity. Obtained velocity and shear strain distributions compared qualitatively and quantitatively well to analogous Computational Fluid Dynamics (CFD) simulations. After validation, four additional catheter designs were studied using CFD: cylindrical lumen with two side holes and tip cut straight (4) or at an angle (5); concentric lumens (6) and Ash Split based design (7). Six parameters concerning shear stress (SS), blood residence time (RT) and Platelet Lysis Index (PLI) which combines the influence of shear stress and exposure time to platelet aggregation, were assessed in the seven catheter tips. Concentric catheter is discarded due to highly elevated SS levels. 'Ash Split' based design has elevated RT values in the distal tip zone as major inflow occurs through the most proximal side holes, but this is compensated by the low average shear stresses. A cylindrical lumen with a preferably straight cut tip and with possibly two side holes are preferred designs when aiming at minimal SS and RT values. This data may lead to more patent catheters.

The contents of this chapter were published in ASAIO J (2007); 53(4): 438-446

Particle Image Velocimetry-Validated, Computational Fluid Dynamics-Based Design to Reduce Shear Stress and Residence Time in Central Venous Hemodialysis Catheters

G. Mareels, R. Kaminsky, S. Eloot, and P.R. Verdonck

1 Introduction

Central venous catheters are commonly used as a vascular access method for hemodialysis.[10] However, apart from several advantages as the ease of insertion and immediate access to the circulation, central venous catheter use is accompanied with a higher incidence of infection and thrombosis as compared to other means of vascular access like grafts or fistulas.[55] Concerning thrombosis, stagnating blood zones in the catheter lumen and regions of elevated shear stress which induce platelet activation may promote the formation of a blood clot. Elevated shear stresses also give rise to damage to red blood cells. Significant levels of shear stress are mostly present in the blood withdrawing ('arterial') lumen of the catheter, more specifically in the distal tip region. Various different catheter (tip) designs are marketed whilst for the time being no proven advantage of one design over another exists. Nevertheless, changes in catheter tip design have shown to cause alterations in local flow pattern and shear stress distributions.[56] Further study of the local hemodynamics of different catheter designs might provide insight in how catheters can be optimized to reduce shear stress and stagnant zones thus leading to possibly less thrombogenic catheters.

In this study, flow and shear stress distributions and blood residence time in different catheter designs are compared. For this analysis, a combined approach of Particle Image Velocimetry (PIV) and Computational Fluid Dynamics (CFD) is used. Computational Fluid Dynamics allows a time efficient study of the hemodynamics of different catheter designs without the time consuming effort of fabricating prototypes suitable for PIV measurements. However, validation of CFD results is necessary as mesh-independent shear stress fields, in contrast to flow fields, are difficult to achieve and are only obtained at very high (local) mesh density.[57] For this purpose, PIV was chosen as a challenging approach to obtain both high resolution flow fields and shear stress distributions *inside* the lumens of different catheter models.

Consequently, this study is conducted in two parts. In a first part, flow field and shear stress distribution in the blood withdrawing lumen of three catheters models is assessed via PIV and CFD. Results of both approaches are compared to validate the numerical approach. Secondly, shear stress distributions and blood residence time in four additional (in total seven) catheter designs are studied using CFD. Throughout the entire study, the distal end or tip of the blood withdrawing ('arterial') lumen is considered, as stagnant blood zones and highest shear stresses are expected there.[56] Results are analyzed to assess which tip design is optimal to reduce shear stress levels and the presence of stagnating blood zones. Adoption of this information can lead to possibly less thrombogenic catheters.

2 Materials and Methods

2.1 Catheter designs

2.1.1 Three catheter designs studied by PIV and CFD

Three catheters were studied by both PIV and CFD for flow and shear stress validation purposes. It concerned three shotgun (or step-tip) type catheters. The ‘arterial’ lumen, which withdraws blood from the vessel, has a round cross section with an internal diameter of 2.1 mm. The ‘venous’ lumen, which returns cleansed blood to the circulation, is also cylindrical with an internal diameter of 2.1 mm, but its tip extends 30 mm further in length. The three catheters differed only in the tip design of the arterial lumen. The distal end of catheter ‘Cut Straight’ (Fig. III-1A) is cut orthogonally to its axis and has no other ‘arterial’ flow entrance than the distal end-opening. This is the most simplistic catheter design and is considered as the reference catheter in the second part of this study. Catheter ‘Cut Straight Sleeve’ (Fig. III-1B) also has a distal end which is cut at 90° but it features a sleeve entrance (1.4 mm wide) at 3.1 mm distal from the ‘arterial’ tip. Catheter ‘Cut Angle’ (Fig. III-1C) has a distal end cut at an angle of 33° and only has one distal end-opening.

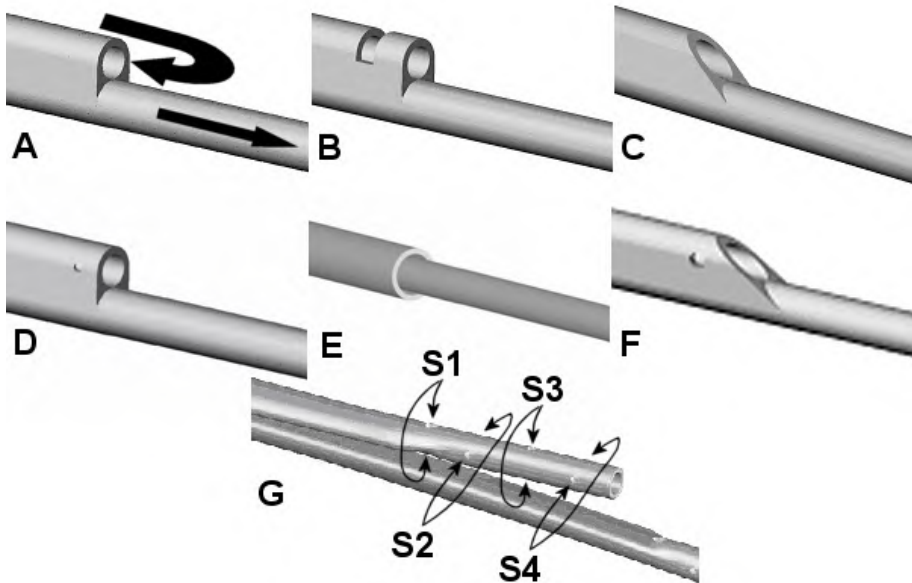


Fig. III-1: Catheter designs studied. A = Cut Straight; B = Cut Straight Sleeve; C = Cut Angle; D = Cut Straight Hole; E = Concentric; F = Cut Angle Hole; G = Ash Split based with four side hole pairs S1-4.

2.1.2 Four additional catheter designs studied by CFD only

For the in-depth CFD study, four additional catheters were also simulated. Catheter ‘Cut Straight Hole’ (Fig. III-1D) is a variant of catheter ‘Cut Straight’ but with two symmetrically placed side holes (inner diameter = 1.2 mm) at 3.1 mm distal from the ‘arterial’ tip. Catheter ‘Concentric’ (Fig. III-1E) is a typical concentric catheter design. The inner ‘venous’ lumen has an inner diameter of 2.1 mm. The surface area of the outer ‘arterial’ lumen annulus is also identical to the ‘arterial’ lumen surface area of the ‘Cut Straight’ catheter – to make comparison to the shotgun-type catheters valid. Catheter ‘Cut Angle Hole’ is analogously a variant of catheter ‘Cut Angle’ with two symmetrically placed side holes (inner diameter = 1.2 mm) at 3.1 mm distal from the ‘arterial’ tip. The last catheter is based on the Ash Split design (Medcomp, Harleysville, PA, USA - Fig. III-1F). It has a D-shaped lumen which changes to a circular lumen with a smaller cross-section towards the tip (inner diameter = 1.8 mm). This catheter was scaled so the D-shaped lumen had the same surface area as the lumen in the reference catheter to allow comparison to other simulation results. It has four pairs of side holes (two pairs on top and bottom each alternating with two pairs on left & right of catheter lumen) extending the entire tip zone. Side holes most distal to the tip S1 have a diameter of 1.3 mm; the other side holes have a diameter of 0.9 mm. Side holes are positioned at respectively 18.3 mm, 13.8 mm, 8.4 mm and 3.2 mm from the tip. The tip of the lumen is positioned under an angle of 3° to the horizontal axis.

The presented catheter designs are virtual designs. Nevertheless they bear high resemblance to existing commercially available catheters so results may be extrapolated to catheters of different manufacturers but with similar designs (e.g. Mahurkar, PermCath (Tyco Healthcare, Mansfield, Massachusetts, USA), Niagara, VasCath, OptiFlow (BARD Access Systems, Salt Lake City, Utah, USA), Duo-Flow and Split Cath (Medcomp, Harleysville, PA, USA)). Adoption of the results of this study may thus lead to better performing catheters.

2.2 PIV analysis

2.2.1 Catheter prototypes

The three catheter prototypes were cast in an aluminum mold using a clear, homogeneous, transparent silicone (CF-2616, NuSil Silicone Technology, Carpinteria, California, USA) with a refractive index (RI) of 1.41. To make casting more feasible, experimental catheter models were scaled so the inner diameter of the lumen is 6 mm. Consequently, a geometrical scaling factor α_L of 2.857 (= 6 mm / 2.1 mm) was used for the entire *in vitro* setup.

2.2.2 Experimental setup

In vivo, the tip of a central venous catheter is located in the superior vena cava (SVC), in the right atrium or at the junction of both. Previous work has shown that this

location has little or no influence on flow or shear stress distribution *inside* the catheter lumens.[56] As such, *in vitro* the catheter is placed in a duct representing the SVC. Following *in vivo* parameters were assumed: catheter flow rate is 300 ml/min, blood density (ρ) is 1060 kg/m³; blood viscosity (μ) is 3.5 mPa.s; SVC diameter (D) is 18 mm [58]; average blood velocity (v) in SVC during systolic inflow is 0.18 m/s [59], corresponding with a SVC blood flow rate of 2.7 L/min. According to the geometrical scaling factor, the hydraulic diameter of the *in vitro* duct has to be 51.4 mm. However, to minimize optical distortion and diffraction of the PIV laser on a curved surface, a rectangular PMMA duct was used. Hydraulic diameter of a rectangular duct equals 4 times the cross-sectional surface area divided by the circumference. As such, cross-section of the duct was chosen to be 40 x 72 mm which complies with geometric similarity.

As a working fluid, 42-58 weight% water-glycerin mixture was used at 50°C to reduce fluid viscosity. The mixture provides a RI of 1.41 matching with the catheter model material (manufacturer's data). Mixture density (ρ) was measured 1150 kg/m³. Kinematic viscosity of the mixture was determined experimentally using an Ubbelohde capillary viscometer (ViscoSystem AVS, Schott-Geräte GmbH, Germany). In five measurements at 50°C, mixture kinematic viscosity (ν) was measured 2.961×10^{-6} m²/s (stdev. 2.8×10^{-9} m²/s). Consequently, a dynamic viscosity ($\mu = \nu \cdot \rho$) of 3.405 mPa.s was obtained. Subsequently, dynamic similarity theory was used to determine the *in vitro* flow conditions in the scaled PIV model. According to dynamic similarity, Reynolds numbers ($Re = \rho \cdot D \cdot v / \mu$) in the *in vivo* and *in vitro* situation must be identical for both the catheter flow ($Re = 937$) and the vein flow ($Re = 981$). From this, an *in vitro* duct flow rate of 9.7 L/min and an *in vitro* catheter prototype flow rate of 784 ml/min were obtained. Consequently, a velocity scale factor α_v of 0.314 and a shear rate scale factor $\alpha_\gamma (= \alpha_v / \alpha_L)$ of 0.11 was calculated. These values are used to scale the results of PIV measurements for comparison with CFD results.

An experimental setup (Fig. III-2) was constructed in which the catheter was mounted securely in the rectangular duct. Working fluid is kept at a constant 50°C and continuously circulated through the duct mimicking the SVC blood flow rate, while another pump draws fluid via the 'arterial' catheter lumen.

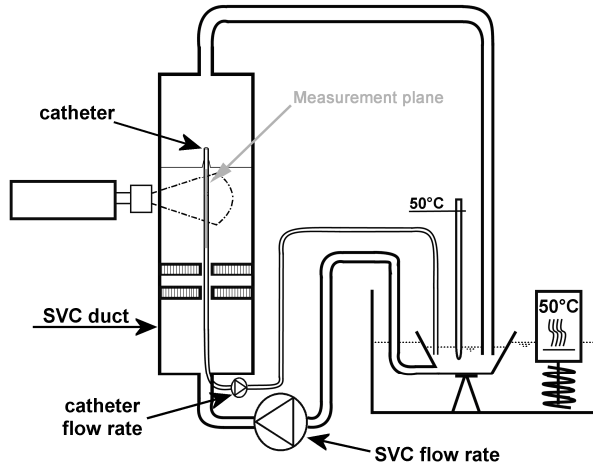


Fig. III-2: Schematic drawing of the PIV set up.

2.2.3 Measurement protocol

For the flow visualization through the catheter model, standard Particle Image Velocimetry was used. Fig. III-2 shows schematics of the PIV set up. As a light source for the measurements we used a double cavity Nd:YAG Solo PIV I (New Wave, Fremont) laser with 532 nm wavelength and 50 mJ of energy per pulse. An articulated mirror arm redirected the laser beam from the laser head to the light sheet optics. 12bit CCD camera Sensicam QE (PCO, Kelheim) with the resolution of 1376x1040 pixels was used to record 100 pairs of images at 4Hz frequency. A Nikorr Micro 60 mm 2.8 lens was attached to the camera. To calibrate the region of interest (ROI) to real units (mm) we used a black aluminum plate with white cross-markers precisely written on it by a laser at given distances. The master of the acquisition procedure was the synchronizer (ILA GmbH, Jülich), which controlled the synchronized recording of the images to the emitted laser pulses in the chosen frequency domain. The camera was orthogonally inclined to the laser light sheet optics and both were fixed to the traverse unit allowing the positioning along the axis parallel to the main flow (Fig. III-2).

Rhodamine-B coated red fluorescent particles, micro-spheres of 10 μm diameter, were added to the working fluid. Fluorescent particles emit red light (λ emission=580-620nm) once they are illuminated with the green laser light (λ excitation = 532 nm) sheet. In order to avoid reflections at the wall of the catheter we applied a red band pass filter in front of the CCD chip. Through this filter only red light ($\lambda = 590 \pm 20$ nm) was visible for the camera.

The resolution is given by an interrogation window size for the adaptive correlation of 32×32 pixels² with an overlap shift of 8 pixels. The light sheet thickness was about 0.7 mm, with a spatial Gaussian distribution. As such, particles in the middle of the sheet are only just detectable while particles out of the middle plane act as noise. The latter is filtered out due to subsequent correlation function and filter algorithms.

For three different catheters we measure 3 ROI serially organized to the flow direction in 2 longitudinal central planes, normal and transverse (Fig. III-3). The combined ROIs in one plane covered approximately $13.7 \times 32.8 \text{ mm}^2$ of the arterial catheter tip region.

For evaluation of the PIV images we used the commercial VidPIV software package (ILA GmbH, Jülich) with iterative window deformation [60], B-Spline grey value interpolation [61] and phase correlation [62]. In all ROIs, ‘in plane’ velocity magnitudes and shear strain values were computed. The evaluation results are computed from statistical average of one hundred instantaneous flow field measurements for each ROI.

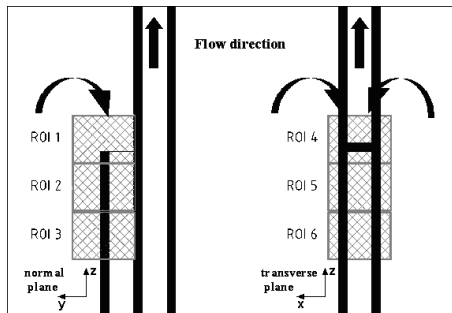


Fig. III-3: PIV measurement planes: normal and transverse plane were measured by combining three subsequent ROIs in each plane

2.3 CFD analysis

All catheter models were constructed in *in vivo* scale in the CAD package SolidWorks 2003 (SolidWorks Corporation, Concord, MA, U.S.A.) and exported into the grid generation software Gambit 2.1 (Fluent Inc., Lebanon, NH, U.S.A.) via the Parasolid data format. Catheter models were inserted concentrically in an *in vivo* scale, straight, rigid cylinder representing the SVC. Fluent 6.2 was used as numerical solver.

2.3.1 Comparison with PIV

For comparison with PIV, blood was modeled as an incompressible, Newtonian fluid. Velocity inlet value of the SVC was set at a constant 0.18 m/s (cfr. *in vivo* flow conditions – supra). Catheter lumen boundary faces were set at 300 ml/min either entering or leaving the fluid domain. All walls in the model were set as rigid, impermeable and with no slip at the wall surfaces. SVC outlet face was set as a pressure outlet to provide a zero reference pressure. A T-Grid mesh was used, which was locally refined to gain better resolution for the assessment of shear stress and to achieve grid independence. Resulting average number of grid cells in the tip volume was 1.5 million cells. Average skewness was 0.35 (range $10^{-5} \sim 0.83$). ‘In plane’ velocities (Eq. III-1) and shear strain values (Eq. III-2) in the PIV measurement

planes of the three catheters were computed and compared to the PIV results ($u_i = i$ -component of velocity vector).

$$\text{velocity magnitude}_{\text{normal plane}} = \sqrt{u_y^2 + u_z^2} \quad \text{Eq. III-1}$$

$$\text{velocity magnitude}_{\text{transverse plane}} = \sqrt{u_x^2 + u_z^2}$$

$$\text{shear strain}_{\text{normal plane}} = -\left(\frac{\partial u_y}{\partial z} + \frac{\partial u_z}{\partial y}\right) \quad \text{Eq. III-2}$$

$$\text{shear strain}_{\text{transverse plane}} = -\left(\frac{\partial u_x}{\partial z} + \frac{\partial u_z}{\partial x}\right)$$

Quantitative comparison was performed by comparing numerical and experimental average velocity magnitudes and average (absolute values of) in-plane strain rates in the measurement planes.

2.3.2 Assessment of shear stress levels and blood residence time

In subsequent simulations to assess possible blood clotting risk in catheters, blood was modeled as a non-Newtonian fluid using the Quemada[63] blood viscosity model (Eq. III-3-5). Hydrodynamic boundary conditions were unchanged.

$$\mu = \frac{\mu_p}{\left(1 - \frac{1}{2}k \cdot H\right)^2} \quad \text{Eq. III-3}$$

Parameter k is function of the intrinsic viscosities k_0 , characterizing the red blood cell aggregation at zero shear stress, k_∞ , describing the orientation and deformation of red blood cells at important shear stress, and the shear rate γ .

$$k = \frac{k_0 + k_\infty \cdot \sqrt{\frac{\gamma}{\gamma_c}}}{1 + \sqrt{\frac{\gamma}{\gamma_c}}} \quad \text{Eq. III-4}$$

With

$$\begin{cases} \ln k_0 = 3.874 - 10.410 \cdot H + 13.800 \cdot H^2 - 6.738 \cdot H^3 \\ \ln k_\infty = 1.3435 - 2.803 \cdot H + 2.711 \cdot H^2 - 0.6479 \cdot H^3 \\ \ln \gamma_c = -6.1508 + 27.923 \cdot H - 25.600 \cdot H^2 + 3.697 \cdot H^3 \end{cases} \quad \text{Eq. III-5}$$

Hematocrit was set at 40%; plasma viscosity is 1.3 mPa.s. Boundary conditions are applied as mentioned above. Grid adaptations were applied to the same extent as was necessary for PIV comparison. Shear stress (SS) levels are calculated by Fluent as the multiplication of viscosity and strain rate. The latter is defined as $(2D_{ij}D_{ij})^{1/2}$ with

$D_{ij}D_{ij}$ the inner product of the strain rate tensor $D_{ij} = \frac{1}{2} \left(\frac{\partial u_i}{\partial x_j} + \frac{\partial u_j}{\partial x_i} \right)$. Blood

residence time (RT) is modeled by solving Eq. III-6 (u_i = velocity x,y,z-components; x_i = x,y,z-coordinate, t = time value) in the ‘arterial’ lumen of the catheter.

$$\frac{\partial(u_i t)}{\partial x_i} = 1 \quad \text{Eq. III-6}$$

This equation is a specific form of the continuity equation for variable ‘ t ’. The value of ‘ t ’ at the inlet faces is set at zero. No flux boundary conditions are imposed on all outflow surfaces. This results in a ‘ t ’ value throughout the ‘arterial’ lumen domain that indicates at any location the time which has elapsed since the fluid in that location has entered the lumen (residence time).

As the flow inside the catheter lumen is proven to be three-dimensional[56], shear stress and blood residence time were evaluated in a constant tip volume of the ‘arterial’ lumen of each catheter model. A tip volume of 0.075 ml was considered, e.g. corresponding to the distal 2.16 cm end of the arterial lumen in the ‘Cut Straight’ reference catheter. Volume averaged shear stress in this tip zone is calculated for all catheters. A shear stress threshold of 10 Pa for platelet activation was selected [52]. As such, also the percentage of the tip volume which is subjected to a shear stress of 10 Pa or more is calculated for each catheter. Concerning residence time, the average value of parameter ‘ t ’ at the end of the tip volume is 0.015 s for each catheter, given the tip volume and the catheter blood flow rate. However, due to local stagnation of blood in the tip zone the time since the blood has entered the ‘arterial’ lumen can locally exceed 0.015s. Consequently, the percentage of tip volume with $RT > 0.015$ s and the percentage of tip volume with $RT > 0.030$ s was evaluated for each catheter design. Extended residence time combined with elevated shear stress can lead to platelet activation and eventually blood clotting. As such, also the average shear stress in zones with $RT \leq 0.015$ s and in zones with $RT > 0.015$ s was calculated for each catheter design.

The choice of the 10 Pa shear stress threshold for platelet activation can be questioned as the range of shear stresses over which platelet adhesion and subsequent aggregation are observed is approximately 0.1 to 20 Pa [64]. Waniewski *et al.*[65] use a two level critical threshold of 2500 s^{-1} (~8.75 Pa) to 7500 s^{-1} (~26.5 Pa) to assess the conditions of thrombosis. As such, to reduce the sensitivity of the results and conclusions of this study to the choice of the shear stress threshold, the Platelet Lysis Index [40,66] (PLI - Eq. III-7) was added. Similar to the Hemolysis Index equation by Giersiepen [40], this experimentally fitted equation describes the lysis of a platelet, taking into account the combined effect of magnitude of shear stress (τ) and the exposure time (t).

$$PLI = 3.66 \cdot 10^{-6} t^{0.77} \tau^{3.075} \quad \text{Eq. III-7}$$

This approach allows linking high shear stress to subsequent low flow zones via path lines. Although the equation is set up for platelet lysis, it can be used to assess possible platelet activation as the same determinants are applicable. As such, the

index is used as a comparative tool in the quantitative assessment of the catheter tip designs, rather than as a predictive tool of actual platelet activation.

For each inlet of a catheter, a minimum of 1000 path lines were computed by Fluent 6. Each path line takes 3000 steps of $10\ \mu\text{m}$ to allow the path line to extend well past the disturbed flow in the tip zone and into the Poiseuillian flow further downstream the catheter lumen. At every point, shear stress and velocity magnitude values are exported. The time value is computed as the distance between to subsequent points along a path line divided by the average velocity over the segment. PLI values of every step along a path line are summed up. Subsequently, for each catheter a weighted average of all path line PLI values is computed using the entrance velocity of a path line as weighing factor. As such, each path line contributes to the PLI according to the amount of catheter inflow they represent.

2.3.3 Influence of a realistic SVC flow

A realistic SVC velocity profile [59] was imposed in one case ('Cut Angle') to assess the influence of pulsatile flow and even backflow in the catheter surrounding vein. Fig. III-4 shows the velocity profile [59] (period = 1 s) imposed at the vein inlet face. Average shear stress in the tip was monitored during the second cycle to avoid transitional flow effects.

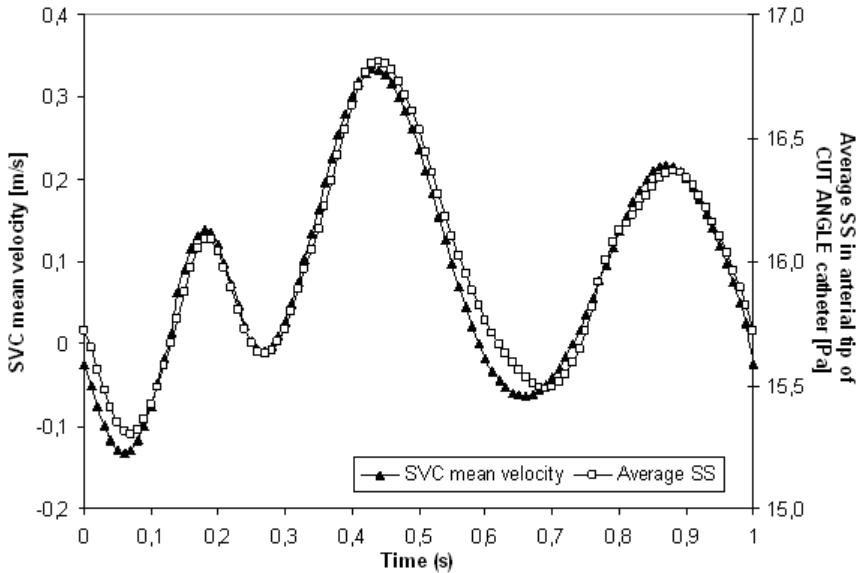
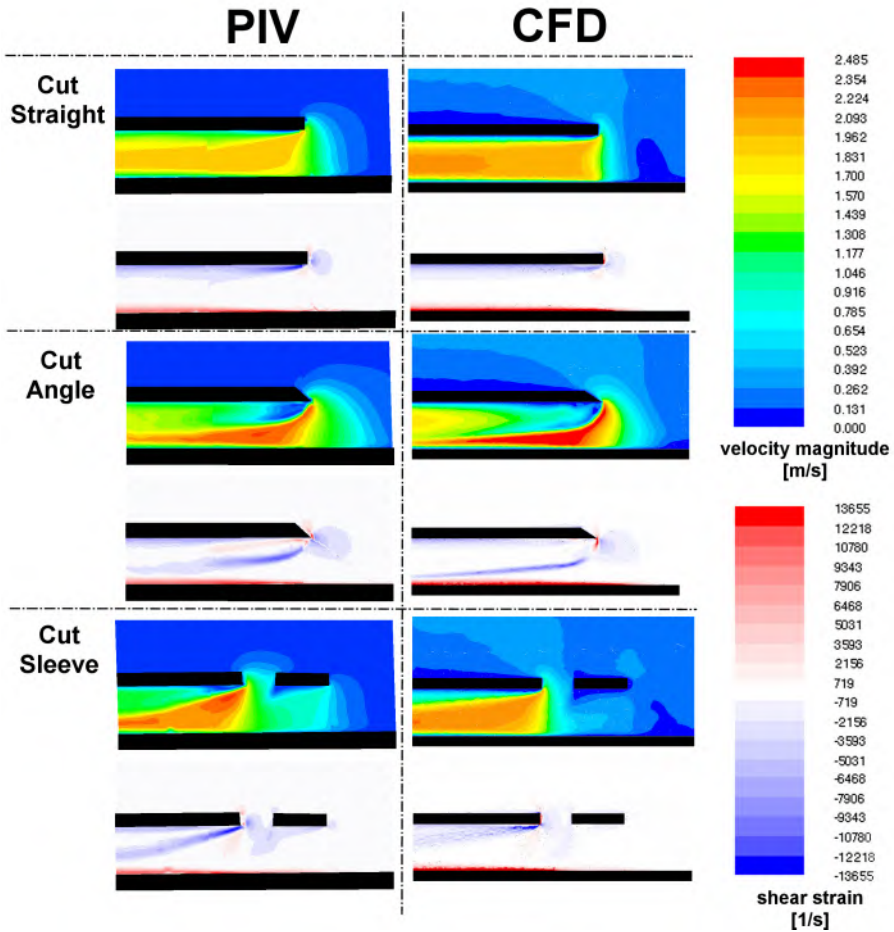


Fig. III-4: Realistic time-dependent superior vena cava average inlet velocity (m/s) and average SS (Pa) in catheter 'Cut Angle' tip under these transient conditions.

3 Results

3.1 CFD validation by PIV measurements for three catheter designs

Figure 5 shows ‘in plane’ velocity magnitudes and strain rates in the normal and transverse plane of the three catheters studied. The range of velocity magnitude and shear strain is set equal for PIV and CFD.



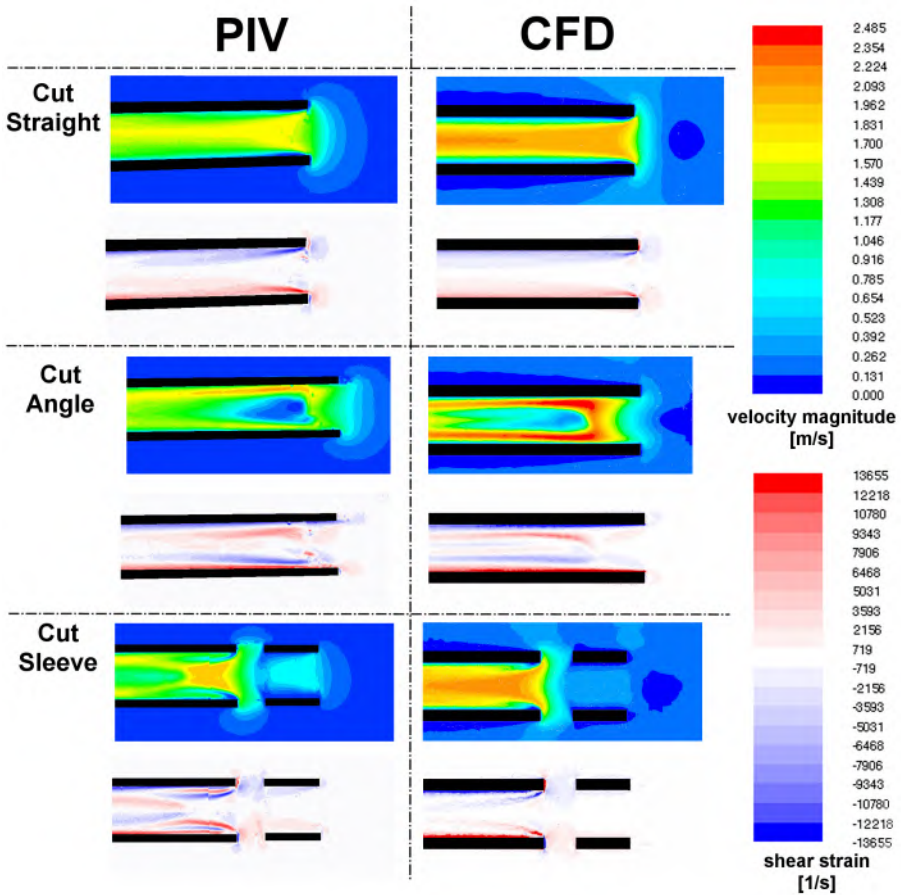


Fig. III-5: CFD and PIV results of in-plane velocity and shear strain distribution defined according to Eq. III-2 in two orthogonal planes in the ‘arterial’ lumen tip of three catheter models (Cut Straight, Cut Angle and Cut Straight Sleeve)

The inflow in ‘Cut Straight’ catheter is homogeneous in both normal and transverse plane. Only very small zones of low velocity and flow separation are present just downstream the inlet and are both visible in PIV and CFD. Shear strains are highest near the inlet where the flow bends around the catheter entrance and near the border of the small recirculation zone and the large inflow. In case the inlet of the catheter is cut at an angle of 33° (‘Cut Angle’), a large zone of low velocities is present close to the top of the ‘arterial’ lumen. Maximal velocity values are higher as compared to the catheter ‘Cut Straight’ as the effective inflow area is reduced. In the transverse plane, velocities are high near the wall and low in the center of the lumen. This illustrates how the major flow enters the lumen. The incoming flow bends to the bottom of the lumen and flows to the top along the side walls and comes back down more downstream in the center of the ‘arterial’ lumen. This swirl motion during arterial inflow was already observed in previous work.[56] As a result of the complex three-dimensional flow, high shear strains are present throughout the tip of the ‘Cut Angle’

catheter. Adding a sleeve entrance to the straight cut catheter ('Cut Straight Sleeve') results in low velocities in the most distal zone of the catheter's tip. Majority of the flow is now drawn into the lumen through the sleeve. A zone of low velocities is noticed near the wall just downstream the sleeve and a relatively large zone near the top of the lumen in the most distal zone extending to the center of the lumen. As such, high strain rate values are mostly present near the sleeve wall and at the bottom of the lumen.

Results show that PIV measurements and CFD simulations are in good qualitative agreement in all cases for both velocity magnitudes and shear strain values. Quantitative agreement is presented in Table III-1.

Table III-1: Quantitative comparison of PIV and CFD results of average velocity magnitude and average absolute value of shear strain in the two PIV measurement planes of the three catheters studied using both PIV and CFD (Cut Straight, Cut Angle and Cut Straight Sleeve).

		Avg. velocity magnitude [m/s]	Relative error	Avg. shear strain [Eq. III-2 - s ⁻¹]	Relative error
Cut Straight - normal	PIV	1.74		1577	
	CFD	1.79	3.2%	1851	17.3%
Cut Straight - transverse	PIV	1.27		1440	
	CFD	1.70	34.0%	1864	29.4%
Cut Angle - normal	PIV	1.34		1703	
	CFD	1.48	10.1%	2069	21.5%
Cut Angle - transverse	PIV	1.24		2368	
	CFD	1.59	29.0%	2040	-13.9%
Cut Straight Sleeve - normal	PIV	1.22		1461	
	CFD	1.45	18.5%	2186	49.6%
	<i>CFD plane shifted lateral 0.5 mm</i>	1.40	14.6%	2431	66.4%
Cut Straight Sleeve - transverse	PIV	1.03		1629	
	CFD	1.58	52.5%	2006	23.1%
	<i>CFD plane shifted vertical up 0.5 mm</i>	1.12	8.7%	2089	29.4%

3.2 CFD assessment of shear stress and residence time in the tip of 7 catheter designs

Following parameters were assessed in the tip zone of the 'arterial' lumen of each catheter: (1) tip volume average SS, (2) percentage of tip volume with SS > 10 Pa, (3) percentage of tip volume with RT > 0.015 s, (4) percentage of tip volume with RT > 0.030 s, (5) average SS in zones with RT ≤ 0.015 s, (6) average SS in zones with RT > 0.015 s and (7) Platelet Lysis Index (PLI). Also flow division is reported in case of different flow entrances. Results are presented in Table III-2. Catheter 'Cut Straight' is set as the reference catheter as its design is no more than just a simple cylindrical lumen.

Table III-2: Following parameters were calculated in the tip zone of the ‘arterial’ lumen of each catheter: (1) tip volume average SS, (2) percentage of tip volume with SS > 10 Pa, (3) percentage of tip volume with RT > 0.015 s, (4) percentage of tip volume with RT > 0.030 s, (5) average SS in zones with RT ≤ 0.015 s, (6) average SS in zones with RT > 0.015 s and (7) Platelet Lysis Index. Percentages show relative difference compared to reference (ref.) case.

	Cut Straight (ref.)	Cut Angle	Cut Straight Hole	Cut Angle Hole	Cut Straight Sleeve	Conc.	Ash Split based
Flow division	End opening	100 %	100 %	48.8 %	46.6 %	18.0 %	6.6 %
	Side entrance	N/A	N/A	51.2 %	53.4 %	82.0 %	S4: 4.2% S3: 8.6% S2: 15.6% S1: 65.0%
avg. SS	12.6 Pa	16.3 Pa	14.2 Pa	14.6 Pa	12.8 Pa	44.8 Pa	11.6 Pa
		+29%	+14%	+17%	+2%	+255%	-8%
% vol. SS > 10 Pa	41.8 %	54.7 %	45.8 %	47.9 %	41.0 %	87.9 %	32.2 %
		+31%	+10%	+15%	-2%	+110%	-23%
% vol. RT > 0.015 s	16.8 %	13.9 %	9.8 %	10.2 %	19.7 %	18.9 %	60.8 %
		-17%	-42%	-39%	+17%	+13%	+262%
% vol. RT > 0.030 s	0.1 %	2.6 %	0.1 %	0.1 %	2.7 %	8.3 %	31.4 %
		x 26	x 1	x 1	x 27	x 83	x 314
avg. SS where RT ≤ 0.015 s	10.7 Pa	15.3 Pa	13.4 Pa	13.7 Pa	10.6 Pa	37.1 Pa	11.0 Pa
		+43%	+25%	+28%	-1%	+247%	+3%
avg. SS where RT ≥ 0.015 s	21.3 Pa	22.7 Pa	21.3 Pa	22.6 Pa	22.0 Pa	77.6 Pa	12.0 Pa
		+6%	0%	+6%	+3%	+264%	-44%
Platelet Lysis Index – PLI	0.0071	0.0448	0.0154	0.0249	0.0497	0.1260	0.0357
		x 6.3	x 2.2	x 3.5	x 7.0	x 17.7	x 5.0

Tip volume average SS in ‘Cut Straight’ catheter attains 12.6 Pa. Cutting the inlet at an angle increases average SS with about 30%. Incorporation of side holes renders quasi-identical results irrespective of at which angle the inlet is cut and leads to about 14-17% higher SS as compared to the reference case. Adding a sleeve entrance does not significantly change tip average SS as compared to the reference catheter. A 3.6-fold avg. SS compared to the reference case is noticed when a concentric catheter design is used. Using an Ash Split design reduces avg. SS with about 8%. Similar trends are noticed in the percentages of volume where SS attains 10 Pa or more.

The percentage of volume with a RT of more than 0.015 s is reduced when the end opening is cut at an angle compared to a straight cut with about 17%. The amount of volume with an RT of more than double the average RT at the end of the tip zone however has strongly increased in this case, up to 2.6% of the tip volume compared to 0.1% in case of 'Cut Straight'. Addition of side holes to catheter 'Cut Straight' or 'Cut angle' both reduce the volume with $RT > 0.015$ s with more than a third compared to the reference case; adding a sleeve to the 'Cut Straight' catheter however increases the volume with $RT > 0.015$ s with about 17%, as well as again increasing the amount of volume with $RT > 0.030$ s to 2.7%. 'Concentric' catheter has 13% more zones with $RT > 0.015$ s in its tip zone, but an 83-fold of volume with $RT > 0.030$ s. Largest increase in percentage of volume with $RT > 0.015$ s and > 0.030 s was found in the 'Ash Split' catheter tip with a respective 3.6-fold and 314-fold of values compared to the reference catheter.

Looking at the SS levels in zones with different RT levels, SS is approximately 21 Pa in zones with RT larger than 0.015 s and approximately 11 Pa in zones with RT smaller than 0.015 s. In case of 'Cut Angle', 'Cut Straight Hole' and 'Cut Angle Hole' the change in tip averaged SS is due to a change in SS levels in zones with $RT < 0.015$ s. In catheter 'Ash Split' the change in average SS is mostly due to the change in SS levels in zones with $RT > 0.015$ s. In case of 'Concentric' catheter, the rise of avg. SS level compared to the reference case is equally pronounced in both RT interval zones.

As for average shear stress and residence time parameters, the PLI is lowest for the reference catheter 'Cut Straight'. Trends for PLI values do not always clearly follow the SS or RT values as both parameters are used to calculate the PLI. Catheter classification according to lowest PLI is: 'Cut Straight' < 'Cut Straight Hole' < 'Cut Angle Hole' < 'Ash Split based' < 'Cut Angle' < 'Cut Straight Sleeve' < 'Concentric'.

Under transient SVC flow, average tip SS in catheter 'Cut Angle' varied between minimally 15.3 and maximally 16.8 Pa, slightly past the period of maximal backflow during atrial contraction and of maximal forward flow during systole, respectively. The average SS during pulsatile SVC flow at the point of steady state flow conditions (= 0.2 m/s inflow) is almost identical to the results of the steady state case.

4 Discussion

CFD allows the most time-efficient assessment of flow and shear stress distribution in central venous catheters.[67] Nevertheless, validation with PIV was found to be relevant and necessary as mesh independence for shear stress distribution was only achieved when using very high mesh densities. For the first time, flow inside a catheter lumen was assessed using Particle Image Velocimetry. This was highly successful due to maximal reduction of optical distortion by matching the RI of the fluid and catheter material and by using red fluorescent particles, while respecting dynamic similarity theory. As such, standard PIV was enhanced to allow the

application to this small scale geometry. Very high resolution of velocity measurements was achieved, even to such a level that it was possible to accurately compute first order derivatives (shear strains). Quantitative agreement between PIV and CFD results was reported in Table III-1. The inconsistency can be due to a slight translational displacement of the PIV laser sheet to the exact position of the normal and transverse plane in CFD, which causes obvious differences in maximal and overall velocity magnitude and consequently shear stress distribution. The relative errors for the average velocity values in the normal planes are well below 20%. The errors in the transverse planes are larger, but this can be understood when looking at the flow field. The slow-flow zone downstream the end-opening (and sleeve) is located at the top of the lumen. As such, the measurement results are more prone to ‘vertical’ shifts of the transverse plane (adding the risk of missing the slow flow zone when not measuring close enough to the top of the lumen) than to ‘lateral’ shifts of the normal plane. To illustrate the sensitivity of the results to the exact positioning of the measurement planes, average velocity and strain rate values were computed for a slightly shifted plane for both normal and transverse planes. In case of the Cut Straight Sleeve catheter, the relative error on velocity magnitude is reduced from 52.5% to 8.7% with a plane shift of only 0.5 mm in the transverse plane. This is illustrated in Fig. III-6. Coincidentally, the velocity field in the 0.5 mm shifted plane more closely resembles the PIV measurement result. Besides translational displacements, another possible source of discrepancy is a rotational displacement of the PIV laser sheet. This is e.g. evident in the PIV results of the transverse plane of catheter ‘Cut Angle’ (Fig. III-5), in which an asymmetrical flow was measured. The quantitative discrepancy between PIV and CFD may be further reduced by devising a procedure for a more accurate positioning of the PIV measurement planes in future work.

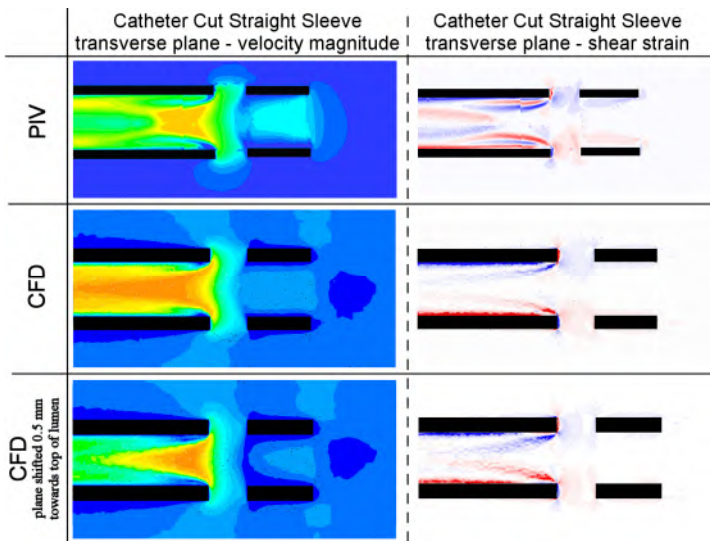


Fig. III-6: Illustration of the sensitivity of velocity and shear strain results in the transverse plane to minor vertical shifts of the measurement plane.

After validation of numerical results with PIV, a second goal of this work was to study possible thrombogenicity of different central venous catheter designs. The methodology used in this study solely concentrates on flow and shear stress parameters inside the catheter lumens. It does not include other major promoters of thrombus formation like inter-dialytic loss of locking solution, type of catheter material used and catheter surface finishing.[29] Also, within a range of elevated shear stresses (> 3 Pa) platelet thrombus production also depends on vWF binding to platelet GpIb/IX/V and GpIIb-IIIa. [64]

Apart from high shear stresses, areas of flow stagnation or recirculation that are characterized by longer residence time may implicate platelet aggregation. Flow induced platelet activation and aggregation has been shown in stenosed human coronary arteries [68] where a volume average SS of approx. 46 Pa and an average transit time of approx. 0.004 s can be calculated (based on an average stenotic diameter of 1.1 mm, 5 mm in length, a peak diastolic blood flow rate of 73 ml/min, wall SS of averagely 70 Pa along the stenosis wall and assuming a linear SS profile across the artery lumen). Given the comparable settings regarding SS and RT values, the results of this study are considered to be relevant and may prove to be of importance in order to minimize risk of blood clotting. *In vitro* validation however may be useful to ascertain the results of this numerical study.

Catheter 'Cut Straight' was set as a reference model as it represents the simplest tip design: a straight cylindrical tip. Blood inflow is highly homogeneous. The tip volume averaged SS attains 12.6 Pa. Theoretically the average SS in laminar flow through a cylinder under the simulated conditions is approximately 12.5 Pa (calculated with constant $\mu = 3.4$ mPa.s). As such, little additional shear stress is induced by the catheter inflow design. Due to the homogeneous inflow, RT values larger than 0.030 s are virtually non-existent. This indicates that almost no local recirculation or zones with low velocities exist in the catheter tip. As a consequence of the low SS and RT, PLI is lowest for this catheter.

Cutting the end opening at an angle (Cut Angle) reduces the effective inflow area as blood is drawn into the 'arterial' lumen as close as possible to the driving force (i.e. pump). This leads to relatively increased SS levels as compared to the reference catheter. The more complex three-dimensional inflow (see Results) gives a slightly better wash-out of blood residing near the wall (= zones with high RT), reducing the percentage of volume with $RT > 0.015$ s. Nevertheless, wash-out is not complete near the inlet as a zone with a significant RT is present near the most distal end of the tip zone, significantly increasing the volume with $RT > 0.030$ s as compared to the reference case. The combination of elevated SS and RT causes the PLI to increase to a more than six fold value as compared to the 'Cut Straight' catheter.

Adding side holes to the reference catheter (Cut Straight Hole) strongly reduced percentage of volume with $RT > 0.015$ s indicating that the side holes provide a more disturbed flow pattern near the wall and consequently a better wash out near the wall. However this is at the cost of a slightly increased SS level. Adding side holes to the angular cut catheter (Cut Angle Hole) disturbs the inflow pattern and reduces the size of the slow-flow zone near the distal tip of the lumen. Consequently, regions with $RT > 0.030$ s have almost disappeared, while the larger effective inflow area decreases average shear stresses. Also, since side holes provide

slightly more than 50% of the total blood inflow rate, the importance of the distal end-opening is reduced. So, quasi-identical results are obtained when adding side holes to the 'Cut Angle' catheter as compared to the 'Cut Straight Hole' catheter and PLI level for catheters with side holes is between the 'Cut Straight' and 'Cut Angle' designs.

Adding a sleeve to the reference design (Cut Straight Sleeve) causes low entrance velocities in the most distal tip zone as more than 80% of the flow enters through the sleeve. More zones with elevated RT are now present: an almost doubled percentage of volume with $RT > 0.015$ s as compared to using side holes. $RT > 0.030$ s zones are at the same level as in 'Cut Angle'. Although average SS levels are maintained at the level of the reference catheter, PLI of 'Cut Straight Sleeve' is strongly elevated, slightly higher than 'Cut Angle'

Although the inflow surface area of the Concentric catheter is identical to the reference catheter and inflow is homogeneous throughout the end opening, the higher SS levels in the Concentric catheter are a consequence of the annular design of the inflow surface. The latter has more inner wall surface, forcing the flow through the thin area between the two walls. Also because of the flow separation near the entrance, percentage of tip volume with $RT > 0.030$ s is also highly elevated. Consequently, this catheter accounts for the highest PLI of all tip designs studied.

The 'Ash Split' based design has multiple side holes which give a more spread inflow pattern. This accounts for the lowest average SS levels of all catheters studied. However, as more than 80% of the incoming flow is drawn by the two most proximal pairs of side holes (S1 & S2), the most distal region of the tip is characterized by very low velocities. This observation can be extrapolated to every catheter design which uses multiple (sets of) side holes which are located longitudinally across the tip length (e.g. Tesio) as the most proximal holes receive the largest blood flow and increase the residence time in the low-flow distal tip region. This strongly increases local RT values causing blood in about a third of the tip volume to be present in the tip zone for longer than twice the average RT of blood passing through the tip zone. For this catheter with a different trend in SS and RT levels, the PLI parameter allows to assess how the combination of decreased SS and increased RT influences the classification of this design according to possible platelet activation. PLI of 'Ash Split type' is between values of the tip designs with side holes and the 'Cut Angle' design. So although RT are highest of all tips studied, the less than linear dependence of PLI on exposure time causes the PLI value to be far lower than the PLI of the 'Concentric' catheter.

Concerning the influence of pulsatile SVC flow, as average SS in the catheter tip closely follows SVC flow rate, catheter classification according to thrombogenicity is not expected to change.

In conclusion, the 'Concentric' catheter is discarded due to the highly elevated SS levels. This numerical study recommends using the reference catheter 'Cut Straight' as a minimal risk to platelet activation. Catheters 'Cut Straight Hole' and 'Cut Angle Hole' render second-to-best results, showing that adding two (relatively large) side holes, symmetrically placed close to the tip are not detrimental to the catheter performance. Catheter 'Cut Angle Hole' (with end opening cut at an angle and with two lateral side holes close to the tip) may be preferred in practice

because of ease of insertion as compared to the ‘Cut Straight catheter’. Catheters ‘Cut Angle’, ‘Cut Sleeve’ and an Ash Split based design render suboptimal results.

5 Conclusions

As crucial factors in blood clot formation, shear stress distribution and low flow zones are assessed in different catheter tip designs using a combined numerical and experimental approach. Computational Fluid Dynamics was validated by using Particle Image Velocimetry (PIV). The chosen standard PIV was a successful method to measure velocity magnitudes in the small scale of a dialysis catheter model. Velocity and derived shear strain distributions in two orthogonal planes of three different catheter models compared qualitatively and quantitatively well to the numerical results.

After validation, four additional catheter designs were studied. In each of the seven catheters studied, six parameters concerning average shear stress (SS) levels and blood residence time (RT) values were assessed. Also Platelet Lysis Index which combines the influence of shear stress level and exposure time is studied. The Platelet Lysis Index proved a fast and comprehensive parameter to assess possible thrombogenicity of catheter tip designs and allowed comparison when shear stress and residence time values showed different trends. In conclusion we state that the concentric catheter designs are not recommended due to elevated shear stress levels and residence time values respectively. ‘Ash Split’ based design has elevated residence time values in the distal tip zone as major inflow occurs through the most proximal side holes, as can be expected with catheter designs with multiple side hole along its tip. Concerning possible platelet activation, the elevated residence times are compensated by low average shear stresses. Nevertheless, a cylindrical lumen, preferably ‘Cut Straight’ or with the addition of only two lateral side holes close to the tip (‘Cut Straight Hole’ & ‘Cut Angle Hole’) are preferred designs when aiming at a combination of minimal shear stress levels and local residence time values. Transient flow in the SVC is not expected to influence this recommendation. *In vitro* validation however may be useful to ascertain the results of this numerical study.

6 Acknowledgments

The authors are very grateful towards Stefaan Bliki and Marcel Antheunis for the construction of the experimental set-up. First author’s research is supported by a BOF-grant (011D09503) from Ghent University, Belgium.

Part B: Bioartificial liver support Improving the efficiency of the AMC Bioartificial Liver

Chapter IV: Liver support systems – a review from Anatomy to Zoonosis

1 The human liver

The liver is one of the – if not *the* most complex organ of the human body - in terms of anatomy, circulation and especially function. If you would look into several general physiology textbooks, chances are you would not even find a chapter entitled ‘The Liver’. As the liver is rumored to have more than 200 functions, the description of liver physiology is scattered throughout multiple chapters which connect its metabolism and functions in the entire body. Consequently, to give a complete description of the liver anatomy and physiology is a gigantic undertaking. A humble attempt is made in the text below.

1.1 Anatomy

1.1.1 Gross anatomy

The liver (Fig. IV-1) is the second largest organ (largest being the skin) and the largest gland in the human body. It is positioned in the upper right quadrant of the peritoneal cavity, below the diaphragm. It is a boomerang-shaped brownish organ which weighs about 1.1 to 1.6 kg, depending on sex and body weight. On gross visual inspection, the liver appears to be divided into two lobes, right and left, which are separated by ligaments. The right lobe is approximately six times the size of the left and accommodates two smaller lobes: the caudate lobe on its posterior surface and the quadrate lobe on its inferior surface. It also forms a kind of bed for the gallbladder. Although separation is apparent, no functional differences between the four lobes exist.

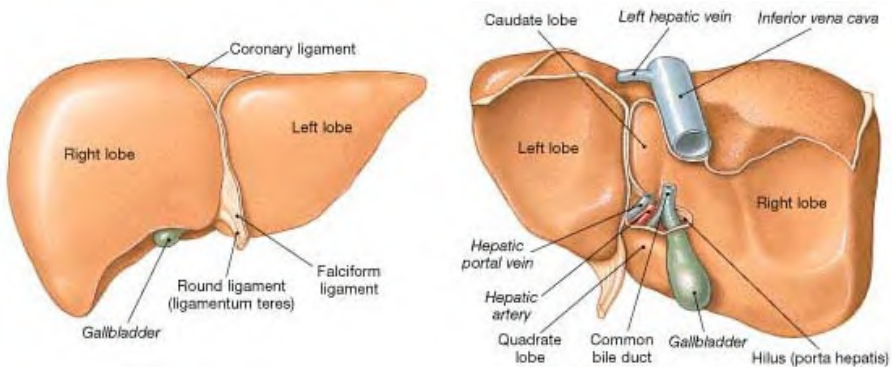


Fig. IV-1: Anatomical view of the human liver

1.1.2 Macrocirculation

Looking at the hepatic blood supply, some unique characteristics are present (Fig. IV-2). First of all, the liver has two afferent blood supplies: one venous, the portal vein and one arterial, the hepatic artery. The portal vein collects all the blood that leaves the spleen (10%), stomach (20%), small and large intestines (60%) and pancreas (10%) and carries it to the liver. As such, it carries a high content of nutrients, drugs and possible toxins which are subsequently metabolized or removed by the liver. Typical for venous blood, it has a low oxygen concentration (oxygen partial pressure $pO_2 = 34 - 46$ mmHg) and its flow is continuous and at low static pressure ($p_{\text{static}} = 7-10$ mmHg [69]). Arterial blood is supplied via the hepatic artery. It is characterized by a high oxygen content ($pO_2 = 74 - 104$ mmHg) and a pulsatile, high pressure (avg. $p_{\text{static}} = 100$ mmHg) flow. Total blood supply to the liver is about 25-30% of the cardiac output, about 1.45 L in total. This is a surprisingly large amount as the liver only represents about 2% of total body weight. 75% (approx. 1100 mL/min) of blood supply comes through the portal vein. The hepatic artery accounts for the remaining 25% (approx. 350-400 mL/min). After passing the microcirculation of the liver, blood exits the liver via the hepatic vein, which drains into the inferior vena cava. Logically, the drained blood has a low oxygen content ($pO_2 = 30-35$ mmHg) and its flow is non-pulsatile and at low pressure ($p_{\text{static}} = 3-5$ mmHg).

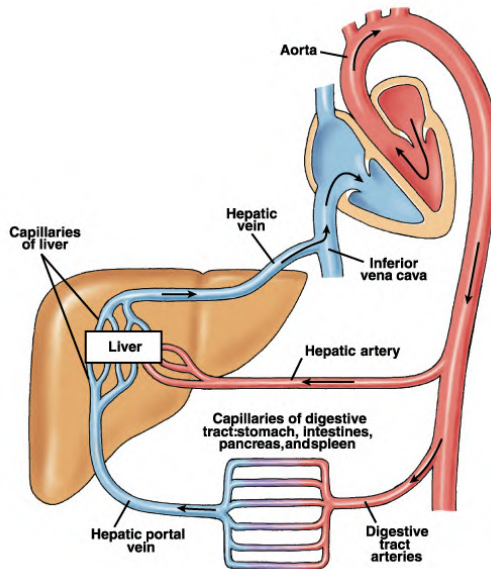


Fig. IV-2: Macrocirculation of the liver

1.1.3 Microcirculation

Both afferent blood vessels branch into increasingly smaller vessels. The hepatic artery closely accompanies the portal vein as it enters the hepatic parenchyma. Terminal branches of both vessels mix into the liver sinusoids. Sinusoids are

distensible vascular channels (diameter = 7 – 15 μm ; length = 223 – 477 μm) lined with highly fenestrated endothelial cells and bounded circumferentially by hepatocytes. Blood flows through these sinusoids and empties into a so-called central vein. The liver is able to regulate mainly arterial flow by means of so-called sphincters, situated at the inlets and outlets of the sinusoids. One of the most important triggers for sphincter function is the need for constant oxygen supply. If the rate of oxygen delivery to the liver varies, the sphincters will react and the ratio of arterial-to-portal blood flow will alter. Oxygen partial pressure (pO_2) is about 60-65 mmHg in the periportal blood and falls to about 30-35 mmHg in the perivenous blood. One central vein collects blood from multiple sinusoids. Central veins finally empty into the hepatic vein, which subsequently drains into the inferior caval vein.

1.1.4 Histology

The tight network of sinusoids provides the different cell types in the liver with the necessary oxygen, and metabolites, toxins and nutrients which need to be processed. Six major cell types exist in the liver: (1) endothelial cells, which line the sinusoids; (2) stellate cells, which contain lipid droplets storing vitamin A and play an important role in fibrogenesis; (3) bile ductular cells, which make out the bile ducts; (4) Kupffer cells, which are macrophages; (5) pit cells, which are natural killer cells; and (6) hepatocytes, the actual functional liver cells. The different functions of these cells and of the liver as a whole are explained more in-depth while discussing the liver microstructure. On a micro level, the different cells are arranged in a unique, complex way around the sinusoids. A histological picture of a liver slice is shown in Fig. IV-3. Different unit structures can be identified, depending on a structural or functional point of view.

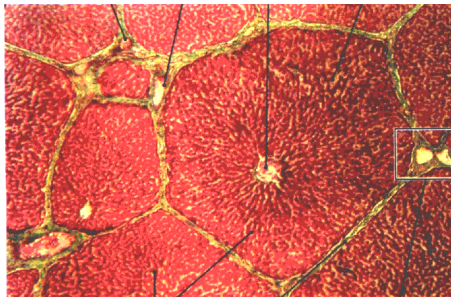


Fig. IV-3: Histological view of a liver slice

a) **Structural unit of the liver: the liver lobule**

The liver is bounded by a connective tissue capsule which extends into the organ as highly branched septae. The afferent blood vessels and lymphatics follow this connective tissue highway throughout the liver. The connective tissue septae folding inwards from the capsule delineate hepatic lobules, the structural units of the liver. They are visual in Fig. IV-3 and schematically represented in Fig. IV-4.

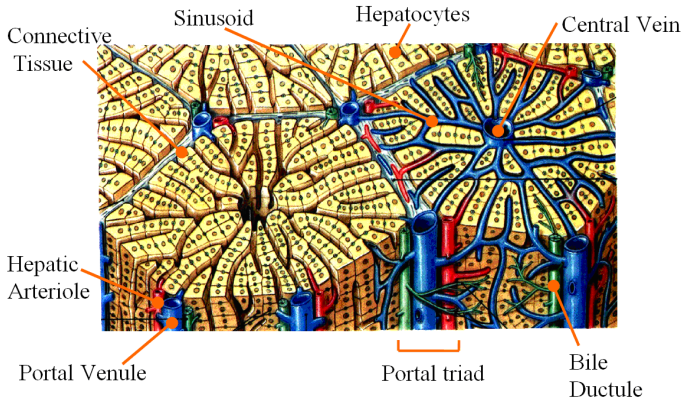


Fig. IV-4: Schematic drawing of the liver microstructure – the 'liver lobule'

The liver lobule (Fig. IV-4) is a hexagonal shaped, cylindrical structure several millimeters in length and 0.8 to 2 mm in diameter. The human liver contains 50'000 to 100'000 individual lobules. Its central axis is the origin of hepatic venous drainage, the central vein. At the vertices of the lobule, regularly distributed portal triads (also known as portal tracts) are present. Examination of a triad reveals a bile duct and branches of the hepatic artery (arterioles) and hepatic portal vein (venules). Lymphatic vessels are also present, but are almost indistinguishable, which is probably why it is not called a portal tetrad. The lobule is composed of a hexagonal arrangement of hepatic cellular plates and sinusoids which radiate centrifugally from the central vein like spokes in a wheel. A detailed schematic of such a spoke is depicted in Fig. IV-5.

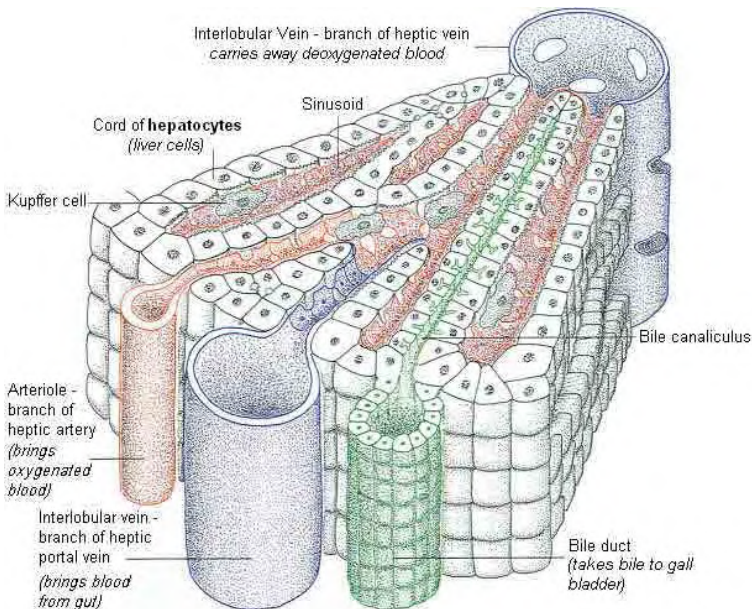


Fig. IV-5: Radial section of a liver lobule

Portal venous and hepatic arterial blood mix in the *sinusoids*, which are surrounded by plates of hepatocytes. However, the hepatocytes are not in direct contact with blood because the sinusoids are lined by endothelial cells. Beneath this lining is a very narrow interstitial space called the *space of Disse*. The endothelial lining has considerably large pores, about 175 nm in diameter, which occupy 6 – 8 % of the surface.[70] Thus, blood cells cannot penetrate the fenestrated endothelial lining so plasma is filtered into this space. The pores in the endothelium are however large enough to allow substances (up to 250'000 MW) in the plasma to move freely into the space of Disse and reach the hepatocytes. As such, the space of Disse is the foremost important place of bidirectional solute exchange between hepatocytes and the blood-filled sinusoids.

Since the space of Disse connects directly with the small lymph vessels in the portal triad, some of the plasma which collects in the space of Disse flows back toward the portal tracts (counter currently to the blood flow), collecting in lymphatic vessels and forming a large fraction of the body's lymph. Filtration is greater at the centrilobular region of the sinusoid as a result of increased porosity of the fenestrae and a widening of the sinusoid. Further, endothelial cells also participate in endocytosis and present numerous surface antigens, which suggest that they might be effector cells for immune responses.[71] Hepatic sinusoids also house numerous Kupffer cells, a highly effective phagocyte.

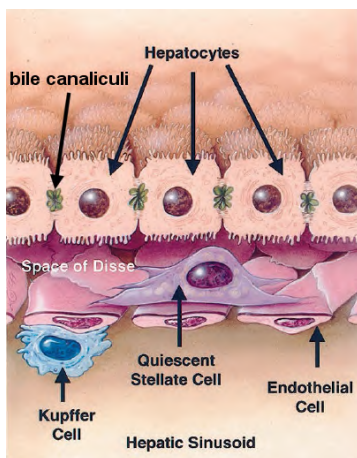


Fig. IV-6: Schematic drawing of the sinusoid lining and the Space of Disse. [72]

Kupffer cells accumulate in periportal areas. They specifically endocytose endotoxin, which activates these macrophages. Lipopolysaccharide, together with interferon gamma, belong to the most potent activators of Kupffer cells. As a result of activation, these cells secrete oxygen radicals, tumor necrosis factor (TNF)⁴, interleukin-1 (IL-1),

⁴ TNF(-alpha) is a cytokine (signaling molecule) involved in systemic inflammation. Its primary role is in the regulation of immune cells. Together with IL-1 and IL-6, it is a member of a group of cytokines that all stimulate the acute phase reaction.

interleukin-6 (IL-6)⁵, and a series of eicosanoids⁶ and become cytotoxic against tumor cells.

The stellate cells and the pit cells are located in the space of Disse surrounding the sinusoids (Fig. IV-6). Stellate cells are primarily fat-storing cells and contain characteristic fat droplets, which contain a large part of the body's depot of vitamin A. These cells have long, contractile processes and probably influence liver (sinusoidal) blood flow together with the sphincters. Stellate cells also play a major role in the synthesis of extracellular matrix⁷ (ECM)[73,74]. However, vitamin A deficiency such as in alcoholic livers transforms fat-storing cells into myofibroblast-like cells with enhanced ECM production. As such, these cells play an important role in the pathogenesis of fibrosis. Pit cells display a high level of spontaneous cytolytic⁸ activity against various tumor cells, identifying themselves as natural killer cells. Pit cell proliferation occurs within the liver, but recent evidence indicates that blood large granular lymphocytes develop into pit cells in 2 steps involving high- and low-density pit cells. Kupffer cells control the motility, adherence, viability, and cytotoxicity of pit cells, whereas cytotoxicity against tumor cells is synergistically enhanced.

Finally hepatocytes, the functional liver cells, are arranged in plates that anastomose with one another. The cells are polygonal, almost cubic in shape (characteristic dimension ~ 20 μm). They are highly polarized, which means that its plasma membrane can be divided into distinctive domains with fixed orientation. Hepatocytes have three distinct surfaces, each with a distinctive ultrastructure: (1) The apical pole or the bile canalicular region is formed by the invagination of two adjacent membranes and delimited by tight junctions. It is modified to form bile canaliculi that empty into bile ducts. As such, bile also (as lymph does) flows counter currently with respect to the blood flow. (2) The basal pole or sinusoidal surface is characterized by many minute projections of the cell membrane (microvilli) that are present abundantly and project into the Space of Disse (Fig. IV-6). These microvilli greatly increase the surface area of the cell and thus promote solute exchange between the cell and the surrounding plasma. (3) The lateral pole or intracellular surface appears smooth but contains the junctions that define cell polarity (tight junctions), bind hepatocytes together (desmosomes) and provide communication between cells (gap junctions). These morphological structures reflect a differentiation in function, i.e., secretion, absorption, and intercellular communication and attachment, respectively.

b) *Functional unit of the liver: the hepatic acinus*

The hepatic or portal acinus is considered the functional unit of the liver.[75] As seen in Fig. IV-7, the acinus is an irregular shaped, roughly ellipsoidal area, with a short

⁵ Interleukin 1 and 6 are pro-inflammatory cytokines involved in immune defence against infection.

⁶ Eicosanoids: signaling molecules derived from omega-3 or omega-6 fats. They exert complex control over many bodily systems, especially in inflammation, immunity and as messengers in the central nervous system.

⁷ Extracellular matrix: complex macromolecular structural network surrounding the liver cells; consists mostly of fibronectin, some collagen type I, and minor quantities of collagen types III, IV, V, and VI.

⁸ Cytolytic: with the ability to destroy cells.

and a long axis. The short axis is defined by the portal triad's distributing branches that run along the border of two classical lobules. The long axis is a line drawn between the two central veins closest to the short axis. Cells in the liver acinus are arranged into three concentric, elliptical zones around the short axis. There are no sharp boundaries between the zones.

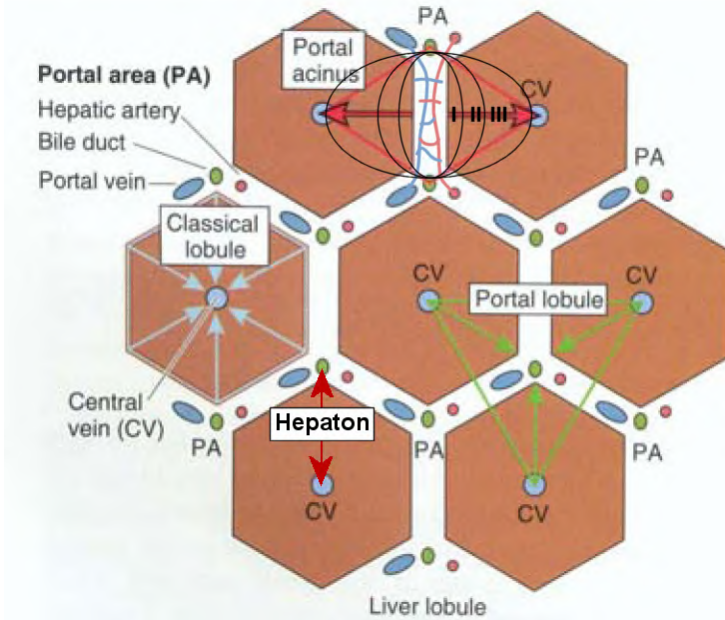


Fig. IV-7: Different unit structures of the liver parenchyma: the liver lobule, hepatic acinus, hepaton and portal lobule

Cells in zone I are closest to distributing arteries and veins. Consequently, these cells are the first to receive both nutrients and toxins. For example, they are the first to take up glucose to store as glycogen after a meal, and the first to break down glycogen in response to fasting. They are also the first to show morphological changes following bile duct occlusion. If circulation is impaired, they are the last to die and the first to regenerate. Cells in zone III are farthest from the distributing vessels and closest to the central vein. They are the first to show ischemic necrosis, and the first to show fat accumulation. They are the last to respond to toxic substances and bile stasis. Cells in zone II have functional and morphological characteristics intermediate between those of zones I and III.

This phenomenon, known as *zonation*, has been described in virtually all areas of liver function. Oxidative energy metabolism, carbohydrate metabolism, lipid metabolism, nitrogen metabolism, bile conjugation, and xenobiotic metabolism have all been localized in separate zones. Such compartmentalization of gene expression is thought to trigger the liver's ability to operate as a "glucostat" as well as to explain the pattern of zonal hepatotoxicity observed with some xenobiotics (e.g., acetaminophen) and environmental agents (e.g., carbon tetrachloride). The distribution of functions

along the sinusoid is thought to be modulated by diverse factors such as oxygen and hormone gradients, nutrients, matrix composition, and even the distribution of non-parenchymal cells [76,77,78,79].

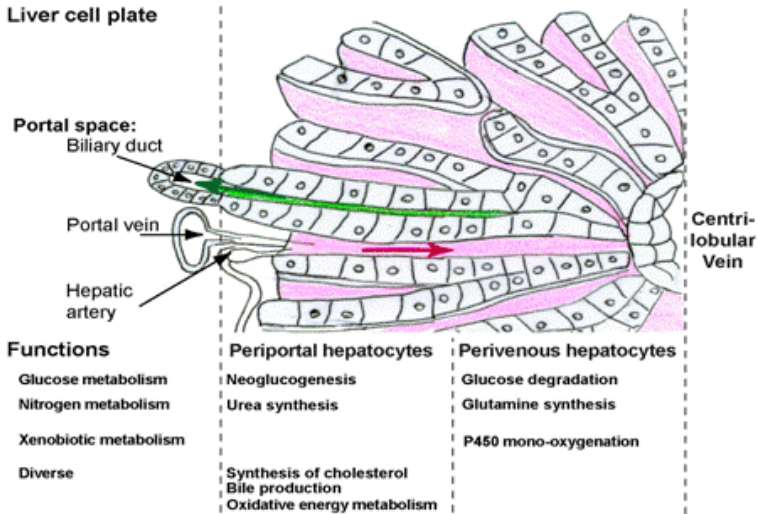


Fig. IV-8: Zonation of liver functions (adapted from [80])

The acinus is more difficult to visualize than the lobule, but represents a unit that is of more relevance to hepatic function because it is oriented around the afferent blood supply to liver parenchyma, rather than its venous drainage.

Although the liver lobule and the acinus are the two most well-known models to describe the organization of the liver, two alternative models can be found in literature.

c) Minimal functional unit of the liver: the hepton

An acinus includes many sinusoids and, as such, does not constitute a minimal structure supporting hepatic function. McCuskey [81] suggested that a functional unit of liver tissue must be defined as the minimum amount of tissue required to perform the function of the organ and, as such, should be built around the sinusoid as illustrated in Fig. IV-7. This model incorporates a sinusoid with a surrounding cylinder of hepatic tissue, including afferent and efferent vasculature, lymphatic, biliary and neural connections. The terminology is derived from the nephron, the basic structural and functional unit of the kidney.

d) Exocrine unit of the liver: the portal lobule

The portal lobule model emphasizes the exocrine function of the liver, namely bile secretion. In this unit structure, the portal bile duct (component of the portal triad) is taken as the centre of the lobule. Its outer margins are imaginary lines drawn

between the three central veins that are closest to that portal triad (see Fig. IV-7). This roughly triangular block of tissue includes those portions of three classic liver lobules that secrete bile that drains into its central bile duct. This model allows description of liver parenchyma in terms comparable to those used for other exocrine glands.

1.2 Physiology

The healthy liver is strategically positioned in the body as the important guard between the splanchnic and systemic circulation in which it has an important role in the regulation of the body homeostasis. It is responsible for protein synthesis, carbohydrate and lipid metabolism, bile production, cholesterol metabolism, acid-base balance, detoxification of protein bound and lipid soluble compounds, and storage of essential compounds like vitamins, minerals and glycogen. In addition, the specific hepatic macrophage system plays an important role in endotoxin removal and immune protection.

– dr. Robert A.F.M. Chamuleau

1.2.1 Functions of the hepatic vasculature system

a) Blood reservoir function

Because the liver is an expandable and compressible organ (due to the extensive compliant vasculature), large quantities of blood can be stored in its blood vessels. About 10-15% of the total blood volume of human body resides in the liver, 60% of which is located in the sinusoids; the remaining 40% in the larger vessels (portal and hepatic vein, hepatic artery). However, when high pressure in the right atrium causes back pressure in the liver, the liver expands, and as much as 1 liter of extra blood can be stored in the hepatic veins and sinusoids. Conversely, if a person hemorrhages so that large amounts of blood are lost from the circulatory system, much of the normal blood in the liver sinusoids drains into the remainder of the circulation to help replace the lost blood.

b) Lymph flow from the liver

The extreme permeability of the liver sinusoids allows large quantities of lymph to forming the space of Disse. As such, about half of all lymph formed in the body under resting conditions originates from the liver (i.e. 1-2 liter per day). Because the pores in the hepatic sinusoids allow ready passage of proteins, the lymph draining from the liver usually has a protein concentration of about 6 grams per deciliter, which is only slightly less than the protein concentration of plasma.

A main function of the lymph is the transport of lipids and lipid-soluble vitamins (A, D, E, and K), absorbed in the gastrointestinal tract, to the venous circulation. The lymphatic system also plays an important role in the immune defense system as it is

responsible for the production, maintenance and distribution of lymphocytes that provide defense against infections and other environmental hazards.

c) *Hepatic macrophage system*

An important function of Kupffer cells is to engulf old or damaged red blood cells, cellular debris and pathogens, removing them from the bloodstream. As a part of the reticuloendothelial system, which is a subsystem of the immune system, Kupffer cells are highly phagocytic cells. So much even that they can remove 99% of bacteria in the portal venous blood before they can pass all the way through the liver sinusoids. Since portal blood drains from the intestines, it contains a considerable amount of colon bacilli. Therefore, the importance of the Kupffer cell filtration system as an immunological barrier between the splanchnic and systemic circulation is evident.

1.2.2 Metabolic functions of the liver

Hepatocytes are metabolic superachievers in the body. The body depends on the liver to regulate, synthesize, store, and secrete many important proteins and nutrients and to purify, transform, and clear toxic or unneeded substances. All these functions are summarized as the metabolic functions of the liver.

a) *Carbohydrate metabolism*

The liver is especially important for maintaining a normal blood glucose concentration. Excess glucose entering the blood after a meal is rapidly taken up by the liver and stored as a glycogen (a process called *glycogenesis*). Glycogen forms an energy reserve that can be quickly mobilized to meet a sudden need for glucose. Only the glycogen stored in the liver can be made accessible to other organs, and hepatocytes have the highest concentration of it of all body cells - up to 8% of the fresh weight in well fed state. In the muscles, glycogen is found in a much lower concentration (1% of the muscle mass), but the total amount exceeds that in the liver.

Thus, when blood concentrations of glucose begin to decline, the liver activates other pathways which lead to depolymerization of glycogen (*glycogenolysis*) and export of glucose back into the blood for transport to all other tissues. This is called the *glucose buffer function* of the liver. These processes are regulated by the interplay between insulin and its hormonal antagonists, such as glucagon and adrenalin among others.

When glycogen storage is low or when blood glucose level falls below normal, hepatocytes are able to synthesize glucose from noncarbohydrate precursors, such as lactic acid (60%), glycerol (10%) or amino acids (mainly alanine, 30%). This process is called *gluconeogenesis*. Furthermore, the liver cells convert galactose and fructose to glucose and are responsible for the formation of many important chemical compounds from the intermediate products of carbohydrate metabolism.

b) *Fat / lipid metabolism*

Few aspects of lipid metabolism are unique to the liver, but many are carried out predominantly by the liver. The liver is extremely active in oxidizing triglycerides to

produce energy. The liver breaks down much more fatty acids than the hepatocytes need, and exports large quantities of acetoacetic acid into blood. This highly soluble acid passes from the liver cells into the extracellular fluids and is then transported throughout the body to be absorbed by other tissues. Inversely, the liver is also the major site for converting excess carbohydrates and proteins into fatty acids and triglyceride, which are then transported in lipoproteins and stored in adipose tissue.

The liver is also a major site of lipoprotein formation and cholesterol and phospholipid synthesis. Lipoproteins are macromolecules comprising proteins and lipids. They transport water-insoluble lipids in the blood, with the exception of about 50% of free fatty acids that are albumin-bound.

About 80% of the cholesterol synthesized is converted into bile salts, which in turn are secreted into the bile (see §1.2.3); the remainder is transported in the lipoproteins, which are carried by the blood to the tissue cells everywhere in the body. Phospholipids are likewise synthesized in the liver and transported principally in the lipoproteins. Both the cholesterol and the phospholipids are used by the cells to form membranes, intracellular structures, and multiple derived chemical substances that are important to cellular function.

c) Protein metabolism

As many processes in protein metabolism only occur in the liver and not in other cells in the body, this part of liver metabolism is indispensable for the human body whereas its contribution to carbohydrate and fat metabolism is important, but certainly not as critical. The most important functions of the liver in protein metabolism are (1) deamination of amino acids, (2) formation of urea for removal of ammonia from the body fluids, (3) formation of plasma proteins and (4) interconversion among the different amino acids and other compounds important to the metabolic processes of the body.

Deamination of the amino acids is required before these can be used for energy or before they can be converted into carbohydrates or fats. However, this deamination brings along the formation of large amounts of ammonia. Additional amounts of ammonia are continuously formed in the gut by bacteria and are subsequently absorbed into the blood. As ammonia is toxic in small concentrations, elimination of ammonia by conversion into non-toxic urea through the *urea cycle* is crucial. In the absence of this function of the liver to form urea, the plasma ammonia concentration rises rapidly and results in *hepatic encephalopathy*, coma and death (see §1.3).

Essentially all the plasma proteins (except for antibodies produced by plasma cells in the lymph tissue) are formed by the hepatocytes. This accounts for about 90% of all plasma proteins. One of the most important proteins produced exclusively by the liver is albumin, which accounts for 50-65% of total plasma proteins. Albumin is responsible for plasma oncotic pressure and acts as a transport protein for the binding of drugs, hormones, various metabolites, bilirubin (an end-product of red blood cell decomposition in the spleen or bone marrow), bile intermediates, enzymes and inorganic ions. As such, albumin transports free fatty acids and bilirubin to the liver. Also, the liver synthesizes many of the clotting factors necessary for blood coagulation like fibrinogen and prothrombin.

Finally, among the most important functions of the liver is its ability to synthesize certain amino acids and also to synthesize other important chemical compounds from amino acids (transamination). For instance, the so-called non-essential amino acids can all be synthesized by the liver.

d) Vitamin metabolism

The liver has a particular predisposition for storing vitamins. The single vitamin stored to the greatest extent is vitamin A, but large quantities of vitamin D and B₁₂ are stored as well.

e) Iron metabolism

Except for the iron in the hemoglobin of the blood, by far the greater proportion of the iron in the body is stored in the liver in the form of ferritin. When iron is available in the body fluids in extra quantities, liver cells convert it to ferritin for storage. Ferritin releases iron when circulating iron levels reach a low level. As such, the liver acts as a *blood iron buffer* and also as an iron storage medium.

f) Biotransformation and detoxification

The elimination of endogenous and exogenous substances from the body is necessary if they do not serve the production of energy, are not needed for the maintenance of structure, or cannot be stored without causing harm. The liver is the central organ for the degradation and/or detoxification of superfluous and harmful substances as well as their excretion from the body. Some of these toxins include alcohol, chemicals, drugs, heavy metals, endogenous toxic metabolic products and other plant, animal or bacterial toxins.

Toxins can be present in water-soluble (hydrophilic) or in fat-soluble (hydrophobic or lipophilic) form. Fat-soluble substances are superior in number (about 70-80%). However, they cannot be excreted in an unchanged state. As such, these substances must be broken down and or detoxified and made water-soluble so they can be excreted via the kidney or (through bile) in the stool. This process of biochemical changes of a lipophilic to a water-soluble substance is called *biotransformation*. It takes place in two phases. In phase I, the lipophilic molecule is provided with a functional hydrophilic group by oxidation, reduction, hydrolysis and hydration processes. In this stage, cytochrome P450 is the most important element in the oxidative metabolism of drugs and toxins. If the metabolites of phase I reactions are sufficiently water-soluble, they may be readily excreted at this point. However, many phase I products are not eliminated rapidly and undergo a subsequent reaction in which an endogenous substrate (e.g., glucuronic acid, sulfonates, glutathione or amino acid) combines with the newly incorporated functional group to form a highly hydrophilic conjugate, which is now readily excreted in the urine and/or bile. This is known as a phase II reaction. The resulting conjugate is now mostly biologically inactive and thus truly detoxified. This is in contrast with phase I reactions, which potentially increases the toxicity of the lipophilic substance. Phase II reactions can also take place without the prior phase I step if the given substance already possesses a group with suitable binding ability.

1.2.3 Formation of Bile

All the hepatic cells continuously form a small amount of yellowish secretion called bile. From the minute bile canaliculi, bile then flows into terminal bile ducts and further to the common bile duct, from which the bile either empties directly into the duodenum or is diverted into the gallbladder for storage. The total secretion of bile each day is about 700 to 1200 mL.

Bile is mainly composed of water (97.5 weight%), bile salts (1.1 w%), bilirubin (0.04 w%), cholesterol (0.1 w%), fatty acids (0.12 w%), lecithin (0.04 w%) and electrolytes of plasma. From the composition of bile, two important functions of bile can be derived.

The first function is related to the presence of bile salts. Liver cells form about 0.5 g of bile salts daily. The precursor of bile salts is cholesterol as mentioned above (§1.2.2b), while bile salts in their turn play a regulatory role in cholesterol metabolism. Bile salts also have a two-fold function in the intestinal tract. First they have a detergent action on the fat particles in the food, which decreases the surface tension of the particles and allows the agitation of the intestinal tract to break the fat globules into minute sizes. This is called the *emulsifying or detergent function* of bile salts. Secondly, bile salts help in the absorption of fatty acids, monoglycerides, cholesterol and other lipids from the intestinal tract by forming minute complexes with these lipids. These complexes (*micelles*) are highly soluble because of the electrical charge of the bile salts. Since bile increases the absorption of fats, it is an important part of the absorption of the fat-soluble vitamins D, E, K and A.

Bile does not only have a *secretion* function, but also an *excretion* function. This is notable by the presence of bilirubin. As mentioned before (§1.2.2f), the liver is well known to metabolize and excrete into bile many compounds and toxins, thus eliminating them from the body (by reabsorption in the small intestine and ultimate elimination by the kidneys; or via the stool). One of the most important and clinically relevant examples of waste elimination via bile is that of *bilirubin*.

Bilirubin is a water-insoluble and toxic breakdown product of hemoglobin, which also means that it is generated in large quantities. In the time it takes you to read this sentence aloud, roughly 20 million of your red blood cells (RBC) have died and roughly 5 quintillion (5×10^{15}) molecules of hemoglobin are in need of disposal (approx. 2 million RBC per second; each containing approx. 270×10^6 molecules of hemoglobin). When red blood cells die, their cell membranes rupture and hemoglobin is released. Tissue macrophages (including Kupffer cells) phagocytize the hemoglobin and split it into globin and heme. The globin chains are protein and are catabolized and its components reused. The heme is separated into free iron that is reused, and further converted through a series of steps into free bilirubin. However, the free bilirubin immediately combines very strongly with plasma albumin and is transported in this combination throughout the blood and interstitial fluids. Even when bound, this bilirubin complex is still called 'free bilirubin'. In this form it is lipophilic and, as such, highly soluble in cell membranes and also very toxic. The mechanisms involved in elimination of bilirubin are similar to those used for elimination of many drugs and toxins (§1.2.2f). Consequently, when the albumin-bound bilirubin reaches the hepatocytes, bilirubin is removed from the carrier and is

conjugated with glucuronic acid or sulfate to make it water-soluble ('conjugated bilirubin'). Conjugated bilirubin is secreted into the bile canaliculus as part of bile and thus delivered to the small intestine. Bacteria in the intestinal lumen metabolize bilirubin to a series of other compounds which are ultimately eliminated either in feces or, after reabsorption, in urine. The major metabolite of bilirubin in feces is sterobilin, which gives feces their characteristic brown color. Lack of bilirubin clearance by the liver causes jaundice, one of the most important and well known symptoms of liver disease (see further §2.2).

1.2.4 Liver regeneration

The liver possesses the unique capacity to undergo rapid regeneration and replacement of damaged tissue after injury. Liver regeneration is associated with proliferation of hepatocytes sufficient to generate a critical mass necessary to maintain normal liver function. As such, during acute regeneration more than 30% to 50% of remaining hepatocytes undergo cell division. The liver can recover from a resection (hepatectomy) of up to 70% of the liver mass within a matter of days to weeks. The liver's capacity to regulate its own growth is also evident in liver transplantation, in which the size of the donor organ either expands or diminishes with time, as appropriate to the size of the patient. This regenerative ability of the liver is also clear in the successful use of single-lobe liver transplantation in children.[82,83]

1.3 Pathology of the liver

Despite of the unique property of being able to regenerate, repair or replace damaged tissue, the liver can still be exposed to many diseases which may destroy its regenerative capability. There are literally hundreds of liver diseases, but some are quite rare. While there are many causes of liver disease, they generally present in a few distinct patterns, usually classified as either:

- Hepatocellular, or
- Cholestatic / obstructive.

In hepatocellular diseases, features of liver injury, inflammation and necrosis predominate. Cholestatic diseases are characterized by an inhibition of bile flow. Some of the most common types of liver disease are discussed below.

1.3.1 Hepatocellular diseases

a) *Hepatitis*

The term hepatitis refers to any inflammatory process of the liver. The most common etiology of acute hepatitis is viral infection. The term chronic hepatitis means active, ongoing inflammation of the liver persisting for more than six months that is detectable by biochemical and histological means. Many etiologies can lead to hepatitis.

(i) Viral hepatitis

Several types of *viral hepatitis* exist:

- *Hepatitis A* is caused by a picorna virus. It is transmitted by the oral-fecal route, transmitted to humans through contaminated food or water. It causes an acute form of hepatitis and does not have a chronic stage. The time between the infection and the start of the illness can run from 15 to 45 days. The illness itself lasts up to 6 weeks and does not cause chronic hepatitis or cirrhosis.
- Hepatitis B is caused by the hepadna virus, which can cause both acute and chronic hepatitis. Incubation time is 50 to 160 days. Identified methods of transmission include blood (blood transfusion, now rare), tattoos, sexually (through sexual intercourse or through contact with blood or bodily fluids), or in utero (from mother to her unborn child, as the virus can cross the placenta). Blood contact can occur by sharing syringes in intravenous drug use, shaving accessories such as razor blades, or touching wounds on infected persons. 5% of patients do not clear the infection and develop chronic infection. A vaccine is available that will prevent infection from hepatitis A and B for life.
- Hepatitis C is caused by the hepatitis-C virus, which is easily transmitted through contact with blood and other methods of transmission as mentioned above. Hepatitis C may lead to a chronic form of hepatitis. 20% of those patients get cirrhosis, 25% get hepatocellular carcinoma. Hepatitis C can remain asymptomatic for 10-20 years. No vaccine is available for hepatitis C.
- Other types of viral hepatitis are hepatitis E, F (unknown), and G.

Acute viral hepatitis is a self-limited disease and requires supportive care only. For the few patients who develop fulminant liver failure, liver transplantation may be required. Chronic infection can develop in patients with hepatitis B, C, and G infection.

(ii) Alcoholic hepatitis

Hepatitis can also be alcohol induced. This usually comes after an extended period of increased alcohol consumption but this depends on genetic predisposition. Alcoholic hepatitis is distinct from cirrhosis caused by long term alcohol consumption as alcoholic hepatitis by itself does not lead to cirrhosis.

(iii) Drug induced hepatitis

Hepatitis can also be induced by a certain number of drugs. Ibuprofen and paracetamol (acetaminophen) are two well know examples. For example, paracetamol has a narrow therapeutic index. This means that the therapeutic dose is close to the toxic dose, so there is a large potential for overdose and toxicity. Because of the wide over-the-counter availability of the drug, it is sometimes used in suicide attempts by those unaware of the prolonged timecourse, and high morbidity associated with paracetamol-induced toxicity.

(iv) Autoimmune hepatitis

Autoimmune hepatitis is characterized by an attack of the immune system on the liver as if it were not an autologous part of the body. It has an incidence of 1-2 per 100,000 per year, and a prevalence of 15-20/100,000. As with most other autoimmune diseases, it affects women much more often than men (8:1). As with other liver diseases, autoimmune hepatitis can progress to cirrhosis.

b) Non-alcoholic fatty liver disease (NAFLD)

Non-alcoholic fatty liver disease is fatty inflammation of the liver when this is not due to excessive alcohol use. Non-alcoholic steatohepatitis (NASH) is the most extreme form of NAFLD, which is regarded as a major cause of cirrhosis of the liver. NAFLD is considered a spectrum of disease activity. This spectrum begins as fatty accumulation in the liver (*hepatic steatosis*). Over time this may lead to cirrhosis.

c) Budd-Chiari syndrome

Budd-Chiari syndrome is an uncommon condition induced by thrombotic or nonthrombotic obstruction to hepatic venous outflow (hepatic vein or inferior vena cava). Possible causes of hepatic vein occlusion include thrombosis (75%) or compression by an outside structure, e.g. tumor (25%). The syndrome can be fulminant, acute, chronic, or asymptomatic.

d) Cirrhosis

Cirrhosis is a consequence of chronic liver disease characterized by replacement of liver tissue by fibrotic scar tissue, leading to progressive loss of liver function. Cirrhosis is most commonly caused by alcoholism or as an end result of hepatitis C.

e) Cancer

Hepatocellular carcinoma (HCC, also called hepatoma) is a primary malignancy of the liver. Most cases of HCC are secondary to either hepatitis infection (usually hepatitis B or C) or cirrhosis. Most malignant cancers in the liver, however, are not primary HCC but metastasis (spread) of cancer from elsewhere in the body, e.g. the colon.

1.3.2 Cholestatic diseases

a) Cholestasis

Cholestasis is a stagnation of bile flow within the liver. Most common cause is obstruction of the large bile ducts by e.g. gallstones.

b) Primary biliary cirrhosis (PBC)

Primary biliary cirrhosis is an autoimmune disease of the liver marked by the slow progressive destruction of the small bile ducts (bile canaliculi) within the liver. When these ducts are damaged, bile builds up in the liver (i.e. cholestasis) and damages the tissue over time. This can lead to scarring, fibrosis, cirrhosis, and ultimately liver failure.

c) Primary sclerosing cholangitis (PSC)

Primary sclerosing cholangitis (PSC) is an inflammatory disease of the bile duct, which leads to cholestasis. Comparable to primary biliary cirrhosis, it can ultimately lead to liver failure.

d) Cancer

Cancer may also affect the biliary system. For example, *cholangiocarcinoma* is cancer of the bile ducts, and is developed by approximately one third of patients with primary sclerosing cholangitis.

2 Liver failure

2.1 Definition and classification

All liver diseases may end in hepatic failure as the most severe consequence. Hepatic failure may appear when 80 to 90 % of the capacity of the liver is destroyed. In this situation, the ability to regenerate liver parenchyma is reduced. This may be the end-stage of a developing disease in chronic progression with or without prior disease. As such, liver failure is classified as either acute or chronic, depending on the amount of time the liver takes to fail. Chronic liver failure is characterized by progressive damage to hepatocytes over the course of years. Acute liver failure is a result of massive loss of hepatic function over the course of days or weeks. This can occur in a previously healthy liver (acute liver failure – ALF) usually due to viral infection or intoxication, or as an acute decompensation of a chronic liver disease already present (e.g. cirrhosis). The latter is called acute-on-chronic liver failure (AoCLF). Two important aspects are at the basis of hepatic failure:

- Loss of hepatocellular function
- Shunting of blood around the liver in portosystemic connections

Combined they lead to weakened synthetic functions and detoxification by the liver. As a result, the body is exposed to several substances and toxins, which the liver usually detoxifies, and the failure reaches systemic influence. Also body-wide metabolic instability, disruption of energy supply, acid-base balance and thermoregulation, uncontrolled bleeding and sepsis are complications associated with liver failure. Ultimately, other organs will also cease to function, which leads to fatal multi-organ failure (MOF). From this, it is clear that acute liver failure is a serious situation and often fatal. Mortality rate is near 60-90%, depending on etiology.

2.2 Symptoms

Several clinical signs are apparent during hepatic failure; all of them resulting from a decreased synthesizing or detoxifying capacity of the liver (Table IV-1).

Table IV-1 : Clinical characteristics of hepatic failure

Jaundice
Hypoalbuminemia
Coagulopathy
Hyperammonemia
Fetor hepaticus
Increased serum levels of hepatic enzymes: LDH, ALAT, ASAT, GGT
Gynecomastia, testicular atrophy, palmar erythema, spider angiomas
Hepatic encephalopathy
Hepatorenal syndrome
Coma

Because of the reduced synthesis of albumin in the liver, *hypoalbuminemia* with consequent *oedema* emerge. Oedema within the peritoneal cavity is known as *ascites*. A *coagulopathy* is also a result of reduced synthesis function of the clotting factors. *Fetor hepaticus* is a characteristic, sweet and sour-like smell detectable in exhaled breath. It originates from sulphur-containing compounds normally metabolized by the liver. The reduced hepatic metabolism of oestrogen and reduced hepatic synthesis of sexual hormone binding globulin (SHGB) causes *hyperoestrogenemia*. These elevated levels of oestrogen in turn lead to *vasodilation*, seen as *palmar erythema*⁹ and *spider angiomas*¹⁰, and to *gynecomastia*¹¹ and *testicular atrophy*¹². *Hyperammonemia* (see further) is a result of reduced urea cycle function in the liver. *Hepatorenal syndrome* is reduced renal function, with hypoperfusion and apparently reduced perfusion pressure of the kidneys, probably due to vasodilatation of the splanchnic vasculature. [84]

Some symptoms can be used as a marker of severity. One example is *jaundice* (or icterus), which is probably the trademark symptom of liver disease. This condition is characterized by a yellow discoloration of the skin, sclera and mucous membranes, due to accumulation of excessive quantities of either free or conjugated bilirubin in extracellular fluid as the liver fails to excrete the bilirubin in bile. Jaundice appears when serum bilirubin levels rise above 2.0-2.5 mg/dL. *Hepatic encephalopathy* (HE) is another marker of hepatic dysfunction.[85] It is a complex neuropsychiatric syndrome and is characterized by changes in mental state ranging from minor, not readily discernible signs of altered brain function to deep coma. The exact cause of hepatic encephalopathy is unknown, but the accumulation of ammonia (hyperammonemia) due to the reduced elimination by the liver is proven to be involved in the pathogenesis. Hepatic encephalopathy is clinically divided into four grades:

- Grade I: Changes of personality and sleeping pattern.
- Grade II: In more severe case, the term slow cerebration is used, seen as prolonged intellectual and muscular reaction time and confusion.
- Grade III: Stupor and somnolence is typical.
- Grade IV: Total loss of any reactions on stimulus i.e. coma.

The degree of encephalopathy is believed to be a strong predictor of outcome from acute hepatic failure. Among patients reaching stage II encephalopathy, the possibility of spontaneous recovery under standard intensive care ranges between 65 and 70%, with stage III between 40 and 50%, and with stage IV 20% or less.

⁹ Reddening of the palms of the hand

¹⁰ Benign tumors that are made up of small blood vessels containing a central red spot, and reddish extensions that radiate outward like a spider's web

¹¹ Development of abnormally large mammary glands in males resulting in breast enlargement

¹² Testes diminish size and may cease to function

2.3 A problem on world scale

Chronic liver disease and cirrhosis is the 10th leading cause of death in the United States, resulting in 360'000 hospitalizations and approximately \$10 billion in annual healthcare costs [86,87]. The World Health Organization estimates that 20 million people worldwide have cirrhosis of the liver and/or liver cancer, arising predominantly among the estimated 520 million persons (almost 8% of world population) who are afflicted with persistent hepatitis B (HBV – about 350 million persons worldwide) or C (HCV – about 170 million persons worldwide) viral infection. An estimated 1–2 million persons worldwide die each year from hepatic failure, with more than 50'000 deaths per year in the United States. Extrapolation of epidemiological data (1993-1994) shows that around 700'000 persons in Belgium ever contracted a hepatitis B infection. The number of people carrying HBV can be estimated around 70'000. At least 100'000 people in Belgium carry HCV virus¹³. More than 50% of those do not know they are infected and can unwillingly cause new infections.[87]

As significant as the numbers above are, they almost certainly underestimate the burden of liver related diseases. Furthermore, that burden is expected to grow for many years to come. For example, currently 10 000–12 000 people worldwide die each year due to chronic HCV infection and HCV related cirrhosis, but due to the high prevalence of HCV infection in the late 1980s and early 1990s, this number is expected to quadruple over the next decade.[86]

2.4 Current treatment of liver failure

2.4.1 Standard medical care

Standard supportive treatment of hepatic failure is directed towards early recognition of the complications and general supportive measures. The major focus is on management of respiration, hemodynamic management (e.g. blood glucose level monitoring, vasopressor therapy, antibiotic treatment to prevent infections and blood purification by dialysis) and intracranial pressure monitoring. However, when the regenerative capabilities of the liver fail and the diagnosis of end-stage liver disease is made, the patient should be considered for a liver transplantation.

2.4.2 Orthotopic liver transplantation (OLT)

The first successful liver transplantation with minimal one-year survival was not performed until 1967 by Dr. Thomas Starzl (Denver, Colorado, United States), when a 1.5-year-old girl with hepatocellular carcinoma was transplanted.[88] She died of recurrent tumor after 17 months. One-year survival in the early years was 25-35%. With the introduction of cyclosporine as an immunosuppressive in the early 1980s,

¹³ http://www.gezondheid.be/index.cfm?fuseaction=art&art_id=2067
<http://www.iph.fgov.be/ncvh/nl/belgie.htm>
<http://www.gastroresource.com/GITextbook/en/chapter14/14-2.htm>

liver transplantation became a clinical reality. OLT is now considered the only therapy to significantly improve survival in end-stage liver failure.

Various liver diseases can eventually progress to the stage where transplantation is necessary. Primary indications for OLT in Europe between early 1988 and late 2005 are shown in Fig. IV-9 as provided by the European Liver Transplant Registry. Cancers and cholestatic diseases account for 13% and 11% respectively. Acute hepatic failure is responsible for about 9% of liver transplantations. However, the majority of liver transplants (58%) are due to liver cirrhosis. Within this group, cirrhosis is mostly virus (41%) or alcohol (33%) related (see Fig. IV-10).

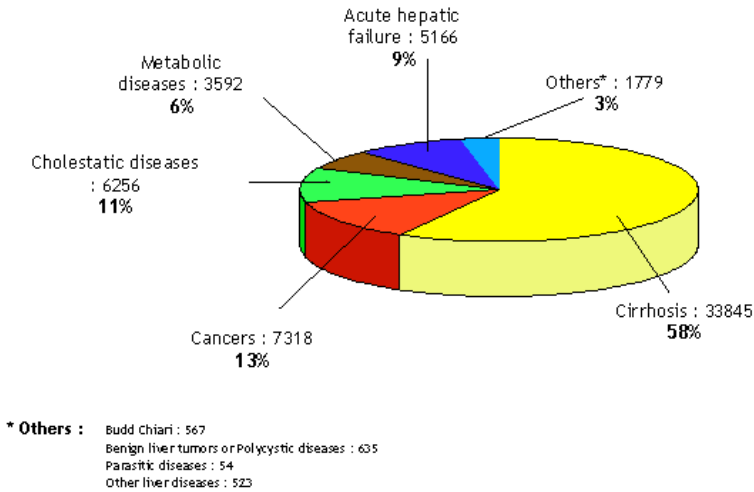


Fig. IV-9: Primary diseases leading to liver transplantation in Europe (01/1988 – 12/2005). Absolute numbers and percentages are given.

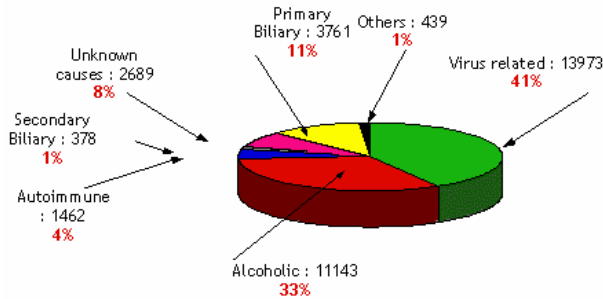


Fig. IV-10: Primary indications of liver transplantation in 33845 cirrhosis patients in Europe (01/1988 – 12/2005). Absolute numbers and percentages are given.

In Austria, Belgium, Germany, Luxemburg, the Netherlands, Slovenia, and Croatia (candidate member), the *Eurotransplant International Foundation* is

responsible for the mediation and allocation of organ donation procedures. When a donor liver comes available, the blood group, height and weight of the donor, and the clinical urgency and waiting time of possible candidates are used as criteria to determine the most suitable recipient. Also the organ condition and geographic distance between donor and recipient are taken into account. Another emerging decision criterium for OLT is the MELD-score [89,90]. The Model for End-Stage Liver Disease (MELD) incorporates 3 widely available laboratory variables including the International Normalized Ratio of prothrombin time (INR), serum creatinine (mg/dL), and serum bilirubin (mg/dL). The mathematical formula for MELD is (Eq. IV-1):

$$MELD = 9.57 \times \ln(\text{creatinine}) + 3.78 \times \ln(\text{bilirubin}) + 11.2 \times \ln(\text{INR}) + 6.43 \quad \text{Eq. IV-1}$$

The MELD score ranges between 6 and 40. A score of 6 indicates the least ill patient and a score of 40 indicates the sickest patient. MELD is a reliable measure of mortality risk in patients with end-stage liver disease and is suitable for use as a disease severity index to determine organ allocation priorities. The model was also validated as a predictor of survival in several groups of patients with varying levels of liver disease severity, such as patients with cirrhosis who have infections, variceal bleeding, as well as in patients with fulminant hepatic failure and alcoholic hepatitis. In contrast to the clear benefit of accurately estimating patients mortality on the waiting list, MELD has not been found to be as useful in predicting mortality following liver transplantation.[91,92] In February 2002, the United Network for Organ Sharing (UNOS) established the Model for end-stage liver disease (MELD) as an evidence-based scale for organ allocation. As of January 2007, Eurotransplant has planned also to use this model in the allocation procedure of donor livers.

OLT is definitely a live-saving procedure. Thanks to improved immunosuppressive therapy and organ preservation systems, survival rates in acute liver failure patients are improved from 10% – 40% to 60% - 90%, depending on the cause of the underlying liver disease.[93] However, in clinical practice some *limitations* are present as not every patient with end-stage hepatic failure is eligible for transplantation. *Contraindications* for liver transplantation allow the best use of scarce donor resources while maximizing patient benefit. The contraindications can be divided into absolute and relative. The absolute contraindications, which prohibit the use of the treatment altogether, are absolute sepsis outside the biliary tree, extra-hepatic malignancy (metastatic cancer), advanced cardiopulmonary disease, HIV positivity, active alcohol and/or substance abuse, and the inability to accept the procedure, understand its nature, and cooperate in the medical care required following liver transplantation. Relative contraindications, which weigh in against transplantation when assessing the risk/benefit ratio, include chronic renal insufficiency, age, vascular problems including prior shunt surgery, and other significant extra-hepatic diseases.

Transplantation also has *inherent drawbacks*, such as the limited time that donor livers can be preserved, the complexity of the surgical procedure, the continuous danger of rejection of the transplanted organ, and the costly, life-long immunosuppressive therapy of the patient which makes him susceptible to infections

and cancer. However, the *major* limitation of liver transplantation therapy is the *shortage of suitable donor livers*. This can be illustrated by data from Eurotransplant and the European Liver Transplant Registry. Fig. IV-11 shows the number of cadaveric and living donor transplants in the Eurotransplant zone between 1995 and 2005, as well as the number of patients on the waiting list and the number of deaths of people on the waiting list for which no suitable liver could be found in time.

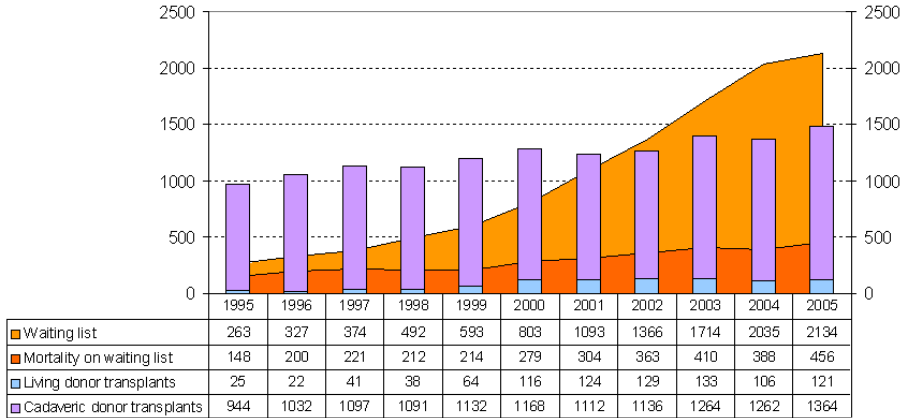


Fig. IV-11: Evolution of number of patients on the waiting list, mortality on waiting list, living and cadaveric donor transplants in the Eurotransplant zone from 1995 – 2005.

The number of people on the waiting list has increased almost ten-fold in 10 years, while the number of transplants only increased by 50%. The same trend of increasingly longer waiting lists for liver transplantation can be seen in Belgium (Fig. IV-12).

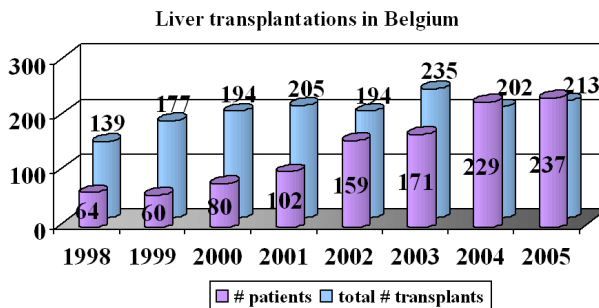


Fig. IV-12: Evolution of number of patients on waiting list and number of all liver transplants in Belgium from 1998 – 2005.

Despite the efforts to increase the donor liver pool by using split livers¹⁴, living related donor livers, and marginal donors¹⁵, the availability of donor livers is still far less than the demand. Since a suitable donor organ sometimes cannot be found in time, mortality on the waiting list is significant. In the Eurotransplant zone in 2005, 2134 people were on the waiting list while 456 patients died waiting for a donor liver.

2.5 The need for liver support systems

In view of the foregoing concerns of increasing prevalence of liver failure and the shortcomings of OLT, it is clear that there is a great interest in devices or therapies that could alleviate time pressure on patients requiring transplantation. This would allow more time available to find a suitable donor organ (*bridge to transplant*). This way, also emergency transplantations could be avoided, increasing transplant success. In some cases, a liver support system could even assist the patient's liver to recovery (*bridge to recovery*). A liver support therapy could also support patients during periods of functional recovery after transplantation with marginal livers (so called primary graft non-function or dysfunction), or after extended liver resections for trauma or cancer. It could also improve survival rates in patients where liver transplantation is not a therapeutic option.

There are three basic approaches to liver support: (1) artificial systems, (2) biological liver support, and (3) hybrid or bio-artificial systems. In the following, brief descriptions of the most important techniques in each field are given.

¹⁴ Whereby a donor liver is given to two recipients; based on the regenerative capability of the liver

¹⁵ Non-heart beating instead of brain dead cadaveric donors, in which the former donor livers have underwent a longer period of warm ischemia which degrades the quality of the donor organ and results in higher rate of potentially lethal primary graft non-function

3 Artificial liver support

The concept of artificial liver support is predicated on the therapeutic benefit of removing toxic substances accumulating in the circulation of liver failure patients. These water-soluble and protein bound toxins (see §1.2.2f) cause multiple organ failure and hepatic encephalopathy, leading to coma and eventually death. As it is impossible to substitute all liver functions by artificial means, early investigators chose to concentrate on only replacing the liver's detoxifying capacity – making this technique historically the first attempt in modern liver support.

3.1 Conventional systems

3.1.1 Hemodialysis

Initially, the intention of hemodialysis was a treatment mode for end-stage renal disease where the blood of the patient flows outside the body through disposable bloodlines into a special filter, the dialysis unit. In this unit, diffusive transport of toxins occurs under a concentration gradient between blood and dialysis fluid through semi-permeable membrane. Initially cellulosic membranes (molecular weight MW cut-off around 2 kDalton) were used. More recently, polysulfon (PS) and polyacrylonitrile (PAN) membranes allowed increasing solute removal. Although there is a temporal improvement of the patient's clinical condition (e.g. amelioration of encephalopathy and cerebral edema), survival times were not improved.[94]

3.1.2 Hemofiltration

Hemofiltration further improved toxin removal by using membranes with a higher molecular weight cut-off allowing active convective transport of solutes across the semi-permeable membrane. There is no dialysis fluid, only a substitution solution replacing the ultrafiltrate. Although now more middle molecular weight molecules (2-3 kD) are removed, outcome remains limited.[95,96]

3.1.3 Hemodiafiltration

As the name suggests, this is a combination of convective and diffusive removal of solutes across a large-pore-sized membrane (such as polymethyl methacrylate PMMA, PS). Similarly, only improvement of chemical parameters and neurological status has been reported.[97,98]

3.1.4 Hemo- and plasmaperfusion: adsorption therapy

Hemodialysis removes mostly water-soluble substances and thus has a *low clearance for protein-bound toxins*. These are removed only to the degree that they dissociate from proteins and diffuse across the membrane. It was speculated that better results might be achieved with more aggressive removal of molecules that are protein bound. This led to the advance of two other major forms of artificial liver support: hemo- and

plasmapheresis. In this therapy, respectively blood or plasma are extracorporeally perfused through a cartridge containing a type of sorbent. Three major types of sorbents exist: (1) activated charcoal, (2) synthetic neutral resins, and (3) anion (positively charged) exchange resins.[99,100]

Activated charcoal is very effective in adsorbing molecules in the 500 to 5000 dalton range, including some protein bound toxins. However, the use of charcoal led to biocompatibility issues (platelet loss and hypotensive reactions) and carryover of charcoal particles into the blood resulting in pulmonary embolism. This may be resolved by encapsulating or coating the charcoal (e.g. with acrylic hydrogel). The problems with charcoal led to the use of resins as an adsorbent. Neutral resins adsorb water insoluble compounds, such as bile acids, phenols and aromatic amino acids. Anion resins bind negatively charged liver toxins, such as bilirubin.

A major obstacle to hepatic failure treatment with sorbent columns is low toxin capacity. The capacity of sorbent columns cannot be increased by simply using a bigger column, because the clinically practical limit to the void volume of the column is the volume that the patient can tolerate to be removed from his internal circulation. Because the amount of sorbent is limited, it is important to get the most performance possible from the available sorbent. The effectiveness of a given mass of sorbent is a function of the amount of surface area and the accessibility of that surface to the species to be adsorbed. Smaller sorbent particles have higher effective capacity. Most of the surface area is internal to the sorbent particle. For smaller particles the distance between the bulk fluid and the interior binding sites is shorter. Thus, toxins have a shorter diffusion time to the binding sites. The pore size must be big enough for the toxins to diffuse into internal pores of the sorbent. This is especially important for large toxins and toxins that are complexed with large molecules, such as bilirubin bound to albumin.[101] Typically, spherical sorbent particles in the range of 100–700 μm are regularly used in columns containing approximately 100 – 350 mL of adsorbent. [102]

Although research for more potent sorbents is ongoing, until now no influence on patient survival of hemo- or plasmapheresis therapy was found. The limited capacity and non-specific approach of this technology was thought to be one of the reasons for its limited success.[103] Some more advanced artificial systems attempt to deal with these issues.

3.2 Advanced artificial support systems

More recent and advanced systems of artificial liver support can be subdivided into two categories: (1) so-called albumin dialysis systems, and (2) systems using sorbent suspensions instead of sorbent columns (as in §3.1.4). Albumin dialysis systems use a type of dialysis using specialized filters in which (non-)autologous albumin is used as a transporter or remover of toxins. Some of these systems have reached the state of advanced animal experiments or clinical trials (MARS, Prometheus, SPAD, Liver Dialysis Unit), others are still under early-stage or pre-clinical investigation (SSR, MDS, SEPET).

Albumin dialysis systems

3.2.1 Molecular Adsorbent Recirculating System (MARS)

Developed in 1993, the MARS (Gambro AB, Stockholm, Sweden) system consists of three inter-connected circuits. Patient's blood cycling at a rate of 100 – 250 mL/min in an extracorporeal circuit is dialyzed against a 20% albumin solution through a specific hemofilter running countercurrently. The membrane of this filter has a pore size of around 50 kDalton, rendering it impermeable to albumin molecules, essential proteins or hormones.

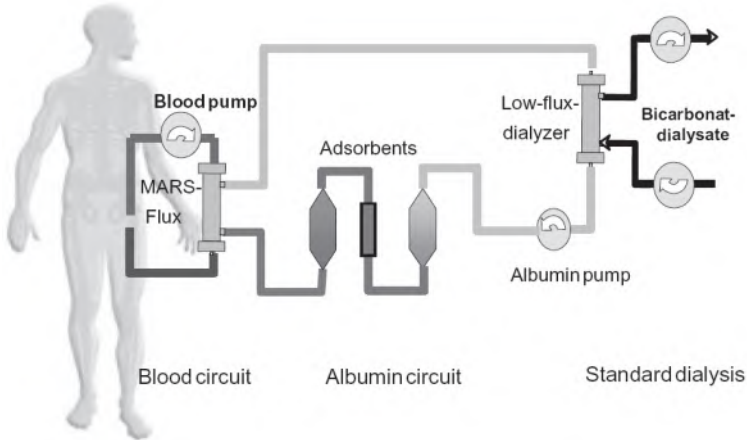


Fig. IV-13: Schematic drawing of the MARS system. [104]

The membrane is the key to the MARS system functioning (Fig. IV-14). It has an asymmetric structure with large caverns on the dialysate side and small pores towards the skin layer of the membrane, which is in contact with the patient's blood. When primed with albumin rich solution, albumin molecules in the dialysate solution permeate from the dialysate into the membrane to be retained by the internal part of the membrane. It has been shown that albumin attached to polymers enhances its affinity to albumin-bound toxins.[105] The passage of the albumin-bound toxins from the patient's blood is carried out via active de-ligandization of plasma albumin, transport of the ligands across the membrane and ligandization of dialysate albumin. Continuous desorption of albumin-bound toxins on the dialysate side maintains a constant gradient that permits passage of toxins from the patient's blood side to the dialysate. The dialysate is then regenerated online by recirculation through a charcoal adsorption column and an anion exchange resin column. Hydro-soluble toxins such as urea, excessive electrolytes and fluid are removed through a third circuit, which consists of a standard hemodialysis machine.

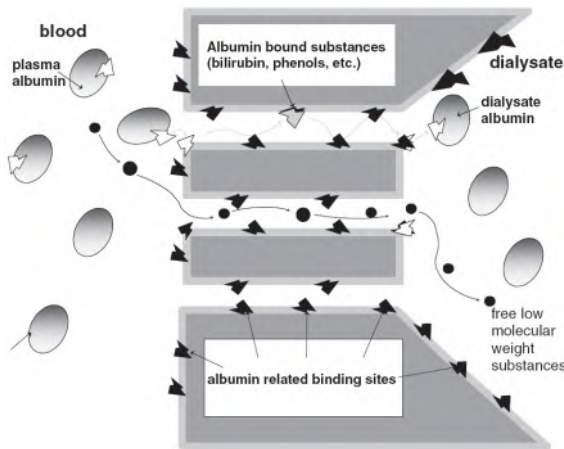


Fig. IV-14: Schematic representation of the MARS membrane and the kinetics of transfer of albumin-bound toxins. [106]

The molecular adsorbent recycling system has been shown to effectively remove water-soluble and albumin-bound low and middle molecular weight toxins. A large number of clinical studies have been published using MARS in AoCLF and ALF patients, including several randomized clinical trials. MARS has been reported to improve multiple organ functions (including mean arterial pressure, hepatic encephalopathy and kidney function). Up to present, it is the only means of artificial liver support to show *proven short term survival benefit* in a subgroup of patients with acute decompensation of chronic liver failure.[104,107] As such, MARS is the most used extracorporeal liver support system in the world.[108,109] The only major drawback of the system is the need for a very large amount of costly albumin.

3.2.2 Fractionated Plasma Separation and Adsorption (FPSA – Prometheus)

The Prometheus system (Fresenius Medical Care AG, Bad Homburg, Germany) is based on the concept of fractionated plasma separation and adsorption (FPSA), first described by Falkenhagen *et al.*[110] Blood is fractionated by means of a capillary albumin filter, the AlbuFlow device. This filter has a molecular weight cut-off of 300 kD. The large pores of the membrane allow albumin-rich plasma to enter the secondary plasma circuit. This fraction is passed over two sorbent columns (a neutral resin and an anion exchanger) to achieve removal of albumin-bound toxins from the albumin. The purified plasma is then transported back to the albumin filter, where part of it is backfiltered into the blood circuit. The remaining plasma continues to recirculate in the secondary circuit. Typical blood flow during clinical application is 200 mL/min. The recirculating flow in the secondary circuit should be approximately 300 mL/min. Finally, the whole blood is then dialyzed by passing through a high flux-dialyzer and returned to the patient.[111]

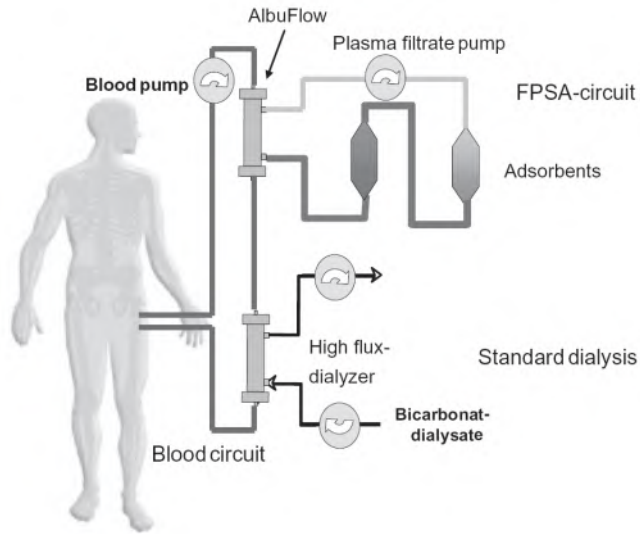


Fig. IV-15: Schematic drawing of the Prometheus / FPSA system [104]

In contrast to the established molecular adsorbent recirculating system (MARS), the Prometheus system does not need supplementation of an albumin solution and thus may prove to be more cost effective in the long run. Furthermore, the patient's own albumin is in direct contact with the high affinity adsorbing material which may facilitate an effective adsorption.

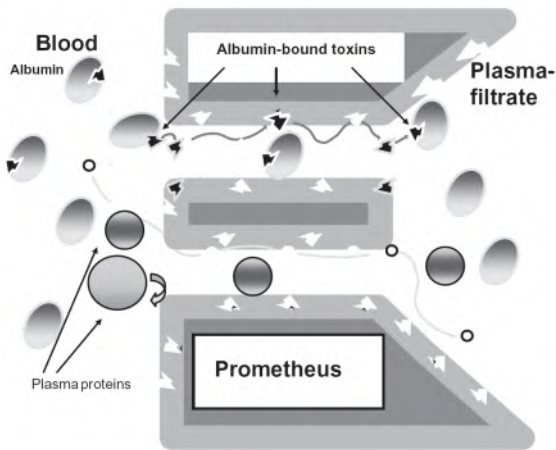


Fig. IV-16: Schematic representation of the Prometheus Albuflow membrane and the kinetics of transfer of albumin-bound toxins [106]

Prometheus has already shown to improve biochemical parameters. Studies comparing MARS with Prometheus *in vivo* showed higher reduction ratios of bilirubin, ammonia and urea in Prometheus.[112] This was confirmed in another

study.[113] However, the latter study also found that only MARS showed significant improvement in attenuating the hyperdynamic circulation in acute-on-chronic liver failure. Clinical experience with Prometheus is limited [87,112] and prospective controlled studies are necessary to evaluate specific clinical endpoints, including the effect of Prometheus on patient survival.

3.2.3 Single-pass albumin dialysis (SPAD)

Single-pass albumin dialysis (SPAD) is a simple method of albumin dialysis, which uses standard renal replacement therapy machines without an additional perfusion system. The patient's blood flows through a circuit containing a high-flux hollow fiber hemodiafilter, identical to that used in the MARS system. The other side of this membrane is cleansed by an albumin solution flowing countercurrently; this solution is discarded after passing the filter. [114]

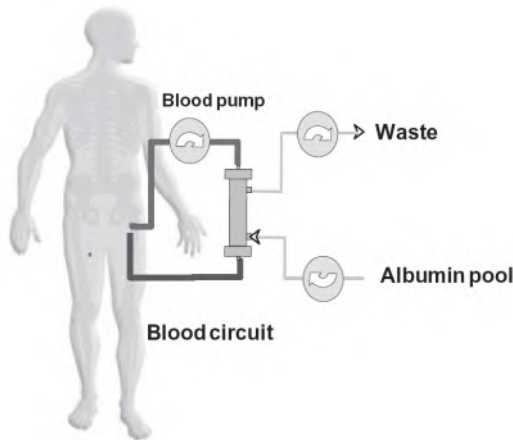


Fig. IV-17: Schematic drawing of the SPAD system [104]

Using only a 4.4% albumin solution in SPAD, an *in vitro* study found a significantly greater reduction in bilirubin levels than with MARS, which uses a recirculating 20% albumin solution. Reductions in bile acid levels were similar for SPAD and MARS. Moreover, the (variable) costs of a seven-hour SPAD treatment is approximately \$810, or about 30% of the cost of an equally efficient MARS treatment. As such, this simple, inexpensive technology merits further research and development. Two major topics which require most attention are the optimal albumin concentration to be used and the validity of the *in vitro* results in the *in vivo* situation.

3.2.4 Selective Plasma Filtration Therapy (SEPET)

Developed by Arbios Systems (Los Angeles, California, USA), the SEPET aims to be more effective than sorbent-based systems (e.g. MARS, Prometheus), because the latter are largely non-toxin specific systems. Also, the sieving cut-off of high performance membranes is not greater than 35 kDa and clearance of pro-inflammatory cytokines and other mediators of inflammation is limited. Even in the

case of membranes used in AlbuFlow (Prometheus) and MARS cartridges, proteins smaller than the cut-off are likely to cross the membrane with difficulty because of factors such as three-dimensional structure of proteins, membrane chemistry and charge, membrane wetting, and resistance due to fouling. For this reason, SEPET uses a blood filtration device with a cut-off of 100 kD, which allows filtration of plasma along with mediators of inflammation (Interleukin-6 - IL6; Tumor Necrosis Factor – TNF α) and inhibitors of hepatic regeneration (Tumor Growth Factor - TGF β 1), while retaining important blood components with a MW greater than 100 kDa, including immunoglobulins, complement system proteins, blood clotting factors and Human Growth Factor (HGF), in the blood circulation. The separated plasma fraction is subsequently replaced with electrolyte solution and a minimal amount of human albumin and fresh frozen plasma. Pre-clinical studies show that SEPET therapy is safe and effective in a pig fulminant hepatic failure model. A phase I trial with AoCLF patients is in progress.[87,115]

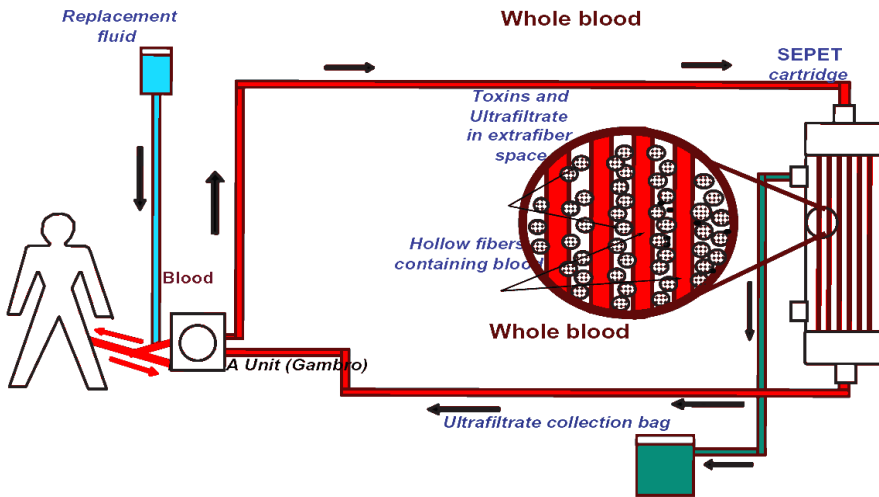


Fig. IV-18: Schematic drawing of the SEPET system. (adapted from [115])

Sorbent suspension systems

There are basically two options to use sorbents in extracorporeal blood treatment devices: perfusing sorbent columns (cfr. hemo-/plasmaperfusion §3.1.4), or using sorbent suspensions. *Columns* have advantages of simplicity, of construction, and high concentration of sorbent for a certain perfusate volume. However, they require larger particle size to function at reasonable perfusion pressures, and the larger particle size results in limitations in the speed and capacity of toxin-binding, especially for large or protein-bound toxins. Carbon with higher porosity might have significantly higher binding for large toxins than the carbons commonly used in columns. Sorbent *suspensions* allow very small particle sizes (only limited by the filter pore size), resulting in greater outer surface area, more accessible active sites, higher toxin capacity and faster binding. By shielding the blood from the sorbent suspension by a membrane a better biocompatibility can be obtained. However, sorbent suspensions are exposed to lower toxin concentrations, require careful design to maintain suspension, and also require membrane restraints to prevent any particle contact with blood. They generally have lower concentrations of sorbent vs. dialysate or filtrate. The sorbent amount is limited by total system volume (as stated above) and the additional necessity of suspending the sorbent in solution. Thus the density of powder in a sorbent suspension is generally less than the packed volume within a sorbent column. [101]

There have been four implementations of extracorporeal detoxification devices using a suspension of sorbents as described below.

3.2.5 Hemodiadsorption: BioLogic-DT (a.k.a. ‘Liver Dialysis Unit’)

Hemodiadsorption is generally the process of dialyzing the patient’s blood using a sorbent suspension as dialysate. This system has been commercialized as the BioLogic-DT (HemoCleanse, Lafayette, IN, USA).

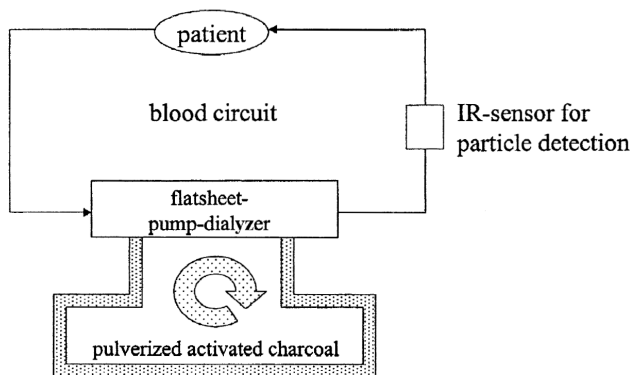


Fig. IV-19: Schematic drawing of the BioLogic-DT system. [116]

The system is schematically shown in Fig. IV-19. Blood is dialyzed across a parallel plate pump-dialyzer with cellulose membranes surrounded by 2L of sorbent suspension. The suspension contains 140 g of powdered charcoal (1-75 μm diameter with 2400 m^2 surface area/g) and 80 g of cation exchanger (125 μm diameter).[101,102,117] The DT employs the compliant membranes of the plate dialyzer as a kind of diaphragm pump in order to pump both the blood and the sorbent suspension. Cyclic dialysate pressure alterations move the membranes of the plate dialyzer to fill and empty; valves on the inlet and outlet of the blood and dialysate circuits directed the flow in one direction (see Fig. IV-20). The sorbent suspension circulated between the dialyzer and reservoir, and it was mixed in the dialyzer by the movement of the dialyzer membranes and by passing through the membrane support screens. Solutes up to 5 kD with moderate protein binding can be removed. An infrared sensor is integrated in the efferent bloodstream to detect microparticles in case of membrane rupture and to avoid their infiltration into the patient. The detection of the microparticles is based on the fact that activated charcoal absorbs light in the infrared range at much higher levels than blood.

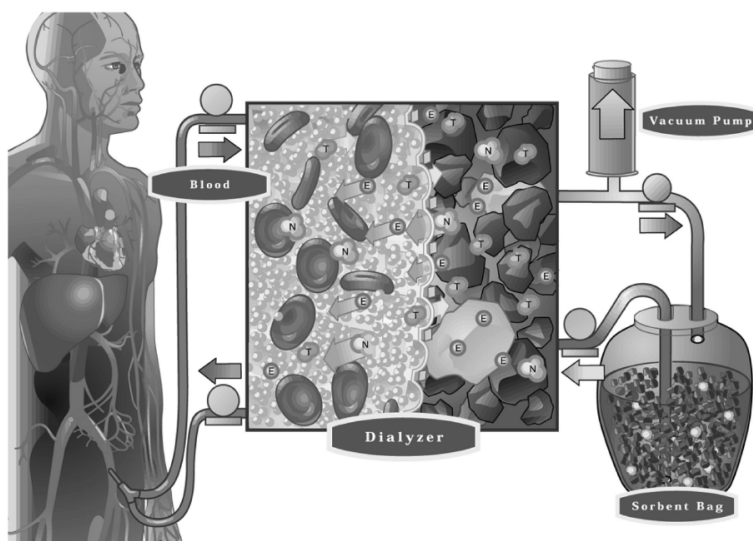


Fig. IV-20: Graphical representation of the Biologic-DT membrane and flat plate dialyzer functionality. [117]

This device showed only short term improvement in biochemical parameters and clinical status, but no increase in survival. The still unspecific approach of this system is illustrated by the fact that researchers found that the negatively charged cation exchangers primarily removed electrolytes such as calcium and potassium and had very little capacity available for ammonium. Ammonium decrease was found due to removal of ammonium precursors by activated carbon rather than ammonium binding to the cation exchanger.[101,117]

3.2.6 Sorbent Suspension Reactor (SSR)

The Sorbent Suspension Reactor (SSR) is a recent configuration of the BioLogic-DT technology. The SSR is designed to be an auxiliary to a standard hemodialysis machine to regenerate the dialysate. A schematic of the SSR system is shown in Fig. IV-21. By separating the sorbent suspension from the dialyzer, the SSR has several advantages over the Biologic-DT system: (1) the dialyzer acts as a biocompatible interface between the patient and the sorbent suspension; (2) more performant dialyzers than the flat plate dialyzer in the DT-system can be used (e.g. hollow fiber dialyzers); (3) removing the sorbent from the dialyzer also eliminates concerns about mechanical interaction of the sorbent with the dialyzer. In the SSR, the sorbent will not be abrading the dialyzer membranes, as was observed during the development of the DT; (4) blood and dialysate flow rates can now also be controlled separately. The dialysate flow can be chosen to give the best balance of mass transfer in the dialyzer and adsorption in the reactor independent of the blood flow. Blood flow can be controlled within the constraints of the patient and their blood access for maximum therapeutic benefit and minimum hemodynamic disturbance.

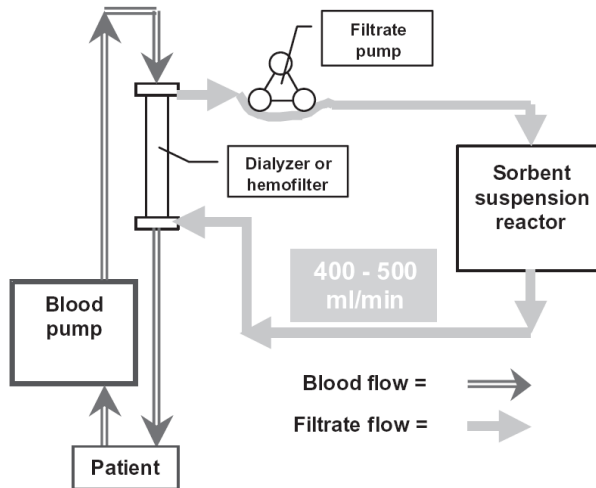


Fig. IV-21: Schematic drawing of the SSR system. [101]

In the SSR, the finely divided suspension of activated charcoal is confined by a sub-micron membrane filter and is mixed by an impeller. Cation exchangers were left out due to their minimal therapeutic benefit. [101,117] The impeller has two blades which are the length of the reactor and rotate on the axis of the cylinder. The impeller tends to act as a centrifuge, generating a pressure gradient from the axis of the reactor to the reactor wall (see Fig. IV-22). This exacerbates the tendency of sorbent to be deposited on the outlet filter on the reactor wall. As charcoal powder is deposited on the outlet filter, the effective permeability of the filter decreases. To counter this phenomenon, shunts were designed at each end of the reactor to keep the pressure gradient between the axis and the wall small. Each shunt is an area at each end of the reactor that is separated from the impeller. The inlet to the shunt is at the reactor circumference; the outlet is at the reactor axis. As the impeller spins and creates a

pressure gradient from the axis of the reactor to the reactor wall, the pressure gradient will cause sorbent suspension to flow back to the reactor axis through the shunts. The shunts have vanes at the inlet to direct the rotating sorbent suspension into the shunt. Inside the shunt, radial vanes keep the fluid in the shunt from rotating together with the fluid in the reactor; instead it flows to the center of the reactor.

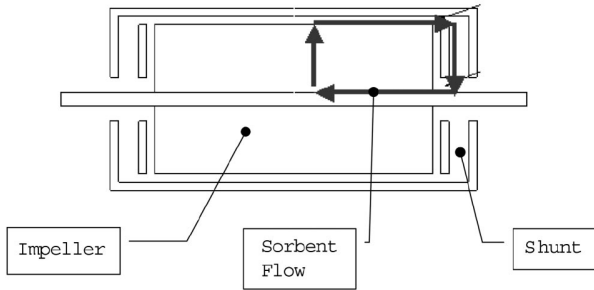


Fig. IV-22: Longitudinal section of the SSR, illustrating sorbent flow in one quadrant of the reactor. [117]

This novel system is yet to show therapeutic advantages for acute support of hepatic failure patients.

3.2.7 Push-Pull Pheresis: Biologic-DTPF / PF-Liver Dialysis Unit

In an attempt to increase the removal of protein-bound and large molecular weight toxins, including cytokines and bilirubin, a plasmaperfusion module was added to the original BioLogic-DT. This module includes a plasma permeable, hollow fiber plasma filter (PF) placed downstream from the DT plate dialyzer. Inside, alternating positive and negative transmembrane pressures cause plasma to transiently pass into a powdered charcoal sorbent suspension around the PF membranes (where direct interaction between plasma and charcoal increases the envisioned removal), and then return to the blood. This system has shown to improve encephalopathy, but investigators currently focus their research on the SSR system.[118]

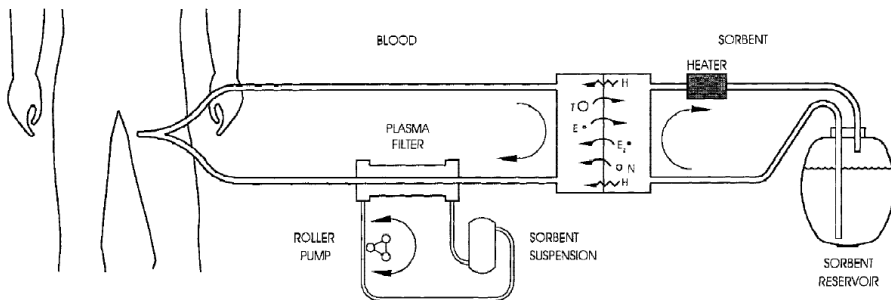


Fig. IV-23: Schematic drawing of the Biologic-DTPF system. [118]

3.2.8 Microspheres-based Detoxification System (MDS)

Schematics of the MDS system are depicted in Fig. IV-24. The blood circuit is perfused by blood pumped from and back to the patient at typically 200-400 mL/min. In this circuit the Albuflow filter, which was developed for the Prometheus/FPSA-System, is used to filter plasma together with albumin molecules into the filtrate circuit. Rather than perfusion of plasma in columns, such as in FPSA, adsorbents are now recirculated and suspended in the plasma. Flow rates are typically between 4 – 6 L/min, inducing effective filtration and backfiltration along the hollow fiber membrane. To enable continuous dialysis and ultrafiltration, an adapted dialysis circuit has to be attached to the plasma circuit (not shown in figure). [102,116]

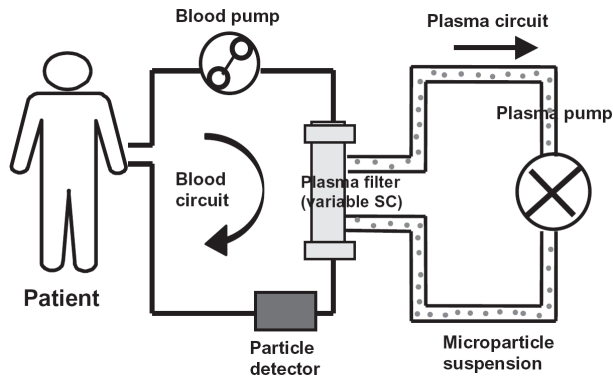


Fig. IV-24: Schematic drawing of the MDS system. [102]

The principle disadvantage of the technology is the potential back-filtration of microparticles into the blood circuit in case of a membrane leakage of the filter. This could be accompanied by infarction of lungs, spleen and liver by microembolism, or by an overreaction of the reticuloendothelial system (RES), depending on the amount and the size of the particles transferred. As a passive safety measure, an advanced fluorescence based particle detection system is present. This system is still under active research, with strong focus on the type and size of particles to be used. [119]

3.3 Conclusion

Historically most liver assist techniques used in the past relied on detoxification, because for many years it was assumed that toxins that cause coma in hepatic failure are small dialyzable molecules. Three decades ago, Zieve *et al.* [120] listed at least 14 categories of biochemical abnormalities in acute hepatitis. Today, we are aware of perhaps twice as many such derangements. The repertoire of substances that accumulate in the blood in hepatic failure includes a wide variety of not only small molecular weight toxins, but also mediators of inflammation, vasoactive substances, endotoxins, cell growth inhibitors and other known and currently unknown substances, many of which are protein-bound. [87]

Clinical studies evaluating the usefulness of these artificial therapeutic measures suffer from small sample size and an absence of appropriate controls. As such, it is difficult to establish meaningful conclusions regarding their efficacy. Nevertheless, although one system (*i.e.* MARS) has shown proven 30-day survival benefit in a group of AoCLF patients, no artificial liver support system has ever shown increased survival for ALF patients. This is probably due to the *limited* and/or *unspecific* removal of the aforementioned substances by means of artificial filtration or adsorption systems. As such, not only major toxins may be cleared but also beneficial blood factors, as has already been demonstrated in a combined hemodiafiltration and plasma exchange therapy.[121] Additionally, the inability to synthesize liver specific proteins and other hepatotrophic factors is another issue in the limited benefit of artificial liver support for ALF patients. The importance of not only detoxification, but also metabolic functions in patient outcome is enforced by the success of orthotopic liver transplantations. Because these functions can only be carried out by hepatocytes, more is to be expected from biological or liver cell containing (bio-artificial) liver support systems. [122]

4 Biologic liver support

In the early 1950's, Sorrentino [123] was the first to introduce the concept of biologic liver support, and demonstrated that fresh bovine liver homogenate¹⁶ was able to perform several liver-specific biotransformations (e.g. urea production from ammonium chloride). Many different biological approaches followed thereafter. [100,122]

4.1 Blood / tissue xeno cross-hemodialysis

In this technique, the patient's blood is dialyzed against blood of a living animal (e.g. dogs) or, more practically, against an animal liver homogenate. Although these techniques could be beneficial to patients with liver failure, they were not considered to be suitable for clinical application because of the complexity of the procedure or rapid loss of effectivity. [124,125]

4.2 Human cross-circulation

One of the most straightforward approaches to biologic liver support was reported by Burnell *et al.*, using human cross-circulation.[126] In this technique, the circulation of the liver patient is directly connected to that of a healthy human. Although this proved beneficial to the patient, the donor suffered from serious adverse reactions during the procedure. This however demonstrated that liver support could be provided with an external liver.

4.3 Human or xenogeneic extracorporeal liver perfusion

Blood of the patient is perfused through a discarded donor liver or an animal liver. Common problems are activation of the clotting cascade, and antibody and immune complex formation. Although temporary improvement in biochemical parameters and the patient's clinical neurologic condition have been shown, the aforementioned problems limited the treatment time per session and its repeated use. Additional technical difficulties including the requirement of large numbers of trained staff, and the supply of animals for each session (*xenogeneic*) or the limited *human* donor liver availability have made these techniques obsolete. [127,128]

¹⁶ Homogenate: a chaotic slurry of tissues and cells which results when cell-tissue structure has been mechanically disrupted

4.4 Exchange transfusion or high volume plasmapheresis

This operates on the principle that either whole blood (exchange transfusion) or toxin-bearing plasma (plasmapheresis) is replaced over time to reduce the toxin content. Although this therapy provides deficient essential factors (e.g. clotting factors), it also lowers blood levels of vital hepatocyte growth factor (HGF) and is ineffective in decreasing the large intracellular pool of hepatotoxins accumulated during hepatic failure.[129] Furthermore, massive plasma transfusions carry certain risks (infection, hypocalcemia, metabolic acidosis, pulmonary and cerebral complications) and require large supplies of costly fresh frozen plasma.[130] Despite these limitations and short-lived therapeutic gains, plasma exchange is a frequently used method of acute hepatic liver support.[87]

4.5 Heterotopic hepatocyte transplantation

This technique concerns direct transplantation of isolated hepatocytes to provide temporary relief to a failing liver. There is much disagreement on how the transplantation is made with best results, considering location, amount and cell arrangement. One solution is to inject isolated living cells directly into the patient's circulation: both the portal vein and the spleen artery have been tested. The cells are thought to adhere to the liver or spleen tissue, and perform their liver-specific function. Transplantation of hepatocytes suspended in a matrix in the peritoneal cavity has also been tested. Hepatocyte transplantation has proven survival improvement in animal studies, but only if transplantation occurred several days prior to the induction of hepatic failure. This seems to suggest that it is necessary to allow time for the vascularisation of the implanted cells to occur or to allow them to recover from the trauma of the cell isolation procedure. Therefore, the usefulness of this therapy to acutely ill patients still needs to be determined.[131]

4.6 Orthotopic liver transplantation

As already discussed (see §2.4.2), this is the procedure of choice, though severely limited by donor organ supply. To circumvent this problem, xenogeneic transplantation is an area of current interest. The development of transgenic animals with genetically modified immune expression to reduce incompatibility for use in organ transplantation is now subject of ethical debate and approval.

5 Bioartificial liver support

A '*bio-artificial*' liver (BAL) is an extracorporeal system that combines a *biological* component, i.e. hepatocytes, and an *artificial* housing, i.e. bioreactor in such a way that it can support or even completely replace human liver function. In the bioreactor, functionally active liver cells are sustained and perfused with the patient's blood or plasma. In principle, the liver cells are not only able to replace the detoxifying function of the liver, but also to provide in the full range of synthesizing, excretory, biotransformational and other metabolic functions needed to compensate the complex metabolic disorders seen in ALF. This makes the bioartificial liver one of the most promising liver assist devices.

An extracorporeal bioartificial liver can be subdivided in two different components:

1. the biological component, i.e. the hepatocytes,
2. the mechanical component, i.e. the bioreactor itself, in which hepatocytes are cultured and perfused

In order to obtain a clinically efficient bioartificial liver, specific requirements and challenges are posed for each component. The following text attempts to comprehensibly describe these demands together with possible solutions and implementations as found in literature.¹⁷

5.1 Biological component: Necessary mass and optimal source of hepatocytes?

5.1.1 Necessary mass of hepatocytes

Calculations indicate there are on the order of $1 - 2 \times 10^{11}$ hepatocytes in a normal adult human liver.[132] According to surgical resection data, the suggested number of functionally active hepatocytes needed to replace the liver function in ALF patients, vary from 10% to 30% of the liver mass, corresponding to 150 – 450 grams of cells, or 10 – 60 billion hepatocytes. The general assumption is that approximately 20×10^9 well-functioning hepatocytes are theoretically needed to keep the ALF patient alive if no active liver mass is left in the patient.[133] However, the viability and function of the cells prior to loading and after culture in the bioreactor may vary considerably. This will influence the effective biomass needed.[122]

¹⁷ Note that the text below does not provide a chronological overview of the *in vitro* research which has led to the various developments in bioartificial liver systems, but rather summarizes the major challenges and possible solutions in the development of a bioartificial liver from a *biomedical engineering* point-of-view. More information can be found in the various references.

5.1.2 Optimal type and source of hepatocytes

The characteristics of the ideal hepatocyte for use in a bioartificial liver are outlined by Jauregui *et al.*: [134]

- Rapidly and easily grown in culture at high densities
- Of normal, non-malignant phenotypes
- Remain in a well-differentiated state for several days or weeks
- Display the synthetic and detoxifying features of mature human hepatocytes

Different cell types are used in the BAL systems currently under clinical study, each with specific advantages and disadvantages concerning availability, functional activity, logistics, immunology, tumorigenicity, and possible risk of zoonosis¹⁸.

a) **Primary human hepatocytes**

Because of their optimal function and compatibility, primary human hepatocytes are the first choice for patient treatment, but their availability is low. The main source of primary human hepatocytes for use in a BAL are discarded donor livers. Hepatocytes derived from these livers are, however, characterized by heterogeneity and low viability.[135,136] Moreover, logistics around discarded donor livers are complex. Some of these problems could be circumvented if primary human hepatocytes were cultured *in vitro*. However, primary human hepatocytes have a static nature in *in vitro* culture. Despite minor progress [137,138,139], this is still a persisting paradox, given the facile proliferation of human hepatocytes *in vivo* (cfr. liver regeneration capability).

b) **Primary pig hepatocytes**

Primary hepatocytes from animals, most often pigs, have been used in the majority of clinically applied bioreactors. Porcine livers are available in large quantities and can be obtained on demand. However, animal hepatocytes produce xenogeneic proteins, which may cause serum sickness within a week of repetitive treatments.[140,141] Such immunologic problems, however, are not expected if treatments with porcine-based BALs do not exceed 5 to 6 days. Importantly, the risk of zoonosis is a severe limitation in the clinical application of porcine hepatocytes-based BAL systems. Even to such an extent that, in many European countries, xenotransplantation-related treatments have been prohibited. An important measure to maximally reduce the risk of zoonosis is the use of so-called Specific-Pathogen-Free (SPF) animals, which are bred under strict conditions and are checked for a wide range of pathogens on a frequent basis. Nevertheless, endogenous retroviruses, like the Porcine Endogenous Retrovirus (PERV), are incorporated in the pig genome and therefore are also present in SPF pigs. Therefore, the risk of zoonosis, although very limited, cannot be neglected in view of the supposed impact on public health. Although no clinical important zoonosis or virus transmission has been reported in the treatment of around 150 patients using various porcine-based systems, the moratorium on porcine hepatocytes is not expected to be relieved in the near future.

¹⁸ Any infectious disease transmittable from animal to humans

c) Human liver cell lines

The growth limitations of primary cells and the ban on xenogeneic hepatocytes have spurred attempts to develop cell lines that can proliferate in culture while maintaining liver-specific functions.

The most commonly used cell lines are the **human hepatoma-derived**, such as HepG2 and C3A. The C3A cell line is a clonal derivative of HepG2. Obvious advantage is the large availability due to their highly proliferating capabilities. Two major drawbacks prevent tumor-derived cell lines from fulfilling the requirements of ideal cell source for BALs. Firstly, the cell lines often lack one or more phenotypes or key functions when compared to human primary hepatocytes. Secondly, the risk of transmitting tumorigenic substances or cell parts into the patient's circulation remains a concern, although this has not been described *in vivo* so far.[142] Nevertheless, at present it should be concluded that hepatoma or hepatocellular carcinoma-derived liver cell lines need drastic improvement of liver-specific function and safety aspects, before they can be considered feasible for BAL support.[143]

Cell lines have also been established by **immortalising human hepatocytes** as an alternative for tumor-derived cell lines. Immortalisation of human cells *in vitro* is a complicated process during which usually successive growth arrests of the cells need to be overcome and parallels to some extent the process of tumorigenesis *in vivo* during which accumulating genetic mutations override the normal mechanisms controlling cellular proliferation.[144,145] In the ideal immortalisation process however, malignant transformation and dedifferentiation associated with progressive tumorigenesis are excluded. Nevertheless, the reduced functional repertoire and the potential tumorigenicity still remain major drawbacks.[146]

Human hepatocytes that have been immortalised have been derived from foetal or mature liver tissue. Foetal hepatocytes have a higher proliferative capacity *in vitro* compared to mature hepatocytes, but, depending on the age of the donor tissue, may not express all differentiated liver functions.[147,148] As an example, an immortalised mature human hepatocyte cell line, HepZ, has been tested in an *in vitro* BAL-setting.[149] However, more research on the functionality of these and other derived cell lines is needed.

d) Stem cells

Another promising source of human hepatocytes are stem cells, which have an excellent growth potential. Human stem cells that have the capacity to hepatic differentiation have been isolated from bone marrow and embryos.[150,151] There are probably also adult stem cells present in the human liver itself, as have been found in rodents ("oval cells").[152] However, there is still an ethical and legal debate ongoing over the use of (embryonic) stem cells. Additionally, two issues need to be resolved before stem cells are applicable to BAL-devices: (1) the undifferentiating propagation of stem cells, and (2) the induction to full hepatic differentiation.

5.1.3 Conclusion

An ideal human hepatocyte cell line may never be developed and perhaps a combination of different cell lines with diverging functional specializations will be used for BAL application.[146] However, additional to the choice for a particular hepatocyte cell line, it is important to maintain optimal functionality of the cells for a prolonged period of time. For this, factors such as the type of cell culture and the bioreactor design itself must be considered. These aspects are now further discussed.

5.2 Mechanical component: Design of a hepatocyte bioreactor system

5.2.1 Essential requirements and challenges

First and foremost, the bioreactor must be able to **(a)** contain a sufficient number of cells, **(b)** maintain hepatocyte viability and functionality for a prolonged period of time, and **(c)** assure adequate bidirectional mass transfer between the hepatocytes and the perfusing medium. In this respect, providing means of sufficient O₂ supply to the hepatocytes is most critical in the design of a BAL as lack of O₂ availability is still regarded as one of the most limiting factors in the efficiency of bioartificial liver devices.[153] Additionally, **(d)** the bioreactor must also provide immune protection for the patient.

Each of these requirements pose different **challenges** to the hepatocyte culture type, perfusion system and the bioreactor design and will play a decisive role in their implementation as described in the text below.

a) Sufficient number of cells

The bioreactor must be able to contain at least 10 – 20 billion viable, functionally active hepatocytes (see §5.1) in a certain volume. Following challenges need to be met.

Limited system volume

This volume needs to be kept as small as possible in order to minimize the total amount of extracorporeal volume as only a limited amount of blood (plasma) can be withdrawn from the patient at any given time.

Scalability

Research on possible bioartificial liver support systems is usually performed with small scale bioreactors for *in vitro* and small animal tests. As such, less hepatocytes are needed for testing one bioreactor and multiple bioreactors can be tested with the same amount of hepatocytes needed for a human-scale bioreactor. Also, experimental

conditions may be more easily controlled. However, already from the earliest stages of bioreactor design, one must keep in mind the ultimate goal: use for human liver support. As such, the concept of the *in vitro* bioreactor must be scalable to *in vivo* use. Some types of bioreactor devices do not lend themselves to easy scale-up due to mass transfer and design limitations. Additionally, some devices have too low cell densities to allow realistic scale-up.

b) Maintain hepatocyte viability and functionality

Maintaining differentiated hepatocyte functions *in vitro* culture, in particular in extracorporeal liver support system, remains a challenge. Hepatocytes tend to lose their metabolic activities within a short period of time *in vitro* due to the deprivation of their original architecture and polarity.[154] A large variety of factors influence the viability, function and differentiation of hepatocytes: in addition to the evident need for vital nutrients and oxygen (see §5.2.1c), the sufficient culture conditions necessary for long-term stability of hepatocyte functions are still being optimized. However, all these factors share a common fundamental principal: to achieve a hepatocyte culture which mimics as closely as possible the *in vivo* environment.

Sufficient supply of nutrients and oxygen
--

See §5.2.1c: Adequate bidirectional mass transfer

Hepatocyte culture type

The *type* of hepatocyte culture inside the bioreactor is crucial for maintaining hepatocyte viability and function. The ultimate goal is to mimic the *in vivo* surroundings of the liver cells in an advanced *in vitro* culture.

Following factors must be taken into account when designing a hepatocyte culture type for use in a bioartificial liver:

(i) Extracellular matrix environment

In the liver, hepatocytes are surrounded by extracellular matrix components (ECMs). The major components of liver ECM are proteins and proteoglycans. The proteins include fibronectin, vitronectin, laminin and tenascin, the collagens (mainly type I and minor quantities of types III, IV and VI), and elastin; the proteoglycans are a heterogeneous group of proteins containing glycosaminoglycan (GAG) side chains. Although the ECM is only a small component of the liver, it plays a major role in the modulation of many biological processes of hepatocytes, including cell migration, differentiation, repair, and development. Hepatocytes are anchorage dependent cells, structurally and functionally polarized *in vivo*, and maintenance of polarization involves both cell-cell (see further) and cell-matrix interactions. [73,74]

However, once hepatocytes are isolated from their natural environment, they detach from the ECMs and undergo apoptosis through detachment-induced cell death that occurs within a short period after isolation.[155] Various forms of providing ECM support *in vitro* have been attempted. Extracellular matrix modulation has included

both variations in composition (e.g. collagen, laminin) and topology (e.g. membranes, gels).

(ii) Perfusing media composition

Adaptations to the composition of the perfusion medium may enhance hepatocyte functionality. For example, amino acid supplementation of the plasma increases both albumin and urea synthesis. Another approach uses high insulin levels during hepatocyte culture prior to clinical application to favor intracellular lipid accumulation. A low insulin preconditioning favors lipid oxidation. Also the local oxygen tension during culture has its effect on hepatocyte metabolism: higher oxygen concentrations increase urea synthesis and decrease cytochrome P450 activity. Other modifications such as hormonally defined media and addition of low concentrations of dimethyl sulfoxide or dexamethasone are known to help stabilize hepatocyte morphology, survival, and liver-specific functions. However, many of the latter approaches are inapplicable to BAL design as systemic exposure of patients to these specialized and non-physiologic media components, is detrimental to the patient's health. [156]

(iii) Shear stress

In vivo, hepatocytes are not directly subjected to shear stress as they are shielded by the sinusoid endothelial lining. As a result, the maximal tolerable level of shear stress is very low. Tilles *et al.* [157] showed in *in vitro* studies on rat hepatocytes that hepatocyte function, measured as albumin and urea synthesis rates, was significantly decreased (resp. 2.6- and 1.9-fold) when hepatocytes were directly exposed to shear stresses higher than 0.5 Pa compared to low shear stresses (< 0.033 Pa). As such, significant shear stress on the hepatocytes in culture must be avoided by shielding the cells from the perfusing flow (see culture types - below), or by choosing proper perfusion flow rates when there is direct contact between the cells and the perfusate (see bioreactor design – below).

(iv) Cell anchorage

Hepatocytes are anchorage dependent cells. This is demonstrated by the rapid loss of viability and function of primary hepatocytes in suspension already a few hours after cell isolation.[158] For this reason, the bioreactor preferably provides anchorage for the hepatocytes. Cells can be anchored internally in a porous volume (matrix, gel, or bead), or externally to a scaffold. The chemical and physical properties of the scaffold material to which the cells are attached play an important role in maintaining cell viability and function.[159] From this point-of-view, it seems that optimal cell anchorage is obtained with a hydrophilic material [160], and electrically charged (either positively or negatively). Surface roughness has no significant impact.[161] Additionally, the material can be coated with extracellular matrix material to enhance adhesion, and consequently cellular integrity.[162,163,164,165]

(v) Homotypic cell-cell interactions

In the liver, hepatocytes find themselves in a dense, three-dimensional structured environment. They have a distinct epithelial polarity and several cell-cell

communication structures including bile canaliculi, a tight junction, and a gap junction to maintain contact with neighboring cells. As such, achieving high levels of three-dimensional cell-to-cell contact among hepatocytes is probably the most critical feature for maintaining hepatocyte viability and function in a BAL. Achievement of these homotypic interactions is highly dependent on the choice of culture system.[165]

(vi) Heterotypic cell-cell interactions

The differentiated function of primary hepatocytes is improved and maintained by co-culture with non-parenchymal cells and probably this is also valid for hepatocyte cell lines.[166,167] The non-parenchymal cells (e.g. fibroblast, endothelial cells) enhance the functionality and differentiation of the hepatocytes through the secretion of paracrine growth factors, the production of an extracellular matrix, and maintenance of the bipolarity of hepatocytes.[139,146] However, their inclusion in a BAL might also have deleterious effects if these cells become activated in culture or during clinical application and produce cytokines such as TGF- β and IL-1 which, among others, are associated with apoptosis of hepatocytes and inhibition of liver regeneration. Nevertheless, this type of heterotypic cell-cell interaction is generally found to be beneficial *in vitro* (see Bhatia *et al.* [168] for a thorough review), but has not yet been applied in a clinical BAL device.

Three general forms of hepatocyte culture in bioartificial liver devices can be identified: [100,169]

- Suspension culture,
- Adhesion / attachment culture, and
- Hepatocyte spheroid culture.

As mentioned above, hepatocytes in a fluid suspension is the least effective method as hepatocytes rapidly lose their function when they are not anchored.[158] Alternatively, cells can be attached to a scaffold (e.g. flat plate membranes, microcarriers¹⁹, hollow fibers), or be cultured in three-dimensional aggregates or spheroids inside a porous matrix, a gel or encapsulated in a bead. These types of culture have shown to promote maintenance of cell integrity and function.[170] Spheroid culture presumably offers best results as it most closely approximates the *in vivo* three-dimensional structure. For instance, HepG2 cells, which are known for their inferior functionality, displayed an ammonia removing capacity equal to 85% of that of primary porcine hepatocytes in monolayer, when they are cultured as spheroids in polyurethane foam.[171]

The bioreactor must thus be able to accommodate the most optimal type of hepatocyte culture, by combining several culture type modifications as described above.

¹⁹ Microcarriers are artificial spherical bodies made from a variety of materials including dextran, polystyrene, biologically modified polyhydroxy-methylmethacrylate (poly-HEMA) or glass.

c) Adequate bidirectional mass transfer

Each cell in the bioreactor must be supplied with sufficient nutrients (e.g. glucose) and oxygen, must be in contact with the toxic substances and catabolites usually removed from the blood by the liver (e.g. bilirubin, ammonia), and must be able to release synthesized metabolites (e.g. albumin, coagulation factors) to the blood stream. Also, all metabolic end products (e.g. CO₂, urea) must be adequately disposed. As such, efficient bidirectional mass transfer aids in the maintenance of cell viability and function, and allows cells to participate in the metabolic process in order to achieve a clinical applicable liver support system.

Implementation of culture type: bioreactor design

One notable feature of the *in vivo* liver is that the transport distance between liver cells and solute supply is typically less than 100 µm.[172] As such, this distance also represents the maximum diffusion transport distance that nutrients must travel from the convective flow source to the hepatocytes of the liver. Consequently, this transport distance should be kept minimal in the design of a BAL. While the *choice* of culture type is determined by the aim for preservation of hepatocyte viability and function, its *implementation* in a bioreactor design plays an important role in the achievement of efficient bidirectional mass transfer. (See §5.2.2 *Bioreactor systems*)

Sufficient oxygen supply to the hepatocytes

Special attention in the bioreactor design must then be paid to ensure sufficient oxygenation of hepatocytes, as they are one of the most oxygen consuming cells in the human body. This can be achieved by optimizing bioreactor design to minimize diffusive barriers between the fluid and the cells (e.g. by optimal type of scaffold, encapsulation size, or membrane material and thickness) and by providing additional oxygenation (especially in case of plasma perfusion). Oxygenation can be performed externally (i.e. increasing oxygen concentration of the circulating fluid prior to bioreactor perfusion by e.g. ‘artificial lung’-type oxygenator) or internally (on-site, inside the bioreactor by e.g. addition of gas capillaries through which an oxygen-rich gas flows).

Perfusion of the bioreactor

Mass transport is strongly influenced by the fluid velocity in the perfusion compartment of the bioreactor. Flow rates are limited to the maximal blood withdrawal rate from the patient. When plasma is separated from blood, it can be temporarily stored in a reservoir in the secondary circuit, and the plasma can be recirculated at higher flow rates. For the optimal flow rate, a balance must be found between high mass transfer rates and the possibility of reduced hepatocyte functioning caused by elevated shear stresses with increasing flow rate.

Also, efficient mass exchange can only be achieved if the entire bioreactor is homogeneously perfused. Channel formation or preferential flow through certain parts of the bioreactor and the associated ‘dead spaces’ (areas with no circulation)

should be minimized, as this could lead to reduced function and cell death in the dead spaces.

Uniform hepatocyte distribution inside the bioreactor

Likewise, the cell seeding procedure must result in a uniform distribution of cells throughout the bioreactor. A non-uniform distribution will result in sub-optimal utilization of bioreactor volume. As such, the viability of seeded cells is maximized through careful design of the cell harvesting and seeding procedure.

d) Immune protection

The need for immuno-isolation is strongly dependent on the type of bioreactor perfusion as is explained below.

Perfusion system: blood or plasma?

Another important issue in the development of a clinically efficient BAL is whether the bioreactor should be perfused with whole blood or plasma. Blood perfusion makes the circuit design easy and uncomplicated. A vascular access (via a central venous catheter or needles in a graft or fistula) brings the blood from the patient's circulation directly to the bioreactor and back. Major drawback of blood perfusion is however the coagulation problem, which requires the use of anticoagulation (e.g. heparin, citrate). Also, when blood is used, an immuno-isolation barrier between the hepatocytes and fluid is needed to limit immunological reactions, even more so with increasing treatment time.

Alternatively, as most solutes related to liver function are dissolved in the blood plasma, it is possible to use only the blood plasma for the perfusion of a bioartificial liver. As white blood cells or leukocytes are removed, the risk of immune response activation is reduced, allowing direct perfusion of the plasma over the hepatocytes, which is beneficial for bidirectional mass exchange. However, as also red blood cells or erythrocytes are removed in plasma filtration, the oxygen-carrying capacity of plasma is very limited as the solubility of oxygen in plasma is very low. Following example illustrates the oxygen carrying capacity of red blood cells. Every liter of blood with a Hb concentration of 15 g/dL can carry about 200 ml of oxygen when fully saturated with oxygen (oxygen partial pressure $pO_2 > 100$ mmHg). At this pO_2 only 3 ml of oxygen will dissolve in every liter of plasma. This may create a major problem in terms of sufficient oxygen supply to the hepatocytes when plasma is used because, as previously stated, they are one of the most oxygen demanding cells in the human body. Special attention must thus be paid to ensure an adequate oxygen supply to the hepatocytes in plasma perfused BAL systems (see above). Additionally, plasma perfusion requires a plasma separator, which increases the cost, complexity and the volume of the extra-corporeal circuit.

Recent BAL systems prefer plasma perfusion, given the aforementioned drawbacks of blood perfusion. Nevertheless, the use of blood should not be discarded

and merits further research considering the possible (not-so-near) future evolution from extra-corporeal to intra-corporeal liver support systems.

5.2.2 Classification of bioreactor designs

The choice of hepatocyte culture type and perfusion system will logically determine the design of the bioreactor. Taking into account the requirements and challenges above, several bioreactor designs for hepatocyte culture have been proposed.[165,173] Each of them tries to find the perfect balance between the sometimes contradictory requirements. They can be classified into four major categories:

1. flat plate based,
2. hollow fiber based,
3. encapsulation based, and
4. direct perfusion systems

a) *Flat plate based systems*

A possible implementation of hepatocyte culture is on a flat surface geometry (*flat plate*). In this design, hepatocytes are seeded in monolayer on a membrane surface. Over the hepatocyte layer, plasma is perfused. As this is technically a direct perfusion system, flow rates in the small channel above the hepatocyte layer may not be too high to minimize shear stress. As plasma has a low oxygen-carrying capacity, the limited flow rates may limit O₂ supply to the hepatocytes. For this reason, the upper wall of the channel is often replaced by a gas-permeable membrane as an additional internal oxygenator. Also the anchorage membrane itself may be oxygen-permeable. This is illustrated in Fig. IV-25.

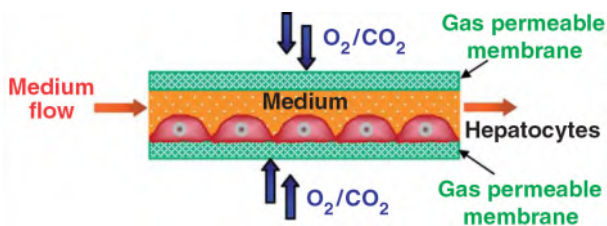


Fig. IV-25: Schematic drawing of a flat plate based bioreactor. [174]

A variation of this design includes the so-called ‘sandwich culture’. In this design, cells are sandwiched by layers of extracellular matrix to mimic the microenvironment of human hepatocytes in the Space of Disse. Cells in this configuration express many liver-specific functions with increased stability.[175,176]

There are several advantages to flat plate culture: it is easy to control the internal flow distribution and ensure that all cells are uniformly distributed and adequately perfused. The main drawback is its scalability. For example, a channel

height of 1 mm and a surface area of 10 m² to culture the required 20 billion hepatocytes would result in a 10 L bioreactor. This is an unacceptably high volume. Decreasing channel height is not a realistic option as this will increase shear stresses on the cells.

In conclusion, the low cell densities, low surface area-to-volume ratio, and the two-dimensional monolayer culture will probably continue limiting the applicability of flat plate designs in a bioartificial liver support system.[177] Attempts to scale up this culture method have had limited success thus far.[178]

b) *Hollow fiber based systems*

Once the need for the inclusion of cellular compounds into an extracorporeal bioreactor became evident, the idea rose of using membrane modules already developed for pure artificial organs. Hollow fiber hemodialyzers, as well as plasmafilters had already proven their capacity for solute and oxygen transport and their relative biocompatibility towards the patient's blood or plasma. Additionally, two properties of hollow fiber membranes allowed using them in a bioartificial liver bioreactor: (i) the ability to provide an immune barrier between hepatocytes and the perfusion fluid, (ii) their possible use for cell anchorage.[165,169]

In most hollow fiber bioreactors, cells are seeded in the extracapillary space [179,180,181], with whole blood or plasma perfusion on the inside of the hollow fiber membrane. However, hepatocytes can also be seeded inside the fibers and the fluid flowing over the outer surface of the fibers.[182] The hollow fibers are made from a semi-permeable membrane. They provide selectivity for the size of biological molecules that will be exchanged between the patient and the device. The membrane in a BAL is typically characterized by its molecular weight cut-off, which is selected both to prevent the exposure of bioreactor cells to components of the immune system and to block the transport of larger non-autologous substances or cellular components into the patient's circulation. The aim of allowing free transport of larger carrier proteins such as albumin (~60 kDa), while preventing transport of immunoglobulins (~150 kDa), complement factors (> 200 kDa), or viruses has led most groups to choose a membrane molecular weight cut-off of 100 to 150 kDa. However, the use of microporous membranes has been reported, with a pore size of 0.2 μm (~2000 kDa) and up to 5000 kDa.[183] These membranes allow the exchange of even high molecular weight proteins, which could result in the aforementioned immunological risk. In a small study with human patients, however, no sustained immune response after six hours perfusion of the hollow fiber bioreactor was found.[184] This may provide some support that systems without immuno-isolation membranes may not have a perceived immunological response problem if treatment time remains limited.

Many culture types have been applied in hollow fiber systems (for a review: Planchamp *et al.* [169]). They are illustrated in Fig. IV-26: cell suspensions, attachment to microcarriers or to the membrane itself, and even in combination with spheroid culture such as in gel embedded culture. Although hepatocytes are anchorage-dependent cells, *suspensions* of freshly isolated hepatocytes are often used as a quick, simple and reproducible technique in the preparation of hollow fiber bioreactors. Attachment culture is the most obvious type of culture employed in

hollow fiber bioreactors. Anchorage to the hollow fiber surface depends to the characteristics of the membrane, as mentioned previously. *Microcarriers* have an advantage over membranes, as they provide an increased surface area for hepatocyte adhesion, increasing the maximal achievable cell density in hollow fiber bioreactors.[163,173,185,186] A *gel matrix* increases the surface area for cell support, also yielding high cell densities with the added advantage of ECM support and consequently increased cell functionality. A disadvantage of this mode of culture is that a steep concentration gradient of solutes may occur throughout the gel layer, resulting in either cell starvation or accumulation of toxic metabolites.[153]

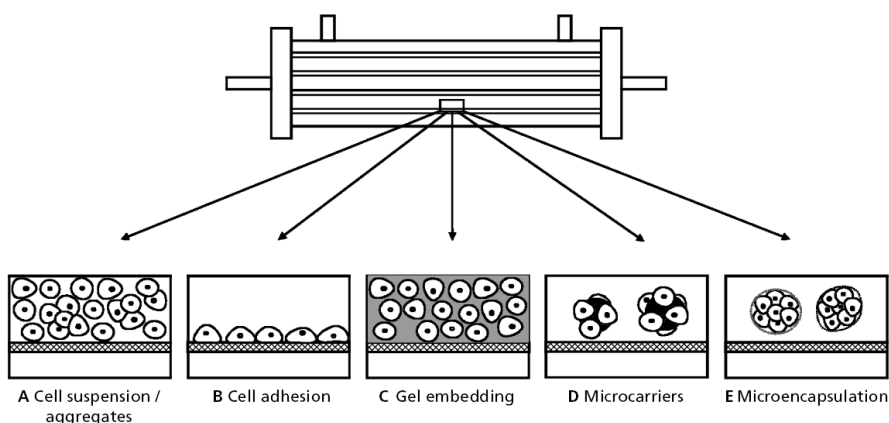


Fig. IV-26: Various forms of hepatocyte culture in a hollow fiber bioreactor. [169]

Besides the aforementioned advantages, the major limitations in hollow fiber based systems is the achievement of sufficient and effective mass transfer through the membrane of O_2 , nutrients, and other molecules that need to be processed by the hepatocytes. In the mass transfer from bulk medium to the cellular mass, an additional barrier is introduced by the hollow fiber membrane. Permeation across the semi-permeable membrane occurs through diffusion and/or convection in response to existing trans-membrane concentration or pressure gradients. For optimal transport, the type of membrane and especially its porosity and thickness are important parameters.[153]

c) **Encapsulation based systems**

The basic approach of encapsulated systems is to encapsulate hepatocytes in a semi-permeable spherical structure usually called 'bead' or 'capsule'. The bead matrix is intended to function similar to a regular (hollow fiber) membrane through providing immune protection while at the same time providing anchorage facilities to hepatocytes and allowing diffusion of smaller molecules to and from the encapsulated hepatocytes. The beads are then contained in a cylindrical bioreactor and usually perfused with whole blood.[165,173]

The advantage of beads over hollow fiber systems is the larger surface area for solute exchange and the capability for higher cell densities, as the hepatocyte capacity is dependent on the surface area (\sim radius) of the hollow fiber, as compared to the volume (\sim radius³) of a bead. [187] The most common hydrogel material used in encapsulation is alginate. While alginate is very biocompatible, it does not perform well as a membrane, and multilayer hydrogel coatings were developed, such as alginate-polylysine or polyacrylate hydrogels.[188]

Two configurations of bioreactors for bead perfusion are proposed: fixed bed, and fluidized bed (Fig. IV-27). In the fixed bed configuration, beads are densely packed into a column. Although this bioreactor showed good functionality in small scale [189], its scalability is limited by the formation of preferential flow channels in the fixed bed, and high shear stresses on the effectively perfused beads, which could lead to damage to the bead structure [187] and release of alginate and cells to the blood stream. Therefore, a novel bioreactor was proposed by Legallais *et al.* [165,190], in which the beads were subjected to a fluidized bed motion. Each bead follows a path from the bottom to the top of the bioreactor, and then fell down. Fluidization is obtained from the fixed bed status by increasing the superficial velocity. The bed expansion implied to use a column with a smaller diameter (to operate at the same flow rate) and a larger height than the fixed bed column. Under optimal hydrodynamic conditions, bed expansion is stable and results in homogeneous mixing of the beads. This significantly increases the mass transfer between the perfusion fluid and the beads as compared to a static configuration.[191] Also, fluidization allows avoiding preferential flows in the bioreactor.

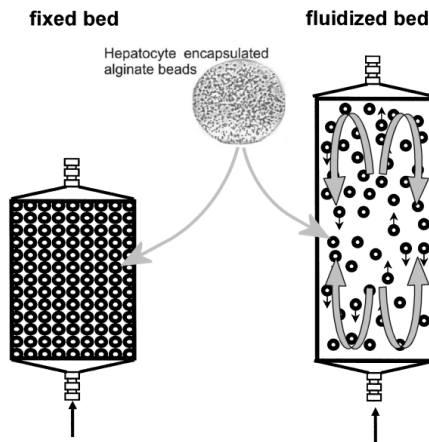


Fig. IV-27: Fixed and fluidized bed bioreactors. (adapted from [165,192])

The encapsulation technique benefits from the presence of a three-dimensional hepatic environment, shielded from shear stress by the encapsulation, and this in combination with an optimal volume-surface ratio of capsules allowing a high capacity of cellular mass. The latter allows an easy scale-up of the design. This

type of bioreactor is very promising, but still needs to deal with the possibly limited mass transfer, caused by the bead diffusive barrier. This may be obtained by decreasing bead diameter, which is now in the order of 0.75 – 1 mm.

d) Direct perfusion based systems

Direct perfusion systems use three-dimensional scaffolds on which hepatocytes are seeded or grown, and perfuse them directly, without any separation or barrier between the perfusing fluid and the cells. This scaffold can be a fabric or foam type support that creates a three-dimensional environment for the cells. As such, this type of bioreactor has the advantages of spheroid culture. Additionally, the lack of separation between fluid and the cells promotes bidirectional mass transfer. As such, direct perfusion seems a promising and simple concept. However, there is another side of the medal. First, the lack of separation exposes hepatocytes to possibly elevated shear stress, which is detrimental to hepatocyte function. Secondly, the lack of separation of the cells theoretically increases the risk of viral transmission (*e.g.* PERV) to the patient, although this has not yet been reported. Moreover, a cell filter in the extracorporeal circuit is needed to prevent any (*e.g.* xenogeneic) cellular debris to enter the patient's circulation. Finally and most importantly, as no immunoisolation is present, a BAL based on this system can only be perfused by plasma. The use of plasma makes the oxygen supply to the cells an important limitation in direct perfused systems. Thus, special attention must be paid to assure sufficient oxygen transport to the hepatocytes.

5.2.3 Additional challenges in bioartificial liver system design

There are several additional, more practical requirements and challenges a bioreactor design has to meet to be able to perform as a bioartificial liver.

a) Biocompatibility

Material selection in the BAL should promote minimal interaction between device and blood that adversely affects device performance, and without inducing uncontrolled activation of cellular or plasma protein cascades.

b) Sterile / aseptic environment

All components of the BAL must be able to be sterilized, and any exposure of process internals to the atmosphere (with the associated risk of contamination) should be avoided if possible. Human intervention in the process must be minimized and all work should be carried out as aseptically as possible.

c) Logistics

The transport of the hepatocytes for BAL treatment from the BAL-preparing laboratory to the center of treatment, either (1) separate from or (2) enclosed in the bioreactor, should be carried out with preservation of function.

In the first option, most efforts have been put in cryopreservation of hepatocytes: the storage of cells in liquid nitrogen (-196 °C) or in its gas phase (-150 °C). Cryopreservation may, however, lead to decreased viability, cell attachment capacity, and function.[132,193] Hepatocytes attached to microcarriers prior to cryopreservation, however, maintain better cell function as compared to cryopreservation of hepatocytes in suspension. Nevertheless, cellular mass used in a BAL should be increased to compensate for the drop in cell viability and function after preservation.

In the second option, the hepatocytes are transported already seeded in the bioreactor. As such, a bioreactor transport system must be devised. This system must perfuse the loaded bioreactor with preferably oxygenated culture medium until arrival at the place of treatment. An important parameter here is the temperature at which the bioreactor is perfused. Perfusion is possible at normothermic (37 °C) temperature. However, a lower temperature may be preferred as this will slow down cellular metabolism, and as such also the cellular processes that lead to cell death or dedifferentiation. In this respect, a cold (4° C) preservation solution has been proposed, in analogy to the golden standard in whole organ preservation. However, studies on a direct perfusion bioreactor with internal oxygenator showed that hepatocyte viability and liver specific functions declined rapidly in the bioreactor after 12 hours of cold-preservation transport. Alternatively, sub-normothermic temperatures (15 – 28 °C) are proposed to decrease reactive oxygen species accumulation caused by cold-preservation.[194]

d) *Need for additional artificial liver support?*

It is often overlooked that the abovementioned BAL bioreactors lack a biliary system for the excretion of *e.g.* conjugated bilirubin. Excretion of metabolites through bile depends on the remnant damaged liver mass. Hepatocytes in the bioreactor will produce bile acids and salts, most of them being toxic protein bound substances, and further increase the concentrations in blood. Furthermore, it has been demonstrated that blood or plasma from the liver failure patient is toxic to hepatocytes in the bioreactor, and extensively disturbs the cellular metabolism and morphology.[195,196]

Considering the two aforementioned problems, incorporation of a detoxification module into the BAL circuit may lower the toxic burden for the hepatocytes in the bioreactor, and for the patient himself. For bridging ALF patients to liver transplantation, the combination of a BAL and an artificial support system may therefore provide optimal conditions for the treatment of ALF patients, although removal of hepatotropic factors should be prevented. The latter is especially important if the goal of BAL treatment is bridging the patient to liver regeneration.

5.3 Overview of Bioartificial Liver systems in *in vitro* or preclinical tests

It is clear from the discussion above that many challenges are to be tackled and many choices to be made in the process of designing a bioartificial liver. As such, a large variety of BAL designs emerged throughout the past decades. In the following, a brief description is given of the most important BAL systems that underwent *in vitro* and preclinical tests, and BAL systems which have been used in clinical trials.

A list of BAL systems, of which only *in vitro* or animal experiments are published, is reported here. The systems are categorized according to working principle as defined above. It is clear that each BAL system combines different solutions to the various challenges set above, aiming to obtain a clinically applicable bioartificial liver support system. Based on the description of challenges and requirements above, the reader can make an informed assessment on the potential of these systems. A short consideration based on the author's opinion is present for each system. This list is non-limiting; sometimes multiple minor variations on some of the presented systems exist.

Flat plate based systems

5.3.1 FMB-BAL

System design : The flat membrane bioreactor (FMB)-BAL was developed by De Bartolo, Bader *et al.*[197] The bioreactor consists of a multitude of stackable flat membrane modules. Isolated porcine hepatocytes are co-cultured with non-parenchymal cells between two layers 20 to 50 μm of type I collagen ('sandwich culture'). The cells as well as the perfusing plasma are oxygenated by diffusion of humidified air across non-porous polytetrafluorethylene (PTFE) membrane. A microporous membrane that separates the cell compartment from the medium compartment is used to protect cells from shear forces and to control mass transfer of different solutes. More recently, further research on this system was conducted by Fruhauf *et al.*[198], and Shito *et al.*[199]

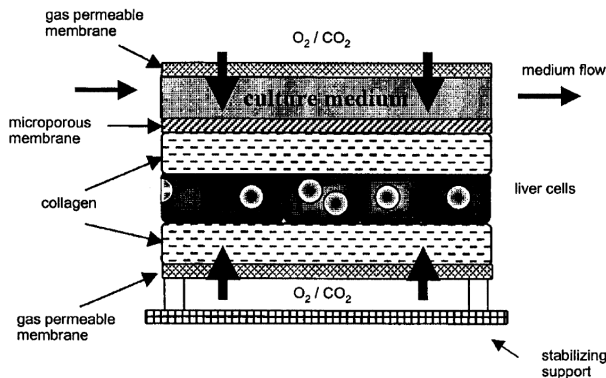


Fig. IV-28: Schematic diagram of hepatocytes embedded in two layers of collagen in a flat configuration used in the flat membrane.

Main consideration : A classical drawback of flat plate based systems is their scalability. Each FMB-BAL module has an oxygenating / seeding surface area of 1150 cm². Up to 50 modules can presently be run in parallel mode. Each module is seeded with 2×10^8 cells, which results in a possible total seeded number of 1×10^{10} cells. The total surface area required is then 5.75 m². If the channel height of the plasma chamber is e.g. 150 μm, the bioreactor volume is 862.5 ml, which is marginally acceptable and leaves little room for further increase in number of hepatocytes for clinical treatment. Additionally, although internal oxygenation is available, achievement of efficient solute exchange between plasma and the hepatocytes might be impaired by the supplementary diffusive barrier of the layers of extracellular matrix themselves (see §5.6).

Hollow fiber systems

5.3.2 LIVERx2000

System design : The LIVERx2000 system was designed and developed by Hu *et al.* at the Minnesota University and commercialized by Algenix (St. Paul, MN, USA).[200,201] The hepatocytes suspended in a collagen gel are injected into the lumen of a hollow fiber with a MW cut-off of 100 kD and the extracapillary compartment is perfused with a recirculating medium. After 24 h, the gel contracts, creating a third space, which is now perfused with the medium, and the extrafiber space is perfused with whole blood (see Fig. IV-29).

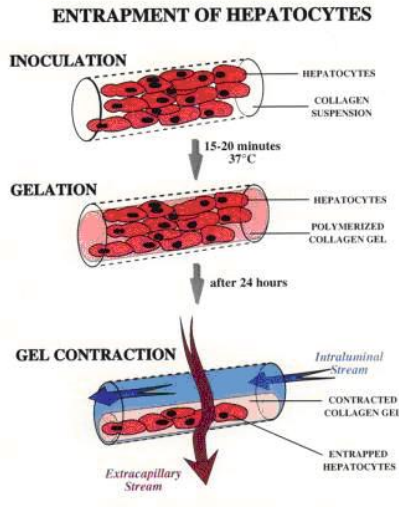


Fig. IV-29: A schematic drawing of the gel-entrapment of hepatocytes in the Liverx2000. [200]

Main consideration : Three-dimensional culture in the gel is favorable for hepatocyte functionality, but in addition to the hollow fiber membrane, the medium

perfusion inside the hollow fiber lumen itself acts as an additional diffusive barrier for solute exchange. This may limit the functionality of this system.

5.3.3 LIVERaid

System design : The LIVERaid BAL system was developed by Arbios System (Los Angeles, CA, USA) founded by the principal investigator of the HepatAssist system (see §5.4.2). This BAL system utilizes a multicompartment hollow fiber module with a fiber-within-fiber geometry (Fig. IV-30). Hepatocytes are seeded on the outer surface of the outer fiber. In the space between the outer and inner fiber, blood is perfused. Inside the inner fiber flows a solution composed of or perfused through charcoal and resin. This geometry allows for the integration of liver cell therapy and blood detoxification within a single module.

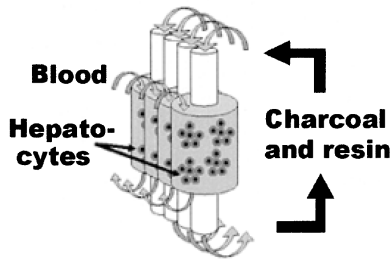


Fig. IV-30: Schematic drawing of the LIVERaid system. [202]

Main consideration : This system has only been presented at few conferences and has yet to show its potential in a peer-reviewed manuscript, although it theoretically seems a promising concept.

5.3.4 LLS-HALSS

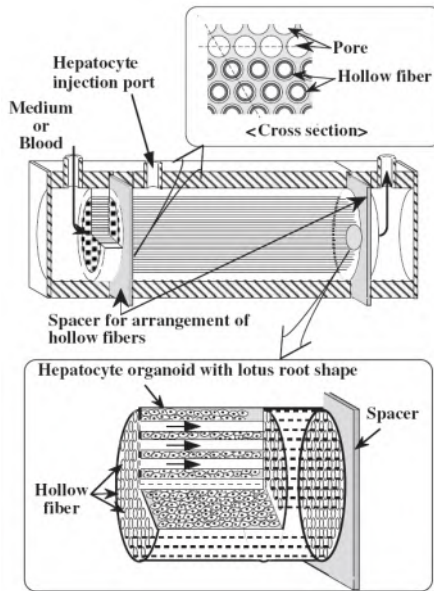


Fig. IV-31: Schematic drawing of the LLS-HALSS system. [203]

System design : The liver lobule-like structure module (LLS) hybrid artificial liver support system (HALSS), which was designed by Mizumoto and Funatsu in Kyushu University, has many hollow fibers (polyethylene coated with ethylene vinyl alcohol, for plasma separation) acting as blood capillaries (Fig. IV-31). They are regularly arranged close to each other. Primary rat hepatocytes are inoculated by a centrifugal force, at a high density in the outer space of the hollow fibers. [203]

Main consideration : Given the tight arrangement of the blood capillaries in the device, it may be impossible to achieve a homogeneous hepatocyte distribution necessary for optimal efficacy of the BAL system. Although small animal experiments are promising, this may limit the potential for scale-up as the device currently contains only 0.6 grams of hepatocytes.

5.3.5 PUF-HALSS

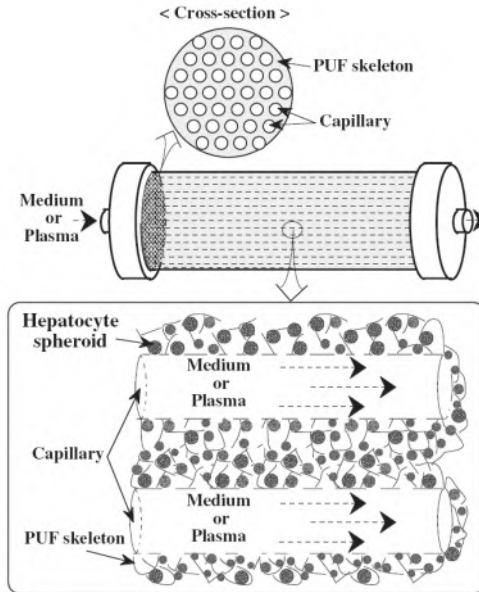


Fig. IV-32: Schematic drawing of the PUF-HALSS system. [203]

System design : This system consists of a cylindrical, polyurethane foam (PUF) block with many capillaries in a triangular arrangement which form a flow channel (Fig. IV-32). The diameter of each capillary is 1.5 mm, and the capillaries are arranged at a 3.0 mm pitch. Blood perfusion is used. Inoculated hepatocytes in the pores of the PUF between each capillary are said to spontaneously form spheroids of 100 – 150 μm diameter. Primary porcine hepatocytes are immobilized at 1.0×10^7 cell/ cm^3_{PUF} . Various sizes of modules from 5 cm^3 that use 0.5 g hepatocytes (the smallest size for a rat experiment) to 1000 cm^3 that use 100 g hepatocytes (for a preclinical study that uses a hepatic failure pig) have been made. Rat [204], dog [205] and pig [206] experiments as a preclinical study have already shown a curative effect.

Main consideration : The spheroid culture is advantageous to the performance of the system, but no comments in any publications are made on how a homogeneous cell distribution is obtained inside a PUF block, which is crucial for the scalability of this system.

Encapsulation based systems

5.3.6 UCLA-BAL

System design : The UCLA-BAL system developed by Dixit and Gitnick, at UCLA (California, USA) involves the direct blood perfusion of microencapsulated hepatocytes in a packed-bed extracorporeal chamber (Fig. IV-33).[187] The hepatocytes are located in biocompatible and semi-permeable calcium alginate–polylysins–sodium alginate composite membranes. Freshly prepared, or cryopreserved, microencapsulated hepatocytes can then be placed within the BAL device for use during liver failure. Microcapsules size approximately 300–700 μm diameter.

Main consideration : This system is a typical implementation of encapsulation based systems, with its advantages and drawbacks mentioned previously. A small animal model study was promising [187] but further research has yet to be published.

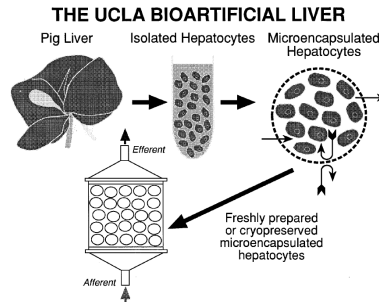


Fig. IV-33: Schematic drawing of the UCLA-BAL

5.3.7 AHS-BAL

System design : The Alginate-entrapped Hepatocyte Spheroid (AHS) BAL system has a configuration similar to that of the UCLA-BAL system.[202] However, the porcine hepatocytes are suspension cultured for 20 hours to form spherical aggregates, called spheroids, before entrapment in Ca-alginate beads.

Main consideration : Similar comments as the previous device. However, the performance of the AHS-BAL system has been claimed to be evaluated at anhepatic pigs but no data has been published yet.

5.3.8 Fluidized bed BAL

System design : A schematic of the fluidized bed BAL designed by Legallais *et al.* is depicted in Fig. IV-34. This BAL system differs from the above encapsulated systems in two aspects: (1) the beads are not in a packed-bed configuration, but are fluidized which increases bidirectional mass transfer, and (2) plasma is perfused instead of blood.

Main consideration : *In vitro* research has been performed with C3A hepatocytes and showed promising. Research on the mechanical aspects of the beads also ensures bead integrity during fluidization. A small or large animal model study should be performed to confirm the positive *in vitro* results.

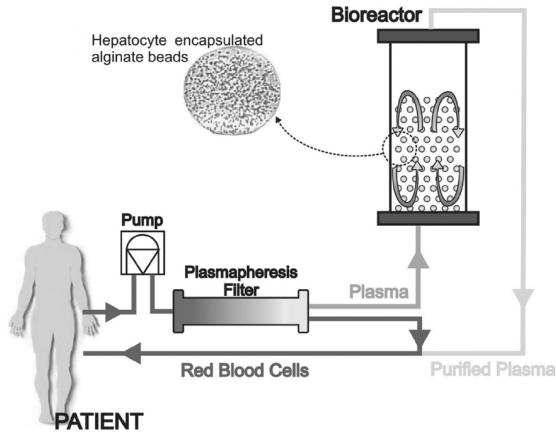


Fig. IV-34: Schematic drawing of the fluidized bed BAL system. [192]

Direct perfusion systems

5.3.9 Oxy-HFB

System design : The oxygenating hollow fiber bioreactor (OXY-HFB) BAL system was developed by Jasmund *et al.*, in Eberhard Karls University, Germany.[207] The OXY-HFB BAL system consists exclusively of oxygenating and integral heat exchange fibers in a simple bioreactor design. Primary porcine liver cells are seeded on the surface of the fibers in the extrafiber space. Oxygen is supplied and the temperature regulated through the fibers. Plasma from patients is perfused through an extrafiber space and brought into direct hepatocellular contact.

Main consideration : The aforementioned advantages and disadvantages of direct perfusion apply (see §5.2.2). Internal oxygenation is available, which is an advantage. Although *in vitro* results are promising, no further studies have been reported.

5.4 Overview of clinically applied BAL systems

In the following text, eight clinically applied BAL systems are described and a brief overview of their clinical outcome is given. Note that only hollow fiber systems and direct perfusion BAL systems have been used in clinical studies. No flat plate or encapsulation based system has yet reached this stadium.

Hollow fiber systems

5.4.1 Extracorporeal Liver Assist Device (ELAD)

Initially developed by Sussman *et al.*, the ELAD [179,186] is the only clinically applied BAL device which uses the human hepatocyte C3A cell line. The cells are seeded in a hollow fiber cartridge; a second cartridge can be connected in series. Heparin anticoagulated blood flows through the cartridge and plasma is filtered through the cellulose acetate fibers into the extracapillary space of the cartridge where it comes into contact with the C3A cells. The membrane MW cut-off is 70 kDa. Before the ultrafiltrate is returned to the bloodstream, it is passed through a dual membrane cell filter to prevent cells and cellular debris from entering the bloodstream.

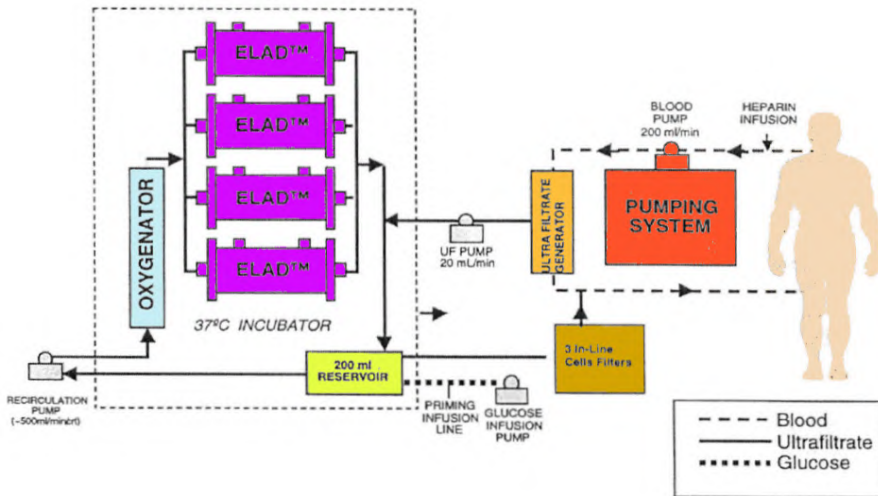


Fig. IV-35: Schematic drawing of the (modified) ELAD system. (adapted from [208])

This BAL system underwent a phase I safety evaluation and a controlled trial. In the uncontrolled clinical trial[209], 6 out of 11 patients died, while one patient completely recovered without an orthotopic liver transplantation (OLT) and four patients underwent a successful OLT. In a pilot controlled trial on 24 acute liver failure

patients, there was no significant difference in survival rate, renal function, and biochemical parameters between the ELAD-treated patients and the controls. In contrast, the plasma ammonia (+8%) and bilirubin (+20%) level were higher than those before the ELAD treatment.[179]

In 2002, a slightly modified version of the ELAD system was developed (see Fig. IV-35). The new system uses filtrated blood (plasma) instead of whole blood, generated by a 120 kD cut off membrane, and uses four cartridges each with approx. 100 g of C3A cells. Perfusion flow rates were increased from 150 – 200 ml/min to 500 ml/min. An external oxygenator is inserted in the plasma circuit to increase oxygen content of the perfusing plasma. In another phase I trial with 5 ALF patients, no adverse events were observed during the ELAD treatment, but ammonia levels were not influenced by the treatment. Bilirubin plasma levels were not mentioned.[208] A randomized, controlled, pilot, multicenter study of approximately 24 ALF patients is ongoing.

5.4.2 HepatAssist

The HepatAssist system was developed by Demetriou *et al.*[210] The biological component consists of $5 - 7 \times 10^9$ cryopreserved porcine hepatocytes. The cells are attached to collagen coated dextran microcarrier beads, and are subsequently inoculated in the extra-fiber space of a hollow fiber bioreactor (Fig. IV-36). Plasma is separated at 50 ml/min by continuous centrifugation of a 90 – 100 ml/min blood stream. Plasma first passes through an activated charcoal column and an external oxygenator before flowing through the lumina of the hollow fibers, which have a 0.2 μm microporous membrane. Plasma is recirculated herein at 400 ml/min. After passing the bioreactor, treated plasma and the blood cells are reconstituted and returned to the patient.

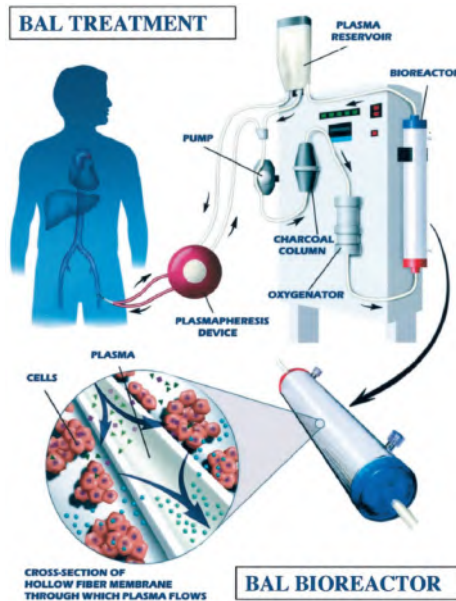


Fig. IV-36: Schematic drawing of the HepatAssist system. [211]

The efficacy of this BAL system was examined in several studies, including a phase I safety evaluation study,[181] and the largest controlled clinical trial for a BAL device until present.[211] In different uncontrolled studies, both the total bilirubin and ammonia concentrations averagely decreased by 18% of the initial concentrations after treatment.[122] The treatment also resulted in some improvement in the patients' neurological states, intracranial pressure (ICP), and biochemical parameters. In the randomized, controlled clinical trial, 171 acute liver failure and primary non-function patients were involved. 30-day survival did not differ significantly between the control group and the BAL treatment group. However, a significant survival advantage of 33% (37% vs. 70% survival) was associated with HepatAssist treatment for an ALF subgroup which included acetaminophen overdose patients. This makes the HepatAssist the only BAL system which has significantly proven a 30-day survival benefit for ALF patients until present.

5.4.3 TECA-HALSS

The TECA Hybrid Artificial Liver Support System, developed in Beijing, China, consists of an extracorporeal hollow fiber bioreactor loaded with $10 - 20 \times 10^9$ porcine hepatocytes. The hepatocytes are suspended in a nutrient medium and recirculated through the extracapillary space of the bioreactor. Plasma is separated from the patient's blood, treated in a carbon absorption column and subsequently perfused through the hollow fiber lumina. [212,213]

In a safety study, no adverse effects were noted. Neurological improvement was found in some patients, and in one patient a respective decrease of ammonia and

total bilirubin levels of 31 % and 15 % was reported.[213] No additional data, however, are available.

5.4.4 Bioartificial Liver Support System (BLSS)

The bioartificial liver support system (BLSS), which was developed in Pittsburgh and commercialized by Excorp Medical (Minneapolis, MN, USA), uses cellulose acetate hollow fibers with a 100 kD-molecular weight cut-off (Fig. IV-37). Primary porcine hepatocytes (70–120 g) are mixed with 20 volume% of a 3.1 weight% collagen solution and the mixture is infused into the extracapillary space. Blood is perfused at 100 – 250 ml/min through the fibers of the bioreactor after passing through an oxygenator.[213,214]

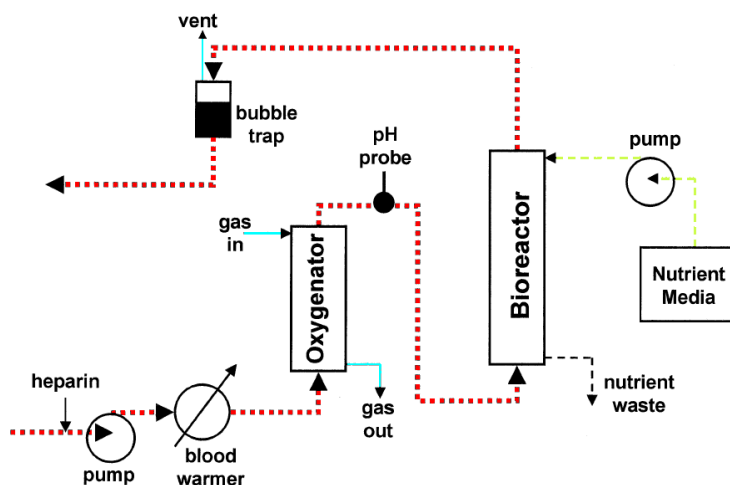


Fig. IV-37: Schematic drawing of the BLSS system. Red dotted lines are the blood flow path; blue full lines are gas flow paths; green dashed lines are nutrient media flow path. (adapted from [214])

In a safety study of four ALF patients, the blood ammonia and total bilirubin levels decreased by 33% and 6% respectively, compared with the initial levels. However, the patients' neurological states are not improved significantly.[215] Also no survival outcome was mentioned. A proper phase I clinical trial is ongoing.

5.4.5 Hybrid Bioartificial Liver (HBAL)

This BAL system consists of a polysulfon hollow fiber bioreactor. 10×10^9 porcine hepatocytes in suspension are loaded into the extra-fiber compartment of the bioreactor. Plasma was perfused through the hollow fibers with a membrane cut-off of 100 kD.[216]

In a phase I trial, twelve patients were treated with the HBAL system. However, a heterogeneous treatment protocol was used. For some patients, plasma was pretreated by perfusion through a charcoal or resin column before entering the

HBAL. No adverse effects were observed, and nine out of twelve patients were described as improved without clear supporting data in the manuscript.[216]

5.4.6 Hybrid Liver Support System (LSS) – Modular Extracorporeal Liver Support System

The Liver Support System (LSS) device, developed in Berlin (Germany), consists of a specially designed bioreactor aiming at improving cell oxygenation and mass exchange.[158,217] The system consists of interwoven hollow fiber membranes, creating a 3-dimensional framework of hollow fibers over which hepatocyte aggregates are distributed. Three bundles of hollow fibers are situated inside the bioreactor (see Fig. IV-38). Two of these bundles consist of hydrophilic fibers (300 kD cut-off) and are used for plasma perfusion at a 100 – 200 ml/min flow rate. By closing one end of each bundle, plasma entering the bioreactor enters the extracapillary space via one fiber bundle, makes contact with the hepatocytes, and leaves the bioreactor via the second fiber bundle. The third bundle of hollow fibers is made of hydrophobic membranes and is used for gas exchange inside the bioreactor. The bioreactor contains up to 500 to 600 g of hepatocytes. The LSS is the only system that has been used in clinical studies with primary porcine hepatocytes as well as primary human hepatocytes derived from discarded donor livers.[136] Seven ALF patients were treated for 8 to 46 hours with the porcine cell-based LSS system.[218] All patients were successfully bridged to OLT. Elevated plasma ammonia levels were, however, not corrected by LSS treatment. No data concerning clinical parameters, total bilirubin, and adverse events have been reported.

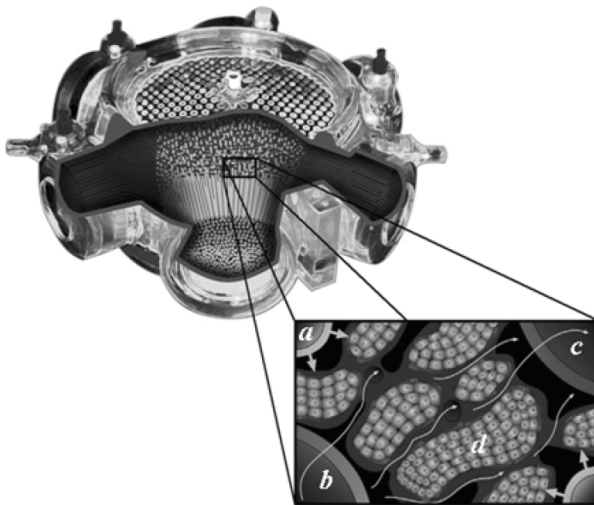


Fig. IV-38: Schematic drawing of the LSS – MELS CellModule: a) oxygen capillary, b) inflow medium capillary, c) outflow medium capillary, d) hepatocyte aggregates. [219]

In a phase I study with primary human hepatocytes, 8 patients were treated with the Modular Extracorporeal Liver Support (MELS) system (see Fig. IV-39). The

MELS concept combines different extracorporeal therapy units, tailored to suit the individual clinical needs of each patient.[136] The MELS consists of the LSS system combined with a DetoxModule based on single-pass albumin dialysis (SPAD) for removing albumin-bound toxins. Human hepatocytes were harvested from donor livers that were discarded because of steatosis, cirrhosis, fibrosis, or mechanical injury. Six of 8 patients were successfully bridged to OLT. The other 2 patients suffered from acute-on-chronic liver failure and were not candidates for OLT due to continuing alcohol consumption. No adverse events were observed. In all 8 cases, neurological status improved, and slight improvement of coagulation was observed during treatment.

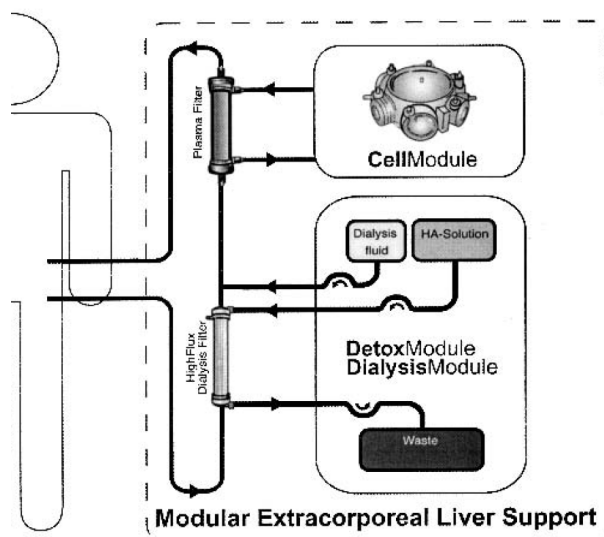


Fig. IV-39: Schematic drawing of the MELS system. [220]

Direct perfusion systems

5.4.7 Radial Flow Bioreactor (RFB)

In this system developed at the University of Ferrara (Italy), blood is removed at 80 ml/min from the patient and plasma is separated at 22 ml/min using a hollow-fiber module. Plasma is then continuously collected into a soft reservoir (500 mL), heated at 37 °C and oxygenated by an on-line hollow-fiber oxygenator using a 95% O₂ / 5% CO₂ gas mixture prior to recirculation at 1 – 1.5 ml/(min.g hepatocytes) through the hepatocyte-filled RFB. The RFB is a cylindrical bioreactor in which the plasma flow passes from the center to the periphery of the module after having crossed the cell-filled compartment. This compartment consists of a woven-non-woven polyester matrix sandwiched between two precision-woven polyester screens, having a 1 μm cut-off. 200-230 grams of isolated porcine hepatocytes are injected into the 6 mm-thick polyester mesh; hepatocytes are entrapped within the microfibers, while the two

screens prevented hepatocyte leakage during the phase of cell loading and following perfusion.

Seven patients have been treated in a phase I safety evaluation study. No adverse effects were observed during or after the treatment. The RFB-BAL system decreased the mean ammonia and bilirubin levels by 33% and 11%, respectively, and was associated with an amelioration of the patient's neurological status.[221,222]

5.4.8 AMC Bioartificial Liver (AMC-BAL)

The internal geometry of the AMC-BAL (Academic Medical Center, Amsterdam, The Netherlands) bioreactor is schematically drawn in Fig. IV-40. The bioreactor consists of a cylindrical polycarbonate housing (inner diameter $\phi = 23.4$ mm; Fig. IV-40-l) in which two pieces of three-dimensional (3D) non-woven polyester matrix mat (Fig. IV-40-e/g) are spirally wound around a massive inner core (Fig. IV-40-i). A space between the two mat segments (Fig. IV-40-f) is left open for an additional hepatocyte seeding port (Fig. IV-40-o). In the hydrophilic matrix, high-density culture of porcine hepatocytes is possible. Between the matrix windings, hydrophobic gas capillaries (outer $\phi = 380$ μm ; Fig. IV-40-m) are positioned in parallel along the entire bioreactor as an internal oxygenator system to supply O_2 to the hepatocytes. Under standard operating conditions, culture gas (95% air, 5% CO_2) is perfused through these capillaries, entering and exiting the system through Fig. IV-40-a/b, respectively. Separated plasma enters the bioreactor at 150 ml/min through an inlet port (Fig. IV-40-c) and flows through the inflow zone (Fig. IV-40-j) past the hydrophilic matrix mat and through the void inter-capillary space (Fig. IV-40-n). The plasma exits the bioreactor via the outflow zone (Fig. IV-40-k) through the outlet port (Fig. IV-40-d). In clinical application, the AMC-BAL module is part of a circuit with a plasmapheresis system, a plasma heater, and a 0.4 μm cell barrier filter. The bioreactor is loaded with $7 - 15 \times 10^9$ primary porcine hepatocytes through three loading ports (Fig. IV-40-c/o/d) in a 25-50-25% ratio. After a 2 hour attachment period, the bioreactor is connected to *in vitro* or *in vivo* circuit.

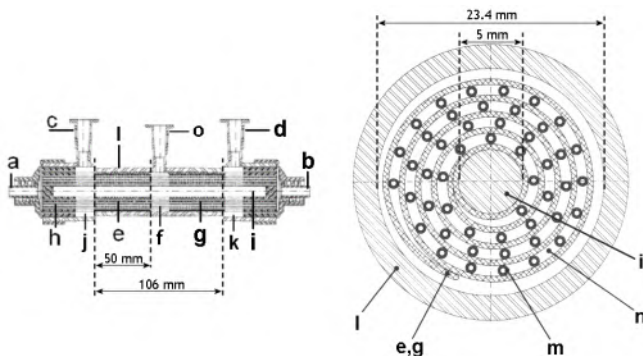


Fig. IV-40: Longitudinal (left) and transverse (right) view of the internal geometry of the AMC-BAL with a = gas outlet; b = gas inlet; c = plasma inlet port; d = plasma outlet port; e = first mat segment; f = interspace; g = second mat segment; h = polyurethane potting to separate gas and fluid compartment; i = inner core; j = inflow zone; k = outflow zone; l = polycarbonate housing; m = gas capillaries; n = inter-capillary space through which fluid flows; o = central hepatocyte loading port.

In a phase I clinical trial, twelve ALF patients were treated.[223] Eleven were successfully bridged to OLT, one patient showed improved liver function after two AMC-BAL treatments and did not need OLT. No severe adverse effects of the treatment were observed. On average, blood ammonia and total bilirubin levels decreased 44% and 35%, respectively, after treatment. A thorough overview of the research on the AMC-Bioartificial Liver can be found in [224].

5.5 Conclusions and motivation of research

The four aforementioned essential requirements for designing a bioartificial liver system – (1) the capacity to hold a sufficient number of hepatocytes, (2) to maintain hepatocyte viability and function, and to provide in (3) adequate bi-directional mass transfer and in (4) an immunological barrier – are fundamental criteria to assess the different BAL systems. A clear trend in experimental stage bioartificial liver systems is the aim for a three-dimensional culture which mimics the *in vivo* situation. Also possible immuno-isolation needs are fulfilled. However, many of these systems still have to deal with either scalability or limited mass transfer issues. To deal with the latter, different approaches are mentioned but these are seldom based on prior research on the influence of these implementations on efficient mass transfer.

This conclusion also applies to some extent to clinically used BAL systems. An excess of liver support devices have reached the stage of clinical applicability, though only with marginal success. Only the HepatAssist has proven some degree of significant improved survival in a subgroup of patients. Although a whole range of bioreactor implementations have been investigated in experimental studies, most clinically used systems (6 out of 8) are hollow fiber-based. The other 2 systems are based on direct perfusion. The design properties of the hollow fibers or of the components of direct perfusion systems vary significantly among the different systems. For example, concerning oxygenation – a major issue in BAL systems – 4 systems use external oxygenation, 2 use internal oxygenation, and 2 (plasma perfused!) systems totally lack any additional oxygenation.

The wide variety of system designs and the lack of a clear advantage of one system over the other illustrate the lack of predictive studies on the influence of various design parameters on the performance of bioartificial liver systems. The influence on fluid flow and mass transfer inside the bioreactor in particular is difficult to assess. This is mainly due to the multiple, time and resource consuming *in vitro* studies necessary to assess this issue. In this dissertation, it will be discussed how numerical techniques can aid in the assessment of these problems, and can significantly shorten development time in bioartificial liver support systems.

5.6 Overview of prior numerical research on perfusion and mass transfer in BAL systems

Catapano *et al.*[153] were among the first to describe oxygen transfer as the most limiting factor in the efficiency of bioartificial liver support. Experimental research on O₂ transport inside BAL devices is time and resource consuming and is typically characterized by a trial-and-error approach. Also, there are no experimental techniques available which allow getting a detailed insight in the O₂ concentration profiles inside a bioreactor. As such, some research groups recognized the benefits of computational modeling to study O₂ transport and consumption inside bioartificial liver systems. Numerical techniques circumvent some of these major drawbacks of experimental research. Additionally, operating parameters or the bioreactor design itself can easily be changed in a numerical model to assess their influence on cellular O₂ availability. In the following text, a brief overview is given of the most important studies which attempt to model a BAL system using numerical techniques.

McClelland *et al.*[225] did a broad computational study on O₂ transport through collagen extracellular matrix (ECM). Since no convective flow through a standard collagen ECM is possible, transport of solutes occurs solely by diffusion. The increased transport distance for O₂ to reach the hepatocytes, combined with the reduced diffusion coefficient of O₂ in ECM led to the hypothesis that O₂ supply to the hepatocytes may be impaired. McClelland therefore devised an enhanced ECM by incorporating 0.1 - 5 µm polystyrene porous microspheres within the collagen type I gel. In contrast to normal collagen, the use of porous microspheres permits convective flow in the gaps surrounding the microspheres and through the pores of the shell of the microspheres themselves. The increased porosity, however, also decreases O₂ diffusion coefficient in the ECM, the extent of which depends on the proportion of microspheres added to the collagen. McClelland used a numerical model to assess the influence of the enhanced ECM on O₂ availability in three generic types of BAL systems: hollow fiber, flat plate, and encapsulation based systems. For this, a one-dimensional (1D) convection-diffusion-reaction equation was solved in a cylindrical, Cartesian, and spherical coordinate system for a simplified hollow fiber, a semi-infinite flat plate and a spheroid model, respectively. In its generalized form, the equation is as follows:

$$\frac{\partial C}{\partial t} = D \frac{\partial^2 C}{\partial x^2} - u \frac{\partial C}{\partial x} - q \quad \text{Eq. IV-2}$$

C is O₂ concentration, D is the diffusion coefficient, u is the convective flow velocity, and q is the O₂ consumption term. The enhanced collagen differed from the standard version in: (1) the convective velocity, which in the enhanced collagen was experimentally fitted to 12 µm/s versus 0 m/s in standard collagen, and in (2) the decreased diffusion coefficient $D_{\text{coll_enhanced}} = (E / Kt^2) * D_{\text{normal}}$ with E the filled fraction ratio equal to ((volume total – void volume total) / volume total), and with Kt the tortuosity of the path equal to ((original length + tortuous length) / original length). The most important boundary conditions are given in Table IV-2.

Table IV-2: Overview of prior numerical research on oxygen transfer in BAL systems.

	McClelland [225]	Sumaru [226]	Moussy [227]	Tilles [157]	Allen [137]	Ledezma [228]	Hay [229]	Hay [230]	Sullivan [101]
Model type	1D – HF, FP, encapsulation	1D – PUF-HALSS (spheroid) 1D – LLS-HALSS (HF)	1D - ELAD (HF)	2D – FP	2D – FP	2D – Radial flow FP	2D – ELAD (HF)	1D – HepatAssist (HF)	HF
Cell layer thickness/radius (μm)	500	75	55	/	/	/	25	196	117
$D_{\text{fluid-zone}}$ [$10^{-9} \text{ m}^2/\text{s}$]	0.6 – 2.5	2.13	/	2.0	2.0	2.0	1.4	/	3.0
$D_{\text{cell-zone}}$ [$10^{-9} \text{ m}^2/\text{s}$]	0.6 – 2.5	1.67	/	/	/	/	0.2	/	2.0
Cell density [$10^6 \text{ cells}/\text{cm}^3$]	1 – 2.5	/	157	0.11 (2D)	0.17 (2D)	0.05-0.2 (2D)	160	28.2	/
O_2 consumption model	constant	constant	/	constant	constant	M-M porcine	M-M HepG2 - rat	M-M porcine	M-M C3A
Hepatocyte source	rat	/	/	rat	rat	0.25 (0.2-0.4)	0.03-0.16-0.63	0.35-0.89	/
V_M [nmole/($10^6 \text{ cells}\cdot\text{s}$)] (nmole / (ml . s))	0.4	/	/	0.38	0.38	/	5-25-100	10-25	25
K_M [mmHg]	n/a	900 – 3100	/	/	/	5.0 (10-20)	0.5 – 5.6	3.0	3.0
$p\text{O}_2$ – fluid [mmHg]	86 – 290	400 – 675	/	154	158 (75-175)	380 (76-456) (blood)	40 (blood)	150-525	5-135
$p\text{O}_2$ – internal oxygenator	/	/	/	154	/	/	/	/	/
Critical O_2 level [mmHg]	0.01	40	/	/	5-10	5 (K_M)	1-2	2	/
Typical cell perfusion velocity [mm/s]	/	/	0.15	0.67	1.2-23.8	0.31-2.65	/	/	/
Max. shear stress [Pa]	/	/	0.83	0.001-2.1	0.12-0.75	0.2-1	/	/	/

HF = hollow fiber; FP = flat plate; Roy *et al.* [231] and Patzer *et al.* [232] were not included due to the fully dimensionless model (Patzer: Critical O_2 level: $V_{\text{ratio}} > 0.9$, see text).

$D_{\text{fluid/cell-zone}}$ = diffusion coefficient in fluid/cell-zone; V_M = maximal oxygen consumption rate; K_M = Michaelis Menten constant; $p\text{O}_2$ = oxygen partial pressure

The accuracy of the model was confirmed by comparison with experimental results of a simplified *in vitro* hollow fiber model. By varying the O₂ boundary conditions and O₂ permeability of the ECM, O₂ transport predictions were determined for each system as a function of time and distance. The results indicated that O₂ transport within all three BAL designs can be improved significantly by enhancement of the collagen gel, in spite of the reduced diffusion coefficient but thanks to convective O₂ transport. As such, maximal O₂ transport distance in the ECM could be increased from 170 μm to 420 μm. McClelland *et al.* also found that the influence of hepatocyte O₂ consumption on the oxygen profiles in the hollow fiber model was negligible.

In this author's opinion, this is due to the very low hepatocyte density in the model (see Table IV-2). Also, if or how the enhanced collagen improves O₂ transport in the spheroid model is not clear, as no convective flow in the enhanced collagen gel is present in the spheroid configuration to compensate for the reduced O₂ diffusion coefficient in the enhanced collagen.

Sumaru *et al.*[226] developed two numerical models to simulate O₂ availability in the PUF-HALSS and the LLS-HALSS. A simplified model with a 1D convection-diffusion equation in spherical coordinates represented the hepatocytes spheroids in the polyurethane foam of the PUF-HALSS. The spheroid had a diameter of 150 μm and was homogeneously designated to contain hepatocytes. The O₂ concentration at the outer spheroid wall was kept constant. As it concerns a 1D equation, an analytical solution could be established. To model the LSS-HALLS, Sumaru supposed a hollow fiber scaffold with an outer wall (outer diameter = 400μm) with constant pO₂. Inside the hollow fiber (inner diameter = 300 μm), a cylindrical cell mass (cylindroid diameter = 150 μm) was surrounded by an annular ring of static culture medium. Further model parameters and boundary conditions are given in Table IV-2. For the hepatocyte spheroid model, oxygen consumption of the hepatocytes was estimated to be 937.5 nmole/(ml.s)²⁰ when a pO₂ of 400 mmHg was imposed at the outer wall, and the pO₂ in the centre of the spheroid was assumed to be 40 mmHg. 40 mmHg was hereby assumed as the critical O₂ level under which necrosis takes place. In the model of the hepatocyte cylindroid, a range of diffusion coefficients in the hollow fiber membrane wall were applied to the model to determine its influence. In a similar simulation, hepatocyte O₂ consumption in this model was estimated as 312.5 nmole/(ml.s).

In this author's opinion, the use of a critical pO₂ of 40 mmHg is questionable, especially when the rationale is that it equals the pO₂ of venous blood. Moreover, this threshold is used to estimate O₂ consumption, by stating that experimentally spheroids with a diameter of 150 μm were formed in the PU foam, and as such the pO₂ in the centre of this spheroid is equal to the critical value of 40 mmHg; otherwise if the pO₂ in the centre was higher, the spheroid is assumed to be able to grow larger in size. This reasoning, combined with the enforced O₂ gradient from 400 mmHg to 40 mmHg over a 75 μm distance could explain the unusually high estimated oxygen consumption ratios. Nevertheless, the model itself is sound and

²⁰ reported as 30 g/(m³.s) = 30 x 10⁻⁶ g/(ml.s) = 30/32 x 10⁻⁶ mol/(ml.s) with MW of O₂ = 32 g/mol

useful qualitative conclusions regarding the influence of membrane properties and hepatocyte oxygen consumption are drawn.

Moussy *et al.*[227] did a numerical study of open shell flow through a hollow fiber model with a cell packed shell region. Open shell flow signifies that the plasma flow hollow fiber is closed at the end of the bioreactor, and as such the plasma must penetrate the hollow fiber wall and the cell bed region and leaves the bioreactor via the cell packed region. In contrast, in closed shell mode, the plasma must re-enter the hollow fiber near the end of the bioreactor (cell shell is closed). Operational parameters were taken from the ELAD system. The fiber model had an inner diameter of 200 μm , an outer diameter of 260 μm , and a length of 234 mm. Around the fiber outer wall, a cell packed shell of 55 μm was present. Blood flowed as a poiseuille flow through the hollow fiber lumen. From this, an axial pressure profile was calculated. Ultrafiltrate (plasma) passes through the hollow fiber wall and the shell region with a certain membrane permeation velocity, which was calculated from the local pressure difference between the blood pressure in the lumen and the shell pressure, and from the membrane ultrafiltration coefficient. The shell pressure was considered constant in the radial direction, and was calculated by integrating Darcy's law: $P_{\text{shell}} = P_{\text{inlet}} - x \cdot (\mu \cdot u_s) / K$, with x the axial distance, u_s the axial velocity in the cell region, and K the hydraulic permeability of the cell region. The hydraulic permeability of a hepatocyte bed can be found theoretically by substituting the cell length d and hepatocyte bed porosity ε into the Carman-Kozeny equation (Eq. IV-3) for a bed of uniformly sized cubes of length d .

$$K = \frac{d^2}{180} \frac{\varepsilon^3}{(1 - \varepsilon^2)} \quad \text{Eq. IV-3}$$

This resulted in a theoretical permeability of $4.62 \times 10^{-9} \text{ cm}^2$ or a viscous resistance of $2.16 \times 10^{12} \text{ m}^{-2}$ for a hepatocyte length of 15 μm and a hepatocyte density of 157×10^6 cells/ml. Fitting experimental pressure data to the simulations revealed, however, a cellular permeability of $1.39 \times 10^{-7} \text{ cm}^2$ or a viscous resistance of $7.2 \times 10^{10} \text{ m}^{-2}$.

The model was further used to assess pressure profiles and backfiltration in the open shell hollow fiber system. Estimated shear stress in the cell packed shell region ranged between 0 and 0.83 Pa. However, the most interesting finding was the two-orders-of-magnitude difference between the experimentally fitted and theoretically determined hepatocyte permeability. This may indicate that preferential flow patterns are possible in the ELAD and that subsequent hypoperfusion of many hepatocytes is a prime reason for the lack of difference in survival rates between the ELAD-treated and the control groups.

Tilles *et al.*[157] used a steady state, dimensionless 2D O_2 convection-diffusion model as a supplement in their experimental studies on a flat plate bioreactor. The model assumed a uniform longitudinal (plug) flow and perpendicular diffusion to the plate where oxygen consumption was imposed through a flux-boundary condition. The upper wall of the channel was either set at a constant O_2 level or either as impermeable, to mimic a flat-plate bioreactor with or without an internal oxygenator. Various flow regimes and channel heights were imposed. The

results showed that the internal oxygenator was mandatory to maintain viability and function of the hepatocytes. Importantly, shear stress calculations showed that, at lower wall shear stresses (0.001 to 0.033 Pa), hepatocyte functions, measured as albumin and urea synthesis rates, were as much as 2.6- and 1.9-fold higher, respectively, than those at higher wall shear stresses (0.5 to 2.1 Pa).

An almost identical model was used by Allen *et al.*[137] to estimate oxygen distribution at the cell surface of their flat plate bioreactor. Their goal was to design a flat plate bioreactor with physiological oxygen gradients from 60-70 mmHg (periportal) at the entrance to 25-35 mmHg (perivenous) at the outlet of the flow channel. The numerical model allowed determining which flow rate should be applied to achieve the envisioned pO_2 profile, depending on the fluid inlet pO_2 value. Experimental measurements of outlet oxygen concentrations from various flow conditions were successfully used to validate model predictions.

Again a similar, but dimensionless model of a flat plate bioreactor was used by Roy *et al.*[231]. As in Tilles *et al.*[157] they numerically assessed oxygen concentration profiles in a flat plate bioreactor with and without an internal oxygenator membrane. The conclusions of this study are very similar to the ones in Tilles *et al.*[157], which is understandable as Tilles is also third author of Roy *et al.*[231], and Roy is third author in Tilles *et al.*[157].

Ledezma *et al.*[228] used a two-dimensional axi-symmetric model to assess fluid flow, shear stress and oxygen tension in a radial flow flat plate bioreactor. A poiseuillan flow profile was calculated in the channel; hepatocyte oxygen consumption was still imposed via a boundary condition as the cell layer itself was not modeled. However, a more realistic Michaelis-Menten O_2 uptake kinetic model was used. The effect of different parameters that may influence the oxygen transport inside the chambers, such as the plasma flow rate, the channel height, the initial oxygen tension in the perfused plasma, the O_2 consumption rate V_M , and the Michaelis-Menten half-saturation constant K_M was investigated. They found that V_M had a significant impact on O_2 availability, while the impact of K_M was negligible if the critical minimal allowable pO_2 threshold was set equal to the K_M value itself. They also found that increasing the flow rate and/or the inlet oxygen tension resulted in improved oxygen transport to cells in the radial-flow microchannels, and allowed a significantly larger reactor diameter without oxygen limitation to the hepatocytes. For a constant plasma flow rate, the chamber height had a negligible effect on the oxygen transport to hepatocytes. In contrast, they found that it strongly affected the mechanical stress on the cells, which is also crucial for the successful design of the BAL reactors. A twofold decrease in chamber height from 50 to 25 microns produced approximately a fivefold increase in maximal shear stress at the inlet of the reactor from 0.2 to 1 Pa. They concluded that the channel height needs to be carefully chosen in a BAL design to avoid deleterious hydrodynamic effects on hepatocytes.

Hay *et al.*[229] used a mathematical model to predict oxygen transport in a hollow fiber bioartificial liver. A typical axi-symmetric model with three concentric cylinders was used (so called Krogh cylinder model). Inside the hollow fiber inner

wall (diameter = 220 μm), laminar blood flow was present. The non-linear hemoglobin-oxygen binding in the blood phase was incorporated in the model by modifying the diffusion term in the axial convection – radial diffusion equation. In the annular hollow fiber membrane zone, only diffusion was possible. In the outer annular cell phase ring (inner diameter = 280 μm ; outer diameter = 330 μm), O_2 consumption according to Michaelis-Menten was incorporated in the diffusion equation. The model was used to simulate pO_2 profiles in the cell annulus, for different O_2 consumption values and membrane permeabilities. In conclusion, axial-flow hollow fiber cartridges were found to be an inappropriate design for bioartificial liver use, as the high oxygen demand of the hepatocytes and the membrane permeability limit the oxygen availability. A highly remarkable conclusion, given the number of hollow fiber BAL systems that have been developed.

In a follow-up study, Hay *et al.*[230] sought out to alleviate these mass transfer problems by studying a ‘convection-enhanced’ hollow fiber design, in which plasma was transported across the hollow fiber membrane. A Krogh cylinder model was again used for the flow and pressure calculations, with geometrical parameters now based on the HepatAssist device (inner diameter HF = 640 μm , outer diameter HF = 760 μm , cell annulus outer diameter = 1152 μm), operated in open shell mode (see Moussy *et al.*). Darcy viscous resistance of the cell based extra-capillary space was set between $10^8 - 10^{12} \text{ m}^{-2}$, which is in the range used by Moussy *et al.*[227] Oxygen transport was modeled using a 1D axial mass balance equation in the cell annulus, using Michaelis-Menten kinetics. Oxygen consumption and membrane permeability were varied in an attempt to match experimental results. It was found that in the cell mass close to the fiber inlet, there was a rapid fall in pO_2 toward 0 mmHg. This occurred as the O_2 consumption rate was greater than the rate at which fresh plasma filtrate carries oxygen through the fiber wall. Further downstream, pO_2 increased significantly as more and more plasma carries oxygen into the cell space. Nevertheless, a substantial proportion (up to 95% under 150 mmHg fluid inlet pO_2 and 25 $\text{nmole}/(\text{s}\cdot\text{cm}^3)$ oxygen consumption) of the hepatocytes in the device were exposed to hypoxic conditions under which metabolism may be impaired. In this author’s opinion, it must be noted however that, since a 1D axial mass balance model is used, the radial pO_2 gradient in the 196 μm thick cellular annulus is averaged-out. This may be a considerable simplification, and a choice difficult to understand as the same author used a 2D model in the previous diffusion controlled ELAD model.

The claim that oxygen transfer in hollow fiber BAL designs is severely limited by diffusion led Patzer *et al.*[232] to investigate the oxygen consumption dynamics in a hollow fiber model. A Krogh cylinder model was used, with blood perfusion through the hollow fiber lumen, and Michaelis-Menten O_2 uptake in the cell layer annulus. A completely dimensionless 2D axi-symmetric numerical model in cylindrical coordinates was constructed. As the model highly resembled the model used by Hay *et al.*[229], an attempt was made to validate the model by comparison of the results with those of Hay *et al.* However, significant differences were present between both model results. As no explanation could be found, this may lead to believe that possibly a miscalculation is present in one of the two models. Using the

model, the effect of different parameters as the hepatocyte annular thickness, the hepatocyte cell mass O_2 permeability, hepatocyte O_2 consumption, and inlet pO_2 was assessed. The “effective hepatocyte utilization ratio”, V_{ratio} was introduced as the ratio of observed oxygen consumption rate to the intrinsic oxygen consumption rate. Results found large regions of $V_{ratio} > 0.9$, which was deemed an acceptable threshold, for model parameters consistent with standard hollow fiber cartridges. The presence of these zones was correlated with a fractional oxygen consumption of the perfusing medium of less than 25%. Combination with experimental results also indicated that the ‘per cell’ oxygen consumption decreases as cell density increases, and that this is not due to diffusion limitations, but due to lower intrinsic oxygen requirements in denser cell suspensions.

Another application of the Krogh cylinder model to predict O_2 concentrations in a hollow fiber BAL was recently performed by Sullivan *et al.*[101]. In a combined numerical and experimental approach, he studied the possibility of adding bovine red blood cells (bRBC) in the medium circulating through a hollow fiber bioreactor to achieve a controlled physiological oxygen gradient in the cell bed, as proposed by Allen *et al.*[137]. Although the full range of *in vivo* oxygen tensions could not be duplicated in the hollow fiber model, it was shown that the hepatocyte oxygen consumption (calculated via the O_2 concentration difference between inlet and outlet medium pO_2) was strongly increased by the addition of the bRBC’s. Depending on the pO_2 of the incoming medium and the amount of bRBC added, an optimal flow rate was established which showed a maximum gain in oxygen consumption as compared to the case without bRBC addition. For this, a 2D axisymmetric model was used (HF inner diameter = 330 μm ; HF outer diameter = 430 μm , cell annulus thickness = 117 μm), and realistic Michaelis-Menten hepatocyte oxygen consumption was applied. Further model parameters are given in Table IV-2. According to this author, caution is however advised regarding the quoted determined oxygen consumption values, which are in the range of 0.2 nmole/(10^6 cells.**hour**). Given numerous other references, this should be more realistic if expressed in nmole/(10^6 cells.**s**). In Sullivan *et al.*[101], comparison of oxygen consumption values was made with Nyberg *et al.*[233], but the latter study is mistakenly referred to as considering oxygen consumption of porcine hepatocytes while the quoted data involves PK-15 porcine kidney cells. Two other references, quoted to validate the unusual hepatocyte O_2 consumption rates of Sullivan *et al.*[101], mention values in nmole/(min.mg dry weight), which does not allow for easy comparison. Possibly, there may be a mistake in the conversion of O_2 consumption ‘per volume’ to ‘per 10^6 cells’ as this requires an estimation of the number of cells after the C3A cell culture in the bioreactor. This number was estimated to increase from 2×10^6 cells initially to 10^9 cells. Another reason may be that perhaps the O_2 consumption was calculated based on only the drop in the pO_2 of the aqueous part of blood, not taking into account the RBC O_2 binding and saturation. This could account for the approximately three orders of magnitude underestimation.

5.7 Research outline

It is clear that numerical modeling of fluid flow and oxygen transport in BAL devices can lead to a better understanding of O₂ transport as a limitation in the efficiency of a BAL system. The numerical model may then be used as a tool to determine the optimal operating parameters by studying their influence on O₂ concentrations in the bioreactor. Besides O₂ transport, also the knowledge of shear stress has proven to be an important determinant in the development of a successful BAL system. Moreover, numerical modeling of fluid flow and oxygen transport has an added value when it is combined with experimental research. As such, *in vitro* research results can be better understood with the aid of numerical simulations. Additionally, and maybe more importantly, they can be used as a validation tool. As in situ measurements of pO₂ inside a BAL bioreactor is practically not feasible, validation of simulation results is, however, usually limited to a black-box, inlet-outlet pO₂ validation.

In the numerical modeling of BAL systems or bioreactors, the imposed boundary conditions and model parameters are of crucial importance. Key parameters for modeling fluid flow are:

- Bioreactor geometry
- Density and viscosity of the fluid
- Imposed flow rate
- Hydraulic permeability of the scaffold and the cell mass

For the modeling of oxygen transport and consumption, additionally a detailed assessment of following parameters must be made:

- Diffusion coefficient in free fluid, the scaffold, and in the cellular mass
- pO₂ of incoming fluid and/or internal oxygenation system
- Hepatocyte O₂ consumption parameters (constant, or Michaelis-Menten V_M, K_M)
- Hepatocyte distribution (in a certain surface area / volume, and at certain density)

Once the simulations are performed, (1) a minimal ('critical') pO₂ threshold needs to be defined to assess the O₂ availability in the bioreactor. Similarly, (2) a maximal threshold for shear stresses to which cells are subjected, needs to be defined to judge if shear stress is a limiting factor.

The choice of all these model parameters is not an easy task. In the abovementioned numerical models, values for each of these parameters differ to a great extent. Values are sometimes chosen without thorough reasoning, such as is often the case for the hydraulic permeability and O₂ diffusion coefficients in the scaffold or cell mass zone, or for the pO₂ and shear stress threshold. Hepatocyte O₂ consumption may be the largest unknown in the numerical modeling of BAL devices. Many more different

values than cited in Table IV-2 have been reported for various types of hepatocytes. Disturbingly, it is possible that none of these values may be applicable to your specific modeling case, as hepatocyte O_2 consumption is strongly dependent on the micro-environment of the cell (cell density, type of scaffold, ...). A detailed, realistic, inhomogeneous hepatocyte distribution has not been assessed or considered in a numerical model until now, as all previous models assume a cell layer or spheroid with theoretically calculated, homogeneous hepatocyte density. Moreover, the numerical models developed until now only assess a unit volume of a BAL system, and often assume a homogeneous distribution of flow over the entire bioreactor. As such, the flow distribution in a BAL bioreactor and its impact on hepatocyte oxygen availability have not yet been assessed on a macro scale.

In the following chapters, an attempt is made to deal with all aforementioned limitations of the current numerical models. A solidly founded numerical model will be developed to assess and possibly improve the fluid flow and oxygen availability in the **AMC Bioartificial Liver** both on a micro (Chapter V) and macro (Chapter VII) scale. An experimental study (Chapter VI) will be used to both qualitatively and quantitatively validate the numerical results, whereas vice versa an attempt will be made to gain more insight in the experimental results using the numerical simulations (Chapter VII). Finally, an attempt is undertaken to numerically model the growth kinetics and metabolism of hepatocytes cultured in the AMC-BAL. This is a further step in gaining insight in the working processes of the bioartificial liver. As such, experimental research may be reduced and the time-to-clinical applicability of the AMC-BAL may be further reduced.

Chapter V: Three-dimensional numerical modeling and computational fluid dynamics simulations to analyze and improve oxygen availability in the AMC bioartificial liver.

A numerical model to investigate fluid flow and oxygen (O_2) transport and consumption in the AMC-Bioartificial Liver (AMC-BAL) was developed and applied to two representative micro models of the AMC-BAL with two different gas capillary patterns, each combined with two proposed hepatocyte distributions. Parameter studies were performed on each configuration to gain insight in fluid flow, shear stress distribution and oxygen availability in the AMC-BAL. We assessed the function of the internal oxygenator, the effect of changes in hepatocyte oxygen consumption parameters in time and the effect of the change from an experimental to a clinical setting. In addition, different methodologies were studied to improve cellular oxygen availability, i.e. external oxygenation of culture medium, culture medium flow rate, culture gas oxygen content (pO_2) and the number of oxygenation capillaries. Standard operating conditions did not adequately provide all hepatocytes in the AMC-BAL with sufficient oxygen to maintain O_2 consumption at minimally 90% of maximal uptake rate. Cellular oxygen availability was optimized by increasing the number of gas capillaries and pO_2 of the oxygenation gas by a factor two. Pressure drop over the AMC-BAL and maximal shear stresses were low and not considered to be harmful. This information can be used to increase cellular efficiency and may ultimately lead to a more productive AMC-BAL.

The contents of this chapter were published in Ann Biomed Eng (2006); 34 (11): 1729-1744

Three-dimensional numerical modeling and computational fluid dynamics simulations to analyze and improve oxygen availability in the AMC bioartificial liver

G. Mareels, P.P.C. Poyck, S. Eloot, R.A.F.M. Chamuleau, and P.R. Verdonck

1 Introduction

Acute liver failure (ALF) is a severe disease with high mortality rates (60-90%). At present, the only efficient therapy is orthotopic liver transplantation (OLT)[234]. To bridge ALF patients to liver transplantation or to regeneration of the native liver, liver support systems are needed. The most promising bridging method for the treatment of ALF patients are bioartificial liver (BAL) support systems. These systems are extracorporeal devices that are generally comprised of a bioreactor in which living hepatocytes are seeded. In a clinical setting, toxic plasma of ALF patients is perfused through a BAL system and detoxified by viable hepatocytes. A major advantage of BAL systems, as compared to other non-biological liver support systems, is the capacity to provide a full range of metabolic functions to compensate for the complex metabolic disorders seen in ALF. Although many BAL systems have demonstrated their detoxifying capacity or liver-specific functions in *in vitro*, *ex vivo* and in phase I clinical studies, no BAL system has shown to significantly improve survival in ALF patients bridged to transplantation in a controlled trial (for review:[122]).

Important issues for the development of an effective BAL system are local plasma flow and oxygen transport. Optimal cell function, i.e. detoxifying capacity, is only obtained when a BAL system is adequately perfused with plasma to enable efficient mass transfer. In this situation, sufficient nutrients (e.g. glucose, fatty acids) and oxygen are supplied, whereas unwanted metabolites (e.g. ammonia) are efficiently detoxified and metabolic end products (e.g. urea, CO₂) subsequently removed. In principle, oxygen (O₂) transfer is the main limitation in the efficiency of a BAL[153], because of the low solubility of oxygen in plasma and high demand for oxygen of functionally active hepatocytes.

The AMC-Bioartificial Liver (AMC-BAL; Academic Medical Center, Amsterdam, The Netherlands, patent No: WO 97/12960) was developed with a special design for on-site oxygenation of hepatocytes and direct contact of plasma to the cells to enhance bidirectional solute exchange. The AMC-BAL has shown promising results in *in vitro* set-ups, small and large animal ALF models, and finally in a phase I clinical study with ALF patients[223,235]. But to increase the efficiency of the AMC-BAL, further optimization of plasma perfusion and oxygenation of hepatocytes may be useful.

Numerical techniques and Computational Fluid Dynamics (CFD) simulations are useful tools to gain insight in local flow field and oxygen transport in hollow fiber BALs[227,230,232] as well as in other types of hepatocyte systems[225,228,236]. These numerical techniques can also be used to determine the optimal working parameters and to further optimize the design of a BAL system. In this respect, we used CFD simulations as a methodological approach to analyze the configuration of the AMC-BAL. We constructed three-dimensional computer models of two representative unit volumes -micro models- of the laboratory-scale AMC-BAL. Fluid flow and oxygen transport and consumption were simulated in these micro models to gain insight in the flow field and local cellular oxygen availability. Numerical parameter studies were performed to assess possible improvements in local oxygen availability of hepatocytes. Several parameters were tested: (1) effect of

the internal oxygenator system, (2) pO_2 of the oxygenation gas, (3) culture medium flow rate, (4) incorporation of an external oxygenator in the extracorporeal circuit, (5) the number of oxygen capillaries, (6) the effect of plasma perfusion versus normal culture medium, and (7) the effect of changes of hepatocyte oxygen consumption characteristics in time. Finally, we discuss the implication of this information for the optimization of the AMC-BAL into a more efficient bioartificial liver.

2 Materials and Methods

The internal geometry of the laboratory-scale AMC-BAL is schematically drawn in Fig. V-1 in a longitudinal and transverse cross-section. The bioreactor is built from a cylindrical polycarbonate housing (Fig. V-1-l) in which two pieces of three-dimensional (3D) non-woven polyester matrix mat (Fig. V-1-e/g) are spirally wound around a massive inner core (Fig. V-1-i). A space between the two mat segments (Fig. V-1-f) is left open for an additional hepatocyte seeding port (not shown). In the hydrophilic matrix, high-density hepatocyte culture is possible. Between the matrix windings, hydrophobic gas capillaries (Fig. V-1-m) are positioned in parallel along the entire bioreactor as an internal oxygenator system to supply additional oxygen to the hepatocytes. Culture gas (95% air, 5% CO_2) is perfused through these capillaries. Plasma enters the bioreactor through an inlet port (Fig. V-1-c) and flows through the inflow zone (Fig. V-1-j) further passes the hydrophilic matrix mat and through the void inter-capillary space (Fig. V-1-n). Plasma exits the bioreactor via the outflow zone (Fig. V-1-k) through the outlet port (Fig. V-1-d). Plasma and culture gas are counter-current flows

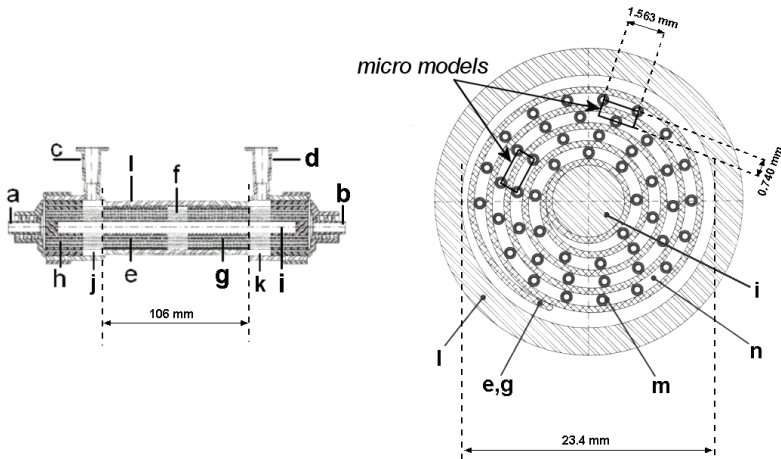


Fig. V-1: Longitudinal (left) and transverse (right) view of the internal geometry of the AMC-BAL with a = gas outlet; b = gas inlet; c = plasma inlet port; d = plasma outlet port; e = first mat segment; f = interspace; g = second mat segment; h = polyurethane potting to separate gas and fluid compartment; i = inner core; j = inflow zone; k = outflow zone; l = polycarbonate housing; m = gas capillaries; n = inter-capillary space through which plasma flows. The inline and triangular micro models are designated.

2.1 Computer model

Since the entire BAL geometry is too large and complex to model, three-dimensional unit volumes -micro models- were isolated from the geometry (Fig. V-1). Each three-dimensional micro model (Fig. V-2) consists of 2 pieces of mat (thickness = 400 μm, height = 1563 μm, length = 50 mm; Fig. V-1-e/g) separated by a void interspace section (length = 6 mm; Fig. V-1-f). At both sides of the mat, gas capillaries (outer diameter = 380 μm) and an inter-capillary space are present. The two micro models differ only in their gas capillaries' position. Either the capillaries are in a rectangular (inline micro model – Fig. V-2) or in a triangular (triangular micro model – Fig. V-2) pattern. These two configurations are the most distinct that could be isolated as the position of the capillaries relative to each other changes continuously along the course of the spiral mat (Fig. V-1). These two micro models were therefore considered to be representative for the entire AMC-BAL. Simulations on both models will allow us to assess the influence of the capillary arrangement.

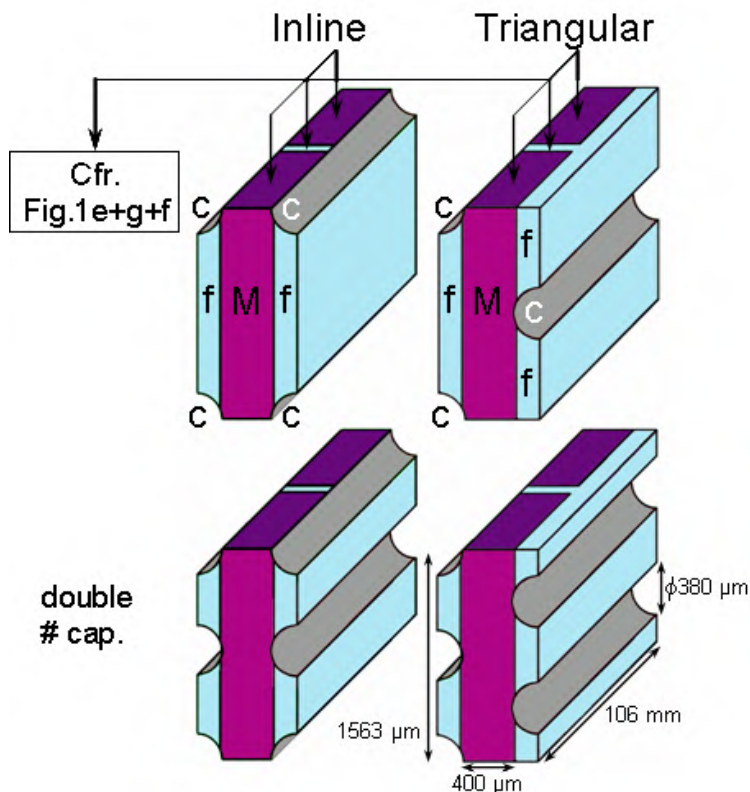


Fig. V-2: AMC-BAL micro models. Upper left: inline micro model; upper right: triangular micro model (*c* = capillary wall, *M* = non-woven matrix mat, *f* = inter-capillary space); lower left: inline micro model with double number of capillaries; lower right: triangular micro model with double number of capillaries.

Both models were created in the modeling software Gambit 2 (Fluent Inc, Sheffield, UK). All dimensions were derived from a laboratory-scale AMC-BAL or were supplied by the manufacturer. The curvature of the mat was neglected and the inflow and outflow zones before and after the mat segments in the AMC-BAL were not included in the micro models. Each standard micro model contains the equivalent capillary wall surface of 1 whole capillary. Since the entire laboratory-scale AMC-BAL contains 300 capillaries, each micro model can thus be considered as 1/300th part of AMC-BAL. Consequently, one AMC-BAL can be regarded as a combination of 300 separate micro models in parallel.

2.2 Modeling fluid flow

2.2.1 Theoretical model

To simulate fluid flow, the commercial CFD package Fluent 6.2 (Fluent Inc, Sheffield, UK) was used to numerically solve the steady-state Navier-Stokes equations. Standard pressure discretization scheme and second order upwind momentum discretization scheme were used. Pressure-velocity coupling scheme was SIMPLE. Fluid properties were set to those of culture medium to allow future validation with *in vitro* experiments. Culture medium was modeled as an incompressible, isothermal, Newtonian fluid composed of 90% water ($\rho = 998 \text{ kg/m}^3$) and 10% serum ($\rho = 1030 \text{ kg/m}^3$) with a resulting density of 1001.2 kg/m^3 . Dynamic viscosity μ of culture medium with 5 g/L bovine serum albumin (BSA) at 37°C was set to 0.691 mPa.s[237]. Plasma viscosity at 37°C was set to 1.3 mPa.s[238].

2.2.2 Resistance to flow of the non-woven polyester mat

The non-woven polyester matrix was modeled as an isotropic homogeneous porous zone. A measure for the viscous resistance of the non-woven polyester matrix used in Fluent 6.2 was determined in an experimental set-up by establishing the pressure drop – flow rate relationship. A sample of this matrix fabric sheet was clamped between two connecting tubes. These tubes were placed in a closed circuit with an overflow reservoir which provided a constant static pressure load over the matrix sample. Pressure difference over the matrix sheet was measured using a calibrated differential pressure transducer (Fuji Electrics FCX, Japan). Flow rate was measured gravimetrically. De-ionized water was used. Static pressure load was set so average velocities in the experiment were in the same order of magnitude as could be expected in the AMC-BAL (1 – 7 mm/s). A viscous resistance factor of $2.7 \pm 0.2 \times 10^{10} \text{ m}^{-2}$ was calculated as an average of ten measurements. Resistance to flow of hepatocyte cell layers (see §2.3.2) was modeled using the same viscous resistance factor.

2.2.3 Boundary conditions

We assumed that total flow rate (15 ml/min) inside the research scale AMC-BAL is homogeneously distributed. In this way, each micro model has the same flow rate of

0.05 ml/min, i.e. 1/300th of the total flow rate. Pressure inlet boundary conditions were used; outlet boundary condition was a zero pressure outflow; the capillary walls were ‘no-slip’ walls and symmetry boundary conditions were used at the side walls of the model.

2.3 Modeling oxygen transport and consumption

2.3.1 Theoretical model

To simulate oxygen transport and consumption, Fluent 6.2 solves the steady-state convection-diffusion-reaction equation (Eq. V-1). Discretization scheme was set to QUICK.

$$\frac{\partial}{\partial x_i}(\rho u_i \phi - \rho D \frac{\partial \phi}{\partial x_i}) = S_\phi \quad \text{Eq. V-1}$$

The transported scalar ϕ is the local oxygen concentration (vol. %), which is also the product of the oxygen solubility α and the local oxygen partial pressure (pO₂) according to Henry’s Law ($\phi = \alpha * pO_2$). Oxygen solubility α is 3.1385 x 10⁻⁵ ml O₂ / mmHg*ml fluid in culture medium and 2.855 x 10⁻⁵ ml O₂ / mmHg*ml fluid in plasma. D is the oxygen diffusion coefficient, which is 2.92 x 10⁻⁹ m²/s in culture medium and 2.18 x 10⁻⁹ m²/s in plasma[239,240,241,242]. Oxygen consumption by the primary porcine hepatocytes in the AMC-BAL was modeled by an additional source term S_φ, which was only implemented in regions that were designated to contain hepatocytes.

$$S_\phi = -\rho V_M \rho_{cell} \frac{\phi}{\phi + \alpha K_M} \quad \text{Eq. V-2}$$

This source term (Eq. V-2) was based on the Michaelis-Menten kinetics of O₂ consumption by hepatocytes. As such, O₂ uptake is dependent on the local hepatocyte density ρ_{cell} and in a non-linear way dependent on the local O₂ availability.

Michaelis-Menten parameters of primary porcine hepatocytes were obtained from Balis *et al.*[243]. Values of culture day 2 were taken as they are characterized by a highly demanding O₂ uptake (V_M = 0.7286 nmole / s*10⁶ cells; K_M = 2 mmHg). These values were measured in 2D culture, whereas hepatocyte culture in the AMC-BAL is three-dimensional and at high density. For this reason, a lower O₂ consumption may be expected as the specific O₂ uptake rate per cell is reported to decrease at increasing cell densities[232]. On the other hand, O₂ consumption may rise significantly when a metabolic load is applied to the cells[244]. As such, the proposed consumption characteristics are justified by assuming these values to represent the most limiting case for oxygen availability. Consequently, attention must be paid when comparing simulation results to other numerical studies[225,228,230].

2.3.2 Hepatocyte distribution in the micro models

In an *in vitro* setting, the laboratory scale AMC-BAL is seeded with 1 billion porcine hepatocytes via three different loading ports, while gently rotating the bioreactor to assure a homogeneous cell distribution. As we assumed that one micro model is one 300th part of an entire laboratory scale AMC-BAL, one micro model contained 3.33 million cells.

Since no detailed information on the internal hepatocyte distribution in the AMC-BAL is available, two cell distributions are hypothesized. In cell distribution 1, all hepatocytes are homogeneously distributed in the non-woven matrix (resulting hepatocyte density ρ_{cell} of 53.7×10^6 cells/ml). In previous macroscopic and microscopic studies of an early prototype AMC-BAL, the majority of the hepatocytes were immobilized within the three-dimensional matrix[245]. However, given the undifferentiated method of hepatocyte seeding, it is possible that hepatocytes also adhere to the surface of gas capillaries. Therefore, in cell distribution 2, 50% of the hepatocytes are located in the matrix ($\rho_{\text{cell}} = 31.7 \times 10^6$ cells/ml) and 50% in a hepatocyte layer around the capillaries. The hepatocyte layer was set to be 122 μm , with a ρ_{cell} of 81.7×10^6 cells/ml. This cell layer thickness is in the range of what is used in other numerical studies[229,230] and is consistent with the size of primary porcine hepatocyte 3D cell clusters found *in vitro* [246]. All proposed cell densities were also considered to be realistic [207,247,248].

The complete AMC-BAL cannot be modeled by using only one cell distribution or only one micro model. Therefore, each cell distribution was applied to both micro models, leading to four basic configurations in total. All four micro model configurations were assessed independently. With a combination of these micro models, the entire AMC-BAL can be modeled in future studies.

2.3.3 O₂ diffusivity constant through non-woven matrix

Free O₂ diffusion through the mat zone is hindered by the non-woven arrangement of hydrophilic polyester fibers, which are considered to be impermeable to O₂. To compensate for this hindered diffusion, a correction factor for the O₂ diffusion coefficient in the mat volume was determined.

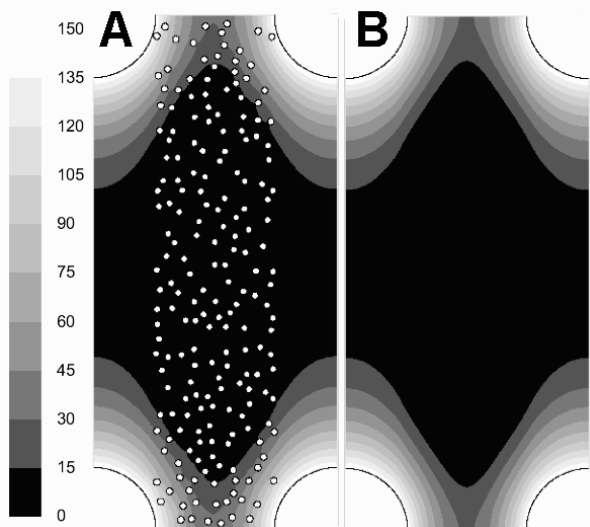


Fig. V-3: Determination of the correction factor for O₂ diffusion through the non-woven polyester mat. A : pO₂ distribution [mmHg] on modified inline micro model (polyester fibers drawn) under standard boundary conditions, no medium flow; B : identical pO₂ distribution [mmHg] obtained with identical simulation settings, but with mat as homogeneous medium with an adjusted diffusion constant (with a factor of 0.85) to account for hindered diffusion.

On a microscopic view of the non-woven matrix, the mat porosity was determined to be 91%. A modified two-dimensional inline micro model was constructed with 250 polyester fiber circles randomly located within the boundaries of the mat volume. On this modified inline micro model, the pO₂ distribution was simulated using hepatocyte distribution 1 (Fig. V-3-A). Standard boundary conditions were used and culture flow rate was zero. O₂ diffusion coefficient in the mat zone of the modified micro model was the same as for free culture medium, since culture medium occupies the void spaces between the polyester fibers. Subsequently, an analogous simulation was performed on a regular inline micro model, i.e. with the mat modeled as homogeneous medium, with an adjusted O₂ diffusion coefficient in the mat zone to match the results of the ‘modified’ model (Fig. V-3-B). A correction factor of 0.85 ($D_{\text{mat}} = 2.48 \times 10^9 \text{ m}^2/\text{s}$) for O₂ diffusion was necessary to take into account the presence of the non-woven polyester matrix mat. This correction factor is in accordance with the equation of Rayleigh (correction factor $\sim \frac{1 - \text{solid fraction}}{1 + \text{solid fraction}} = 0.835$), which has been experimentally verified for various sheets of porous media[249,250,251].

2.3.4 O₂ diffusion constant through zones containing hepatocytes

Oxygen can diffuse through both continuous fluid spaces as well as through hepatocytes. In regions seeded with hepatocytes, the resulting “effective” diffusion coefficient D_{eff} will be lower than in free medium, since O₂ diffuses more slowly

through hepatocytes. The extent to which the diffusivity is reduced will logically depend on the local hepatocyte density. Since experimental data on O_2 diffusion constants through hepatocyte cell layers with different cell densities is not readily available, a theoretical approach was chosen.

Riley *et al.*[252] developed an empirical relation (Eq. V-3) that relates the effective diffusion coefficient D_{eff} to the local free diffusion coefficient D_o , the intracellular diffusion coefficient D_{cell} and the cell volume fraction ϕ . This equation, based on Monte Carlo simulations, shows a good agreement with available data throughout a wide range of cell volume fractions ($0.04 < \phi < 0.95$).

$$\frac{D_{eff}}{D_o} = 1 - \left(1 - \frac{D_{cell}}{D_o}\right)(1.727\phi - 0.8177\phi^2 + 0.09075\phi^3) \quad \text{Eq. V-3}$$

D_{cell} was set to $0.25 \times 10^{-9} \text{ m}^2/\text{s}$, which is an average of intracellular O_2 diffusion constants in hepatocytes reported by Jones *et al.*[253]. Cell volume fraction ϕ is the local volume percentage of space that is occupied by hepatocytes and was calculated as the product of the local hepatocyte cell density and the average hepatocytes cell volume[254]. Local free diffusion coefficient D_o is dependent on the perfusion fluid, e.g. culture medium or plasma, and on the location of hepatocytes in the model; either in the inter-capillary space or in the mat zone. O_2 diffusivities in different regions of both micro models are presented in Table V-1.

Table V-1: O_2 diffusion constants in different zones of the micro models. The ratio of the effective diffusion constant to the free diffusion constant D_{eff}/D_o is calculated from the local free oxygen diffusion constant D_o and the local cell volume fraction ϕ using Eq. V-3. The local effective diffusion coefficients D_{eff} in culture medium and plasma per region are presented in the last column.

Region in the micro model	D_o [$10^{-9} \text{ m}^2/\text{s}$]		ρ_{cell} [10^6 cells/ml]	ϕ	$\frac{D_{eff}}{D_o}$	D_{eff} [$10^{-9} \text{ m}^2/\text{s}$]	
	Cult Med	Plasma				Cult Med	Plasma
No hepatocytes							
Inter-capillary space	2.92	2.18	0	0	1	2.92	2.18
In mat	2.48	1.85	0	0	1	2.48	1.85
Cell distribution 1							
In mat	2.48	1.85	53.7	0.172	0.75	1.87	1.41
Cell distribution 2							
In mat	2.48	1.85	31.7	0.102	0.85	2.11	1.59
In hepatocyte cell layer around capillaries – part in mat zone	2.48	1.85	81.7	0.262	0.64	1.59	1.22
In hepatocyte cell layer around capillaries – part in inter-capillary space	2.92	2.18	81.7	0.262	0.64	1.86	1.41

The obtained local diffusion coefficients are in the range of reported values for hepatocytes and other cell types[236,255,256,257,258].

2.3.5 Boundary conditions

Oxygen partial pressure (pO₂) of incoming culture medium was set to 146.5 mmHg, which was an average of three culture medium pO₂ measurements using an ABL505 blood-gas analyzer (Radiometer Copenhagen). Axial and radial O₂ transport resistances in gas capillaries were neglected, since the culture gas flow rate through the gas capillaries and their O₂ permeability are high[259]. As such, O₂ supply through gas capillaries was modeled by imposing a constant 150 mmHg pO₂ on the capillaries' outer walls, which corresponded to the pO₂ of culture gas used *in vitro* (95% air, 5% CO₂). All other boundary faces have no-flux boundary conditions.

2.4 Grid dependency

In a transverse cross-sectional plane of the mesh, the inter-capillary space counted 4800 face cells and the mat zone 4920 face elements to capture the sharp transverse pO₂ gradients. Longitudinally along the mat segments and along the interspace between the mat segments, 143 and 100 mesh points, respectively, were used with a double sided successive mesh ratio of 1.02 to capture the axial gradients near the start and end of the mat segments and the transition to the interspace. Consequently, one micro model mesh contained approximately 3.75 million finite volume mesh elements. Further increase in the number of cells resulted in identical outcome. Note that this is not the minimal amount of cells necessary to achieve sufficient accuracy. But as grid dependency was not carried out for every simulation case and different gradients may rise within each case, a certain surplus was taken into measure.

2.5 Simulations overview and assessment

As previously stated, four micro model configurations were used: (a) the inline micro model with cell distribution 1, (b) the inline micro model with cell distribution 2, (c) the triangular micro model with cell distribution 1, and finally (d) the triangular micro model with cell distribution 2. Fifteen case studies (Table V-2) were performed on each configuration.

Chapter V

Table V-2: Overview of simulations. Each case is applied to the four basic micro model configurations (inline and triangular micro model each with cell distribution 1 or 2).

Case	Fluid	pO ₂ gas (mmHg)	pO ₂ medium (mmHg)	Q _{medium} (ml/min)	# capillaries	K _M (mmHg)
Reference case						
1. Standard boundary conditions	Culture medium	150	146.5	0.05	1	2
Effect of the internal oxygenator						
2. pO ₂ gas = 0	Culture medium	0	146.5	0.05	1	2
3. pO ₂ gas = 0; pO ₂ medium ×2	Culture medium	0	293	0.05	1	2
Increasing oxygen availability						
4. pO ₂ gas ×2	Culture medium	300	146.5	0.05	1	2
5. pO ₂ gas = carbogen	Culture medium	722	146.5	0.05	1	2
6. pO ₂ medium ×2	Culture medium	150	293	0.05	1	2
7. pO ₂ medium = carbogen	Culture medium	150	722	0.05	1	2
8. Fluid flow rate Q _{medium} ×2	Culture medium	150	146.5	0.10	1	2
9. Fluid flow rate Q _{medium} ×10	Culture medium	150	146.5	0.50	1	2
10. N° capill. ×2	Culture medium	150	146.5	0.05	2	2
11. N° capill. ×2; pO ₂ gas ×2	Culture medium	300	146.5	0.05	2	2
Clinical vs. experimental setting						
12. Plasma	Plasma	150	146.5	0.05	1	2
13. Plasma; pO ₂ gas ×2	Plasma	300	146.5	0.05	1	2
Changes of hepatocyte O₂ consumption in time						
14. K _M day 4	Culture medium	150	146.5	0.05	1	4.75
15. K _M day 5	Culture medium	150	146.5	0.05	1	7.5

The first case study was simulated using standard boundary conditions as described in previous paragraphs. This 'reference case' study (1) is the internal control for all other case studies with the same micro model configuration. The effect of the internal oxygenation system was assessed by disabling culture gas flow (2), and by assessing the effect of an external oxygenator that oxygenates incoming medium to a doubled pO₂ as an alternative for internal oxygenation (3). To increase oxygen availability to the hepatocytes, different strategies were assessed. First, by using a more oxygen rich culture gas, i.e. a doubled pO_{2 gas} (4) or carbogen gas (95% O₂) (5). Secondly, by incorporating an external oxygenator to increase incoming medium pO₂ to a doubled (6) or carbogen (7) level. Thirdly, by changing culture medium flow rate to a doubled (8) or ten-fold (9) flow rate. Finally, by doubling the number of capillaries (10) or by combining the double number of capillaries with a doubled culture gas pO₂ (11). In cases with a doubled number of capillaries, cell density in the hepatocyte layer around the capillaries was kept constant. This led to a cell layer thickness of 68 μm, keeping the number of hepatocytes around all capillaries equal to 50% of total, as was initially proposed. In micro models with double number of capillaries the distance between the capillaries is halved (see Fig. V-2).

In the next case studies, we studied the effect of plasma versus culture medium, since this is the main difference in perfusion in a clinical setting as compared to an experimental setting. Standard boundary conditions (12) and a doubled pO_{2 gas} (13) were used and compared with cases (1) and (4). Finally, time-related changes in oxygen consumption characteristics of hepatocytes were investigated by varying K_M values. K_M values of culture day 4 (14) and 5 (15) were compared to the reference case (1). According to Balis *et al.*[243], K_M values change remarkably throughout the first five days, whereas V_M values remain constant. We therefore kept V_M constant in these simulations.

The proposed simulation cases on the four different micro model configurations were assessed by examining pO₂ distributions. However, not every simulated pO₂ profile can be shown due to brevity reasons. To evaluate the effect of the parameters discussed in the parameter study, the local *effective hepatocyte utilization ratio* V_{ratio} (Eq. V-4) was studied[232].

$$V_{ratio} = \frac{\phi}{\phi + \alpha K_M} \quad \text{Eq. V-4}$$

V_{ratio} is the ratio of the observed oxygen consumption rate to the maximal hepatocyte oxygen consumption rate, i.e. V_M, and ranges between 0 and 1 (asymptotically). A threshold for V_{ratio} of 0.9 was chosen as introduced by Patzer *et al.*[232] and corresponds with a minimal pO₂ level of 18 mmHg when K_M = 2 mmHg. Consequently, oxygen availability in the AMC-BAL was quantified by determining the percentage of hepatocytes with V_{ratio} > 0.9.

3 Results

3.1 Fluid flow and shear stress distribution

Fig. V-4 represents an example of colorimetric contour plots of fluid flow and shear stress distributions in two different micro models with different hepatocyte distributions. In the upper part, velocity magnitudes (m/s, left legend) in a transverse plane midway through the first mat segment are shown for the reference case (case 1) of an inline micro model with hepatocyte distribution 1 (Fig. V-4-A1) and for a triangular micro model with hepatocyte distribution 2 and with a double number of capillaries (case 10-11) (Fig. V-4-B1). The contour plots can be mirrored with respect to the horizontal axis as micro models are symmetrical.

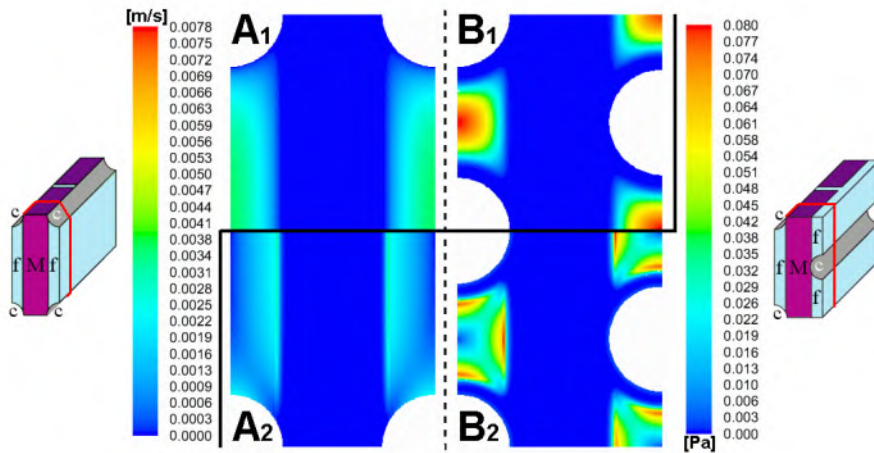


Fig. V-4: Colorimetric contour plot of velocity magnitudes (m/s, left legend, upper part 1) and shear stress levels (Pa, right legend, lower part 2) in a transverse plane midway through the first mat segment, in the reference case (case 1) of an inline micro model with hepatocyte distribution 1 (A1 and A2 resp.) and in a triangular micro model with hepatocyte distribution 2 and with double number of capillaries (case 10-11) (B1 and B2 resp.).

Fluid flows in the non-woven matrix mat zone and in the hepatocyte cell layers were orientated axially and are uniform in size (approx. $8 \mu\text{m/s}$ in Fig. V-4-A1 and $37 \mu\text{m/s}$ in Fig. V-4-B1). In the inter-capillary space, flow velocities have a poiseuille-like (parabolic) profile with maximal velocities of approx. 3.6 mm/s in Fig. V-4-A1 and 7.8 mm/s in Fig. V-4-B1. In the interspace between two mat segments, flow lines expand radially due to the sudden increase in local cross-sectional area. However, these flow lines re-converge when entering the second mat segment, where the velocity profile was identical compared to the first mat segment (not shown). Static pressure drop over the entire micro model was 15.7 Pa in the reference case of the inline micro model with hepatocyte distribution 1 (Fig. V-4-A) and 69.3 Pa for the triangular micro model with hepatocyte distribution 2 and double number of capillaries (Fig. V-4-B). The lower parts of Fig. V-4 (A2 and B2) show corresponding

shear stress distributions (Pa, right legend). Maximal shear stresses were generally located near the mat side surfaces and also –in case of cell distribution 2– at the boundary between the hepatocyte cell layer and inter-capillary space.

In Table V-3, an overview is given of maximum velocity magnitudes in the inter-capillary space, uniform velocity magnitudes in the mat/hepatocyte layer zone, as well as static pressure losses over the entire micro model and maximal local shear stresses for all simulation cases.

Table V-3: Overview of the maximum velocity in the inter-capillary space, the uniform velocity in the mat/hepatocyte layer zone, the static pressure loss over the entire model and the maximal shear stress for all simulation cases and for different hepatocyte distributions. Values for the inline and triangular micro model are identical.

Cases	Hepatocyte distr. 1	Hepatocyte distr. 2
<i>Velocity in mat/hepatocyte cell layer (mm/s) – Maximum velocity in inter-capillary space (mm/s)</i>		
1,2,3,4,5,6,7,14,15.) Standard flow rate	0.0085 – 3.59	0.011 – 4.60
8.) Q _{medium} ×2	0.017 – 7.17	0.022 – 9.20
9.) Q _{medium} ×10	0.084 – 35.7	0.11 – 45.0
10,11.) N° capillaries ×2	0.0195 – 5.69	0.037 – 7.75
12,13.) Plasma	0.0085 – 3.59	0.011 – 4.60
<i>Static pressure loss over micro model (Pa)</i>		
1,2,3,4,5,6,7,14,15.) Standard flow rate	15.7	20.6
8.) Q _{medium} ×2	31.4	41.1
9.) Q _{medium} ×10	155.7	203.3
10,11.) N° capillaries ×2	36.1	69.3
12,13.) Plasma	30.0	39.3
<i>Maximum shear stress (Pa)</i>		
1,2,3,4,5,6,7,14,15.) Standard flow rate	0.032	0.041
8.) Q _{medium} ×2	0.064	0.083
9.) Q _{medium} ×10	0.31	0.40
10,11.) N° capillaries ×2	0.056	0.083
12,13.) Plasma	0.057	0.073

Maximum velocities in the inter-capillary space ranged between 3.6 and 45 mm/s, whereas uniform velocities in the mat/hepatocyte layer ranged between 8 and 110 μm/s. Simulation results showed that velocities in the mat zone and in hepatocyte layers were consistently two orders of magnitude smaller than in the inter-capillary space. Velocity profiles and shear stress profiles were similar for the different simulation cases, but differed in magnitude between cases when flow rate was altered or when the internal geometry had been changed, e.g. due to additional gas capillaries

and/or hepatocyte layers around the capillaries. Static pressure loss over the entire micro model and local shear stress levels were additionally influenced by the type of fluid, e.g. plasma or culture medium. Static pressure loss over the entire micro model ranged from approx. 16 to 203 Pa. Maximum shear stress ranged between approx. 0.03 and 0.40 Pa. Largest maximum values were reached in hepatocyte distribution 2 with a 10-fold flow rate.

Importantly, both the inline and triangular micro model had the same flow field, static pressure loss and shear stress distributions within a simulation case with certain boundary conditions and hepatocyte distribution (comparison not shown).

3.2 Oxygen transport and consumption

Results of oxygen transport and consumption simulations are presented by means of two contour plots of pO_2 and V_{ratio} distributions (Fig. V-5). Also, Table V-4 presents detailed information for each simulated case and micro model configuration on the percentage of hepatocytes that consume oxygen at a minimal V_{ratio} level of 0.9.

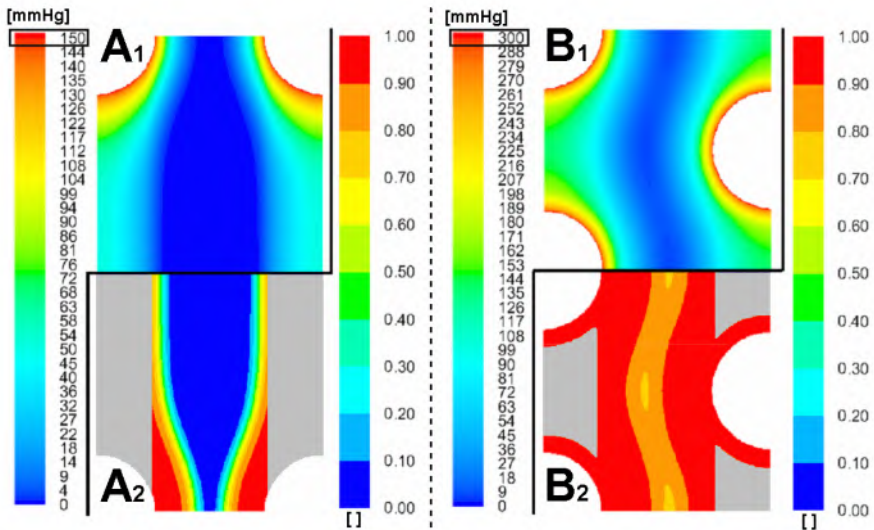


Fig. V-5: Colorimetric contour plot of pO_2 (mmHg, left legend, upper part 1) and effective hepatocyte utilization ratio V_{ratio} (dimensionless, right legend, lower part 2) in a transverse plane midway through the first mat segment, in the reference case (case 1) of an inline micro model with hepatocyte distribution 1 (A1 and A2 resp.) and in a triangular micro model with hepatocyte distribution 2 and with double number of capillaries and doubled culture gas pO_2 (case 11) (B1 and B2 resp.). (Note: Fig. 5-B1 different scale compared to Fig. 5-A1) Grey depicts fluid zones where V_{ratio} has no physical meaning.

Table V-4: Percentages of total hepatocyte cell amount that attain a $V_{ratio} > 0.9$. In the case of hepatocyte distribution 2, distinction is made between the percentage of the total number of hepatocytes in the mat and the percentage of total number of hepatocytes in the cell layers around the capillaries.

% Hepatocytes with $V_{ratio} > 0.9$					
Case	Hepatocyte distribution 1		Hepatocyte distribution 2		
	INLINE	TRIANGULAR	INLINE		TRIANGULAR
			<i>Mat</i>	<i>Capill.</i>	<i>Mat</i> <i>Capill.</i>
Reference case					
1.) Standard boundary conditions	15.7%	15.8%	28.8%		28.6%
			3.3%	54.1%	3.3% 53.5%
The effect of the internal oxygenator					
2.) $pO_{2\text{ gas}} = 0$	1.7%	1.7%	1.7%		1.7%
			3.1%	0.4%	3.1% 0.4%
3.) $pO_{2\text{ gas}} = 0$; $pO_{2\text{ medium}} \times 2$	6.2%	6.2%	6.3%		5.9%
			11.0%	1.7%	10.3% 1.7%
Increasing oxygen availability					
4.) $pO_{2\text{ gas}} \times 2$	30.4%	30.2%	50.3%		50.3%
			5.1%	95.1%	5.0% 94.9%
5.) $pO_{2\text{ gas}} = \text{carbogen}$	62.4%	64.5%	80.7%		88.3%
			61.2%	100%	76.3% 100%
6.) $pO_{2\text{ medium}} \times 2$	20.1%	20.2%	34.5%		33.9%
			11.8%	57.0%	11.0% 56.5%
7.) $pO_{2\text{ medium}} = \text{carbogen}$	35.5%	35.1%	54.2%		53.4%
			40.6%	67.7%	37.5% 69.1%
8.) $Q_{\text{medium}} \times 2$	17.9%	18.1%	31.6%		31.4%
			6.6%	56.4%	6.5% 56.0%
9.) $Q_{\text{medium}} \times 10$	28.4%	28.6%	45.7%		45.6%
			22.2%	68.9%	22.1% 68.9%
10.) N° capillaries $\times 2$	31.8%	31.8%	56.7%		56.8%
			14.1%	100%	14.3% 100%
11.) N° capillaries $\times 2$; $pO_{2\text{ gas}} \times 2$	61.0%	59.9%	87.5%		84.8%
			75.3%	100%	69.9% 100%
Clinical vs. experimental setting					
12.) Plasma	12.0%	12.0%	22.9%		23.0%
			2.6%	43.0%	2.6% 43.0%
13.) Plasma; $pO_{2\text{ gas}} \times 2$	22.8%	22.9%	40.8%		40.9%
			2.9%	78.4%	2.9% 78.3%

Changes in hepatocyte O₂ consumption in time					
14.) Km day 4	8.7%	8.7%	18.9%	18.9%	
			1.1%	36.4%	1.1%
			12.9%	13.0%	
15.) Km day 5	5.0%	5.1%	0.3%	25.3%	0.3%
					25.5%

3.2.1 Reference case simulations (case 1)

Fig. V-5-A1 illustrates the pO₂ distribution in a transverse plane midway through the first mat segment in the reference case (case 1) for the inline micro model with hepatocyte distribution 1. Highest pO₂ (150 mmHg) was found close to the capillary wall. A large pO₂ gradient extended radially from the capillary and was steeper at the side of the capillary in the mat zone. At a radial distance of 86 μm from the capillary, pO₂ in the mat zone dropped already below 20 mmHg. A region where oxygen was depleted (0 mmHg) is present in the centre of the hepatocyte-seeded mat throughout both mat zones. Analogous pO₂ distributions were found in cross-sections of the micro model further downstream to the plane of Fig. V-5-A1, but with overall decreasing average oxygen level. Oxygen content of the perfused culture medium in the inter-capillary space dropped from its initial value of 146.5 mmHg to approx. 60 mmHg midway the first mat segment and further decreased downstream to 28 mmHg at the end of the first mat segment. At the start of the second mat segment, culture medium pO₂ in the inter-capillary space was increased to 40 mmHg and again decreased to 22 mmHg at the end of the mat segment.

As a standard for cellular oxygen availability, the effective hepatocyte utilization ratio V_{ratio} was calculated (Fig. V-5-A2). Complying with pO₂ distribution, hepatocytes in the centre of the mat zone cannot consume oxygen at all ($V_{ratio} \sim 0$), whereas hepatocytes closest to the capillaries have enough oxygen available to consume oxygen at near maximum capacity ($V_{ratio} \sim 1$). Approximately 16% of all hepatocytes in the model consumed oxygen with $V_{ratio} > 0.9$ (Table V-4). A change to hepatocyte distribution 2 was characterized by a larger radial pO₂ gradient around the capillaries and a more extended zone of zero oxygen content in the mat segments. Due to the additional presence of a dense hepatocyte layer around the capillary, pO₂ dropped below 20 mmHg from a radial distance of 65 μm from a capillary (compare to 86 μm in hepatocyte distribution 1). Nevertheless, 29% of all hepatocytes attained a V_{ratio} of more than 0.9. Fifty four percent of the hepatocytes in cell layers around the capillaries reached the threshold of $V_{ratio} > 0.9$, whereas 3% of the hepatocytes in the mat zone.

PO₂ and V_{ratio} distributions for the reference case of the other three micro model configurations are not shown for brevity reasons.

Simulation results also showed that inline and triangular micro models, using the same hepatocyte distribution, showed qualitative and quantitative identical pO₂ distributions.

3.2.2 The effect of the internal oxygenator (case 2,3)

Disabling culture gas flow ($\sim pO_{2\text{ gas}} = 0$ – case 2) led to a reduction of cells with $V_{\text{ratio}} > 0.9$ to approximately 2% for all micro model configurations. Replacing the internal oxygenator by an external oxygenator, which doubles culture medium pO_2 (case 3), led to a “ $V_{\text{ratio}} > 0.9$ ” fraction of approx. 6% for all micro model configurations. More specifically, in cell distribution 2, this was true for only 1% and 2% of the hepatocytes around the capillaries, and for 3% and 11% of the hepatocytes in the mat zone, for case 2 and 3 respectively.

3.2.3 Increasing oxygen availability (case 4-11)

Doubling culture gas pO_2 (case 4) almost doubled “ $V_{\text{ratio}} > 0.9$ ” percentages (Table V-4) from approximately 16% to 30% in micro models with hepatocyte distribution 1; an increase of 93%. A 75% increase (29% to 50%) was obtained in micro models with cell distribution 2. This increase mainly occurred in the hepatocyte layer around capillaries, i.e. 55% in case 1 to 95% in case 4. A further $pO_{2\text{ gas}}$ increase to carbogen level (case 5) led to an approximate quadruple and triple “ $V_{\text{ratio}} > 0.9$ ” fraction compared to the reference case for distribution 1 and 2, respectively. In the latter, hepatocytes in both the mat zone as well as in the cell layers have increased threshold percentages. Furthermore, about 7% more hepatocytes attained the threshold in the triangular capillary arrangement compared to inline when using hepatocyte distribution 2. In distribution 1, inline and triangular configurations rendered quasi-identical results.

Doubling culture medium pO_2 (case 6) led to a 28% and 20% increase in V_{ratio} percentages for cell distribution 1 and 2, respectively. In the latter, the relative increase was higher in the mat zone as compared to the hepatocyte layers. Further increase of $pO_{2\text{ medium}}$ to carbogen level (case 7) led to a 125% and 88% increase in “ $V_{\text{ratio}} > 0.9$ ” percentages compared to the reference case for distribution 1 and 2 respectively. Inline and triangular models rendered identical results under the same hepatocyte distribution.

Doubling culture medium flow rate (case 8) resulted in a 14% and 10% increase in “ $V_{\text{ratio}} > 0.9$ ” fraction for distribution 1 and 2, respectively. Further increase of culture medium flow rate up to a 10-fold (case 9) resulted in an 81% and 59% increase for distribution 1 and 2, respectively. Typically in cases with increased flow rate in cell distribution 2, V_{ratio} percentages in the mat zone changed remarkably, whereas in the hepatocyte layers there was only a minor increase. Again, inline and triangular models rendered identical results under the same hepatocyte distribution.

A 2-fold increase in the number of capillaries (case 10) resulted in a doubled percentage of cells that attain the $V_{\text{ratio}} > 0.9$ threshold in cell distribution 1 (+102%) and 2 (+98%). In the latter, this increase occurred in the mat zone as well as in the cell layer around the capillaries. The combination of a double number of gas capillaries and a doubled $pO_{2\text{ gas}}$ (case 11) increased the threshold percentages to almost quadruple (+280%) for cell distribution 1 and triple (+200%) for cell distribution 2. Again, only minor differences existed between inline and triangular micro models.

Fig. V-5-B1 shows the pO_2 distribution in a transverse plane midway through the first mat segment in the triangular micro model with cell distribution 2 (case 11). In this case, highest pO_2 levels (~ 300 mmHg) were only found close to the capillary walls. A very steep radial gradient was noted in the hepatocyte cell layer around the capillaries. PO_2 in the centre of the mat zone was 7 mmHg. As in the reference case, pO_2 distributions of cross-sections further downstream showed analogous results as compared to Fig. V-5-A1, but with overall decreasing average oxygen level. The distribution of V_{ratio} corresponding to the pO_2 distribution of case 11 is depicted in Fig. V-5-B2. The entire hepatocyte layer (100%) around the capillaries and large parts of the mat zone (70%) had a V_{ratio} of at least 0.9. Consequently in case 11, 85% of all hepatocytes had a V_{ratio} higher than 0.9 (Table V-4).

3.2.4 Clinical vs. experimental setting (case 12,13)

Changing fluid properties from culture medium to plasma resulted in a 24% decrease in $V_{ratio} > 0.9$ percentages in micro models with cell distribution 1 and a 20% decrease in cell distribution 2 (case 12). Doubling $pO_{2\text{ gas}}$ in the clinical setting (case 13) showed a relative rise of 91% and 78% compared to the clinical reference case (case 12) in cell distribution 1 and 2, respectively. Compared to the analogue case in *in vitro* settings (case 4), the change of fluid properties also corresponds with a respective 25% and 19% decrease of the “ $V_{ratio} > 0.9$ ” fraction.

3.2.5 Changes in hepatocyte O_2 consumption in time (case 14,15)

Changing K_M values to the situation on day 4 (case 14) or 5 (case 15) causes slight increases in absolute pO_2 level. Also, pO_2 gradients are less steep and the oxygen depleted zone in the centre of the matrix is slightly smaller (not shown). However, “ $V_{ratio} > 0.9$ ” fractions decreased 45% and 68% for cell distribution 1 and 34% and 55% for distribution 2 compared to day 2 (case 1) for day 4 and 5, respectively.

4 Discussion

4.1 Fluid flow and shear stress distribution

Perfusion of a micro model was largely influenced by the presence of the non-woven mat. Although the cross-sectional area of the inter-capillary space and the non-woven mat are roughly the same size, fluid flow in the mat zone was generally two orders of magnitude smaller as compared to the flow in the inter-capillary space. This effect is caused by the higher resistance to flow of the non-woven mat, forcing the majority of fluid flow through the inter-capillary spaces which have a negligible flow resistance. This also causes the overall pressure loss to be minimal. Since the same hydraulic permeability is used for the hepatocyte layers, fluid velocities there are also in the range of micrometer per second. Consequently, apart from the incorporation of additional gas capillaries (case 10-11), also the presence of hepatocyte layers around the capillaries (cell distribution 2) increased flow velocities and pressure loss in the model as the free cross-sectional area of the inter-capillary space is reduced. Fluid flow simulations for the inline and triangular variant of the different case studies render identical results for velocity profiles, pressure loss and shear stress distributions. This was expected as the micro models consist of the identical geometrical entities, which are only changed in location relative to each other. From a fluid dynamical point of view, we conclude that the change in capillary arrangement along the course of the spiral mat in the AMC-BAL does not influence fluid flow, pressure drop or shear stress distribution.

The static pressure loss over one micro model can be regarded as the total pressure drop over the entire AMC-BAL without the inflow and outflow zone (fig. 1-e/f/g), since the AMC-BAL can be represented by 300 micro models in parallel. This pressure drop, i.e. max. 200 Pa ~ 1.5 mmHg, is negligible when compared to the pressure losses in the extracorporeal circuit. These low pressure gradients are in accordance with the *in vivo* situation in the liver lobule, in which pressure drops of approximately 3 mmHg over the sinusoids are normal[260,261]. This is considered advantageous for cell culture inside the AMC-BAL.

Shear stress was also assessed as it is a possible determinant of cellular damage and reduced metabolic function. Shear stress is directly proportional to the local velocity gradient and the fluid viscosity. Consequently, shear stresses are generally more elevated in cases with higher velocity magnitudes in the inter-capillary space (e.g. in case of increased flow rate, doubled number of capillaries, cell distribution 2) and where fluid viscosity is increased (e.g. when plasma was used instead of culture medium - 'clinical setting' - case 12-13). Results show that only hepatocytes located at the side of the mat and at the border of the hepatocyte layers with the inter-capillary space are subjected to a certain level of shear stress.

In vivo values of hepatocyte wall shear stress are difficult to obtain, and comparison is therefore difficult. In human, liver sinusoid wall shear stress τ can be calculated as $\tau = \frac{\Delta p \cdot D}{4L} \sim 1$ Pa (with static pressure drop $\Delta p \sim 3$ mmHg; sinusoid diameter $D \sim 9$ μm ; length $L \sim 1$ mm[260,261]; and considering laminar flow and a cylindrical shape of the sinusoid). In mice sinusoids, shear stress was calculated to be 0.55

Pa[227,262]. However, *in vivo*, hepatocytes are not directly subjected to this shear stress as they are shielded by the sinusoid endothelial lining. As a result, the maximal tolerable level of shear stress is lower than 1 Pa. Tilles *et al.*[157] showed in *in vitro* studies on rat hepatocytes that hepatocyte function, measured as albumin and urea synthesis rates, was significantly decreased (resp. 2.6- and 1.9-fold) when hepatocytes were directly exposed to shear stresses higher than 0.5 Pa compared to low shear stresses (< 0.033 Pa). Under standard conditions, maximum shear stress values in the AMC-BAL do not exceed 0.04 Pa. Additionally, the majority of the hepatocytes are not subjected to significant shear stresses. Small zones with increased shear stress exist but maximal values are considered to be acceptable and not detrimental for the viability and function of hepatocytes. However, shear stresses may increase up to 0.4 Pa when flow rate is increased 10-fold (case 9). Moreover, should plasma be used in this case, instead of culture medium, maximal shear stress values may then reach up to 0.71 Pa (not simulated; obtained by data extrapolation), which is in the critical range (> 0.5 Pa[157]). Additionally, very high flow rates, e.g. 10-times the normal culture flow rates, may cause detachment of hepatocytes and therefore should not be used in spite of any possible increase in local O_2 availability. Subsequently, case 9 (culture medium flow rate $\times 10$) can already be discarded in the search for optimal O_2 availability, based on fluid dynamical grounds.

4.2 Oxygen transport and consumption

We assessed the oxygen availability in different case studies and in different micro model configurations. In this paragraph, the results are discussed per case.

4.2.1 Reference case simulations (case 1)

Highest oxygen concentrations in the mat zone are located near the gas capillaries and near the border of the mat and the inter-capillary space. In zones with limited flow velocities, cellular oxygen supply is clearly dependent on diffusion, which causes large radial pO_2 gradients. On the other hand, diffusive O_2 transport from the culture medium towards the hepatocytes also causes an axial gradient in culture medium oxygen content. As a consequence, culture medium only oxygenates the mat near the very start of the first mat segment and near the side of the mat. The depth of O_2 penetration into the mat decreases rapidly further downstream, since as the majority of oxygen content in the convective flow is already consumed in the first part of the micro model. Nevertheless, oxygen level in the culture medium is not totally depleted at the end of the micro model as the fluid transit time is not sufficiently long for all oxygen to diffuse to the hepatocytes.

In contrast, the O_2 concentration in the gas capillaries remains constant along the micro model axis, so the zone around the capillaries which oxygenated has a constant radius throughout the entire micro model. This pattern of oxygenation leads to about 80% higher V_{ratio} percentages in hepatocyte distribution 2 as compared to 1, since more hepatocytes are close to the gas capillaries in cell distribution 2. So despite steeper pO_2 gradients near the gas capillaries and consequently a larger zone of depleted oxygen in the mat zone in case of hepatocyte distribution 2, this cell

distribution leads to significantly higher V_{ratio} percentages. However, this effect is related to the maximal oxygen diffusion distance which is limited by the Michaelis-Menten oxygen consumption parameters, local hepatocyte density and local diffusion coefficient in general and by the specific local gas capillary and culture medium $p\text{O}_2$ in this reference case.

Since regions which are oxygenated by one gas capillary in particular do not overlap or influence each other in the reference case simulations, diffusive oxygen supply by the capillaries is independent of relative capillary location. Convective oxygen transport is also identical as flow distribution is irrespective of capillary placement (see §4.1). Consequently, inline and triangular capillary pattern give identical results concerning oxygen transport and consumption in these reference cases within when the same hepatocyte distribution is used, as is confirmed by simulation results.

Concerning oxygen transport, we can conclude that the oxygen supply in the AMC-BAL is not fully adequate to provide all hepatocytes with sufficient oxygen to maintain O₂ consumption at minimally 90% of the maximal uptake rate ($V_{\text{ratio}} > 0.9$). Given that the AMC-BAL can be modeled as a combination of micro model configurations, 16-28% of the hepatocytes in the AMC-BAL are adequately oxygenated. In other words, between 72% and 84% of the hepatocytes are subjected to a $p\text{O}_2$ of less than 18 mmHg under the current conditions. Normal physiological $p\text{O}_2$ values in the liver sinusoids are between 70 mmHg in the periportal area and 20 mmHg in the pericentral area[263]. But it is difficult to determine the effect on viability and function of hepatocytes below this threshold. Studies indicate that hepatocyte respiration becomes impaired below 1 – 2 mmHg $p\text{O}_2$ [264]. With respect to these values, further investigation of simulation results showed that under current conditions 67% and 52% of the hepatocytes in cell distribution 1 and 2 have a $p\text{O}_2$ below 2 mmHg and will suffer from hypoxia. The remaining 17 to 20% of the hepatocytes are likely to be characterized by shifts to more anaerobic metabolic processes[265]. However, it should be noted that the low “ $V_{\text{ratio}} > 0.9$ ” percentages are largely influenced by the very stringent hepatocyte oxygen consumption ratios used in this numerical model. Also, hepatocytes which are subjected to low oxygen levels for a prolonged period of time might show changes in oxygen consumption characteristics (V_M , K_M) to compensate for the lack of oxygen. This could account for higher oxygen availability *in vitro*. The use of different (V_M , K_M)-values throughout the model to address this behaviour can be implemented in future work. Nevertheless, further increase in O₂ availability may prove useful to increase the cell viability and subsequently the efficiency of the AMC-BAL.

4.2.2 The effect of the internal oxygenator (case 2,3)

Disabling the internal oxygenator leads to detrimental results and reduces the percentage of adequately oxygenated hepatocytes to virtually zero. This confirms the importance of the internal oxygenator and illustrates the small contribution of the incoming convective oxygen flux by culture medium. Incoming culture medium flow adds only 0.17 nmole O₂ per second to the micro model, while maximal oxygen uptake V_M equals 0.7286 nmole / s*10⁶ cells. As such, theoretically no more than 0.2 x 10⁶ cells, i.e. 6% of the total amount of hepatocytes per micro model, would be able

to consume at maximal uptake rate. In reality, only 1.7% of the hepatocytes can consume at a $V_{\text{ratio}} > 0.9$ due to the presence of $p\text{O}_2$ gradients. Replacing the internal oxygenator by an external oxygenator, which doubles the flow $p\text{O}_2$ and thus the convective oxygen flux, will only increase the “ $V_{\text{ratio}} > 0.9$ ” percentage to about 6%. Since this is still considerably less than in the reference cases, external oxygenation – even at elevated $p\text{O}_2$ levels– is a not suitable replacement for the internal oxygenation system as the gas capillaries constitute the main oxygen supply. As such, the internal oxygenator is an essential part of the AMC-BAL.

4.2.3 Increasing oxygen availability (case 4-11)

In the reference case models, merely 16% to 28% of the hepatocytes are adequately supplied with oxygen to consume at a $V_{\text{ratio}} > 0.9$, depending on hepatocyte distribution. We therefore assessed several strategies to increase overall oxygen availability.

Culture medium flow rate (case 8,9) does not have a considerable effect on cellular oxygen availability. A two-fold increase in flow rate resulted in an increase in regions with $V_{\text{ratio}} > 0.9$ of only 14%. This was expected as the convective oxygen supply is only a minor contributor to the overall oxygen supply. Consequently, doubling the medium $p\text{O}_2$ (case 6) does not greatly increase the amount of regions with sufficient oxygen either. As already discussed, changes in culture medium properties are reflected in a small increase of regions with V_{ratio} in the mat zone, and more specifically in the first mat segment as oxygen content of the fluid is rapidly decreased downstream. It is interesting to note that doubling the flow rate and doubling the medium $p\text{O}_2$ both supply exactly the same amount of oxygen to the micro model: in the latter, oxygen is supplied at increased $p\text{O}_2$, whereas in the former oxygen is supplied at standard level but with a higher flow rate. Nevertheless, doubling $p\text{O}_2$ medium is preferred compared to increasing flow rate when aiming at a better effective hepatocyte utilization ratio since the doubled flow rate does not give the oxygen enough time to diffuse to the hepatocytes as the residence time before oxygen exits the micro model is cut in half. However, a disadvantage of increasing $p\text{O}_2$ in the medium is the requirement of an external oxygenator, which makes the extracorporeal circuit more complex and costly and increases the extracorporeal plasma volume in a clinical setting.

Doubling the $p\text{O}_2$ of the oxygenation gas (case 4) is much easier to achieve in practice. Importantly, the “ $V_{\text{ratio}} > 0.9$ ” percentage increases significantly to almost a doubled level as compared to the reference case. In comparison, culture medium flow rate has to be increased more than 10-fold (case 9) to achieve similar results as with a 2-fold increase in $p\text{O}_2$ of the oxygenation gas. This illustrates how oxygen supply is only minor dependent on fluid flow rate. However, saturation of “ $V_{\text{ratio}} > 0.9$ ” percentages with increased flow rate is not yet achieved at 10-fold flow rate. Nevertheless, a 10-fold flow rate is not preferred because of possible detachment of the hepatocytes and an increased risk of possible shear stress damage to the hepatocytes.

The effective hepatocyte utilization ratio can even be further improved. Culture medium $p\text{O}_2$ can be set to carbogen level (case 7) or the number of capillaries

can be doubled (case 10). On average and for both hepatocyte distributions, these two methods lead to a 2-fold increase in the amount of hepatocytes consuming oxygen at $V_{\text{ratio}} > 0.9$ as compared to the reference case. When both approaches are compared for hepatocyte distribution 1, the results are slightly better when using the carbogen medium pO₂. But for hepatocyte distribution 2, the double number of capillaries leads to better results. An increase in the number of capillaries is preferred over carbogen medium perfusion, since carbogen medium perfusion leads to extremely high and possible toxic[266] pO₂ values of almost 720 mmHg. Carbogen medium perfusion also requires an additional external oxygenator. Therefore, increasing the number of capillaries by two-fold is a more easy and safe method to increase the effective hepatocyte utilization ratio.

The results obtained with double capillary numbers are also better when compared to the doubling of the oxygenation gas pO₂. In cell distribution 2, this is mainly caused by the redistribution of the hepatocytes located around the capillaries. By increasing the number of capillaries, the hepatocyte layer thickness decreased (§2.3). As a consequence, the region that a gas capillary can sufficiently oxygenate now spans the entire hepatocyte layer so 100% of the cell layer (Table V-4) is sufficiently oxygenated. In cell distribution 1, the total region with $V_{\text{ratio}} > 0.9$ has also increased by two, as each additional capillary supplies an additional (constant) volume of hepatocytes with $V_{\text{ratio}} > 0.9$. In contrast, doubling the oxygenation gas pO₂ increases the region surrounding a single capillary with $V_{\text{ratio}} > 0.9$ with a factor of less than two.

The ultimate results in improving cellular oxygen availability and effective hepatocyte utilization ratio are found when oxygenation gas is set to carbogen level (case 5) or when a double number of capillaries is used in combination with a doubled oxygenation gas pO₂ (case 11). $V_{\text{ratio}} > 0.9$ percentages have quadrupled for cell distribution 1 and tripled for cell distribution 2 as compared to the reference case for both approaches.

Simulation results show that in case 11, the respective gains in $V_{\text{ratio}} > 0.9$ regions are cumulated when the case of a double number of capillaries and a doubled pO_{2 gas} are combined. It can also be noted that there is a small but significant difference between the inline and triangular capillary pattern in case 5. When carbogen oxygenation gas is used, the region with $V_{\text{ratio}} > 0.9$ surrounding a capillary has grown to such an extent that it could overlap with the region of surrounding capillaries. If a capillary is present straight opposed to another (inline pattern), this overlap is present. Consequently, the intersection of the two regions only contributes once to the amount of region with $V_{\text{ratio}} > 0.9$. In contrast, when capillaries are in a triangular pattern, the region surrounding the capillary can extend to its fullest, thus increasing the percentage $V_{\text{ratio}} > 0.9$ more compared to the inline micro model. This effect is more pronounced in the cell distribution 2 compared to distribution 1.

Given the possible toxicity of the hyperoxic oxygen levels when carbogen oxygenation gas is used (case 5), the preferred method to optimally and maximally increase oxygen availability in the AMC-BAL is to double the number of gas capillaries together with a 2-fold increase in culture gas pO₂. We note, however, that the calculated improvements in O₂ availability and $V_{\text{ratio}} > 0.9$ percentages do not necessarily translate into identical increases in cell viability or functional activity.

Nevertheless, similar trends between simulation results and the *in vitro* situation are expected, but have to be validated.

4.2.4 Clinical vs. experimental setting (case 12,13)

An important 20 to 25% decrease in the amount of hepatocytes with $V_{\text{ratio}} > 0.9$ is caused by the lower diffusion coefficient (-9%) and oxygen solubility (-25%) in plasma as compared to culture medium. As in reference case 1, results are independent of capillary pattern and are higher in cell distribution 2 as compared to cell distribution 1. Doubling the oxygenation gas pO_2 in the clinical setting leads to approximately the same relative increase in V_{ratio} percentages as it does in the experimental setting. As such, we conclude that any relative increase in oxygen availability found in the experimental setting by any possible strategy can also be applied to the clinical setting, taking into account that the absolute $V_{\text{ratio}} > 0.9$ fractions are decreased with a constant percentage depending on hepatocyte distribution.

4.2.5 Changes in hepatocyte O_2 consumption in time (case 14,15)

Higher K_M values of day 4 and 5 cause the decrease in oxygen consumption to start at higher oxygen levels compared to lower K_M values of day 2. Consequently, pO_2 gradients are less steep and oxygen penetrates further into the mat zone or into hepatocyte layers because of the reduced local O_2 uptake. Paradoxically, " $V_{\text{ratio}} > 0.9$ " fractions have decreased. This is understood when converting the V_{ratio} threshold to the minimal cellular pO_2 to which the hepatocytes must be subjected to, using Eq. 4. Whereas in the reference case, hepatocytes are considered to be sufficiently oxygenated when cellular pO_2 reaches at least 18 mmHg, threshold values are now approximately 43 and 68 mmHg for day 4 and 5, respectively. Since the overall pO_2 level in the latter cases is not equally elevated, $V_{\text{ratio}} > 0.9$ fractions are strongly reduced. Conversely, when applying an identical pO_2 threshold instead of V_{ratio} , hepatocyte percentages in case 14 and 15 are increased with 3% and up to 20% compared to day 2. As such, an increase in K_M causes average cellular pO_2 to increase, but whether there is also an increase in the number of hepatocytes that are sufficiently oxygenated is difficult to determine based on computer simulations, as this depends on the criteria, i.e. minimal V_{ratio} vs. minimal pO_2 , used.

5 Conclusions

A numerical model to investigate fluid flow and oxygen transport and consumption in the AMC-BAL was developed and applied to two representative micro models of the AMC-BAL. Two different gas capillary patterns, i.e. 'inline' and 'triangular', were used and combined with two proposed hepatocyte distributions, leading to four basic configurations in total. Fifteen case studies were performed on each of the configurations in order to gain insight in the fluid flow, shear stress distribution, oxygen availability and effective hepatocyte utilization ratio (V_{ratio}) of the AMC-BAL and to assess possible strategies to further improve cellular oxygen availability. We found that the AMC-BAL does not provide sufficient oxygen to all hepatocytes to allow them to consume oxygen at 90% of their maximal uptake rate under standard operating conditions. The internal oxygenator is an essential part of the AMC-BAL. Doubling the number of gas capillaries together with a 2-fold increase in the oxygenation gas pO_2 was found to be the optimal method to maximally increase O₂ availability. Additionally, pressure drop over the AMC-BAL and cellular shear stress levels were found to be low and advantageous to cell culture. The developed model also allowed us to assess the effect of the transition from the *in vitro* to the clinical setting and the effect of the change of hepatocyte O₂ consumption characteristics in time. Since large variations in simulation results between hepatocyte distributions are shown, an assessment of the *in vitro* hepatocyte distribution in the AMC-BAL is useful. Subsequently, an attempt to validate the numerical model with *in vitro* experiments should be made. Eventually, adoption of this information may lead to a more efficient and productive AMC-BAL in the near future.

6 Acknowledgments

First author's research is supported by a BOF-grant (011D09503) from Ghent University, Belgium. The authors also express their gratitude to the Netherlands Digestive Diseases Foundation (MLDS), the Technology Foundation of NWO (The Netherlands), and the European Union (QLTR-2000-01889) for financial support.

7 Addendum

7.1 Modeling methodology and limitations

Several remarks and limitations concerning modeling methodology are discussed below.

7.1.1 Resistance to flow of the non-woven polyester mat

Flow resistance of the non-woven polyester matrix was determined on a specimen which contained no hepatocytes. However, flow resistance of a hepatocyte-seeded mat would be larger since hepatocytes entail an additional resistance to flow. Nevertheless, the viscous resistance factor of the porous mat has not been adjusted to account for this. Since the hepatocytes only take up an additional 10 or 17% of space (cfr. ϕ - Table V-1) and flow velocities inside the mat are already two orders of magnitude smaller than in the inter-capillary space, the error made within this assumption was considered negligible. Also, transverse flow through the mat was used in the experimental set-up, whereas in the model only longitudinal (axial) flow exists and thus the subsequent use of the determined hydraulic permeability as an isotropic value was assumed to be acceptable given the non-woven nature of the matrix mat.

7.1.2 Resistance to flow of hepatocytes

The same hydraulic permeability of the non-woven mat was used for the hepatocyte layers in the realistic cell distribution model. Since the 'porosity' of the non-woven mat (91%) is larger than the porosity of the hepatocyte layer (74%, i.e. 100% minus the cell volume fraction of 26% (Table V-1)), the use of the experimentally determined mat permeability is likely to be an overestimation of the permeability of the hepatocyte layer. But since flow velocities in the hepatocyte layer using this permeability are already two orders of magnitude smaller than the average velocity in the inter-capillary space, the use of a more stringent flow resistance for the hepatocyte layer was considered unnecessary, particularly when considering that O₂ transport is already highly diffusion-controlled. Also, the determined hydraulic permeability compares very good with values used by other researchers (see Table IV-2).

7.1.3 O₂ diffusion constant through zones containing hepatocytes

Oxygen diffusion coefficients were determined dependent on local hepatocyte density. However, it should be noted that hepatocyte permeability to oxygen is not only dependent on the O₂ diffusion constant, but also on local O₂ solubility (permeability = $DO_2 * \alpha$). Dutta *et al.*[267] reported that lipid content of hepatocytes may increase O₂ solubility. Therefore, hepatocyte O₂ permeability could be compensated or even increased in spite of a reduced O₂ diffusivity. In this study, the O₂ solubility is constant throughout the model. Nevertheless, the resulting local diffusion coefficients and corresponding permeabilities through different cell zones

are in the range of reported values for hepatocytes and other cell types[236,255,256,257,258].

7.1.4 O₂ supply by the hydrophobic gas capillaries

By imposing a constant pO₂ on the gas capillary outer surfaces, the transport process of O₂ flow inside the capillaries and subsequent diffusion in the capillary wall was not incorporated in the model. By using this boundary condition, pO₂ loss over the full capillary length and over the capillary wall was excluded. One reason for these simplifications was that with a culture gas flow rate of 150 ml/min through 300 gas capillaries (inner diameter = 200 μm), the static pressure loss along a capillary is only about 3 mmHg and corresponds to a maximal pO₂ loss of about 0.6 mmHg. Secondly, in the hypothetical case that all 10⁹ hepatocytes consume at maximal uptake rate (i.e. V_M) and all oxygen is supplied by the capillaries only, then the average pO₂ of the culture gas at the outflow could maximally drop 4.7 mmHg. Thus combined, the pO₂ along the capillaries can maximally -and hypothetically- drop to 96.5% of its initial value, which was considered negligible. Furthermore, the radial resistance to O₂ transport through the capillary wall was neglected as the gas capillaries used (Oxyplus®, Membrana GmbH) have very high oxygen permeability, typically in the range of 0.35 cm³/(m².s.mmHg)[259]. Considering the total capillary surface area in the AMC-BAL, this only causes a 1.2 mmHg pO₂ loss across the capillary wall in the abovementioned hypothetical case, which was also considered negligible.

7.1.5 Hepatocyte oxygen consumption parameters

Oxygen consumption parameters were based on values from 2D porcine hepatocyte culture at 0.25*10⁶ cells/ml[243]. In contrast, hepatocyte culture in the AMC-BAL is reported to be three-dimensional and at hepatocyte densities two orders of magnitude larger. A difference in oxygen consumption characteristics between those two cases is likely, as specific oxygen uptake per cell is reported to decrease in 3D culture with increasing cell density[247]. Whether this is a natural phenomenon or an artefact due to diffusional limitations in *in vitro* experiments is under discussion[232].

Nevertheless, oxygen uptake rate and hepatocyte densities and total number of cells in the models are set to the most demanding levels to put the oxygenation capabilities of the AMC-BAL to the test. As a consequence, the cellular oxygen levels and “Vratio > 0.9” percentages in the standard reference cases are quite low and are to be taken as worst case scenario. Consequently, careful attention must be paid when comparing results to simulations of other BAL systems where V_M (or hepatocyte count or density) is often set to significantly lower values[225,228,230]. In this paper, oxygen consumption per 10⁶ cells V_M is 0.7286 nmole/s; oxygen consumption per unit of volume V_M*ρ_{cell} ranges between 24 and 60 nmole/s*cm³ depending on the location in the micro model.

7.2 Future work

Future work may comprise an attempt to extrapolate the conclusions of the micro model results to the entire AMC-BAL. Differences may arise as some features cannot be incorporated in the micro models; for example the equidistant positioning of the gas capillaries along the course of the spiral mat may not be guaranteed, total flow rate may not be homogeneously distributed across the AMC-BAL and elevated culture gas pO_2 may additionally increase the oxygen content of the flow prior to entering the mat segments. Also, since simulation results of oxygen availability vary greatly depending on the imposed hepatocyte distributions, assessment of *in vitro* hepatocyte densities and distributions may prove useful (see Chapter VII). For this, similar analysis of fluid flow and oxygen availability on a full scale AMC-BAL computer model is needed. Subsequently, an attempt to validate the numerical model with *in vitro* experiments can be made (see Chapter VI).

Chapter VI: Enhanced oxygen availability improves liver-specific functions of the AMC bioartificial liver

Long-term culturing of primary porcine hepatocytes (PPH) inside the AMC-bioartificial liver is characterized by increased anaerobic glycolysis. Recommendations to increase oxygen availability were proposed in a previous numerical study and were experimentally evaluated in this study. Original bioreactors as well as new configuration bioreactors with 2.2-fold thinner non-woven matrix and 2-fold more capillaries were loaded with PPHs and oxygenated with different gas oxygen pressures resulting in medium pO_2 (pO_{2-med}) of either 135-150 mmHg or 235-250 mmHg. After 6 days culturing, new configuration bioreactors with pO_{2-med} of 250 mmHg showed significantly reduced anaerobic glycolysis, 60% higher liver-specific functions and increased transcript levels of five liver-specific genes compared to the standard bioreactor cultures. Changed bioreactor configuration and increasing pO_{2-med} contributed equally to these improvements. Histological examination demonstrated small differences in cell organization. In conclusion, higher metabolic stability and liver-specific functionality was achieved by enhanced oxygen availability based on a prior modeling concept.

The contents of this chapter are accepted for publication in *Artif Organs* (2008), January issue

Enhanced oxygen availability improves liver-specific functions of the AMC bioartificial liver

P.P.C. Poyck, G. Mareels, R. Hoekstra, A.C.W.A. van Wijk, T.V. van der Hoeven, T.M. van Gulik, P.R.

Verdonck, and R.A.F.M. Chamuleau

1 Introduction

Orthotopic liver transplantation (OLT) is currently the only effective treatment for end-stage liver disease. Patients suffering from acute or acute-on-chronic liver disease may benefit from temporary extracorporeal liver support to tide them over until OLT or to allow regeneration of their own liver. Promising options for extracorporeal liver support comprise bioartificial liver (BAL) devices that rely on the synthetic and detoxification activities of viable hepatocytes. These cells are highly active and exhibit high oxygen uptake rates in various 2D and 3D culture conditions.[153,243,268,269,270,271,272] Adequate oxygen supply inside BAL devices is crucial for maintenance of sufficient and stable liver-specific functions. Therefore several BAL devices have been equipped with incorporated membrane or capillary oxygenators.[157,158,197,199]

One of the clinically applied BAL devices that incorporate an integrated oxygenation system is the AMC-BAL. This liver support system is further characterized by direct plasma-cell contact to enhance efficient mass transfer and a polyester matrix, to which small aggregates of hepatocytes are attached.[245] The polyester matrix is circularly wound around a polycarbonate core and the gas capillaries are situated in a parallel fashion between the matrix layers. The AMC-BAL has shown liver specific detoxification and synthesis capacity *in vitro* [245,273], significantly improved survival time in small and large animal models of ALF [235,274,275,276], and safety in a phase I clinical study [223]. However, from *in vitro* studies using primary porcine hepatocytes, we observed an increase in anaerobic glycolytic metabolism after culturing for four days [219,273,277], suggesting a limited oxygen availability in at least some parts of the bioreactor. In an attempt to analyze and improve oxygen availability, we addressed this issue by computational modeling [278].

Numerical modeling and computational fluid dynamics (CFD) simulations are important engineering analysis tools to determine optimal working parameters and to indicate alternative designs for the improvement of bioreactor performance [232]. These methods have been applied to analyze flow and oxygen transport in hollow fiber BALs [227,229,230,232] as well as for other types of hepatocyte culture systems [225,228,236]. Mareels *et al.* have developed a three-dimensional computer model of the AMC-BAL, in which fluid flow and oxygen transport were simulated to gain insight in possible improvements in oxygen availability to the hepatocytes [278]. The main conclusion of this study was that 15.7% to 28.8% of all porcine hepatocytes inside the AMC-BAL could consume oxygen at 90% of their maximal uptake rate, confirming the hypothesis of anaerobic areas inside the bioreactor as observed with *in vitro* experiments. Furthermore, convective oxygen transport inside the matrix layers was extremely low resulting in low oxygen availability inside the matrix layers. Histological analysis of bioreactors with porcine hepatocytes cultured for 7 days supported these hypotheses; viable cells were preferentially located around capillaries or adjacent to matrix layers, whereas less viable hepatocytes were present in the middle of the transverse matrix [219]. To improve oxygen availability to the majority of cells inside the AMC-BAL, two important recommendations were made, i.e. (1)

double the number of capillaries, and (2) double the pO_2 of the oxygenation gas. Additionally, we hypothesize that by decreasing the thickness of the non-woven matrix a more efficient cell distribution and therefore, exposure to the available oxygen might be achieved.

The aim of this study was to define the most optimal culture pO_2 and bioreactor design according to the study of Mareels *et al.*[278]. We developed a new configuration bioreactor based on its original design [245] by doubling the amount of gas capillaries and by reducing the thickness of the original polyester non-woven matrix by 2.2-fold. Both types of bioreactors were loaded with 1.0×10^9 porcine hepatocytes and oxygenated with various oxygen concentrations resulting in a medium pO_2 of 135-150 mmHg or 235-250 mmHg. Primary outcome parameters were glucose consumption and lactate production as key indicators of anaerobic glycolysis. In addition, hepatocyte-specific functions and cell damage parameters were analyzed during a 6-day culture period. We furthermore analyzed cellular morphology and transcriptional changes of liver-specific genes, genes related to hepatic de-differentiation, oxidative stress, general metabolism and apoptosis at the end of the culture period.

2 Materials and methods

2.1 Bioreactor configurations

We used a downscaled bioreactor of the second generation AMC-BAL as described previously [273]. The original configuration of the bioreactor consists of a polycarbonate housing containing a non-woven hydrophilic polyester matrix (400 μm thick) circularly wound around a polycarbonate core. Between the matrix layers, 300 hydrophobic polypropylene gas capillaries are situated in a parallel fashion. In this study, a *new* configuration was constructed from the original configuration by the following; 1. doubling the number of capillaries to 600, and 2. decreasing the matrix thickness to 183 μm (Table VI-1).

2.2 Experimental set-up

Two variables were investigated: (1) the effect of increased oxygen concentration in the supplied gas; and (2) the effect of the new configuration. In total, 20 bioreactors were equally divided into four groups: (1) normal configuration bioreactors with culture gas oxygenation (95% air / 5% CO_2 ; resulting in 20% O_2) (G1), (2) normal configuration bioreactors with increased oxygenation, i.e. culture gas mixed with carbogen (95% oxygen / 5% CO_2) (G2), (3) new configuration bioreactors with culture gas oxygenation (G3), and (4) new configuration bioreactors with increased oxygenation (G4) (Table VI-1). G1 and G3 bioreactors received the same culture gas, whereas G2 and G4 bioreactors received the same mixture of culture gas and carbogen. For increased oxygenation (G2 and G4), culture gas and carbogen were

mixed in proportion leading to a O₂ concentration of \pm 40% and a medium pO₂ (pO_{2-med}) of 235-250 mmHg measured at the outflow port, reaching 100 mmHg higher pO_{2-med} levels (+167%) when oxygenated with culture gas alone (Table 1). The pO_{2-med} and pH in all groups were measured daily -at least 3 times- using an off-line ABL505 blood-gas analyzer (Radiometer Copenhagen). Before overnight culture, culture medium pH of all bioreactor groups was adjusted with NaHCO₃ to 7.35 or higher. All bioreactors were tested at d1 (day 1), d3 and d6 after cell loading. Four bioreactors, each from one group, were used for histological analysis and fixed in 10% formalin at d6. RNA for RT-PCR analysis was isolated from two G1 and two G4 bioreactors at d6.

Table VI-1: Specification of bioreactors and conditions of the four experimental groups. Values are means \pm SE as shown in Figure 1A.

	Bioreactor configuration			Type of oxygenation gas		pO _{2-med} at 22 hrs * (mmHg)
	Matrix thickness (μ m)	Capillaries (no.)	Culture gas	Carbogen		
Group 1 (G1)	original	400	300	+	-	134.1 \pm 1.3
Group 2 (G2)	original	400	300		Mixture	236.1 \pm 4.2
Group 3 (G3)	new	183	600	+	-	148.3 \pm 1.3
Group 4 (G4)	new	183	600		Mixture	251.8 \pm 3.9

2.3 Hepatocyte isolation

Hepatocytes were isolated from livers of female pigs (20-24 kg) by a two-step collagenase perfusion technique according to a modified protocol of Seglen [279] as previously described [273]. Procedures were in accordance with the institutional guidelines of the local Animal Ethical Committee. Hepatocytes were suspended in ice-cold culture medium, consisting of Williams' E medium supplemented with 10% (v/v) heat inactivated fetal bovine serum (BioWhittaker, Verviers, Belgium), 2 mM L-glutamine, 1 μ M dexamethason, 20 mU/mL insulin, 2 mM ornithine, 100 μ g/mL streptomycin, 100 U/mL penicillin and 0.25 μ g/mL fungizone. Total yield of isolated hepatocytes was estimated by determination of the cell pellet volume after 3-times of centrifugation at 50x g for 3 min [273]. Viability was determined by trypan blue exclusion test.

2.4 Hepatocyte culture

One billion viable hepatocytes were injected under sterile conditions into the bioreactor through three loading ports. Bioreactors were then placed in a culture cabinet at 37°C and oxygenated with culture gas at a flow rate of 150 mL/min during the 2-hour attachment period. To ensure optimal cell attachment and an even cell distribution, bioreactors were rotated 340° (back and forth) along the longitudinal

axis at 1 revolution/min. After this attachment period, dead and unattached cells were removed by flushing 100 mL of fresh culture medium through the bioreactor at 7.5 mL/min. From then on, all bioreactors were oxygenated either with culture gas or with the mixture of culture gas and carbogen according to the experimental group assignment. Bioreactors were perfused with 150 mL recirculating culture medium overnight at 7.5 mL/min for 16 hours. After the first night of culture and before starting the first hepatocyte function test, perfusion rate was increased to 15 mL/min and maintained during the 6-days culture period.

2.5 Hepatocyte function test

Each test consisted of an oxygen consumption test (OCT) followed by a function test, as described previously [273]. Briefly, oxygen consumption was determined by measuring the decrease in oxygen tension during the first 15 min after closing the oxygen supply to the bioreactor. G2 and G4 bioreactors were oxygenated with culture gas for 45 min prior to the OCT to create similar testing conditions as for G1 and G3. A function test was performed by flushing the bioreactor with 100 mL of test medium composed of culture medium supplemented with 500 µg/mL lidocaine.HCL, 2 mM L-lactate, 2.75 mM D-galactose and 5 mM NH₄Cl; and followed by recirculation of 100 mL test medium for two hours at 37°C. All bioreactors were oxygenated during the function test according to the experimental group assignment. Medium samples were taken at 30, 60, 90 and 120 min and subsequently analyzed for concentrations of ammonia, urea, lidocaine, albumin, galactose, glucose and lactate as well as activities of aspartate aminotransferase (AST) and lactate dehydrogenase (LDH). Ammonia, galactose and lidocaine elimination, urea and albumin production capacity, AST and LDH release, glucose and lactate consumption and/or production rates were determined by calculating the changes in concentration in test medium per hour per billion cells loaded in the bioreactor.

2.6 Quantitative reverse transcription-PCR (qRT-PCR)

Solutions, conditions and calculations for qRT-PCR analyses were as described previously [277,280]. RT and PCR primer sequences are presented in Table VI-2. Transcript levels were normalized for 18S ribosomal RNA.

Table VI-2: RT-PCR primers.

Gene		primer 5' - 3'
Pepck1	RT	CTCTGCCAGCCACCCCTCCTCCTT
	S	CTGGGGGGCGGGCGAGTTCATCA
	AS	ATTTCTCGGCGGTTCGGGCAGGTG
Pfkfb1	RT	TTTGCAGCCATAAGCCACAGG
	S	GAGATTGATGCGGGTGTCTGTG
	AS	TCCTGYCGTTCTAGCTCCATTAT
SOD1	RT	GAGGGAATGTTTACTGGGTGAT
	S	GCAGGGCACCATCTACTTC
	AS	ACACCACAGGCCAAACGACTTC
SOD2	RT	CGGTGTGAGGCTGCTGTTTTACT
	S	CGCGGCCTACGTGAACAACCT
	AS	CCCAGCAGCGGAACCAGACC
18S, AAT, AFP, Bax- α , Bcl-X _L , CPS, CYP _{3A29} , GS, GST π , LDH and UCP-2 see Poyck <i>et al.</i> [277]		
RT, reverse transcriptase primer; S, sense primer; AS, anti-sense primer. Pepck1, cytosolic phosphoenol-pyruvate carboxykinase 1; Pfkfb1, 6-phosphofructo-2-kinase/fructose-2,6-biphosphatase 1; SOD1, [Cu/Zn] superoxide dismutase 1; SOD2, [Mn] superoxide dismutase 2		

2.7 Histological analysis

Bioreactors were fixed in 10% formalin after the function test at d6 and stored at 40C. Complete transverse 8 μ m sections of the laboratory-scale bioreactor (ϕ I.D. 22 mm) were obtained after embedding the whole bioreactor as described (6,19). All sections were stained with hematoxylin and eosin (HE) to evaluate tissue architecture and organization.

2.8 Statistical analysis

Repeated measurement ANOVA tests (adjusted for cell isolate) were used to calculate differences between each group for the whole culture period. Two-way ANOVA tests were used to compare differences between each group per day. One-sample t-tests were used to calculate differences in relative mRNA levels of G4 normalized for G1 (%) from 100% as hypothetical value. Significance was reached if $P < 0.05$. SPSS 12.0.1 (SPSS Inc., Chicago, IL, USA) was used for statistical analysis. Prism version 4.0 (GraphPad Prism Inc, San Diego, CA, USA) was used for graphical presentation of the data. Average values (\pm standard error) are reported.

3 Results

3.1 Bioreactor configurations

In Fig. VI-1, full transverse scans of paraffin blocks containing samples of bioreactors with the original configuration (A) and new configuration (B) demonstrate the higher number of capillaries and the thinner matrix of the new bioreactor configuration. Although the distance between individual capillaries varied, resulting in areas lacking capillaries, average capillary-to-capillary distance was smaller in new configuration bioreactors.

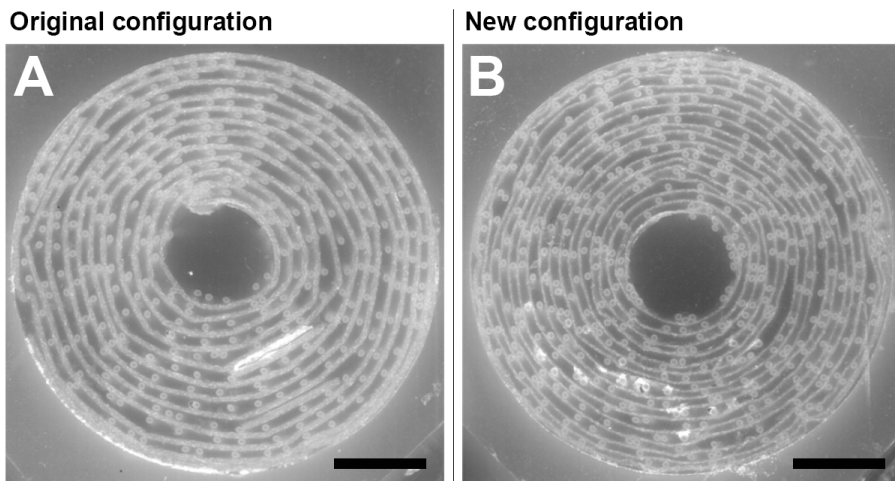


Fig. VI-1: Full transverse view of paraffin blocks with embedded samples of bioreactors with the original configuration (A) and new configuration (B). Bars in A and B indicate 5 mm.

3.2 Isolation outcome and loading

Bioreactors were loaded with 1.0×10^9 viable hepatocytes originating from five liver cell isolates. Average yield was $7.7 \pm 1.7 \times 10^9$ viable cells with a mean viability of 97.5 ± 1.3 %. Per isolate a series of four bioreactors were loaded and assigned to the four different groups.

3.3 Medium pO₂ and pH

After 22 ± 3 hours (d1), pO_{2-med} at the outflow port was 134.1 ± 1.3 mmHg, 236.1 ± 4.2 mmHg, 148.3 ± 1.3 mmHg and 251.8 ± 3.9 mmHg for G1 to G4, respectively (Fig.

VI-2A). Hence, doubling the number of capillaries resulted in an initial average increase of 14.9 mmHg in $pO_{2\text{-med}}$ between G1 and G3, and G2 and G4.

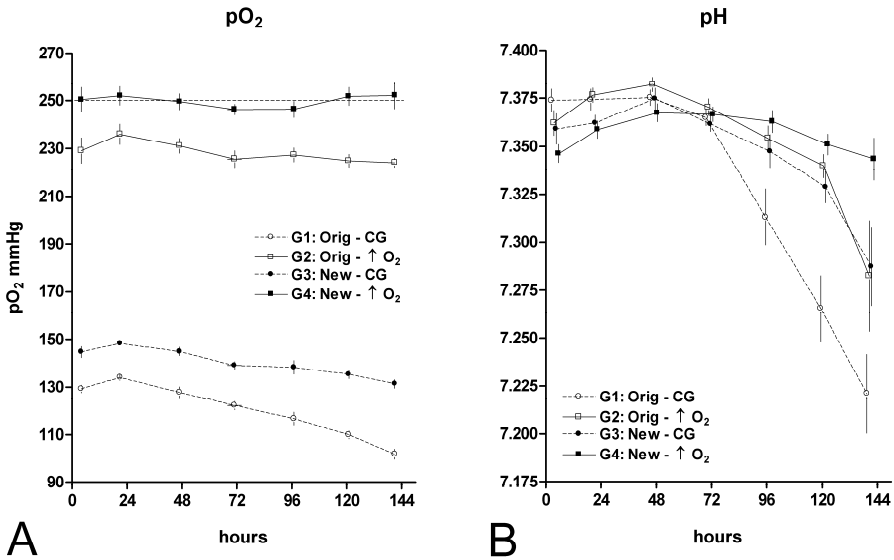


Fig. VI-2: Culture medium pO_2 (A, mmHg) and pH (B) of the four groups of bioreactors cultured for 6 days. G1-4, group 1-4; Orig, original AMC-BAL bioreactor configuration; CG, culture gas oxygenation; New, new bioreactor configuration; ↑ O_2 , increased oxygen tension. Mean ± SE.

From d1 to d6, average $pO_{2\text{-med}}$ of bioreactors oxygenated with culture gas decreased by 23.9% (G1) and 11.4% (G3). Average $pO_{2\text{-med}}$ of G2, i.e. original bioreactors oxygenated at higher oxygen pressure, decreased by 5.1%. No changes were observed for G4 bioreactors, since $pO_{2\text{-med}}$ was maintained at 250 mmHg. During the first 72 hours, pH was stable or increased for all groups (Fig. VI-2B). After 78 hours, the pH strongly decreased for G1 and moderately for G2 and G3, whereas the pH of G4 remained stable. After 120 hours, a strong decrease in pH for G2 and G3 was observed, whereas the pH of G4 decreased moderately. In summary, culture medium acidified in time according to the following group order: G1 > G2 ~ G3 > G4.

3.4 Carbohydrate metabolism and oxygen consumption

All groups were gluconeogenic and consumed lactate at d1 (Fig. VI-3A and B). At d3, G4 still produced glucose and consumed lactate in contrast to G1 ($P < 0.05$). Although all groups consumed glucose and produced lactate at d6, significant differences were observed. G4 consumed 2.3-fold less glucose and produced 2.6-fold less lactate than G1. G2 and G3 did not differ between each other; both groups

consumed 1.6-fold less glucose than G1 and produced 1.4 to 1.5 less lactate than G1, respectively. These results indicate that anaerobic glycolytic metabolism was significantly reduced according to the following group order: G4 > G2 ~ G3 > G1. This indicates that an increased pO₂-med or the configurational change can improve carbohydrate metabolism with a trend for an additive effect as observed in G4. Galactose elimination (Fig. VI-3C) decreased in the following group order: G1 > G2 ~ G3 > G4. Oxygen consumption (Fig. VI-3D) followed the same trend as for glucose, lactate and galactose, although less pronounced. At d6, oxygen consumption was significantly higher for G1 as compared to G4.

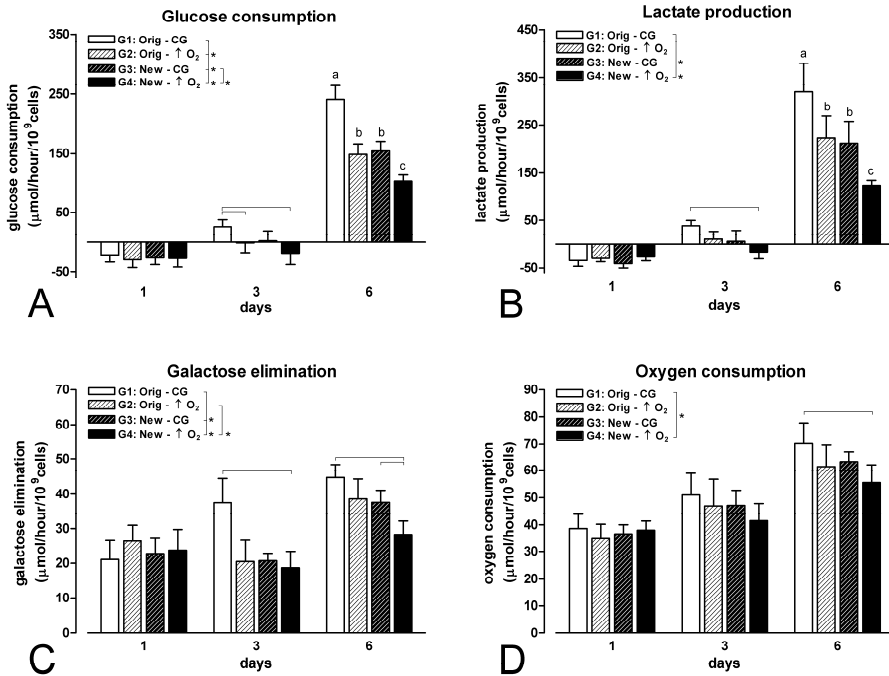


Fig. VI-3: Carbohydrate metabolism and oxygen consumption. A. glucose consumption; B. lactate production, C. galactose elimination and D. oxygen consumption. Expressed in $\mu\text{mol}/\text{hour}/10^9$ viable hepatocytes (mean \pm SE). G1-4, group 1-4; Orig, original AMC-BAL bioreactor configuration; CG, culture gas oxygenation; New, new bioreactor configuration; \uparrow O₂, increased oxygen tension. Vertical brackets with asterisks indicate $P < 0.05$ between bioreactor groups over 6 day period. Horizontal brackets indicate $P < 0.05$ between bars at specified days. Roman characters indicate $P < 0.05$ between other roman characters at d6.

3.5 Hepatocyte function test

Ammonia elimination of G4 was significantly higher than that of the other groups during the whole culture period (Fig. 4A). Average ammonia elimination during 6 days of culture was 71.0 ± 6.2 , 67.7 ± 11.2 , 70.9 ± 14.9 and 89.4 ± 10.2 $\mu\text{mol}/\text{hour}/\text{billion}$ hepatocytes for G1, G2, G3 and G4, respectively. Although G4

eliminated more ammonia than G1, the decrease in ammonia elimination capacity between d1 and d6 was similar, i.e. 21.1 % for G1 and 16.5 % for G4. Urea production (Fig. 4B) was higher and more stable for G4 as compared to G1. Average urea production during 6 days of culture was 32.5 ± 9.6 , 39.1 ± 6.2 , 35.1 ± 5.9 and 47.6 ± 3.2 $\mu\text{mol}/\text{hour}/\text{billion}$ hepatocytes for G1, G2, G3 and G4, respectively. In addition, urea production of G1 decreased by 57.4 %, whereas this was only 16.8 % for G4, resulting in a 46 % significantly higher urea production for G4 at d6 as compared to G1. Albumin production increased in time in all groups (Fig. 4C). G4, however, produced significantly more albumin than G1 with an average over 6 days of 110.5 ± 33.5 and 83.9 ± 19.8 $\mu\text{g}/\text{hour}/\text{billion}$ hepatocytes, respectively. At d6, G4 produced 67 % significantly more albumin than G1. Lidocaine elimination (Fig. 4D) followed the same trend as ammonia elimination and the production of albumin and urea. Average lidocaine elimination during 6 days of culture was 73.6 ± 9.7 , 79.9 ± 8.2 , 79.2 ± 6.4 and 86.9 ± 2.9 $\mu\text{mol}/\text{hour}/\text{billion}$ hepatocytes for G1, G2, G3 and G4, respectively. In addition, lidocaine elimination of G1 decreased by 30.5 %, whereas this was only 9.1 % for G4, resulting in a 35 % significantly higher lidocaine elimination for G4 at d6 as compared to G1.

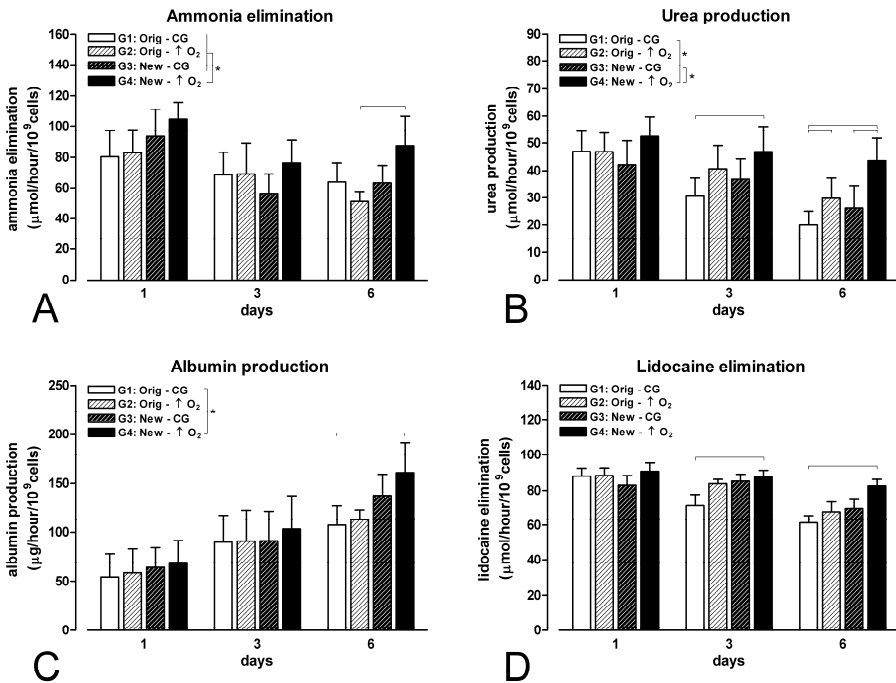


Fig. VI-4: Hepatocytes-specific functions. A. ammonia elimination; B. urea production, C. albumin production and D. lidocaine elimination. A, B, D expressed in $\mu\text{mol}/\text{hour}/10^9$ viable hepatocytes (mean \pm SE). C, expressed in $\mu\text{g}/\text{hour}/10^9$ viable hepatocytes (mean \pm SE). G1-4, group 1-4; Orig, original AMC-BAL bioreactor configuration; CG, culture gas oxygenation; New, new bioreactor configuration; $\uparrow O_2$, increased oxygen tension. Vertical brackets with asterisks indicate $P < 0.05$ between bioreactor groups over 6 day period. Horizontal brackets indicate $P < 0.05$ between bars at specified days.

For urea and albumin production as well as lidocaine elimination, G2 and G3 were both intermediate in these functions and stability as compared to G1 and G4. In summary, the level of liver-specific functions were according to the following group order: G4 > G3 ~ G2 > G1.

3.6 AST and LDH release

AST release at d1 and d6 did not differ significantly between all groups, suggesting that higher pO₂-med did not change the level of hepatocyte damage (Fig. VI-5A). All groups did not differ in LDH release at d1 and d3. However, at d6, a significant increase in LDH release was observed for G1 as compared to G3 and G4 (Fig. VI-5B).

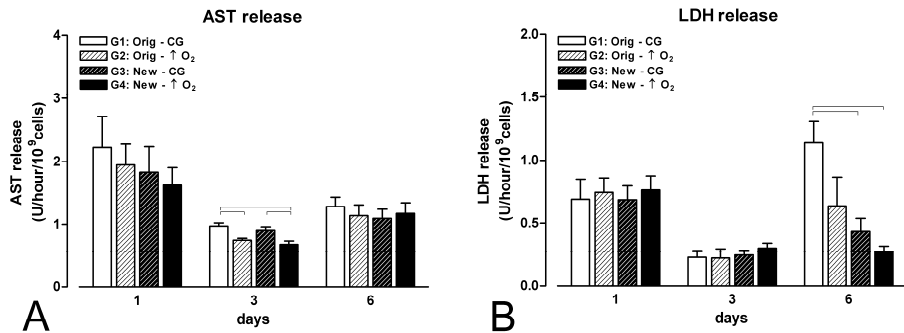


Fig. VI-5: AST release (A) and LDH release (B). Expressed in U/hour/10⁹ viable hepatocytes (mean ± SE). G1-4, group 1-4; Orig, original AMC-BAL bioreactor configuration; CG, culture gas oxygenation; New, new bioreactor configuration; ↑ O₂, increased oxygen tension. Horizontal brackets indicate $P < 0.05$ between bars at specified days.

3.7 qRT-PCR

Transcript levels of Pepck1, as a gluconeogenesis marker, and LDH, as a marker associated with increased anaerobic glycolysis, were, respectively, 1.9-fold higher and 2-fold lower in G4 as compared to G1 at d6 ($P < 0.05$) (Table VI-3). These results are in agreement with the suggestion that hepatocytes inside G4 bioreactors were more gluconeogenic and less anaerobic than in G1 bioreactors. The mRNA levels of Pfkfb1, a key enzyme for glycolysis, were, however, not significantly different. All tested genes related to amino acid metabolism/urea cycle and miscellaneous mature liver-specific functions were not significantly differentially expressed. The transcript level of α -fetoprotein (AFP), a marker for hepatic dedifferentiation, was significantly reduced in G4. Transcript levels of tested genes encoding pro- and anti-apoptotic markers as well as oxidative stress related markers were not significantly different between both G1 and G4. Although not significant, UCP-2 mRNA levels were 2-fold higher in G4.

Table VI-3: Results of gene expression analysis of AMC-BAL cultures at d6. Values are relative 18S RNA normalized mRNA levels of Group 4 cells expressed as % of Group 1 cells (\pm SE). Asterisks indicate significance ($p < 0.05$).

	Gene	Mean	\pm	SE	
Carbohydrate metabolism	Pepck1	187	\pm	26	*
	Pfkfb1	84	\pm	15	
	LDH	52	\pm	10	*
Amino acid metabolism/urea cycle	CPS	87	\pm	30	
	GS	146	\pm	61	
Miscellaneous mature liver functions	Albumin	135	\pm	31	
	Cyp3A29	84	\pm	16	
	AAT	127	\pm	17	
Hepatic dedifferentiation	AFP	69	\pm	11	*
Oxidative stress related	SOD1	96	\pm	22	
	SOD2	97	\pm	27	
	GST π	221	\pm	33	*
	UCP-2	203	\pm	76	
Apoptosis	Bcl-X _L	96	\pm	33	
	Bax- α	122	\pm	28	

AAT, α -1-antitrypsin; AFP, α -fetoprotein; Bax- α , Bcl2-associated X protein; Bcl-X_L, Bcl-X_L protein; CPS, carbamoyl-phosphate synthetase; CYP3A29, cytochrome P450 3A29; GS, glutamine synthetase; GST π , π class glutathione S transferase; LDH, lactate dehydrogenase; Pepck1, cytosolic phosphoenolpyruvate carboxykinase 1; Pfkfb1, 6-phosphofructo -2-kinase/fructose-2,6-biphosphatase 1; SOD1, [Cu/Zn] superoxide dismutase 1; SOD2, [Mn] superoxide dismutase 2; UCP-2, uncoupling protein 2.

3.8 Histological analysis

Histological sections of all four groups showed an overall similar morphological architecture (Fig. VI-6 G1-4). Tissue-like structures were preferentially located next to or in close vicinity of gas capillaries, or in areas through which culture medium primarily flows i.e. between and adjacent to the matrix layers. These tissue-like structures consisted of cells showing hepatocyte morphology. For G1 bioreactors, viable cells appeared to form distinct cell layers of app. 125 μ m around capillaries, whereas in areas further away from a capillary more anuclear cells were found. These typical cell layers, however, were not observed in G2, G3 and G4 bioreactors as large cell aggregates seem to be constituted mainly of viable cells with randomly scattered anuclear cells.

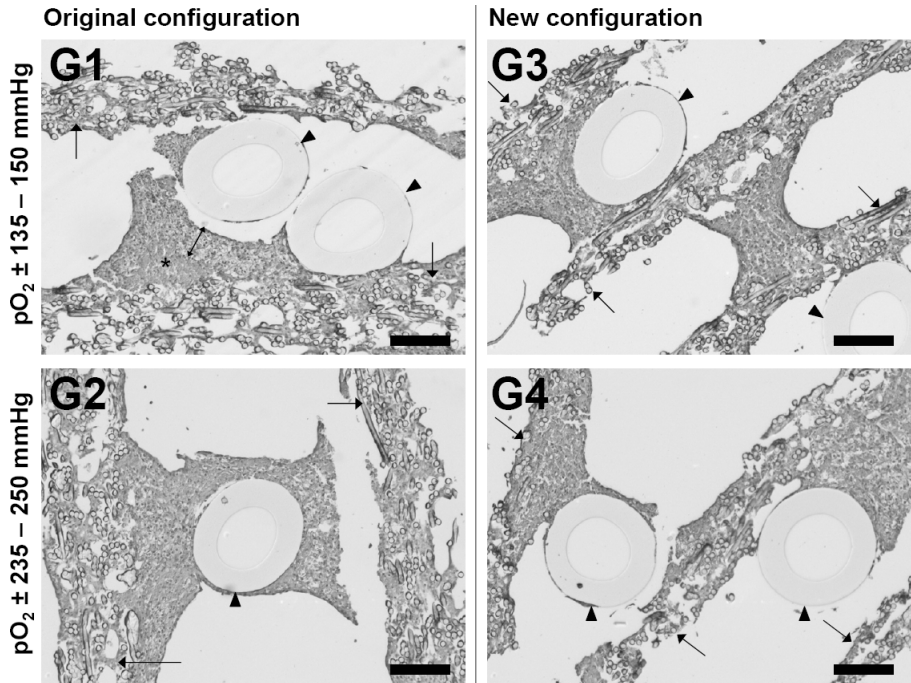


Fig. VI-6: Histological sections of bioreactors with the original configuration (G1-2) and new configuration (G3-4). G1 and G3 are histological samples of bioreactors oxygenated with culture gas. G2 and G4 are histological samples of bioreactors oxygenated at higher oxygen tensions. Bars in G1 to G4 indicate 200 μm . Arrows indicate matrix layers. Arrowheads indicate capillaries. Double headed arrow (G1) indicates cell layer, whereas asterisk indicates area of anuclear cells.

4 Discussion

Recently, Mareels *et al.* [278] concluded by numerical modeling and computational fluid dynamics (CFD) of the AMC-BAL that oxygen availability of hepatocytes could be improved by configurational changes and increased oxygenation of the AMC-BAL. In this study, we showed that changes according to the recommendations based on this concept indeed led to increased stability in metabolism and liver specific functionality.

We created a new configuration of the AMC-BAL, based on the original design of Flendrig *et al.* [245], by incorporating a double number of capillaries and by using a 2.2-fold thinner non-woven matrix. Additionally, we varied the O_2 tension of the medium ($\text{pO}_{2\text{-med}}$) by changing the culture gas composition. The results clearly demonstrate that hepatocytes inside bioreactors with the new configuration and an increased $\text{pO}_{2\text{-med}}$ (G4) showed less anaerobic glycolysis and maintained hepatocyte-specific function for a longer culture period than hepatocytes in the original

configuration bioreactors cultured under standard culture conditions (G1). Lactate production and glucose consumption were 2.6-fold and 2.3-fold lower compared to standard culture conditions at d6, respectively. The less anaerobic glycolytic state of G4 bioreactors was confirmed by qRT-PCR analysis of genes related to carbohydrate metabolism, i.e. *Pepck1* and *LDH*. In addition, tested hepatic functions remained more stable and were on average 60% higher at d6 as a result of the new configuration and increased oxygenation compared to the standard culture conditions. Although no significant differences were identified in the expression of individual liver-specific genes, a tendency towards an average 15% higher expression of these genes, i.e. *GS*, *CPS*, *albumin*, *CYP3A29* and *AAT*, was observed. Additionally, the *AFP* mRNA level, as an indicator of hepatic dedifferentiation, was significantly reduced by 1.5-fold.

Average galactose elimination of G1 was higher than G4 at d3 and d6. This might be explained by the higher anaerobic glycolytic metabolism of G1 in which galactose was used as an additional source for glucose. The higher oxygen consumption of G1 as compared to G4 (Fig. VI-2A and Fig. VI-3D) can be the result of impaired mitochondrial activity resulting in uncoupling of the oxidative phosphorylation. However, conclusions drawn from the oxygen consumption test (OCT) between G1 and G4 (Fig. VI-3) should be done with some reservation. Oxygen consumption is measured as the difference in pO_2 in the medium in time. During an OCT, cells not only consume oxygen from the medium, but also from the capillaries as oxygen supply is cut off but residual oxygen is still present in the capillaries. Since G4 bioreactors were constructed with 2-fold more capillaries than G1 bioreactors, cells could consume relatively more oxygen from capillaries of G4 bioreactors, possibly resulting in lower oxygen consumption rates of G4.

Bioreactors with the original configuration cultured at higher pO_{2-med} (G2) and bioreactors with the new configuration cultured at standard culture conditions (G3) were similar in their outcome and were intermediate between G1 and G4 bioreactors. The pO_{2-med} in bioreactors with the new configuration was only 14 mmHg higher (G3) than G1 bioreactors. This is a modest increase in comparison to the 102 mmHg higher pO_{2-med} as a result of increased oxygen pressure (G2). Since oxygen availability inside the matrix is nearly absent due to a strong reduction in convective oxygen transport, reduction of the matrix volume, in combination with a doubling of gas supplying capillaries, would reduce areas with critically low pO_2 . As a result, these configurational changes alone were as effective in maintaining the functionality of the hepatocytes as solely increasing pO_{2-med} levels. Thus, not only the level of pO_{2-med} is relevant, but also an improvement in potentially favorable location for cell attachment with sufficient oxygen availability is -equally- important.

The influence of pO_2 on cell viability, cell attachment and function has been investigated in different hepatocyte culture models with various outcomes. Some studies found beneficial effects at low or normal oxygen conditions (12% O_2) [281,282], whereas other reports described high oxygen concentrations (24-43%) to improve hepatic functionality [185,283,284,285,286]. Comparison of these reports is difficult, since a variety of different 2D and 3D culture systems, species-differences in cells, and parameters were used. Yanagi *et al.*, however, investigated the effect of different oxygen concentrations on hepatic function of rat hepatocytes in a packed-

bed bioreactor loaded with polyvinyl formal resin cubes [285]. Under high oxygen tension, i.e. 250-460 $\mu\text{mol/l O}_2$ ($\sim 180\text{-}330$ mmHg $p\text{O}_2$), albumin production at d1 and ammonium metabolic rate constant (K_m) at d2 were 17.9% and 10% higher, respectively, when compared to bioreactors cultured at normal oxygen tensions, i.e. 140-180 $\mu\text{mol/l O}_2$ ($\sim 100\text{-}130$ mmHg $p\text{O}_2$)[285]. So, in their experimental set-up the effects of increased oxygen availability were similar to our data, but were tested only scarcely. In our study covering an extended culture period and assessing more parameters we definitively show that increased oxygenation improves hepatic functionality of cells inside a BAL.

High oxygen concentrations may, however, lead to an increase in oxidative stress and to the formation of reactive oxygen species (ROS), e.g. superoxide anion O_2^- , hydrogen peroxide H_2O_2 and hydroxyl radical $\text{HO}\cdot$. When the formation of ROS exceeds the antioxidant capacity of the cell, protein and lipid macromolecules can be damaged, leading to cell damage, DNA mutations and initiation of apoptotic cascades [287]. To investigate the adaptation of hepatocytes to high oxygen tensions and possible ROS formation, we analyzed mRNA levels of SOD1 (cytosolic copper and zinc superoxide dismutase) and SOD2 (mitochondrial manganese superoxide dismutase), as well as GST π and UCP-2. SODs are cytoprotective antioxidant enzymes that eliminate superoxide byproducts [283]. GST π is associated with carcinogenesis and the development of different tumors, but has also an important role in the detoxification and reduction of ROS [288]. UCP-2 mediates regulated proton leak, whereas increasing evidence supports that UCP-2 might function to control the production of superoxide and other ROS [287,289,290]. In this study, no differences were found in SOD1 and SOD2 gene expression between G1 and G4. However, a two-fold upregulation was found for GST π and, although not significant, also for UCP-2 in G4 bioreactors, possibly indicating a modulatory effect of hepatocytes to increased O_2 concentrations. Since AST release was not higher in G2 and G4 bioreactors, we conclude that increased oxygen concentration was not detrimental to hepatocyte viability. In addition, mRNA expression levels of both pro- and anti-apoptotic proteins Bax- α and Bcl-XL were not different between G1 and G4 bioreactors, suggesting a balanced apoptotic metabolism in low and high O_2 concentration bioreactors. LDH release is generally used as a cell damage parameter. However, in our experimental setting an increased LDH release does not indicate increased cell damage per se, since intracellular LDH concentration might be increased under conditions of relative oxygen shortage.

An essential issue for BAL development and application, in particular for long-term culture of cell lines, is the influence of cell density on oxygen consumption rates per cell. Various theoretical and experimental reports have led to the conclusion that oxygen consumption per cell -independent of possible oxygen diffusion limitations- decreases when cell density increases [232]. These studies provide sufficient evidence that on-line oxygen consumption measurements in BAL devices are required to follow in time the dynamic oxygen requirements of cultured hepatocytes. Moreover, several reports have shown time-dependent changes in oxygen requirements in rat hepatocyte monolayer cultures [243,283,291]. In general, maximal oxygen consumption rates were found in the initial phase of culture, i.e. just after seeding, whereas in a stable long-term culture oxygen consumption rates had

decreased to more physiological requirements. This initial hypermetabolic state of hepatocytes was found to correlate well with the degree of cell spreading [272,286,291]. As a consequence, it is important to consider these differences in oxygen consumption rates when assessing functionality of an operating BAL device [268]. In this study, however, all bioreactors were continuously oxygenated according to the group assignment for a culture period of 6 days. Possibly, dynamic adjustment of oxygen concentration to specific cell requirements in time may further improve the performance of the AMC-BAL.

In our current studies, numerical modeling and computational fluid dynamics simulations have shown their potential as powerful tools in the development and improvement of BAL devices. Current numerical models of BAL devices are mainly focused on configurational parameters (hardware design), general cellular activity (oxygen consumption) and mature hepatocytes. An important challenge for future numerical modeling of BAL devices is to use hepatic function as a 'parameter'. All cells, however, change in an *in vitro* culture system as a result of adaptation to the environment, depending on medium flow, oxygen and substrate supply and cell-cell contact. Metabolic flux analysis (MFA), however, may help to analyze these dynamic processes by studying the relevant metabolic and regulatory pathways of hepatocytes inside a BAL device ([292]). Integrating MFA in numerical modeling of BAL devices will increase the predictive value of future models and may lead to new insights on how to maintain or improve high liver functions of a BAL device.

In conclusion, we were able to achieve a more stable general metabolism and higher BAL performance by increasing the pO_2 as well as by changing the configuration of the AMC-BAL.

5 Acknowledgements

The authors thank G. Huyzer, A. Maas and P. Ousema of the Surgical Laboratory for their assistance in porcine liver harvest surgery, dr. M. Tanck of the Clinical Epidemiology, Biostatistics and Bioinformatics department (AMC) for his help with the statistical analysis. The authors express their gratitude to the Netherlands Digestive Diseases Foundation (MLDS), the Technology Foundation of NWO (The Netherlands) and the European Union (QLTR-2000-01889) for financial support. Second author's research was supported by a BOF-grant (011D09503) from Ghent University, Belgium.

Chapter VII: A full-scale numerical model of the AMC Bioartificial Liver correlated with *in vitro* experimental data.

*A realistic numerical model of the AMC Bioartificial Liver (AMC-BAL) was developed to investigate the perfusion and oxygen (O_2) transport as well as to estimate the oxygen consumption of porcine hepatocytes inside the AMC-BAL. For this, the *in vitro* hepatocyte distribution in the AMC-BAL was quantified experimentally based on histological sections, and subsequently applied to a full-scale computer model (macro model) of the AMC-BAL. Computational Fluid Dynamics (CFD) simulations allowed studying the oxygen availability and outlet medium pO_2 in four configurations: in the original as well as in a new configuration bioreactor with 2.2-fold thinner non-woven matrix and 2-fold more capillaries, both oxygenated with either 150 mmHg (standard) or 300 mmHg (doubled) oxygenation gas pO_2 . Preferential flows were observed near the core of the original configuration, but were absent in the new configuration bioreactor. Oxygen availability was most optimal in the case of the new configuration bioreactor with increased oxygenation gas pO_2 . Oxygen availability and outlet medium pO_2 were dependent on the hepatocyte O_2 consumption rate (OCR). As such, *in vitro* OCRs of hepatocytes in the four AMC-BAL configurations were estimated by matching simulated medium outlet pO_2 to experimentally measured values of Poyck et al.[293]. This resulted in almost identical OCRs in both designs. However, increasing oxygenation gas pO_2 resulted in higher OCR values. This macro model provides new insights in fluid flow and oxygen transport inside the bioreactor as well as in the relation between O_2 availability, *in vitro* O_2 consumption and functional activity of porcine hepatocytes inside the AMC-BAL.*

The contents of this chapter are submitted for publication in *Artif Organs*

A full-scale numerical model of the AMC Bioartificial Liver correlated with *in vitro* experimental data

G. Mareels, P.P.C. Poyck, S. Eloot, R.A.F.M. Chamuleau, and P.R. Verdonck

1 Introduction

The healthy liver has an essential role in a wide range of metabolic and homeostatic processes. Massive loss of liver function has a devastating effect on the patient's health. Acute liver failure (ALF) is the most dramatic form with a mortality of 60-90%, depending on etiology.[234,294] For ALF, orthotopic liver transplantation remains the current treatment of choice. Limited organ availability, however, has created the need for temporary extracorporeal artificial liver support that can tide ALF patients over to liver transplantation or to allow regeneration of their own liver. Bioartificial liver (BAL) support systems are promising, as these extracorporeal systems rely on the full range of detoxification and synthesizing functions of viable liver cells, in contrast to artificial liver support systems which only replace the liver's detoxifying function.

One of the clinically applied BAL devices is the AMC Bioartificial Liver (AMC-BAL; Academic Medical Center, Amsterdam, The Netherlands, patent No: WO 97/12960). This device contains functionally active hepatocytes seeded in a non-woven mat which is spirally wound around an inner core. Gas capillaries run between the mat windings as an internal oxygenator. The AMC-BAL has shown promising results in *in vitro* set-ups, significantly improved survival time in small and large animal ALF models, and proven safety in a phase I clinical study with ALF patients.[223,235]

Two requirements for an efficient BAL are sufficient oxygen (O_2) availability for the highly O_2 demanding hepatocytes and a homogeneous perfusion to supply nutrients to and remove unwanted metabolites from the hepatocytes. Previous *in vitro* studies with the AMC-BAL using porcine hepatocytes showed an increase in anaerobic glycolytic metabolism after 4 days, suggesting limited O_2 availability.[219,275,277] To assess the O_2 availability inside the AMC-BAL and to attain clues for improvements, a numerical model was developed to investigate fluid flow and O_2 transport in the AMC-BAL using computational fluid dynamics (CFD) simulations.[278] This model was previously applied to two three-dimensional representative unit volumes – micro models – of the AMC-BAL, each combined with two proposed hepatocyte distributions. Under standard operating conditions and with the imposed stringent O_2 uptake rates, only 16 to 29% of all hepatocytes were able to consume O_2 at minimally 90% of their maximum uptake rate ($V_{ratio} > 0.9$). This measure of O_2 availability was doubled by either doubling the number of gas capillaries or by doubling the pO_2 of the oxygenation gas (pO_{2-gas}). Combination of the latter two strategies resulted in 3- to 4-fold $V_{ratio} > 0.9$ values.

These recommendations to increase O_2 availability were experimentally evaluated in an *in vitro* study.[293] This study compared four configurations: the *original* AMC-BAL and a *new* design bioreactor with double number of gas capillaries and a 2.2-fold thinner mat, both under standard and doubled pO_{2-gas} . The *new* design AMC-BAL combined with doubled pO_{2-gas} showed significantly reduced anaerobic glycolysis, and obtained significantly higher metabolic stability and approx. 1.6- to 2-fold liver-specific functionality of porcine hepatocytes as compared to the original design under standard oxygenation.[293] As such, this *in vitro* study

qualitatively confirmed the classification of the bioreactor configurations based on O₂ availability as simulated in the micro model study.[278]

However, the aforementioned simulated increase in O₂ availability was persistently larger than the increase in functionality found *in vitro*. This was illustrated by the fact that although a 2-fold increase in O₂ availability was predicted in the micro model study, the new design bioreactor with standard oxygenation did not show a significantly improved hepatic function as compared to the original design under standard oxygenation. This discrepancy could still be due to local limited O₂ availability or to inhomogeneous perfusion in the AMC-BAL, as the micro model approach has several limitations which preclude extrapolating results to the *in vitro* situation. Important limitations are (1) the difference between the *in vitro* cell distribution of the AMC-BAL vs. the two proposed -hypothetical- cell distributions in the micro model; (2) the observed irregular placement of gas capillaries inside the AMC-BAL vs. the equidistant location in the micro model; (3) the presence of an inlet and outflow zone in the AMC-BAL containing oxygenation gas capillaries, which was not constructed in the micro model, and (4) the imposed hepatocyte O₂ consumption rate (OCR).

To more accurately assess perfusion and O₂ availability in the AMC-BAL and to gain insight in the *in vitro* O₂ consumption of primary porcine hepatocytes in the AMC-BAL, a more realistic model is required. In this study, we quantitatively assessed the *in vitro* hepatocyte distribution in the AMC-BAL and applied it to full scale computer models of the AMC-BAL. In the original design 'macro' model, as well as in a 'macro' model of the new design with double number of capillaries and a 2.2-fold thinner mat, fluid flow and O₂ availability was analyzed while varying the pO_{2-gas}. Furthermore, the influence of the imposed hepatocyte O₂ consumption parameters (V_M and K_M) was studied by using two sets of values in the numerical analysis. As possible validation, simulated culture medium outlet pO₂ (pO_{2-med}) was compared to *in vitro* measured pO_{2-med} values. Subsequently, *in vitro* hepatocyte O₂ consumption parameters were also estimated by matching in numero and *in vitro* outlet pO_{2-med} for different bioreactor configurations. As such, the influence of different AMC-BAL configurations on the possible *in vitro* hepatocyte oxygen consumption rate (OCR) in the AMC-BAL was assessed. Finally, the relation between simulated O₂ availability, estimated O₂ consumption and *in vitro* functionality is discussed.

2 Materials and Methods

2.1 Full scale computer model of the AMC BAL

The internal geometry of the laboratory-scale AMC-BAL bioreactor is schematically drawn in Fig. VII-1. The bioreactor consists of a cylindrical polycarbonate housing (inner diameter $\phi = 23.4$ mm; Fig. VII-1-l) in which two pieces of three-dimensional (3D) non-woven polyester matrix mat (Fig. VII-1-e/g) are spirally wound around a massive inner core ($\phi = 5$ mm; Fig. VII-1-i). A space between the two mat segments (Fig. VII-1-f) is left open for an additional hepatocyte seeding port (Fig. VII-1-o). In the hydrophilic matrix, high-density hepatocyte culture is possible. Between the matrix windings, hydrophobic gas capillaries (outer $\phi = 380$ μm ; Fig. VII-1-m) are positioned in parallel along the entire bioreactor as an internal oxygenator system to supply O_2 to the hepatocytes. Under standard operating conditions, culture gas (95% air, 5% CO_2) is perfused through these capillaries. Culture medium enters the bioreactor through an inlet port (Fig. VII-1-c) and flows through the inflow zone (Fig. VII-1-j) past the hydrophilic matrix mat and through the void inter-capillary space (Fig. VII-1-n). Culture medium exits the bioreactor via the outflow zone (Fig. VII-1-k) through the outlet port (Fig. VII-1-d). These and other dimensions were determined on a single specimen or were supplied by the manufacturer.

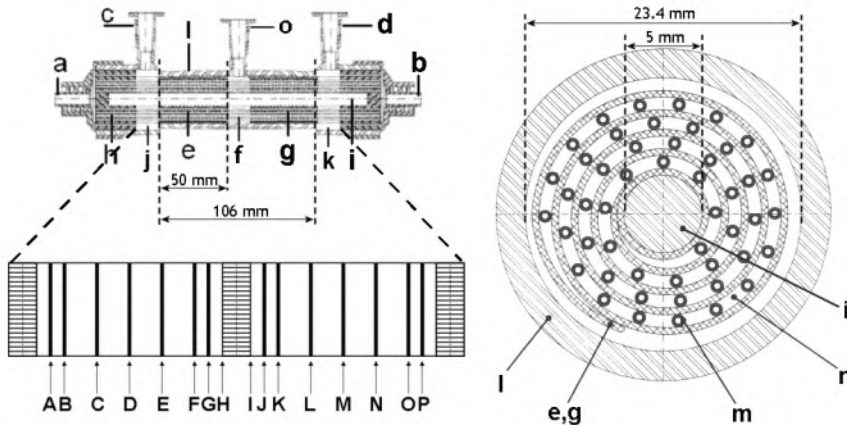


Fig. VII-1: Longitudinal (upper left) and transverse (right) view of the internal geometry of the AMC-BAL with a = gas outlet; b = gas inlet; c = plasma inlet port; d = plasma outlet port; e = first mat segment; f = interspace; g = second mat segment; h = polyurethane potting to separate gas and fluid compartment; i = inner core; j = inflow zone; k = outflow zone; l = polycarbonate housing; m = gas capillaries; n = inter-capillary space through which fluid flows; o = central hepatocyte loading port. Locations of histological slices through the mat segments are indicated (lower left).

Two full scale –macro– computer models were created using the modeling software Gambit 2 (Fluent Inc, Sheffield, UK): (1) the *original* design with 300 capillaries along the 400 μm thick mat; and (2) the *new* design with a double number of capillaries (600) along a 2.2-fold thinner mat (183 μm).

To match the spiral course of the mat, parameters of a logarithmic spiral equation were determined in Matlab (The MathWorks Inc., Natick, Massachusetts, U.S.A.) using the mat thickness, the diameter of the capillaries and the inner and outer radius of the geometry. A complementary spiral equation was found to describe the location of the capillaries along the matrix windings. Capillary locations along the spiral mat were randomized –as seen *in vitro*– by arbitrarily varying the distance between two consecutive capillaries between a minimal (2 x 160 μm , i.e. two times the maximal hepatocyte cell layer thickness around a capillary found *in vitro*), and a maximal distance (2 x distance between two equidistant capillaries, which is equal to spiral mat length divided by ‘the number of capillaries minus 1’).

The outer housing was drawn manually, but Matlab generated ‘journal’ files were used to automate the construction of the gas capillaries. The matrix was not effectively drawn but was implemented by using a user-defined spatial variable in the solver software (Fluent, Fluent Inc, Sheffield, UK) indicating the mesh elements belonging to the matrix windings. A layer of mat was also implemented to cover the inner housing wall as seen *in vitro*.

2.2 Mesh independency

Mesh independence was studied by performing simulations on a micro model with a mesh equivalent to the macro model and comparing these results to the previous mesh independent study[278]. The latter mesh is illustrated in Fig. VII-2-left. Numbers indicate number of nodes on the edge (s.r. = successive ratio; ds = double sided). The location of the mat and of the intercapillary space (ICS) where the fluid flows are depicted. Node numbers along the Z-axis show longitudinal mesh resolution in the first mat segment, the interspace, and the second mat segment respectively. This mesh independent grid contains approx. 3.75 million finite volume elements (see also Chapter V:2.4). As the size of the macro model corresponds to at least 300 micro model equivalents (plus the inlet and outlet zones), the mesh resolution must be lowered to limit the number of elements to a feasible number. The reduced macro model mesh is illustrated in Fig. VII-2-right. A six-layer boundary layer is applied to each capillary with 24 (= 4 quadrants of 6 nodes) nodes on its circumference. A triangular grid is paved across the inlet boundary face. The Cooper mesh technique is used to construct a longitudinally structured grid. The micro model with the macro model equivalent mesh contains approximately 30’000 finite volume elements; two orders of magnitude less than the micro model mesh used in Chapter V. The entire macro model contains between 17.2 and 18.4 million finite volume cells.

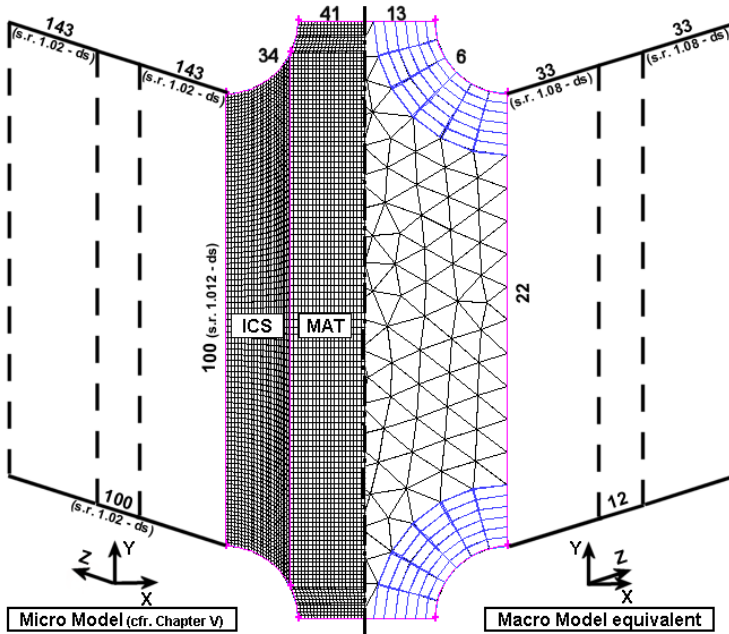


Fig. VII-2: Finite volume mesh on the inlet plane of the micro model used in the (mesh independent) micro model study in Chapter V (left) as compared to a micro model with a mesh equivalent to the one used in the macro model (right). Numbers indicate number of nodes on the edge (s.r. = successive ratio; ds = double sided). The location of the mat and of the intercapillary space (ICS) where the fluid flows are depicted. Node numbers along the Z-axis show longitudinal mesh resolution in the first mat segment, the interspace, and the second mat segment respectively. The Cooper mesh technique is used to sweep the mesh along the Z-axis to a longitudinally structured grid. By comparing simulation results of oxygen availability between both micro models, the error of using a lower resolution mesh in the macro model (right) can be determined.

Simulation of oxygen availability on the inline micro model with hepatocyte distribution 2 (cfr. Chapter V) was repeated on the micro model with a macro model equivalent mesh. Results of oxygen availability are depicted in Table VII-1.

Table VII-1: Oxygen availability in the inline micro model with hepatocyte distribution 2 as described in Chapter V, on the micro model with mesh independent solution and on a micro model with a mesh equivalent used to the macro model of Chapter VII. Relative errors are given between brackets.

% Cells with $V_{ratio} > 0.9$	Mesh independent micro model (cfr. Chapter V)	Macro model equivalent
Total	28.8%	29.8% (+3.3%)
In mat	3.3%	3.6% (+9.2%)
In capillary cell layer	54.1%	53.2% (-1.7%)

Despite the large difference in mesh resolution, a relative error of only +3% in O_2 availability percentages (% cells with $V_{ratio} > 0.9$) of the macro mesh equivalent as compared to the mesh independent solution was found and considered acceptable.

2.3 *In vitro* hepatocyte distribution in the AMC BAL

Two original design bioreactors (BAL₁ and BAL₂) were used to analyze the *in vitro* hepatocyte distribution inside the AMC-BAL. Each bioreactor was seeded with 1 billion freshly isolated porcine hepatocytes and cultured for 7 days, as described previously.[273] After 7 days, each bioreactor was fixed in 10% formalin and embedded in paraffin, as described previously.[270,277] At sixteen positions along the longitudinal axis (Fig. VII-1), two consecutive 8 μm thick cross-sectional slices were cut and stained with hematoxylin and eosin (HE). High resolution digital images of these histological sections were processed into black-and-white format, in which cellular mass was designated as black, using digital image processing software (CS2, Adobe Systems Inc., CA, USA). On these images, the area between the inner core and the outer housing was subsequently divided in 300 subsections using a cylindrical grid. The blackness of each subsection (Fig. VII-3) was determined as the average grey value (dimensionless, range 0 – 1) in the subsection area, and considered a measure for local hepatocyte number and density.

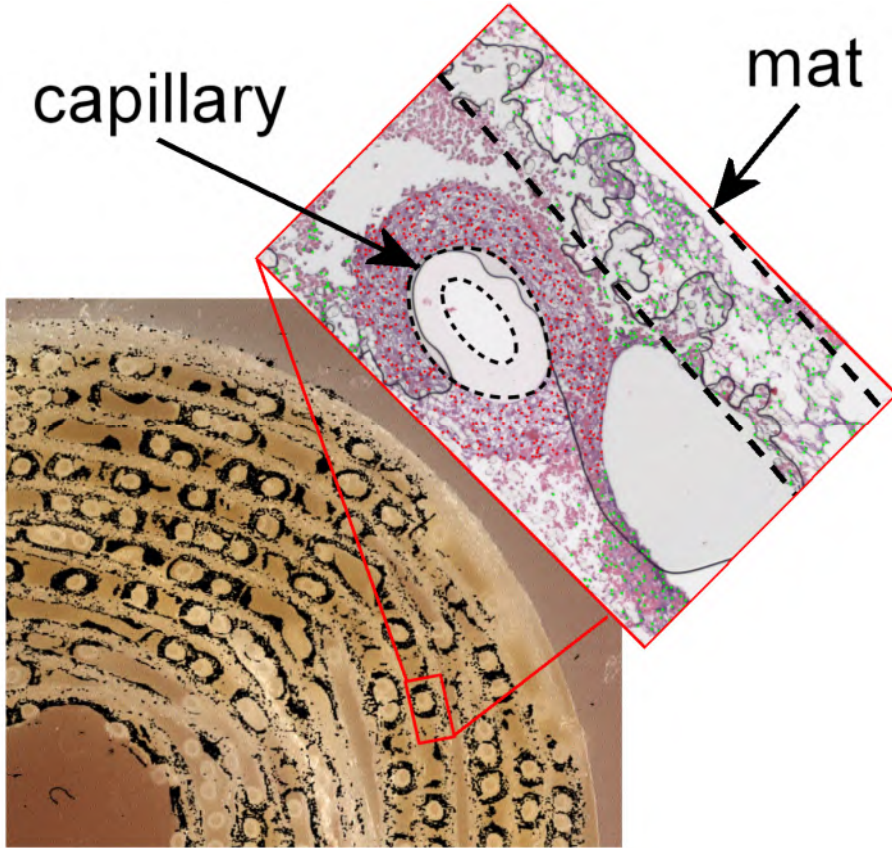


Fig. VII-3: Cross-section of the paraffinized AMC-BAL with superimposed a black-white image of a HE staining (black designates cellular mass). Insert shows a microscopic picture of a subsection from which cell number and surface area were determined.

To correlate blackness to local hepatocyte number and density per subsection, eight categories of blackness values were selected, i.e. 0, 5, 10, 15, 20, 25, 30 and 35% blackness. For each category, 4 subsections were randomly identified on the histological sections, resulting in 32 allocated subsections. Per allocated subsection, the number of individual hepatocytes was counted manually on a microscopic view of the specific subsection in a self-written routine in Matlab. A distinction was made between hepatocytes located inside the matrix and hepatocytes located in a cell layer around a gas capillary. Furthermore, the surface area containing hepatocytes was determined on each of the subsections (DicomWorks; <http://dicom.online.fr/>). This surface area was converted to volume by multiplication with slice thickness (8 μm). Dividing the cell count by this volume resulted in a three-dimensional hepatocyte density.

The correlations between blackness and cell count and between blackness and cell density in a subsection were split based on the presence of a capillary cell layer. As a result, three "blackness to cell count and density" correlations were identified: (1) a correlation for the cell layer around the capillaries (if present), (2) a

correlation for the mat in case a capillary cell layer (CCL) was present, and (3) a correlation for the mat if no CCL was present. To determine which of the three correlations should be used per subsection category, a relation between subsection blackness and the probability of a cell layer around the capillary was needed. For this, twelve hundred (4 x 300) subsections (blackness range 0 – 40%) from 4 arbitrary slices were scored for the presence of a cell layer around the capillary. From this, a piece-wise linear function relating subsection blackness to the presence of a cell layer around a capillary was then calculated.

To translate the experimental data to the numerical model, the average of duplicate blackness values of each subsection was used and interpolated axially in between slice locations to the axial positions of the structured numerical grid. If part of a slice was lost in the histological process, the blackness of the corresponding subsection of the duplicate slice was used. Using the piece-wise linear function, the appropriate correlations, i.e. cell layer present or not, were used to determine the cell numbers and densities around capillaries and inside the matrix. The mat volume containing hepatocytes and capillary cell layer thickness were calculated from the obtained density and number of cells. For the "original" design macro model, the information determined from one subsection was applied to one capillary and one 300th of the mat in the corresponding transverse cross-section of the numerical model. For the "new" design, the cell layer thickness was divided by two, hereby maintaining hepatocyte cell density.

2.4 Modeling fluid flow

To simulate fluid flow, the commercial CFD package Fluent 6.2 (Fluent Inc, Sheffield, UK) numerically solved the steady-state Navier-Stokes equations. Standard pressure discretization and second order upwind momentum discretization were used. Pressure-velocity coupling scheme was SIMPLE. Culture medium was modeled as an incompressible, isothermal, Newtonian fluid with a density ρ of 1001.2 kg/m³ and a dynamic viscosity μ of 0.69 mPa.s at 37°C.[278] The non-woven polyester matrix was modeled as an isotropic homogeneous porous zone. At locations marked by the user-defined variable which designates the mat, a viscous resistance term was imposed in the momentum equation to mimic the hydraulic resistance of the matrix.[278] Resistance to flow of hepatocyte cell layers was modeled using the same viscous resistance factor. An inlet flow rate of 15 ml/min was applied at the entrance of the inlet luer lock. Outlet boundary condition was a zero pressure outflow; the capillary walls were 'no-slip' walls.

2.5 Modeling O₂ transport and consumption

To simulate O₂ transport and consumption, Fluent 6.2 solved the steady-state convection-diffusion-reaction equation (Eq. VII-1). Discretization scheme was set to QUICK.

$$\frac{\partial}{\partial x_i} (\rho u_i \phi - \rho D \frac{\partial \phi}{\partial x_i}) = S_\phi \quad \text{Eq. VII-1}$$

In Eq. VII-1, the transported scalar ϕ is the local O₂ concentration (vol. %), which is also the product of the O₂ solubility α and the local O₂ partial pressure (pO₂) according to Henry's Law ($\phi = \alpha \cdot pO_2$). Oxygen solubility α is 3.1385 x 10⁻⁵ ml O₂ / mmHg*ml fluid in culture medium. D is the O₂ diffusion coefficient, which is 2.92 x 10⁻⁹ m²/s in free culture medium and 2.48 x 10⁹ m²/s in the matrix.[239,240,241,242] Hindered O₂ diffusion by the reduced diffusivity of O₂ through hepatocytes was modeled by an empirical equation which relates the effective diffusion coefficient to the local free diffusion coefficient, the intracellular diffusion coefficient, and the cell volume fraction, as previously described. [251,278]

Oxygen consumption by primary porcine hepatocytes inside the AMC-BAL was modeled by an additional source term S_ϕ based on Michaelis-Menten kinetics (Eq. VII-2), and implemented only in regions containing hepatocytes.

$$S_\phi = -\rho V_M \rho_{cell} \frac{\phi}{\phi + \alpha K_M} \quad \text{Eq. VII-2}$$

In this term, ρ_{cell} is the hepatocyte density, and V_M and K_M are the maximum O₂ consumption rate and the Michaelis-Menten constant respectively. O₂ supply through gas capillaries was modeled by imposing a constant 150 or 300 mmHg pO₂ on the capillaries' outer walls, corresponding to standard or doubled pO₂ of culture gas used *in vitro* (95% air, 5% CO₂). Recirculation of culture medium in the *in vitro* set-up was modeled by setting inlet boundary pO₂ value equal to the mass weighted average of the culture medium outlet boundary face. All other boundary faces had no-flux boundary conditions.

Hepatic O₂ availability was quantified using the 'effective hepatocyte utilization ratio V_{ratio} ', which was defined as the ratio of the observed O₂ consumption rate (OCR) to the maximal hepatocyte OCR.[232,278] The percentage of hepatocytes that reached a $V_{ratio} > 0.9$, i.e. being able to consume at minimally 90% of the maximal uptake rate, was reported as a measure for O₂ availability.

2.6 Simulation overview

An overview of simulations and numerical results of O₂ availability is presented in Table VII-2 (see p.209).

Four AMC-BAL configurations, as were tested *in vitro* [293], were simulated using full-scale macro models with *in vitro* determined hepatocyte distribution: the *original* macro model design with standard (G1) and doubled pO_{2-gas} (G2); and the *new* design macro model with standard (G3) and doubled pO_{2-gas} (G4). To allow comparison with previous micro model results, identical O₂ consumption parameters were used as derived from Balis *et al.* [243] (V_M of 0.7286 nmol/(s.10⁶ cells) and K_M of 2.0 mmHg). These values correspond to most stringent O₂ requirements for primary porcine hepatocytes in plate culture. Simulations were repeated using a lower O₂ uptake rate ($V_M = 0.04$ nmol/(s.10⁶ cells); $K_M = 7.0$ mmHg; from Custer *et*

al.[232,247]) as measured for porcine hepatocytes in microcarrier culture. As such, the influence of hepatocyte O₂ uptake on O₂ availability and outlet pO_{2-med} was determined.

Finally, outlet pO_{2-med} values of G1 to G4 were compared with experimental measurements [293]. As outlet pO_{2-med} of a bioreactor with a given design, operating conditions (e.g. flow rate, pO_{2-gas}), and hepatocyte distribution is only determined by the O₂ uptake characteristics of the hepatocytes, a relation between outlet pO_{2-med} and hepatic OCRs (i.e. V_M) can be determined. For this purpose, simulations were performed on G1 through G4 with several V_M values between 0 and 0.22 nmol/(s.10⁶ cells). K_M was kept constant at 7 mmHg.[243,247] Using these relations, the experimentally measured outlet pO_{2-med} values allow extrapolating estimated *in vitro* hepatocyte OCR (V_M) in the AMC-BAL, together with the corresponding percentage of cells with V_{ratio} > 0.9 as a measure for hepatic O₂ availability.

3 Results

3.1 *In vitro* hepatocyte distribution in the AMC-BAL

The piece-wise linear function relating subsection blackness to the presence of a cell layer around a capillary was calculated according to Eq. VII-3.

$$\begin{cases} \text{blackness} \leq 4.5\% \Rightarrow \text{probability}_{\text{cell layer}} = 0 \\ 4.5\% < \text{blackness} \leq 24.4\% \Rightarrow \text{probability}_{\text{cell layer}} = 5.026 \cdot \text{blackness} - 0.226 \quad (R^2 = 0.94) \\ 24.4\% < \text{blackness} \Rightarrow \text{probability}_{\text{cell layer}} = 1 \end{cases} \quad \text{Eq. VII-3}$$

Relations between subsection blackness and absolute number (Fig. VII-4A) and volumetric cell density (Fig. VII-4B) were calculated for three topologies, i.e. (1) the mat if a capillary cell layer (CCL) is present, (2) the CCL in case it is present, and (3) the mat in case no CCL is present. Correlation equations to translate the blackness of each subsection to cell number (# cells) and density (ρ_{cell}) are reported as Eq. VII-4 and Eq. VII-5, respectively.

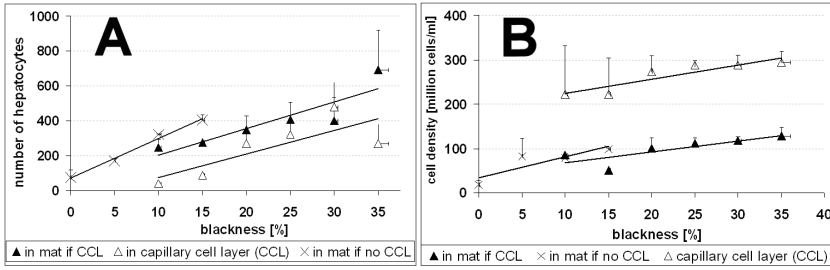


Fig. VII-4: Relations between subsection blackness versus absolute number (A) and volumetric cell density (B). Relations were calculated for three topologies: (1) the mat in case a capillary cell layer was present (\blacktriangle); (2) the capillary cell layer (\triangle), and (3) the mat in case no capillary cell layer was present (\times). Results are given as a mean in each blackness category with average deviations on the results (y-fault bars) and on category blackness (x-fault bars).

$$\left\{ \begin{array}{l} \# \text{ cells in capillary cell layer (CCL)} = 13.56 \times \text{blackness} - 61.11; \mathfrak{R}^2 = 0.63 \\ \# \text{ cells in mat if CCL is present} = 15.23 \times \text{blackness} + 51.76; \mathfrak{R}^2 = 0.80 \\ \# \text{ cells in mat if no CCL is present} = 22.57 \times \text{blackness} + 73.33; \mathfrak{R}^2 = 0.99 \end{array} \right. \quad \text{Eq. VII-4}$$

$$\left\{ \begin{array}{l} \rho_{\text{cell}} \text{ in capillary cell layer (CCL)} = 3.26 \times \text{blackness} + 190.74; \mathfrak{R}^2 = 0.83 \\ \rho_{\text{cell}} \text{ in mat if CCL is present} = 2.45 \times \text{blackness} + 44.10 + 51.755; \mathfrak{R}^2 = 0.68 \\ \rho_{\text{cell}} \text{ in mat if no CCL is present} = 4.75 \times \text{blackness} + 33.49; \mathfrak{R}^2 = 0.76 \end{array} \right. \quad \text{Eq. VII-5}$$

Assessing average blackness of the cross-sectional slices along the longitudinal axis of the AMC-BAL shows a predominant location of hepatocytes near the outer ends of the matrix segments (Fig. VII-5). In the middle parts of the matrix segments, however, less hepatocytes were located. Markedly, no correlation was found between subsection blackness and the location of the subsection within a single cross-sectional slice, although there is a significant variation of blackness within a slice.

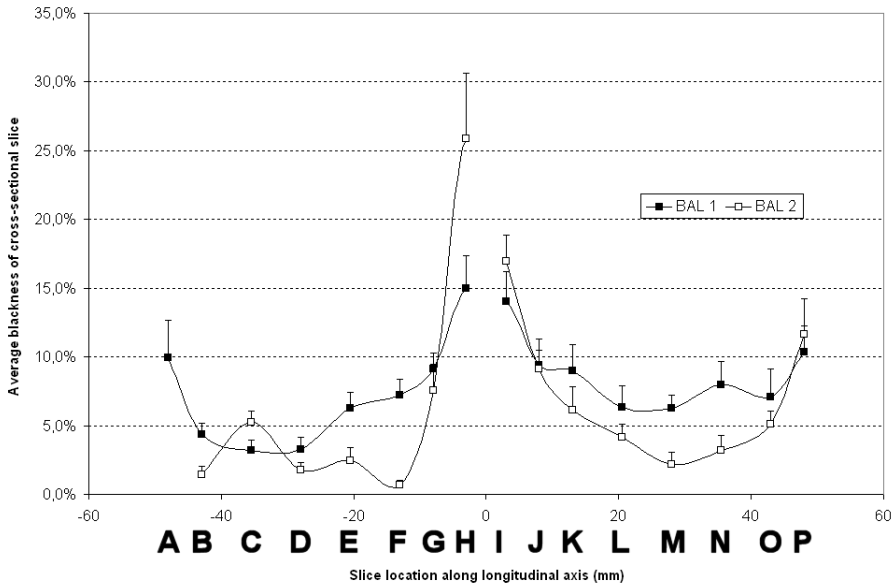


Fig. VII-5: The *in vitro* determined hepatocyte distribution in the AMC BAL for BAL1 and BAL2. This profile illustrates the blackness averaged over all duplicate subsections in a cross-sectional slice along the longitudinal axis of the bioreactor. Fault bars indicate the average deviation of the 2×300 subsections to the average blackness of duplicate cross-sectional slices. Slice locations correspond with Fig. VII-1.

Only the *in vitro* determined hepatocyte distribution of BAL1 was implemented in the full scale AMC-BAL computer model because, (1) both duplicates of the entire cross-sectional slice A of BAL2 were lost during the histological procedures, and (2) the average of all relative difference between the duplicate slice blacknesses was lower for BAL1 (20%) as compared to BAL2 (28%). Hepatocyte densities in the mat ranged from 0 to 210×10^6 cells/ml, whereas hepatocyte densities in the capillary cell layer ranged from 0 to 410×10^6 cells/ml with cell layer thicknesses between 0 and 155 μm . The full scale AMC-BAL model contained 919.2×10^6 hepatocytes; of which almost 8% of the hepatocytes (70.5×10^6) were located in cell layers around the capillaries.

Fig. VII-6 illustrates the implementation of the *in vitro* determined hepatocyte distribution in the full scale AMC-BAL computer model in a cross-sectional plane close to the start of the first mat segment for both the *original* (Fig. VII-6A) and *new design* (Fig. VII-6B).

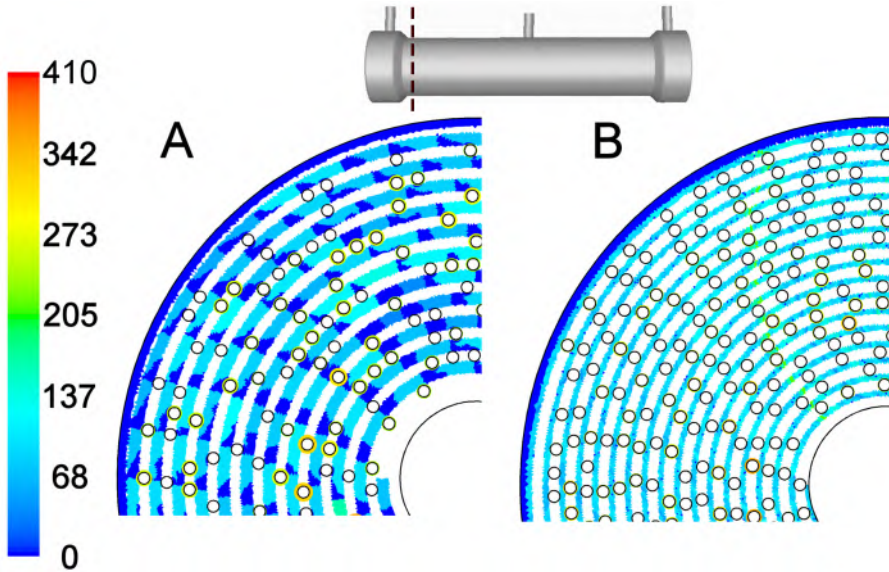


Fig. VII-6: Colorimetric contour plots of hepatocyte density [10^6 cells/ml] in a cross-sectional plane near the beginning of the first mat segment of the AMC BAL model, based on the in vitro determined hepatocyte distribution for the original (A) and new (B) bioreactor design. Black circles indicate gas capillary locations, whereas white spaces indicate the inter-capillary spaces where culture medium flows.

3.2 Fluid flow in a full scale model of the original and new design AMC-BAL

Fluid velocity (mm/s) was simulated in the original design (Fig. VII-7C), as well as in the new design (Fig. VII-7D) full scale model of the AMC-BAL. Velocity magnitudes inside the matrix were two orders of magnitudes lower than in the region between capillaries and matrix windings. Maximal velocities in these inter-capillary spaces were approx. 2.2 mm/s for the original design (Fig. VII-7C) and 2.4 mm/s for the new design AMC-BAL (Fig. VII-7D). Velocities in the inter-capillary spaces were significantly lower when the distance between two consecutive capillaries was smaller than the distance between the mat windings ($340 \mu\text{m}$). High velocities, i.e. max. 13.3 mm/s, were present in the original design near the inner core. This phenomenon of preferential flow was almost negligible in the new design AMC-BAL.

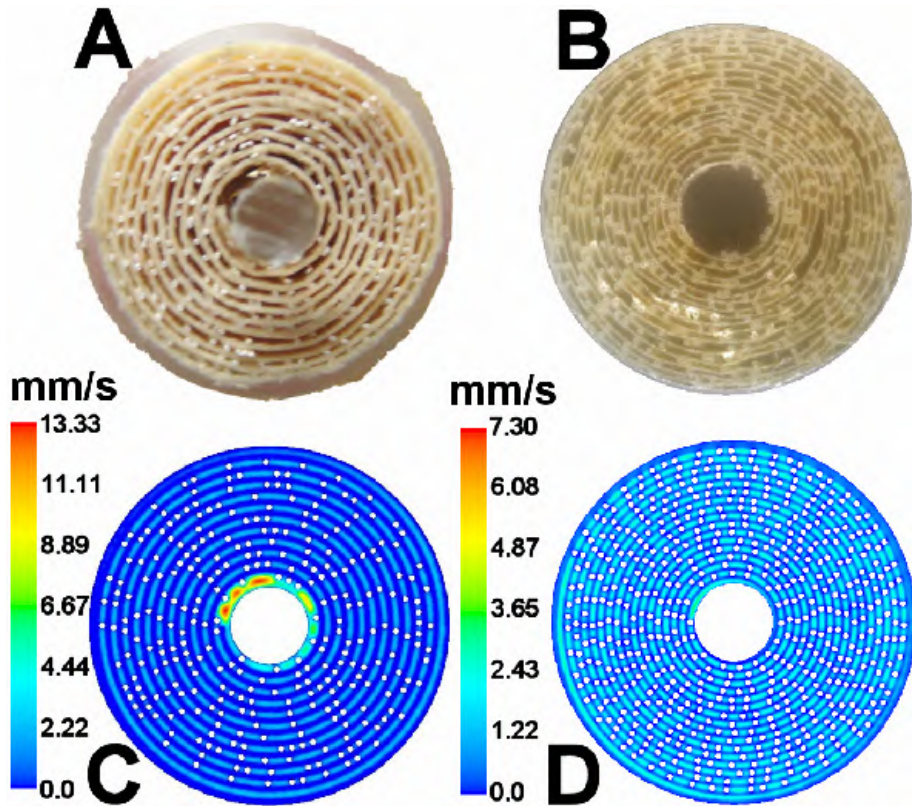


Fig. VII-7: Transverse cut of an in vitro original design (A) and new design AMC-BAL (B), with double number of capillaries and 2.2-fold thinner mat. Colorimetric contour plots show velocity magnitudes (mm/s) in a cross-sectional plane (cfr. Fig. VII-6) through a mat segment of the original (C), and in the new design (D) AMC-BAL macro model. A strong preferential flow location in a gap near the core (see A) is visible in (C).

3.3 Oxygen availability and medium outlet pO_2 in the AMC-BAL

Table VII-2 gives the results of O_2 availability of all numerical simulations on different macro models and under different operating conditions.

Table VII-2: Simulation overview and numerical results of O₂ availability expressed as the percentage of hepatocytes with V_{ratio} > 0.9 and outlet pO₂ values of recirculating culture medium obtained from simulations and experimental measurements. MT = mat thickness; No. Caps = number of capillaries, pO_{2-gas} = oxygenation gas pO₂, pO_{2-med} = medium pO₂ at outlet. In vitro pO_{2-med} values were derived from Poyck et al.[293]

Case	Model	MT [μm]	No. Caps	pO _{2-gas} [mmHg]	V _M [nmol/(s. 10 ⁶ cells)]	K _M [mmHg]	<i>in numero</i>		<i>in vitro</i>
							% cells V _{ratio} > 0.9	pO _{2-med} [mmHg]	pO _{2-med} [293] [mmHg]
G1	Original	400	300	150	0.7286	2.0	12.4 %	56	127.7±2.4
					0.04	7.0	96.0 %	116	
G2	Original	400	300	300	0.7286	2.0	27.1 %	116	231.2±3.1
					0.04	7.0	100 %	264	
G3	New	183	600	150	0.7286	2.0	34.9 %	70	144.9±1.8
					0.04	7.0	99.1 %	136	
G4	New	183	600	300	0.7286	2.0	70.8 %	156	249.5±3.3
					0.04	7.0	100 %	286	

The O₂ availability of the original design under standard oxygenation (G1) was 12.4%, which is below the range specified by the micro model study by Mareels *et al.*[278] (15.7% - 28.7%), illustrating the limitation of this micro model study.

The impact of several strategies on O₂ availability and outlet pO_{2-med} were assessed in three subsequent macro model configurations, i.e. G2 to G4. When compared to G1 (12.4%), O₂ availability increased in G2 (27.1%), G3 (34.9%) and was highest in G4 (70.8%). Nevertheless, outlet pO_{2-med} in G3 (144.9 mmHg) was lower than G2 (231.2 mmHg), maximal in G4 (249.5 mmHg), and lowest in G1 (127.7 mmHg). These simulations were done with the stringent OCR from Balis *et al.*[243] (V_M = 0.7286 nmol/(10⁶ cells.s) and K_M = 2.0 mmHg).

The same simulations were also performed with a second set of less stringent hepatic O₂ uptake rates (V_M = 0.04 nmol/(s.10⁶ cells); K_M = 7 mmHg) to demonstrate the change in apparent O₂ availability and outlet pO_{2-med}. V_{ratio} > 0.9 percentages increased in all cases, ranging from 96% to 100%. Outlet pO_{2-med} increased to 116, 264, 136 and 286 mmHg for G1, G2, G3 and G4, respectively.

Fig. VII-8 relates various hepatic O₂ uptake rates (V_M) to simulated outlet pO_{2-med} values and hepatic O₂ availability, in the four bioreactor configurations. From this graph, V_M values of G1 to G4 were estimated using the experimentally measured outlet pO_{2-med} of Poyck *et al.*[293]. Hepatocytes in G1 and G3 bioreactors consume approx. the same amount of O₂ (Table VII-3), whereas hepatocytes in G2 and G4 bioreactors consume generally 3-4-fold and 7-fold more O₂ as compared to G1 and G3, respectively. V_{ratio} > 0.9 percentages in these working points of each BAL were higher than 97-98% in all case (Fig. VII-8).

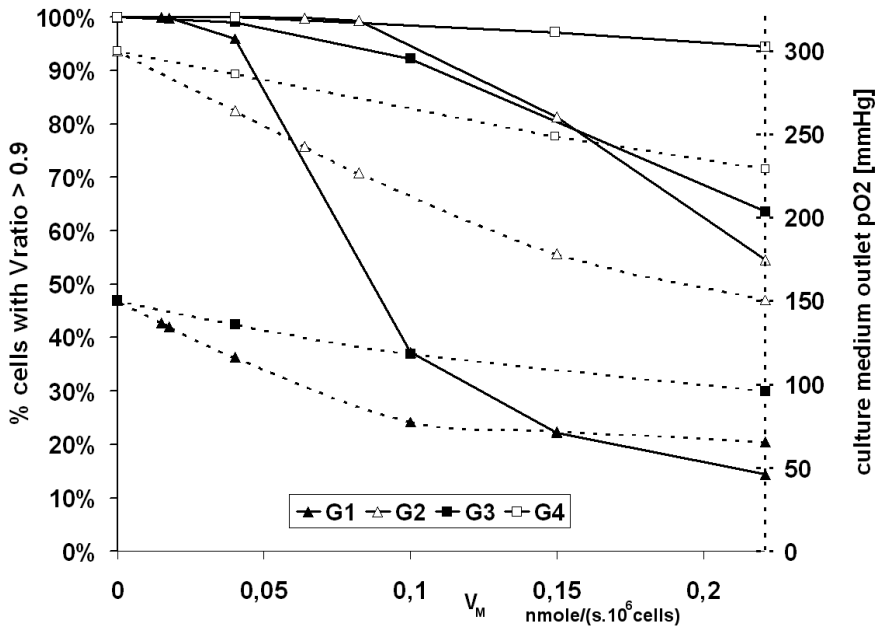


Fig. VII-8: Relation between hepatocyte O_2 consumption (V_M) and culture medium outlet pO_2 (mmHg; right axis, dashed line) as well as '% hepatocytes with $V_{ratio} > 0.9$ ' (left axis). Four AMC-BAL macro models with in vitro hepatocyte distribution are shown, i.e. original design with standard (G1) and doubled pO_{2-gas} (G2), and new design with standard (G3) and doubled pO_{2-gas} (G4).

Table VII-3: Numerically estimated hepatocyte oxygen consumption (V_M) in the four AMC-BAL configurations based on matching of in vitro and in silico pO_{2-med} values.

AMC-BAL macro model	<i>In vitro</i> [293] pO_{2-med} outlet medium	Estimated <i>in vitro</i> V_M [nmol/(s. 10^6 cells)]
G1	127.7±2.4 mmHg	0.02-0.03
G2	231.2±3.1 mmHg	0.07-0.08
G3	144.9±1.8 mmHg	0.01-0.02
G4	249.5±3.3 mmHg	0.14-0.15

4 Discussion

The hepatocyte distribution in the AMC-BAL was quantified and implemented in a full-scale macro model of the AMC-BAL. This model was used to evaluate the AMC-BAL design and to gain insight in the *in vitro* O₂ consumption in the AMC-BAL.

4.1 *In vitro* hepatocyte distribution in the AMC BAL

Two AMC-BAL bioreactors loaded with 1 billion porcine hepatocytes and cultured for 7 days were used to quantify (1) the number of hepatocytes, (2) the cross-sectional as well as the longitudinal hepatocyte distribution and (3) the cell density in specific areas. Total hepatocyte count calculated by applying the determined correlations on all histological slices of BAL₁, was 919 million and closely corresponds with the one billion hepatocytes initially seeded into the AMC-BAL. No preferential distribution of hepatocytes in a cross-sectional plane was found. This is probably due to the continuous 340° rotation of the bioreactor during the 2-hour attachment period after seeding.[293] The axial distribution of hepatocytes in the AMC-BAL, however, showed a clear trend of preferential location of hepatocytes near the extremities of the mat segments. This is explained by the position of the three loading ports through which hepatocytes were seeded according to an approximate 25%-50%-25% loading distribution. Furthermore, the thin inter-capillary spaces (about 340 μm wide) might prevent deep penetration of large porcine hepatocytes aggregates in the mat segments. This *in vitro* hepatocyte distribution was further implemented in full-scale AMC-BAL models.

4.2 Fluid flow and oxygen availability in the *original* design AMC-BAL

Velocity magnitudes in the mat were two orders of magnitude lower than in the inter-capillary space, as also reported earlier.[278] The distance between two consecutive capillaries is quite variable in reality due to the manual fabrication process, but this did not result in large velocity differences in different inter-capillary spaces. The maximal velocity magnitude was determined by the smallest dimension of inter-capillary space, i.e. 340 μm. In case capillaries were very close together, i.e. near 340 μm, the distance between two consecutive capillaries became the limiting distance and maximal velocity dropped.

The loose attachment of the mat to the inner core, however, caused a significant preferential flow near the inner core. Calculations showed that approx. 45% of the bioreactor inflow was shunted through this gap, resulting in a reduction of 55% in effective culture medium flow rate. Although culture medium flow rate is not a

very influencing factor on O_2 availability in the AMC-BAL[278], special attention should be paid during the manual fabrication process.

Under the stringent O_2 uptake rates, 12.4% of the cells in the *original* design AMC-BAL (G1) have enough O_2 to consume at minimally 90% of the maximal O_2 uptake rate ($V_{ratio} > 0.9$). Outlet pO_{2-med} of the recirculating culture medium was 56 mmHg. Oxygen availability is less than predicted in the previous micro model study[278] (15.7% - 28.7%). This is due to the limitations of the micro model approach, and in particular to the more concentrated hepatocyte distribution found *in vitro*, resulting in higher cell densities as were hypothesized in the micro model study (200-400 x 10^6 cells/ml vs. 30-80 x 10^6 cells/ml, respectively). As a consequence, larger local O_2 gradients were present resulting in lower local O_2 availability.

4.3 Strategies to improve O_2 availability in the AMC-BAL

O_2 availability in the original AMC-BAL design (G1) was low when stringent hepatocyte O_2 uptake rates were imposed. We therefore evaluated several strategies to increase O_2 availability according to the recommendations of the numerical micro model study.[278]

The design changes in the *new* AMC-BAL, i.e. double number of capillaries and 2.2-fold thinner mat, have considerable impact on flow distribution inside the bioreactor. Despite the double number of capillaries, average distance between two consecutive capillaries decreased from 1.53 mm to only 1.19 mm, since the thinner matrix allows more mat windings (16 vs. 11). As the distance between mat windings remains the same, more inter-capillary flow surface area is available and velocity magnitudes were expected to drop. However, simulation results showed that maximal velocities were on average slightly higher in the new design, which is explained by the tighter attachment of the thinner mat to the core preventing large preferential flows. This can be translated to the manufacturing process as the thinner mat is more flexible and will allow a closer packed winding around the core in the production process. As a result of the reduced preferential flow, a larger fraction of medium flow rate is available to flow through the inter-capillary spaces, leading to higher velocities.

The design changes in the *new* AMC-BAL also influenced O_2 transport and consumption. O_2 availability (22.5% absolute increase) as well as outlet pO_{2-med} values (+14 mmHg) were increased in the new design (G3) as compared to the original design (G1). Doubling the pO_{2-gas} in the original design (G2) increased outlet pO_{2-med} from 56 mmHg (G1) to 116 mmHg. Despite this higher outlet pO_{2-med} values, O_2 availability of G2 (27.1%) did not increase up to the level of the *new* BAL design (34.9%). This indicates steeper local O_2 gradients and a less homogeneous oxygenation in the original design as compared to the new bioreactor design. Maximal increase in O_2 availability is obtained by doubling outlet pO_{2-gas} in the new

design (G4), resulting in 70.8% of cells with $V_{\text{ratio}} > 0.9$. From these simulations, we conclude that the present strategies to increase cellular O_2 availability are in accordance with the previous numerical micro model study.[278]

4.4 Influence of imposed O_2 consumption rates

All previously mentioned simulations were performed with stringent O_2 consumption parameters (V_M , K_M) derived from monolayer porcine hepatocyte culture (Balis *et al.*[243]). Since O_2 consumption parameters are dependent on the method of cell culture, i.e. monolayer vs. 3D culture, as well as on cell density in 3D culture[232,247,271,272,295] O_2 consumption parameters derived from 3D microcarrier culture of porcine hepatocytes were also imposed on the G1-G4 macro models. These less stringent parameters resulted in increased O_2 availability of minimally 96% for all configurations. From these simulations, one may conclude that if hepatocytes do not consume more O_2 than imposed in this case, O_2 availability in the original AMC-BAL is already sufficient enough. Nevertheless, as mentioned above, the *new* design AMC-BAL is capable of providing more O_2 to the hepatocytes in a more homogeneous way than the *original* design, even if in the latter double oxygenation gas $p\text{O}_2$ is used. In addition, O_2 availability is further improved by also using double oxygenation gas $p\text{O}_2$ in the *new* design. The need to increase oxygen supply is, however, dependent on the hepatocyte O_2 consumption *in vitro*.

4.5 Estimating *in vitro* hepatocyte oxygen consumption rates based on experimental data

Simulated outlet $p\text{O}_{2\text{-med}}$ values did not match experimentally measured outlet $p\text{O}_{2\text{-med}}$ values at day 2 of Poyck *et al.*[293], for any of the previously imposed OCR. As such, additional simulations were performed in G1 to G4 macro models with various OCR (i.e. V_M) to gain insight in how O_2 availability and $p\text{O}_{2\text{-med}}$ change with hepatocyte oxygen requirements. For V_M values smaller than $0.05 \text{ nmol}/(\text{s}\cdot 10^6 \text{ cells})$, O_2 availability is in excess of 95% for any bioreactor configuration. For higher V_M values O_2 availability decreases sharply in the original design. New design (G3) and original design with doubled $p\text{O}_{2\text{-gas}}$ (G2) perform equally better, where in G2 the decline in O_2 availability is steeper than in the new design (G3). The new design bioreactor with increased oxygenation (G4) is able to maintain a 95% O_2 availability up to $0.2 \text{ nmol}/(\text{s}\cdot 10^6 \text{ cells})$ O_2 consumption. Markedly, outlet $p\text{O}_{2\text{-med}}$ is less sensitive to hepatocyte OCR than O_2 availability, and even less so in case of the new design (G3, G4). This again illustrates the improved oxygenation capabilities of the new design AMC-BAL.

As O_2 availability is strongly dependent on imposed OCR, it is useful to assess the *in vitro* oxygen consumption in the AMC-BAL, which also allows assessing the need to increase O_2 supply in the AMC-BAL. Therefore, *in vitro* hepatocyte O_2 consumption (V_M) in the AMC-BAL was estimated by fitting V_M to match simulated outlet pO_{2-med} to the experimentally measured values (Fig. VII-8). However, the relative small decrease of pO_{2-med} with increasing V_M renders the estimation of *in vitro* hepatocyte OCRs sensitive to small changes in measured outlet pO_{2-med} . As such, a range was specified for each case.

From Fig. VII-8, we derived similar OCR estimates for G1 and G3 bioreactors, despite the larger oxygenation capacity of G3 due to the double number of capillaries. Both estimated OCR values corresponded well with experimental OCR values for porcine hepatocytes in a hollow fiber configuration with almost identical hepatocyte densities measured by Patzer *et al.*: $V_M = 0.008 - 0.023$ nmol/(s.10⁶cells); $\rho_{cell} = 150 - 450 \times 10^6$ cells/ml [232]. However, fitted OCR estimates of G2 and G4, both with increased pO_{2-gas} , were higher as compared to hepatocytes in bioreactor designs with standard oxygenation (G1 and G3). Since O_2 availability for all four designs was at least 96%, we conclude from this analysis that estimated *in vitro* hepatocyte OCR values are primarily influenced by the pO_2 levels at which the cells are exposed, rather than spatial, i.e. direct and on-site O_2 supply by additional capillaries. The current estimation analysis also suggests that hepatocytes adapt their OCR to the local environment in the AMC-BAL while maintaining maximal local hepatic O_2 availability. However, as the bioreactor (e.g. G3) is able to sustain higher OCR values with almost maximal O_2 availability, OCR in the new bioreactor design is not limited by a lack of oxygen. As such, other factors besides absolute O_2 level and local O_2 availability must also play an important role in the regulation of hepatocyte OCR.

4.6 Relation between simulated O_2 availability, estimated OCR and *in vitro* functionality

Poyck *et al.*[293] have shown that anaerobic glycolytic metabolism was lower and hepatocyte-specific functionality was higher and more stable at the end of a 6 day culture period according to the group order $G4 > G3 \sim G2 > G1$.

Qualitative agreement of this classification with increased O_2 availability results is present when using the stringent O_2 consumption parameters; cases for which simulated outlet pO_{2-med} did not match *in vitro* measured outlet pO_{2-med} . Using the estimated OCR by matching outlet pO_{2-med} , simulation results show almost maximal hepatocyte O_2 availability in all cases, whereas clearly differences in anaerobic glycolytic metabolism has been shown *in vitro*[293]. This suggests that O_2 availability (as defined in this study: % cells with $V_{ratio} > 0.9$) may not be used as an indicator of *in vitro* improvement. Similarly, the estimated OCR itself cannot be directly correlated to the increase in functional activity found *in vitro*. Although the bioreactor with highest functionality found in Poyck *et al.*[293] (i.e. G4) was found to consume most O_2 , G2 and G3 showed highly similar *in vitro* functionality, but their

estimated OCR differed greatly. This proves that other factors than O_2 availability (e.g. pO_2 level, increased cell-to-cell and cell-to-matrix contact) play a determining role in anaerobic glycolytic metabolism and hepatocyte functionality between bioreactor configurations, as was already suggested for the regulation of hepatocyte OCR. These factors are not included in the numerical model at this point. In this regard, it is noted that the estimated OCR must be regarded as an average value for the entire BAL. A more realistic methodology could include a spatial variation of V_M value in the AMC-BAL model, based on local absolute pO_2 and hepatocyte density. Subsequent simulations may show a better correlation between e.g. local O_2 availability and reduced anaerobic glycolytic metabolism in the different AMC-BAL configurations, while maintaining a validated pO_{2-med} . This V_M distribution however cannot be deduced from pO_{2-med} only.

5 Conclusions

A protocol was successfully devised to accurately quantify *in vitro* cell distributions in a bioreactor, based on histological sections. Simulations on full scale AMC-BAL macro model with a realistic *in vitro* determined hepatocyte distribution facilitated a more accurate analysis of fluid flow and O_2 availability in the AMC-BAL as compared to the previous micro model of Mareels *et al.*[278] We observed a large preferential flow near the inner core in the original design bioreactor. This preferential flow, however, was absent in the new design bioreactor with a double number of gas capillaries and 2.2-fold thinner mat. This configuration also led to a more homogeneous perfusion and higher O_2 availability for the hepatocytes. Doubling the oxygenation gas pO_2 further increased O_2 availability. Using stringent O_2 consumption parameters, the classification of the four AMC-BAL configurations (*original* and *new* design under standard or doubled oxygenation gas pO_{2-gas}) according to simulated O_2 availability corresponded to the functional results observed in the *in vitro* study by Poyck *et al.*[293].

Hepatocyte OCR in the four configurations of the AMC-BAL were also estimated by matching simulated pO_{2-med} to *in vitro* values. This resulted in almost identical OCR for both design under standard oxygenation. Doubling of the pO_{2-gas} resulted in 3- to 7-fold higher hepatocyte oxygen consumption. Using the estimated OCR's, maximal hepatocyte oxygen availability was found in all configurations. This suggests that hepatocytes adapt their OCR to the local *in vitro* environment in the AMC-BAL while maintaining maximal local hepatic O_2 availability. However, as the new bioreactor design is able to sustain higher oxygen consumption values, hepatic OCR is not limited by a lack of oxygen in the new design bioreactor.

No straight-forward correlation could be established between simulated O_2 availability, OCR, and the *in vitro* anaerobic glycolysis and functional activity of the hepatocytes in the four AMC-BAL configurations. For this, other factors which play an important role in the regulation of hepatocyte OCR and metabolic function (e.g.

pO₂ level, increased cell-to-cell and cell-to-matrix contact, dependency on hepatocyte density) should be implemented in future models.

6 Acknowledgements

The authors are grateful to Daniele Galavotti of the RanD company (Italy) for the very careful construction of the remodelled bioreactor. First author's research is supported by a BOF-grant (O11D09503) from Ghent University, Belgium. Third author was supported by the Belgian Fund for Scientific Research-Flanders (FWO grant 'Krediet aan Navorsers' 1.5.115.06) and is working as a post-doctoral fellow for FWO-Flanders. The second and fourth authors express their gratitude to the Netherlands Digestive Diseases Foundation (MLDS), the Technology Foundation of NWO (The Netherlands) and the European Union (QLTR-2000-01889) for financial support.

7 Addendum: micro vs. macro model

7.1 Introduction

The results of this study clearly indicate that modelling flow and oxygen transport in a bioreactor may not be sufficiently accurate when using a simplified unit volume and a hypothetical hepatocyte distribution. Three major modelling simplifications have been identified: (1) the difference between the *in vitro* cell distribution of the AMC-BAL vs. the two proposed -hypothetical- cell distributions in the micro model; (2) the observed irregular placement of gas capillaries inside the AMC-BAL vs. the equidistant location in the micro model; (3) the presence of an inlet and outflow zone in the AMC-BAL containing oxygenation gas capillaries, which was not constructed in the micro model. In this addendum, the individual impact of each of these limitations will be determined to assess which is most important when performing numerical simulations in a bioreactor environment.

7.2 Methods

For this purpose, a third macro model of the AMC-BAL was developed. It concerns a so-called 'equidistant original' design macro model with 300 capillaries and a 400 μm thick mat (as in the *original* design), but with the capillaries fixed at equidistant positions (instead of at the more realistic, randomized locations). Simulations on this model will allow assessing the different limitations of the micro model. An overview is given in Table VII-4. Simulations and results of the micro model study (cases 1 and 2 in Table VII-4) by Mareels *et al.* [278] are shown to facilitate comparison with the macro models. Hypothetical hepatocyte distributions were used in these cases. In case 1, all hepatocytes were distributed in the mat ($\rho_{\text{cell, mat}} = 53.7 \times 10^6$ cells/mL),

whereas in case 2, 50% of the cells are homogeneously spread in the mat ($\rho_{\text{cell, mat}} = 31.7 \times 10^6$ cells/mL) and 50% reside in cell layers around the 300 capillaries (thickness = 122 μm ; $\rho_{\text{cell, cap}} = 81.7 \times 10^6$ cells/mL). Using two additional simulations on the ‘equidistant original’ macro model (case 3 and 4 in Table VII-4), the three limitations of the numerical micro model [278] approach were studied.

Firstly, the limitation of modeling only a part of the geometry was assessed by comparing the micro model (case 2) with the ‘equidistant original’ macro model (case 3), both with the hypothesized hepatocyte distribution. *Secondly*, the validity of the hypothesized cell distributions of the micro model study[278] was assessed by comparing the ‘equidistant original’ macro model with a hypothetical (case 3) cell distribution to the case with the *in vitro* determined hepatocyte distribution (case 4). *Finally*, the influence of the irregular capillary location was assessed by comparing the ‘equidistant original’ macro model (case 4) with the *original* design macro model (G1). Both cases use the standard $p\text{O}_{2\text{-gas}}$ and the *in vitro* determined hepatocyte distribution. All simulations were made using standard boundary conditions and the O_2 consumption parameters derived from Balis *et al.*[243] (V_M of 0.7286 $\text{nmol}/(10^6 \text{ cells.s})$ and K_M of 2.0 mmHg)

Table VII-4: Additional simulation overview for the assessment of the micro model study limitations.

#	Model	Hepatocyte distribution	% cells $V_{\text{ratio}} > 0.9$	<i>in numero</i> $p\text{O}_{2\text{-med}}$
MICRO model study (Mareels <i>et al.</i>)				
1	Micro-1	100% in mat	15.7 %	-
2	Micro-2	50% in mat 50% around cap.	28.7 %	-
MACRO model study				
3	Equidistant original	50% in mat 50% around cap.	25.2 %	44 mmHg
4	Equidistant original	<i>in vitro</i> determined	12.2 %	62 mmHg
G1	Original (G1)	<i>in vitro</i> determined	12.4 %	56 mmHg

7.3 Results

O_2 availability between micro-2 model (see Table VII-4; 28.7%) and macro model ‘equidistant original’ (case 3; 25.2%) using the same hypothesized hepatocyte distribution differed only 3.5%, indicating a high similarity between the micro and macro model. ‘ $V_{\text{ratio}} > 0.9$ ’ value of the ‘equidistant original’ macro model with the *in vitro* determined hepatocyte distribution (case 4) was about half compared to the analogous model using the hypothesized hepatocyte distribution (case 3), supporting

the importance of a realistic hepatocyte distribution. In contrast, outlet $pO_{2\text{-med}}$ was 18 mmHg higher for case 4 when compared to case 3. With only different capillary locations, O_2 availability of case 4 (12.2%) was similar to the original macro model (G1; 12.4%). However, outlet $pO_{2\text{-med}}$ was 6 mmHg higher for case 4 (62 mmHg) as compared to case 5 (56 mmHg).

7.4 Discussion

Oxygen availability in the original AMC-BAL design (G1, 12.4%) was lower than in the micro model study using hypothesized hepatocyte distributions (15.7–28.7%). The *in vitro* determined hepatocyte distribution showed that almost 8% of the hepatocytes were located in capillary cell layers. As a result, we expected O_2 availability to be close to 17–18%. Simulations, however, resulted in values of 12.2–12.4%, which can be explained by the limitations of the micro model approach.

The first reason is related to the intrinsic effect of modeling the entire bioreactor. This was assessed by comparing case 2 and 3. The influence on the value of oxygen availability was relatively small. Although modelling the entire bioreactor and implementing the recirculation of the culture medium does not seem necessary to assess the general oxygen availability in the bioreactor, the macro model allows conclusively determining possible preferential flow paths inside the bioreactor, and calculating the outlet $pO_{2\text{-med}}$.

Secondly, the influence of the hepatocyte distribution was determined by comparing simulation results in ‘equidistant original’ macro models with either a hypothesized (case 3) or the *in vitro* determined (case 4) hepatocyte distribution. The strong decrease in O_2 availability in case of the *in vitro* cell distribution was due to the fact that the hepatocyte distribution *in vitro* was not homogeneous throughout the longitudinal axis, resulting in higher cell densities than presumed and hypothesized in the micro model study (200–400 $\times 10^6$ cells/ml vs. 30–80 $\times 10^6$ cells/ml, respectively). As a consequence, larger local O_2 gradients were present that resulted in lower local O_2 availability.

Finally, the influence of the irregular capillary placement in the AMC-BAL was assessed. Hepatic O_2 availability in the ‘equidistant original’ and ‘original – G1’ macro model, both with *in vitro* hepatocyte distribution, were almost identical (12.2% vs. 12.4%, respectively). However, the different capillary placement did have a noticeable influence on outlet $pO_{2\text{-med}}$ leading to an approx. 10% (+6 mmHg) variation when capillaries were placed equidistant. This was probably caused by the more efficient oxygenation of culture medium by the capillary bundles in the inflow and outflow zone when capillaries are more homogeneously spaced.[296]

7.5 Conclusions

A realistic, *in vitro* determined cell distribution is mandatory for realistic simulations of mass transport in bioreactor systems. The implementation of this cell distribution generally requires a full-scale model of the bioreactor design. However, some geometrical simplifications in the bioreactor computer model may be made to facilitate construction of the model.

Part C:

Conclusions and future prospects

Chapter VIII: Conclusions and Future Prospects

In this dissertation, a combined approach of numerical and experimental techniques was used to assess and improve the performance of an extracorporeal liver support system. Both a potential means of vascular access (central venous catheters) and a promising bioartificial liver system (AMC Bioartificial Liver) were studied. As such, the conclusions and discussion of future prospects of both topics is split in two parts.

1 Central venous catheters

1.1 Conclusions

The study of central venous catheters in this dissertation started with a general overview of possible means of vascular access. Central venous catheters were identified as easy access method, applicable in nearly all patients, and less hemodynamically stressful to the cardiovascular system as compared to e.g. arteriovenous fistulas. However, clinical complications as infection, thrombosis, and stenosis limit the performance of central venous catheters. In this dissertation, the hemodynamic performance parameters of several catheter designs are studied. The flow and shear stress distribution inside the catheter are important as stagnating blood zones and shear stress damage to platelets may promote blood clot formation. Highly elevated shear stresses (>200 Pa) may even induce hemolysis. Access recirculation is studied as it is an important factor in the efficiency of any extracorporeal therapy.

Using Computational Fluid Dynamics simulations, the influence of the presence and size of catheter side holes in the blood withdrawing ('arterial') lumen was studied on a generic step-tip (shotgun-type) dual lumen catheter. The catheter was inserted in a hollow tube which mimics the vein in which it is inserted *in vivo* (tube model). Side holes were open, closed or with reduced in size to half the diameter to assess the impact of this widespread design feature. The flow and shear stress distribution inside the arterial lumen of the catheter was highly influenced by both presence and size of the side holes. More than 50% of the flow enters the lumen through the side holes, which is remarkably high given the fact that side holes were intended as back-up flow paths in case the end-opening gets obstructed. Halving side hole diameter gives a flow pattern which is intermediate between the case of open and closed side holes. They are now responsible for 17% of the inflow. Velocities in the side holes have only slightly increased compared to the normal size side holes. Highly elevated shear stresses were mainly present near the bottom wall of the blood withdrawing lumen, due to the curved inflow over the end-opening upper wall. Also inside and downstream of the side holes, elevated wall shear stresses (> 50 Pa) were common, with peaks up to 350 Pa. Especially the location of elevated shear stresses was influenced by the presence of side holes, whereas smaller side holes led to a more extended area of elevated shear stresses. In addition, access recirculation, which amounted to about 15% in case of reversed catheter connections, was only marginally influenced by side holes. As such, a distinct classification of the use and size of catheter side holes according to hemodynamic performance is not readily evident, although smaller side holes seem to enlarge the area with elevated shear stresses.

Some of the above simulations were repeated with the catheter now inserted in a three-dimensional model of the right atrium, reconstructed using medical images. The insertion of the catheter model in this realistic environment did not significantly influence the flow and shear stress distribution inside the catheter – using similar steady-state flow conditions. Only the access recirculation percentages differed due to the very different flow patterns surrounding the catheter. Access recirculation also varied slightly with catheter or vein blood flow rate. As such, a simple tube model suffices for the study of flow and shear stress inside central venous catheters, but not for access recirculation. Finally, this study was the *first* to use advanced CFD models to assess flow, shear stress and access recirculation in central venous catheters.

In a second study, seven virtual catheter designs were studied using a combined experimental and numerical approach to assess possible platelet activation in central venous catheters. As not only the level of shear stress, but also the exposure time of platelets to the shear stress is important in the assessment of possible platelet activation and subsequent blood clotting, a *novel* numerical model was developed. A specific form of the continuity equation for a flow time variable was solved in the numerical domain. As such, a distribution of the time since the blood has entered the lumen (i.e. residence time in the lumen) is available. Using shear stress and residence time information, several performance parameters (e.g. average shear stress, percentage of blood volume with residence time larger than 15 – 30 ms) were calculated. As one of them, the Platelet Lysis Index (PLI) combines the evolution of shear stress and exposure time along flow paths in the arterial catheter lumen to a single quantitative parameter. It proved a fast and complete tool to classify catheter designs when parameters of shear stress and residence time show opposite trends.

As a detailed internal shear stress field was necessary in this study, an experimental validation was required as mesh-independent shear stress fields are difficult to achieve and are only obtained at very high (local) mesh density. *For the first time*, standard Particle Image Velocimetry was adapted to this small scale application to visualize the flow and calculate strain rate distribution inside a catheter lumen. The matching of the refractive index of the test fluid and the catheter material, and the use of Rhodamin-B coated particles combined with the red-band pass filter on the PIV camera proved invaluable to obtain high resolution data. Qualitative and quantitative agreement with the numerical results was satisfactory.

From the numerical analysis, it is concluded that the end-opening of a step-tip catheter is best cut orthogonally to its axis for minimal shear stress, residence time and PLI. Side holes are only recommended when the catheter tip is cut at an angle. Catheters with concentric lumina are discarded due to the highly elevated shear stress levels and blood residence time in the lumen. An Ash-Split based design has low average shear stresses as compared to the straight cut step-tip catheter, but this is offset by the elevated blood residence times as the major inflow occurs through the most proximal side holes, leaving low velocities in the distal tip zone. Applying a realistic pulsatile flow rate in the vein did not change the classification of the catheter designs, but nevertheless showed that the hemodynamics (flow, shear stress) in the

catheter lumen are somewhat dependent on the surrounding vein blood flow rate. This information can be used to design more performant catheters in the near future.

1.2 Future prospects

Although no significant advantage of one catheter design over another has been found in *in vivo* studies, the information derived from the studies in this dissertation clearly shows that there is a large difference in the local hemodynamics of catheter designs. Most notably, the Platelet Lysis Index shows a significant difference in platelet activation between catheter designs. However, whether the flow, shear stress and Platelet Lysis Index related differences found in these numerical studies between the several catheter designs are clinically significant, should be determined in an *ex vivo* or *in vivo* study. Although this was not the case in past clinical studies, larger patient numbers, or more in-depth study of the clinical outcome²¹ may finally prove an added benefit of one catheter design over another.

Concerning the presented studies, simplifications such as a tube model and steady state blood flow boundary conditions are allowed for qualitative comparison of the hemodynamics of central venous catheters. However, the models used in this dissertation can be made more realistic by e.g. adding a realistic pulsatile flow pattern of the caval veins and a more realistic tricuspid valve model in the three-dimensionally reconstructed right atrium model. Also fluid-structure-interaction (FSI) modelling may be added to model the movement of the atrial wall during the heart cycle, and the movement of the tip of the catheter lumina. These enhancements may only prove necessary in the study of very specific cases, such as e.g. in the accurate quantitative numerical calculation of access recirculation, or in the study of the contact between catheter and blood vessel or atrial wall, which may cause central vein thrombosis or stenosis. However, the classification of catheter designs as found in this dissertation is – in this author’s opinion – not expected to change.

As such, more can be expected from shifting the focus of the study from the hemodynamics of a catheter *during* extracorporeal treatment to the hemodynamics *in-between* treatments. The loss of locking solution from the catheter tip is likely the main cause of catheter lumen thrombosis. The presence of side holes and the catheter design may prove to be very critical and clinically relevant in this phenomenon. Numerical models comparable to those used in this dissertation may be used to assess the loss of locking solution from central venous catheters. However, as the catheter movement itself evidently plays an important role in the loss of locking solution, very advanced modelling (e.g. FSI) may be necessary. At this point, this type of numerical models may be too time and resource consuming, and *in vitro* or *in vivo* studies may be more appropriate.

²¹ In this regards, the author refers to the study of Tal et al. [30] in which an increased infection risk in a catheter *with* side holes (as compared to *without*) may be due to an increased risk for the formation of a blood clot in the catheter which acts as a nest for infection. (cfr. Chapter 1:3.3.3)

2 AMC Bioartificial Liver

2.1 Conclusions

As insufficient oxygen availability for the hepatocytes is considered to be the major limitation in the efficiency of bioartificial liver systems, a numerical and experimental study of the oxygen transport in the AMC Bioartificial Liver was conducted. First, a comprehensive, widely applicable numerical model was developed to simulate fluid flow, shear stress, and oxygen transfer and consumption in a cellular bioreactor. This model was applied to two three-dimensional unit volumes (micro models), which were isolated from the AMC-BAL geometry. The two micro models only differed in their gas capillary position ('inline' or 'triangular'). Two hepatocyte distributions were hypothesized and applied to each micro model, leading to four micro model configurations which were studied. Under standard operating conditions and using a stringent hepatocyte oxygen consumption value, numerical simulations show that the AMC-BAL can only supply 16-29% of all hepatocytes with sufficient oxygen to consume oxygen at minimally 90% of their maximal oxygen uptake rate ($V_{\text{ratio}} > 0.9$). This percentage was strongly dependant on the proposed hepatocyte distribution, but not on the gas capillary pattern. Pressure drop over the AMC-BAL and maximal shear stresses were low and not considered to be harmful. The internal oxygenator proved to be an essential part of the bioreactor. Increasing the culture medium flow rate or the oxygen content (pO_2) of the medium by external oxygenation were inefficient in increasing hepatocyte oxygen availability. A new and improved bioreactor design with double number of gas capillaries, combined with a doubled oxygen concentration of the oxygenation gas (300 mmHg instead of 150 mmHg pO_2) was the most optimal way to maximize oxygen availability in the AMC-Bioartificial Liver.

These findings were subsequently tested in an *in vitro* study. Four configurations of the AMC-BAL were compared: (G1) 'original' design, (G2) 'original' design with doubled oxygen concentration of the oxygenation gas, (G3) 'new' bioreactor design with 2.2-fold thinner mat and 2-fold number of gas capillaries, and (G4) the 'new' bioreactor design combined with an increased oxygen concentration of the oxygenation gas. After 6 days culturing, the new configuration bioreactor with increased oxygenation (G4) showed significantly reduced anaerobic glycolysis, 60% higher liver-specific functions, and increased transcript levels of five liver-specific genes compared to the standard bioreactor culture. Changed bioreactor configuration and increasing pO_2 of the culture medium contributed equally to these improvements. *Thanks to prior numerical modeling, a higher metabolic stability and liver-specific functionality in the AMC-BAL was achieved by enhancing the oxygen availability.*

However, the simulated increase in O_2 availability in the micro model was persistently larger than the increase in functionality found *in vitro*. This discrepancy could still be due to local limited O_2 availability or to inhomogeneous perfusion in the AMC-BAL, as the micro model approach has several limitations which preclude

extrapolating results to the *in vitro* situation. Thus to more accurately assess perfusion and O₂ availability in the AMC-BAL, a more realistic model was developed. For this purpose, a *novel* protocol was successfully devised to accurately quantify the *in vitro* hepatocyte distribution in a bioreactor, using histological cross-sections of a fixed bioreactor specimen. This *in vitro* determined hepatocyte distribution was subsequently applied to full-scale computer models of the ‘original’ and ‘new’ design bioreactor. A large preferential flow near the inner core in the original design bioreactor was found. This preferential flow, however, was absent in the new design bioreactor with a double number of gas capillaries and 2.2-fold thinner mat. This configuration also led to a more homogenous perfusion and higher O₂ availability for the hepatocytes. Doubling the oxygenation gas pO₂ further increased O₂ availability.

Simulated O₂ availability and outlet culture medium pO_{2-med} were strongly dependent on the imposed O₂ consumption rate. Subsequently, *in vitro* hepatocyte O₂ consumption rate was *estimated* by matching in numero and *in vitro* outlet pO_{2-med} for different bioreactor configurations. It was concluded that the hepatocyte OCR in the original and new design bioreactors under standard oxygenation (cfr. G1 and G3) is very similar. Doubling of the pO_{2-gas} resulted in 3- (cfr. G2) to 7-fold (cfr. G4) higher hepatocyte oxygen consumption values. This OCR estimation analysis suggests that hepatocytes adapt their OCR to the local environment in the AMC-BAL while maintaining maximal local hepatic O₂ availability. However, as the new design bioreactor (i.e. G3) is able to sustain higher OCR values with almost maximal O₂ availability, *OCR is not limited by a lack of oxygen in the new bioreactor design*. As such, other factors must play an important role in the regulation of hepatocyte OCR.

Using estimated OCR, all bioreactor configurations maintain maximal oxygen availability, whereas clearly differences in anaerobic glycolytic metabolism and liver-specific functionality have been shown *in vitro*. This suggests that O₂ availability (as defined in this study: % cells with V_{ratio} > 0.9) may not be used as an indicator of *in vitro* improvement. Similarly, the estimated OCR itself could not be directly correlated to the increase in functional activity found *in vitro*. This again proves that other factors than O₂ availability (e.g. pO₂ level, increased cell-to-cell and cell-to-matrix contact) play a determining role in anaerobic glycolytic metabolism and hepatocyte functionality between bioreactor configurations.

Simulations on these full-scale AMC-BAL macro models with realistic hepatocyte distribution *facilitated a more accurate analysis* of fluid flow and O₂ availability in the AMC-BAL as compared to the previous micro models. The models also allowed studying the relation between simulated O₂ availability, estimated O₂ consumption and *in vitro* functionality.

2.2 Future prospects

Future models could include a spatial variation of V_M value in the bioreactor model, based on local absolute pO₂ level and hepatocyte density. Subsequent simulations on a macro scale model may show a better correlation between e.g. local O₂ availability and reduced anaerobic glycolytic metabolism in the different AMC-BAL configurations, while maintaining a validated pO_{2-med}. However, further *in vitro* research is necessary to quantify the parameters of this model.

Concerning the improvement of the efficiency of the AMC Bioartificial Liver, it can be stated that the new design and operating conditions have resulted in a bioreactor which can sustain cells with considerable oxygen consumption demands and which allows hepatocytes to maintain a higher functional activity for a longer period of time. Therefore no large gain in efficiency of the AMC Bioartificial Liver should be expected from an even further increase in oxygen availability. Future research on this bioartificial liver system should therefore focus on the development and testing of a cell line to be used in the bioreactor, which inherently outperforms the porcine hepatocytes used until now.

The field of numerical modeling in bioartificial liver systems can be expanded to modelling other aspects of *hepatocyte metabolism* beyond oxygen consumption alone, and to the modelling of *cellular growth* of hepatocyte cell lines. However, this requires vast amounts of experimental work to determine the model parameters of such advanced numerical models. In Appendix A, early investigations and preliminary results in the domain of modeling hepatocyte growth and metabolism in the AMC-BAL are presented.

Appendix A: Modeling of cellular growth and metabolism

1 Modeling cellular growth

The modeling of hepatocyte growth in the AMC-BAL is relevant given the change in cell type from the non-proliferating primary porcine hepatocytes to cell lines which may be cultured inside the bioreactor prior to their clinical application. Many references can be found in literature describing and modeling cellular growth, especially in the field of tumor growth, bacteria culture and bone remodelling. However, few research has been performed on modeling hepatocyte growth in a bioartificial liver. Glicklis *et al.*[236] developed a mathematical model which describes the relationship between hepatocyte spheroid size and cell viability via an oxygen mass balance equation. Eq. VIII-1 described the change in spheroid diameter ($D_{spheroid}$) in time. The equation is composed of two terms: one describing the increase in spheroid size according to a first-order kinetics and the second describing the reduction in spheroid size growth rate by a second-order kinetics. K and β are the kinetic constants for the growth and inhibition terms, respectively, and their value was determined by fitting experimental growth data. This equation was then combined with a one-dimensional oxygen convection-diffusion-reaction equation.

$$\frac{dD_{spheroid}}{dt} = KD_{spheroid}(1 - \beta \cdot D_{spheroid}) \quad \text{Eq. VIII-1}$$

In the following, it is illustrated how a model for hepatocyte growth can be developed for use in a Fluent-based numerical model of a bioartificial liver or hepatocyte system. The model is focused on HepG2 cells as it is one of the most used cell lines and the experimental data necessary for the development of the model can be found more ‘easily’. It is stated here for the rest of the chapter that finding useful data for the development of kinetic growth models is very hard as most experimental studies lack a reliable quantitative assessment of the evolution of the number of cells in culture. Usually secondary means of assessing the number of cells (via cell function tests or optical assays) are used. Also too small sample sizes or too short culture time limit the usefulness of some experimental studies for the development of a numerical model. Even contradictory growth information on specific cell types can be found in literature.

In general, the basic kinetics of biomass growth can be modeled by Eq. VIII-2, with X the biomass, and μ the (exponential) growth rate.

$$\frac{\partial X}{\partial t} = \mu \cdot X \quad \text{Eq. VIII-2}$$

The growth rate μ is usually not constant, but can be dependant on various factors. In the model developed in this work, two limiting factors in cellular proliferation will be taken into account: (1) the limitation by oxygen availability, and (2) inhibition of growth due to contact inhibition. The latter is the logical consequence of the fact that the amount of cells that can reside in a certain area or volume is physically limited. However, cellular growth can decrease far before the point that this physical constraint is reached due to increased cell contact and signalling. This phenomenon is called contact inhibition.

The growth rate μ can be substituted by $\frac{\ln(2)}{DT}$, in which DT is the doubling time (assuming each cell divides in two with each proliferation step). A model for the doubling time is now derived for the HepG2 cell line, which takes into account the two aforementioned growth inhibition factors.

a) Proliferation rate depending on local O_2 concentration

Doubling time of HepG2 cells under normoxic conditions ($pO_2 = 150$ mmHg) is reported as 24 ± 3 hours.[269,297] To model the decrease in cell growth under lower oxygen concentrations, experimental data must be found. The most useful article we found concerns a study on cellular metabolic and proliferative response to hypoxia in two transformed human cell lines with different metabolic backgrounds: HepG2 and 143B. [298]

Table 1. Growth in HepG2, 143B, and Corresponding ρ° Cells Under Hypoxic Conditions*

	HepG2	HepG2 ρ°	143B	ρ° 143B
% of cell number (hypoxia vs. normoxia)	27.4% ± 2.2	62.0% ± 5.1	52.3% ± 4.3	59.9% ± 12.1

Fig. VIII-1: Experimental data showing the ratio of the growth of HepG2 cells under hypoxic ($pO_2 = 1\% \sim 7.5$ mmHg) conditions to the growth under normoxic ($pO_2 = 150$ mmHg).

As after a 72 hour culture period only 27.4% of the number of HepG2 cells are present as compared to a 72 h normoxic culture period, the doubling time under hypoxic conditions ($pO_2 = 1\% \sim 7.5$ mmHg) can be calculated as 63.59 hours. For use in a numerical model, a doubling time equation must be constructed which gives doubling times for any given oxygen concentration. To fit the equation, we assume that the growth rate follows Michaelis-Menten kinetics: $\mu = A \cdot \frac{pO_2}{pO_2 + b}$. From this, following

doubling time equation was found:

$$DoublingTime = \frac{21.91 h}{\frac{pO_2}{pO_2 + 1.9015}} \tag{Eq. VIII-3}$$

This equation is shown in Fig. VIII-2. At 1% and 20% the equation matches the experimentally found doubling times.

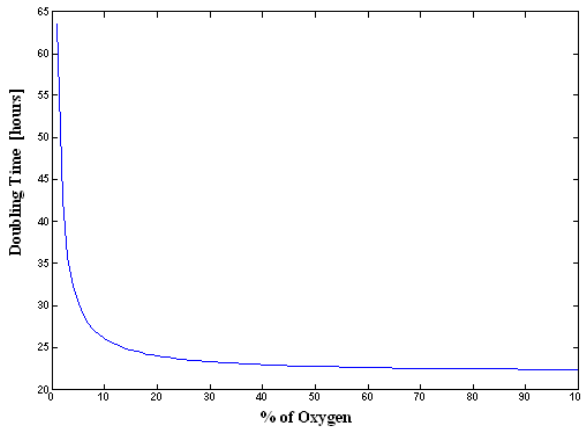


Fig. VIII-2: Doubling time in function of oxygen concentration according to Eq. VIII-3.

b) Proliferation rate depending on local cellular density

To model contact inhibition or the physical constraint (confluence) of cell growth, the doubling time (DT) equation must be modified. The literature offers a great amount of articles, but often they are reporting data based on different criteria such different cell lines, different environment of culture, different methods of analysis.

In the reference we considerate for our study [299], approximately 10'000 HepG2/cm² are seeded in 6-well plates and allowed to grow to high density. Proliferation rate is measured on serum protein synthesis, values are reported as milligrams total cellular protein per square centimetres of culture area.

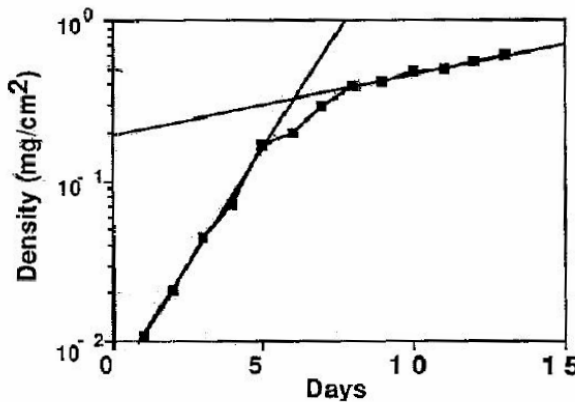


FIG. 1. Growth curve of Hep G2. Cells were grown in MEM/MAB plus 10% fetal calf serum as described in Methods. Every twenty four hours, duplicate cultures were dissolved in guanidine HCl and the total cell protein was measured. The respective doubling times for high and low density cells was 193 ± 5 h and 24 ± 3 h.

Fig. VIII-3: Growth curves of HepG2 cells in six-well plates. The abrupt change in growth rate coincides with the reaching of confluence in the culture plates..

As the figure shows, cells proliferate with a doubling time of 24 ± 3 hours, until they reach confluence, approximately at density of 0.2 mg/cm^2 . At this moment the doubling time of the culture slowed abruptly and dramatically, reaching a new steady state doubling time of 193 ± 5 hours. These data showed that HepG2 exhibited a degree of contact inhibition, they feel the stress performed by neighbouring cells and they might also be capable of altering liver specific function with division rate. Despite the fact that this study clearly illustrates contact inhibited growth, the data cannot be quantified for use in a three-dimensional hepatocyte culture, such as in the AMC Bioartificial Liver. Therefore, only several modelling strategies will be presented which allow modifying the doubling time-equation in order to incorporate growth inhibition based on biomass concentration, or contact inhibition.

A first option is to use the frequently used Contois growth kinetic model, as reported by C.J. Galban and B.R.Locke.[300] The general form of this model is depicted in Eq. VIII-4, with μ the growth rate, μ_{\max} the maximal growth rate, S the substrate, K_c a type of Michaelis-Menten constant, and X the biomass (e.g. hepatocyte number or density) itself.

$$\mu = \mu_{\max} \left(\frac{S}{S + K_c \cdot X} \right) \quad \text{Eq. VIII-4}$$

The Contois equation for modeling cell growth inhibition differs from the common Michaelis-Menten kinetics, previously used to model the oxygen dependence on cell growth, in the fact that growth inhibition is implemented by multiplying the constant in the denominator by the biomass concentration itself (cfr. Eq. VIII-2).

As such, the doubling time equation is modified to account for the contact inhibition of growth. Now, an equation to model the change in hepatocyte density [10^6 cells/mL] can be proposed, taking into account both types of growth inhibition (Eq. VIII-5).

$$\frac{d\rho_{cell}}{dt} = \frac{\ln(2)}{1 / \left(\frac{1}{21.9015} \cdot \frac{pO_2}{1.9015 \cdot \rho_{cell}(t) + pO_2} \right)} \cdot \rho_{cell}(t) \quad \text{Eq. VIII-5}$$

The effect of multiplying the constant Michaelis-Menten term by the cell concentration in the Contois model, is illustrated in Fig. VIII-4. Here, the evolution of number of cells in time ($t=0 : 1 \text{ cell}$) is depicted using a 24h doubling time (under constant normoxic conditions), and using the Contois model under constant normoxic conditions ($pO_2 = 20\%$).

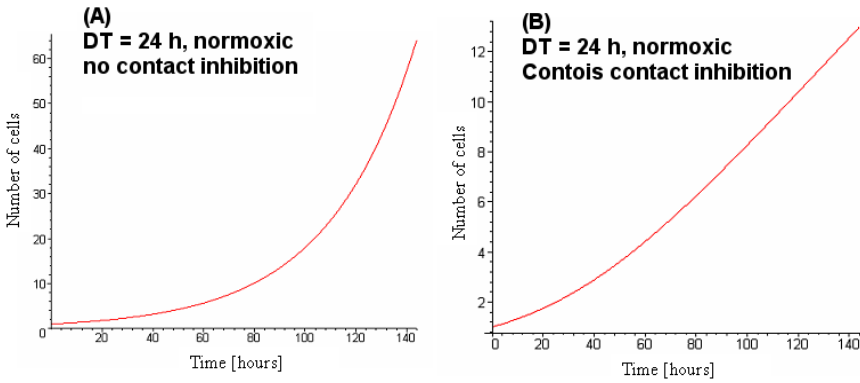


Fig. VIII-4: General comparison between proliferation modeling using (A) Michaelis-Menten, and (B) Contois kinetics. The latter clearly illustrates an inhibition of growth with increasing cell number. (Simulations under constant $pO_2 = 20\%$, 1 cell at time zero)

As shown by the graphs, after 144 hours of proliferation the Contois model predicts 13 cells in the culture instead of 64, as obtained by the previous model without cell density based inhibition. This result seems to correctly model cell proliferation depending on local density. But if we plot the doubling time in function of cell density (Fig. VIII-5), we can clearly see that doubling time changes linearly with cell density, starting already from a zero cell concentration. This insight can also be derived from Eq. VIII-5 and the fact that $\mu = \ln(2) / DT$.

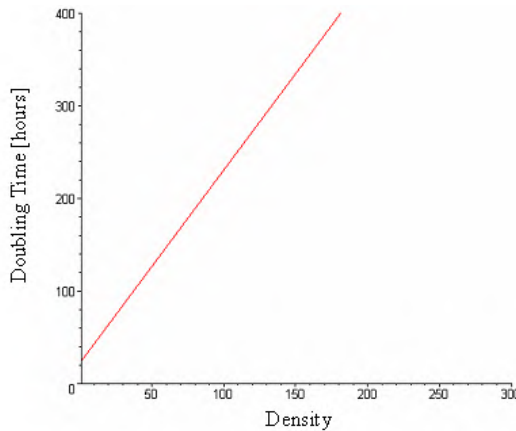


Fig. VIII-5: Doubling time in function of cell density [10^6 cells/mL] in the Contois model

In fact, this is not the right modelling. The doubling time increases too rapidly, we want it to stay almost constant until the cells feel the contact inhibition. For this reason, the frequently used Contois model is abandoned.

To more accurately model the inhibition of cellular growth with increasing hepatocyte density, two new models are introduced: (1) a hyperbolic growth inhibition model presented by Stein *et al.*[301]; and (2) a newly developed exponential growth inhibiting model. In the first, a maximal cell density is defined which is subsequently incorporated in the equation of the doubling time using a hyperbolic growth rate curve. Applied to our previously determined dependency on pO_2 , the doubling time equation using the hyperbolic growth inhibition model is:

$$DT = 1 / \left(\frac{1}{21.9015} \cdot \frac{pO_2}{1.9015 + pO_2} \left(1 - \frac{\rho(t)}{\rho_{\max}} \right) \right) \quad \text{Eq. VIII-6}$$

The maximal cell density is determined as 490×10^6 cells / mL using the diameter of a HepG2 cell (12.5 μm ; [269]), while assuming that half of the volume of a hepatocyte aggregate consists of free space.

The exponential growth inhibition model adds a two-parameter exponential term to the base value of the doubling time, as is illustrated in *Eq. VIII-7*.

$$DT = 1 / \left(\frac{1}{21.9015 + e^{\frac{\rho(t)-100}{50}}} \cdot \frac{pO_2}{1.9015 + pO_2} \right) \quad \text{Eq. VIII-7}$$

The parameter ‘100’ and ‘50’ have a physiological significance: ‘100’ is the cell density (in 10^6 cells / mL), at which the doubling time starts to rise significantly; the parameter ‘50’ is a measure for how steep the doubling time will increase when it passes the first parameter value. Of course, the values of 100 and 50×10^6 cells / mL are chosen quite arbitrarily. Further *in vitro* research is necessary to determine these factors in a bioreactor environment.

Fig. VIII-6 shows the evolution of doubling time under constant normoxic conditions with increasing cell densities. This graph can be compared to Fig. VIII-5.

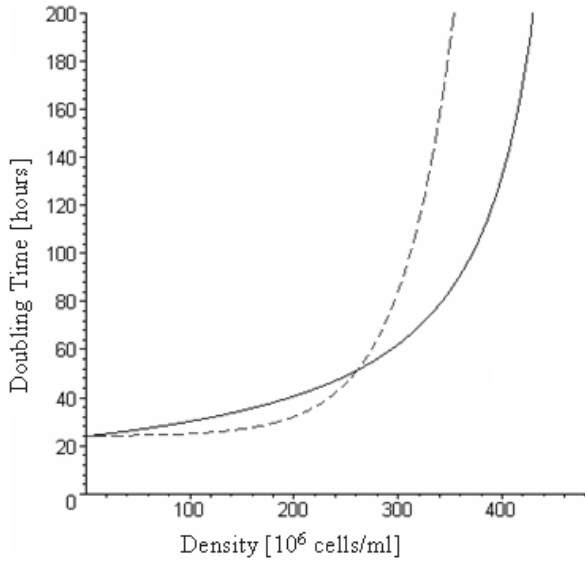


Fig. VIII-6: Doubling time in function of cell density under normoxic conditions using the hyperbolic (full line), or exponential (dashed line) inhibition model.

As shown in the graph, the cells do not feel the contact inhibition in the early proliferation phase, so doubling time stays almost constant, until the density is getting too high and the growth rate slows down. The newly developed exponential inhibition model seems to keep the growth rate constant for a longer period of time, which is probably more realistic and in accordance with experimental data, such as Fig. VIII-3.

By applying these two doubling time equations to Eq. VIII-2, as in Eq. VIII-5, the governing equation for HepG2 growth can be implemented in Fluent. As a feasibility study, three-dimensional simulations of HepG2 growth were performed on a micro model of the AMC-BAL with inline gas capillary pattern, and an initial cell seeding of 175 million HepG2 cells homogeneously spread over the mat, and with an HepG2 OCR of $0.05 \text{ nmole}/(\text{s} \cdot 10^6 \text{ cells})$. For further modeling details concerning oxygen transport and consumption, please refer to Chapter V.

The simulations showed preferential growth of HepG2 cells around the gas capillaries. Simulations were performed with either only the pO_2 dependence of the growth rate as determined in part (a) of this section, or either with the inclusion of the limitation of cell growth with increasing cell density using the hyperbolic or exponential inhibition model. In Fig. VIII-7, an overview of the evolution of the total number of cells in the AMC-BAL is given, based on these three approaches.

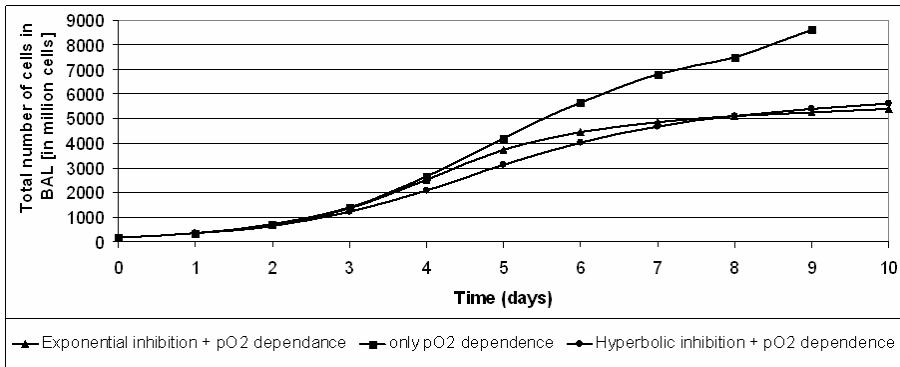


Fig. VIII-7: Numerical simulation of the evolution of the number of HepG2 cells in the AMC-BAL, using the inline micro model, and an initial cell seeding of 175×10^6 HepG2 cells. Three modeling approaches were used: either growth rate was only limited by oxygen availability, or the inhibition by an increased cell density was added using the hyperbolic or exponential inhibition model.

In the first three days, the contact inhibition modeling has no influence because the cell density has not yet increased to the level at which this inhibition significantly influences growth rate. Without the modeling of contact inhibition, the number of cells keeps rising until about 8.5 billion HepG2 cells. The decrease in rise is due to a limited oxygen availability. However, as no contact inhibition is implemented, cell densities in the model surpass values which are physically possible. Therefore, using the contact inhibition models is crucial in modeling cell growth in bioreactor systems. Both the hyperbolic as the exponential inhibition model render similar results, both reaching a plateau of about 5.5 billion HepG2 cells after 9 to 10 days of culture.

The presented models have several limitations that should be addressed in future work. The model only incorporates cell growth, but no *cell death*. As the number of cells rise, oxygen availability will drop and not only the growth will halt, but cells will also start to die. As such, the numbers presented in Fig. VIII-7 represent the cumulative total number of cells which have existed in the AMC-BAL, but the actual cell number at a certain time period will surely be smaller. Also, evidently more accurate and *in vitro* based model parameters are needed for an accurate modeling of cell growth in the AMC-BAL. For this, more *in vitro* research is necessary. This model was tested on a micro model, but future studies should be performed using the realistical full-scale model with an *in vitro* based *initial* cell distribution. Also the implementation of the model should be improved to incorporate the fact that cell growth does not only imply an increase in hepatocyte density (as modeled here), but possibly also an increase in the volume that the hepatocyte culture occupies, which is the case in e.g. the increase in thickness of a cell layer around a capillary. This is not yet possible with the currently developed model. Finally and most importantly, quantitative validation of simulation results is crucial for the credibility of these models. However, validation may require that the model is further expanded with other dependencies on cell growth, such as hormones, growth factors and other metabolites.

2 Modeling cellular metabolism

In the clinical setting, hepatocytes in the BAL are exposed to toxic plasma of the patient. This may severely influence the effectiveness of the therapy. On the other hand, the biochemical composition of the culture medium can improve the functionality of bioartificial liver systems prior to their clinical application. For example, it has been shown that preconditioning the hepatocytes in low insulin media followed by amino acid supplementation within the plasma dramatically increases hepatic function and reduces intracellular lipid accumulation.[302] Thorough reviews on modeling of cellular (and hepatocyte in particular) metabolism can be found in [303,304,305]. Generally, there are two groups of modeling approaches: (1) stoichiometric models, and (2) kinetic models.

a) *Stoichiometric models*

Stoichiometric models are based on the time invariant characteristics of metabolic networks. Metabolic Flux Analysis (MFA) is one type of stoichiometric model. It has been widely used for the quantification of the intracellular fluxes in the central metabolism of bacterial, yeast, filamentous fungi and animal cells. In MFA, mass balances over all the intracellular metabolites are used to calculate the fluxes through the different branches of the network. Hereby it is possible to get a snapshot of the metabolism under a particular condition. Thus, based on a stoichiometric model for the metabolic reaction network in hepatocytes, intracellular reaction fluxes are estimated by mass balances around each intracellular metabolite and extracellular flux measurements. Firstly, a stoichiometric matrix S is defined that appropriately describes the metabolism under investigation, based on available biochemical information. Secondly, the stoichiometric matrix 'S' is multiplied by the so-called vector of reaction rates 'v', defining the mass balance equation. This is illustrated in Fig. VIII-8.

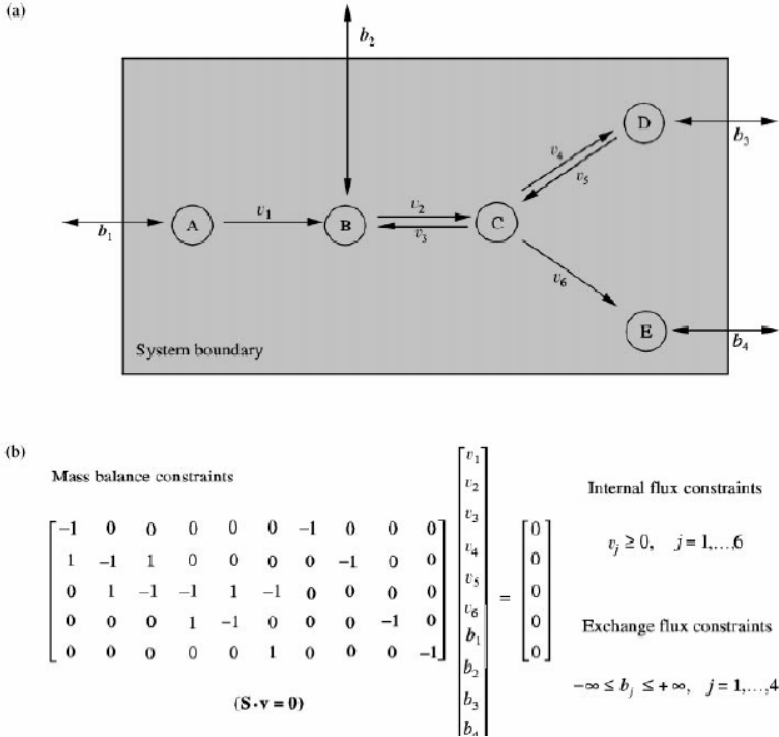


Fig. VIII-8: (a) Reaction network consisting of five metabolites (A-E) and four internal fluxes (two reversible) with in total six internal fluxes 'v' and four external fluxes 'b'. (b) Stoichiometric matrix S

Finally, algebraic manipulation of the stoichiometric matrix can be carried out by different means, depending on the objective of the analysis. It is sometimes possible to impose some constraints (e.g. by measuring some fluxes) so that the system becomes determined and can be solved by simple linear algebra. In this case, the analysis is usually called Metabolic Flux Balancing (MFB). If further constraints are imposed by measuring the labelling state of some metabolites, however, it may be possible to combine flux balancing with labelling balancing and the system has to be solved numerically. In this case, a better estimation of the fluxes is attained. If the system cannot be constrained to a determined one, linear optimisation can be applied to find the maximum or minimum of a suitable objective function. Chan *et al.* [292] have developed a MFA model for cultured rat hepatocytes. The mathematical model consists of mass balances around 45 intracellular metabolites considering 76 reactions. The sum of fluxes to and from the metabolite pools is assumed to be zero (pseudo steady-state assumption): $S \times v = 0$, with S_{ij} is the coefficient of metabolite i in reaction j , and each v_j of vector 'v' is the net flux or conversion rate of reaction j . This equation is separated into measured and unknown fluxes, v_m and v_u , respectively, as follows: $S_u \times v_u = -S_m \times v_m$. The measured fluxes represent measured rates of uptake or release of extracellular metabolites and thus can lead to

estimates of intracellular fluxes. Chan used the model to study how the insulin level in the culture medium influences hepatic functional activity.

Stoichiometric models are clearly very powerful, but their main drawback is the limited predictive power, which is due to the lack of regulatory information in the model formulation.

b) Kinetic models

When detailed information is available about the kinetics of specific cellular processes, it is possible to describe the dynamics of these processes by combining kinetics with the known stoichiometry of metabolic pathways. This is illustrated in Fig. VIII-9.

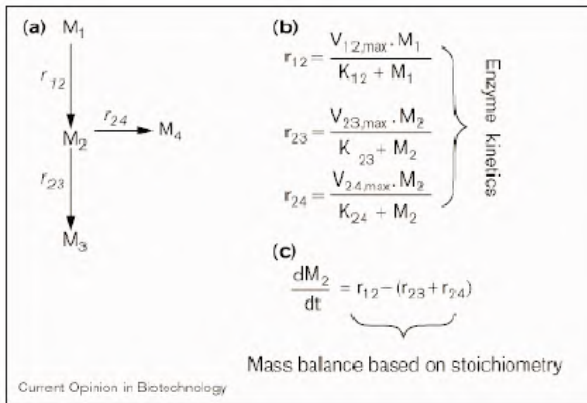


Fig. VIII-9: Principles of kinetic modeling. [303]

In this case, a simple reaction network stoichiometry (a) is used in combination with simple Michaelis–Menten type enzyme kinetics (b) to yield the mass balance over metabolite M2, as shown (c). If the parameters V_{max} and all K_{ij} (the Michaelis constant for reaction r_{ij}) are known, as well as the concentration of metabolite M1 (which may be a substrate), it is possible to calculate the time profile of metabolite M2. Kinetic modeling allows predicting how a metabolic network will react on external manipulation. As a downside, however, large amounts of quantitative data on reactor rate and kinetic constants are necessary, which are sometimes difficult to collect or measure. An interesting example of this type of model is given in Kuchel *et al.* [306], who described the kinetics of the hepatic urea cycle.

c) Combination of stoichiometric and kinetic modeling, applied to the AMC Bioartificial Liver

Another very interesting model is presented by Venkatasubramanian *et al.* [307]. Their model incorporates a realistic description of primary energy metabolism within reaction-diffusion equations to predict local glucose, oxygen, and lactate concentrations and an overall spheroid growth rate. The model development is based on the assumption that local cellular growth and death rates are determined by local ATP production generated by intracellular energy metabolism. Their approach

combines kinetic modeling with information derived from basal energy reaction stoichiometry.

The model of the basic energy metabolism combines glucose, oxygen and lactate information. Briefly, the uptake rate of each extracellular metabolite is based on the availability of the nutrient in the extracellular environment and the stoichiometric limitations of intracellular metabolism. Three transmembrane transport equations represent the maximum uptake rates based on extracellular nutrient concentrations. The transmembrane uptake rates are the upper limits of the metabolic uptake rates and are described using the following Michaelis-Menten equations:

$$Q_{Gluc,transmembrane} = \frac{Q_{Gluc,max}c_{Gluc}}{K_{m,Gluc} + c_{Gluc}}$$

$$Q_{Ox,transmembrane} = \frac{Q_{Ox,max}c_{Ox}}{K_{m,Ox} + c_{Ox}}$$

$$Q_{Lac,transmembrane} = \frac{Q_{Lac,max}c_{Lac}}{K_{m,Lac} + c_{Lac}}$$

The actual glucose uptake by the cell is assumed to be only limited by its transmembrane transport. As such:

$$Q_{Gluc} = Q_{Gluc,transmembrane}$$

In contrast to glucose, oxygen uptake can be limited either by its own transmembrane transport or by transmembrane transport of glucose and lactate. When the extracellular concentration of oxygen is low, the transmembrane uptake of oxygen ($Q_{O_2,transmembrane}$) will be limiting. However, when the concentrations of glucose and lactate are low, the stoichiometry of intracellular metabolism will limit the rate of oxygen uptake. If all reductive equivalents (NADH and FADH) are converted into ATP by the electron transport system, which consumes oxygen and produces water. The complete oxidation of one molecule of glucose consumes six molecules of O_2 and the oxidation of one molecule of lactate in the TCA cycle consumes three molecules of O_2 . Therefore cellular oxygen consumption is defined as:

$$Q_{Ox} = \min(Q_{Ox,transmembrane}, 6Q_{Gluc} + 3Q_{Lac,transmembrane})$$

The rate of lactate consumption and/or production is dependent on the rates of glucose and oxygen uptake, and is determined by the stoichiometry of the intracellular reactions. One molecule of glucose can produce two molecules of lactate and the oxidation of one molecule of lactate requires three molecules of oxygen. Therefore cellular lactate consumption is defined as:

$$Q_{Lac} = -2Q_{Gluc} + Q_{Ox}/3$$

This stoichiometric balance describes both the production ($Q_{Lac} < 0$) and consumption ($Q_{Lac} > 0$) of lactate. If the uptake of glucose is stoichiometrically greater than the uptake of oxygen, then the excess glucose will be converted into lactate. Conversely, if the uptake of oxygen is stoichiometrically greater than the uptake of glucose, then lactate will be consumed and oxidized as a carbon source.

In a preliminary study, this simplified energy model was implemented in Fluent with following parameters: $Q_{Lac,transmembrane}$ is $4.23 \text{ nmol}/(\text{s}\cdot 10^6 \text{ cells})$ and K_M is 0.00055 mM [307]. *To make the modeling more realistic, some parameters were taken from the previous experimental and numerical studies.* Oxygen consumption characteristics were taken from the estimated OCR values of Chapter VII: $Q_{Ox,transmembrane}$ is $0.025 \text{ nmol}/(\text{s}\cdot 10^6 \text{ cells})$. The glucose uptake rate $Q_{Gluc,transmembrane}$ was taken from the *in vitro* study of Chapter VI. The value of bioreactor G1 on day 6 was taken as only glucose consumption can be simulated in this model: $Q_{gluc} = 0.07 \text{ nmol}/(\text{s}\cdot 10^6 \text{ cells})$, K_M of glucose was set to 0.04mM [307]. Concentration of the incoming culture medium were:

- [glucose] 10.2 mM
- [lactaat] 1.1 mM
- pO₂ 146 mmHg

This model was subsequently applied to the inline micro model of the AMC-BAL with cell distribution 1 (all hepatocytes in mat). As such, axial and radial concentration profiles of glucose, lactate and oxygen can be studied in the micro model.

Most importantly, the model allows predicting the lactate production inside the AMC-BAL. Based on this simulation case, the one billion hepatocytes in the AMC-BAL produce $0.13 \text{ nmol}/(\text{s}\cdot 10^6 \text{ cells})$ lactate. This numerical results can be compared to *in vitro* measurements (Fig. VIII-10). Correspondence of this simulation result with the experimental value of $0.09 \text{ nmol}/(\text{s}\cdot 10^6 \text{ cells})$ is considered very good, given the simplicity of the model used.

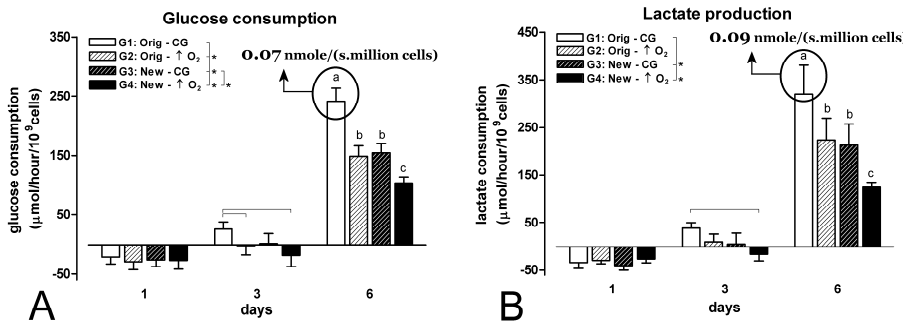


Fig. VIII-10: Values of glucose consumption and lactate production of the original AMC-BAL (G1) on day 6 (glucose consumption) can be used to validate simulation results in the AMC-BAL based a simplified basal energy model

This energy model was tested on a micro model of the AMC-BAL, but future studies should be performed using the realistical full-scale model with the *in vitro* based cell distribution. Also the sensitivity of the model to the selection of the model parameters (as e.g. O₂ consumption) should be further determined, and the model should be expanded to allow modeling of the *production* of glucose of the hepatocytes in the AMC-BAL on day 1 of the culture period.

References

1. III-NKF-K/DOQI. Clinical Practice Guidelines for Vascular Access: update 2000. *Am J Kidney Dis* 2001;37:137-181.
2. Hodges TC, Fillinger MF, Zwolak RM, Walsh DB, Bech F, Cronenwett JL. Longitudinal comparison of dialysis access methods: risk factors for failure. *J Vasc Surg* 1997;26(6):1009-19.
3. NKF-K/DOQI. Clinical Practice Guidelines for Vascular Access: update 2006. *Am J Kidney Dis* 2006;48(Suppl 1):187-317.
4. Jungers P, Zingraff J, Albouze G, Chauveau P, Page B, Hannedouche T, *et al.* Late Referral to Maintenance Dialysis - Detrimental Consequences. *Nephrol Dial Transplant* 1993;8(10):1089-1093.
5. Friedman AL, Walworth C, Meehan C, Wander H, Shemin D, DeSoi W, *et al.* First hemodialysis access selection varies with patient acuity. *Adv Ren Replace Ther* 2000;7(4):S4-S10.
6. Stehman-Breen CO, Sherrard DJ, Gillen D, Caps M. Determinants of type and timing of initial permanent hemodialysis vascular access. *Kidney Int* 2000;57(2):639-645.
7. Sehgal AR, Silver MR, Covinsky KE, Coffin R, Cain JA. Use of standardized ratios to examine variability in hemodialysis vascular access across facilities. *Am J Kidney Dis* 2000;35(2):275-281.
8. Erben J, Kvasnicka J, Bastecky J, Vortel V. Experience with routine use of subclavian vein cannulation in haemodialysis. *Proc EDTA* 1969;6:59-64.
9. Twardowski ZJ. Advantages and limits of the jugular catheter approach. *Nephrol Dial Transplant* 1995;10(12):2178-82.
10. Pisoni RL. Vascular access use and outcomes: results from the DOPPS. *Contrib Nephrol* 2002;(137):13-9.
11. Ash SR. Fluid mechanics and clinical success of central venous catheters for dialysis-answers to simple but persisting problems. *Semin Dial* 2007;20(3):237-56.
12. Moran JE. Subcutaneous vascular access devices. *Semin Dial* 2001;14(6):452-7.
13. Canaud B, Leray-Moragues H, Kamoun K, Garrigue V. Temporary vascular access for extracorporeal therapies. *Ther Apher* 2000;4(3):249-55.
14. Work J. Chronic catheter placement. *Semin Dial* 2001;14(6):436-440.
15. Almirall J, Gonzalez J, Rello J, Campistol JM, Montoliu J, Puig de la Bellacasa J, *et al.* Infection of hemodialysis catheters: incidence and mechanisms. *Am J Nephrol* 1989;9(6):454-9.

References

16. Kessler M, Hoen B, Mayeux D, Hestin D, Fontenaille C. Bacteremia in patients on chronic hemodialysis. A multicenter prospective survey. *Nephron* 1993;64(1):95-100.
17. Saad TF. Central venous dialysis catheters: catheter-associated infection. *Semin Dial* 2001;14(6):446-51.
18. Beathard GA. Catheter thrombosis. *Semin Dial* 2001;14(6):441-5.
19. Bayes B, Bonal J, Romero R. Sodium citrate for filling haemodialysis catheters. *Nephrol Dial Transplant* 1999;14(10):2532-3.
20. Twardowski ZJ, Vanstone JC, Jones ME, Klusmeyer ME, Haynie JD. Blood Recirculation in Intravenous Catheters for Hemodialysis. *J Am Soc Nephrol* 1993;3(12):1978-1981.
21. Depner TA. Catheter performance. *Semin Dial* 2001;14(6):425-431.
22. Oliver MJ. Acute dialysis catheters. *Semin Dial* 2001;14(6):432-5.
23. Cimochoowski GE, Worley E, Rutherford WE, Sartain J, Blondin J, Harter H. Superiority of the internal jugular over the subclavian access for temporary dialysis. *Nephron* 1990;54(2):154-61.
24. Trerotola SO, Kuhn-Fulton J, Johnson MS, Shah H, Ambrosius WT, Kneebone PH. Tunneled infusion catheters: increased incidence of symptomatic venous thrombosis after subclavian versus internal jugular venous access. *Radiology* 2000;217(1):89-93.
25. Little MA, Conlon PJ, Walshe JJ. Access recirculation in temporary hemodialysis catheters as measured by the saline dilution technique. *Am J Kidney Dis* 2000;36(6):1135-9.
26. Vesely TM. Central venous catheter tip position: a continuing controversy. *J Vasc Interv Radiol* 2003;14(5):527-34.
27. Mandolfo S, Galli F, Costa S, Ravani P, Gaggia P, Imbasciati E. Factors influencing permanent catheter performance. *J Vasc Access* 2001;2:106-109.
28. Petersen J, Delaney JH, Brakstad MT, Rowbotham RK, Bagley CM, Jr. Silicone venous access devices positioned with their tips high in the superior vena cava are more likely to malfunction. *Am J Surg* 1999;178(1):38-41.
29. Twardowski J, Moore HL. Side holes at the tip of chronic hemodialysis catheters are harmful. *J Vasc Access* 2001;2(1):8-16.
30. Tal MG, Peixoto AJ, Crowley ST, Denbow N, Eliseo D, Pollak J. Comparison of side hole versus non side hole high flow hemodialysis catheters. *Hemodial Int* 2006;10(1):63-7.
31. De Wachter DS, Weijmer MC, Kaušlyas M, Verdonck PR. Do catheter side holes provide better blood flows? *Hemodial Int* 2002;6(1):40-46.

32. Senecal L, Saint-Sauveur E, Leblanc M. Blood flow and recirculation rates in tunneled hemodialysis catheters. *Asaio J* 2004;50(1):94-7.
33. Trerotola SO, Kraus M, Shah H, Namyslowski J, Johnson MS, Stecker MS, *et al.* Randomized comparison of split tip versus step tip high-flow hemodialysis catheters. *Kidney Int* 2002;62(1):282-9.
34. O'Dwyer H, Fotheringham T, O'Kelly P, Doyle S, Haslam P, McGrath F, *et al.* A prospective comparison of two types of tunneled hemodialysis catheters: the Ash Split versus the PermCath. *Cardiovasc Intervent Radiol* 2005;28(1):23-9.
35. Richard HM, 3rd, Hastings GS, Boyd-Kranis RL, Murthy R, Radack DM, Santilli JG, *et al.* A randomized, prospective evaluation of the Tesio, Ash split, and Opti-flow hemodialysis catheters. *J Vasc Interv Radiol* 2001;12(4):431-5.
36. Akoh JA. Dialysis access: past, present and future. In: Akoh JA, Hakim NS, eds. *Dialysis access - Current practice*, 1st Edition. London: Imperial College Press, 2001;1-21.
37. Gotch FA, Sargent JA. A Mechanistic Analysis of the National Cooperative Dialysis Study (NCDS). *Kidney Int* 1985;28(3):526-534.
38. Blakeshear PL. Mechanical hemolysis in flowing blood. In: Fung YC, eds. *Biomechanics. Its foundation and objectives*, Englewood Cliffs, New Jersey: Prentice-Hall, 1972.
39. Sallam AM, Hwang NHC. Human Red Blood-Cell Hemolysis in a Turbulent Shear-Flow - Contribution of Reynolds Shear Stresses. *Biorheology* 1984;21(6):783-797.
40. Giersiepen M, Wurzinger LJ, Opitz R, Reul H. Estimation of Shear Stress-Related Blood Damage in Heart-Valve Prostheses - Invitro Comparison of 25 Aortic Valves. *Int J Artif Organs* 1990;13(5):300-306.
41. Borow M, Crowley JG. Evaluation of Central Venous Catheter Thrombogenicity. *Acta Anaesthesiol Scand* 1985;29:59-64.
42. Rhodes NP, Kumary TV, Williams DF. Influence of wall shear rate on parameters of blood compatibility of intravascular catheters. *Biomaterials* 1996;17(20):1995-2002.
43. Hall MW, Goodman PD, Solen KA, Mohammad SF. Formation of occlusive platelet aggregates in whole blood caused by low concentrations of ADP. *ASAIO J* 2000;46(6):693-695.
44. Zhang JB, Kuang ZB. Study on blood constitutive parameters in different blood constitutive equations. *J Biomech* 2000;33(3):355-360.
45. Grigioni M, Daniele C, Morbiducci U, D'Avenio G, Di Benedetto G, Del Gaudio C, *et al.* Computational model of the fluid dynamics of a cannula inserted in a vessel: incidence of the presence of side holes in blood flow. *J Biomech* 2002;35(12):1599-1612.
46. Krueger U, Zanow J, Scholz H. Computational fluid dynamics and vascular access. *Artif Organs* 2002;26(7):571-575.

References

47. Moore JA, Steinman DA, Ethier CR. Computational blood flow modelling: errors associated with reconstructing finite element models from magnetic resonance images. *J Biomech* 1998;31(2):179-184.
48. Hochmuth RM, Mohandas N, Spaeth EE, Williams J, Blackshear PL, Johnson DW. Surface Adhesion, Deformation and Detachment at Low Shear of Red-Cells and White Cells. *Trans. Amer. Soc. Artif. Int. Organs* 1972;18:325-334.
49. Engbers GHM, Dost L, Hennink WE, Aarts P, Sixma JJ, Feijen J. An in vitro Study of the Adhesion of Blood-Platelets onto Vascular Catheters. *J Biomed Mater Res* 1987;21(5):613-627.
50. Nevaril CG, Lynch EC, Alfrey CP, Hellums JD. Erythrocyte damage and destruction induced by shearing stress. *J. Lab. & Clin. Med.* 1968;71:781-790.
51. Blackshear PL, Dorman FD, Steinbach EJ. Shear, Wall Interaction and Hemolysis. *Trans. Amer. Soc. Artif. Int. Organs* 1966;12:113-120.
52. Hellums JD, Hardwick RA. Response of Platelets to Shear Stress - a Review. In: Gross DR, Hwang NHC, eds. *The Rheology of Blood Vessels and Associated Tissues*, Alphen aan den Rijn: Sijthoff & Noordhoff, 1981;160-183.
53. McIntire LV, Martin RR. Mechanical Trauma Induced PMN Leucocyte Dysfunction. In: Gross DR, Hwang NHC, eds. *The Rheology of Blood Vessels and Associated Tissues*, Alphen aan den Rijn: Sijthoff & Noordhoff, 1981;214-235.
54. Feigenbaum H *Echocardiography*, 5th Edition. Indianapolis: Lippincott Williams & Wilkins, 1994.
55. Schwab SJ. Assessing the adequacy of vascular access and its relationship to patient outcome. *Am J Kidney Dis* 1994;24(2):316-20.
56. Mareels G, De Wachter DS, Verdonck PR. Computational fluid dynamics-analysis of the Niagara hemodialysis catheter in a right heart model. *Artif Organs* 2004;28(7):639-48.
57. Prakash S, Ethier CR. Requirements for mesh resolution in 3D computational hemodynamics. *J Biomech Eng* 2001;123(2):134-44.
58. Twardowski ZJ, Seger RM. Dimensions of central venous structures in humans measured in vivo using magnetic resonance imaging: implications for central-vein catheter dimensions. *Int J Artif Organs* 2002;25(2):107-23.
59. Cohen ML, Cohen BS, Kronzon I, Lighty GW, Winer HE. Superior vena caval blood flow velocities in adults: a Doppler echocardiographic study. *J Appl Physiol* 1986;61(1):215-9.
60. Scarano F. Iterative image deformation methods in PIV. *Measurements Science and Technology* 2002;13:R1-19.

61. Thévenaz P, Blu T, Unser M. Image interpolation and resampling. In: Bankman IN, eds. *Handbook of medical imaging, processing & analysis*, San Diego, CA: Academic Press, 2000;393-420.
62. Wernet M. Symmetric phase only filtering: a new paradigm for DPV data processing. *Measurements Science and Technology* 2005;16:601-618.
63. Cockett GC. The rheology and tube flow of blood. In: Skalak R, Chien S, eds. *Handbook of bioengineering*, London: Mc Green Hill, 1987.
64. Kroll MH, Hellums JD, McIntire LV, Schafer AI, Moake JL. Platelets and shear stress. *Blood* 1996;88(5):1525-41.
65. Waniewski J, Kurowska W, Mizerski JK, Trykozko A, Nowinski K, Brzezinska-Rajszyz G, et al. The effects of graft geometry on the patency of a systemic-to-pulmonary shunt: a computational fluid dynamics study. *Artif Organs* 2005;29(8):642-50.
66. Goubergrits L, Affeld K. Numerical estimation of blood damage in artificial organs. *Artif Organs* 2004;28(5):499-507.
67. Verdonck P. The role of computational fluid dynamics for artificial organ design. *Artif Organs* 2002;26(7):569-70.
68. Strony J, Beaudoin A, Brands D, Adelman B. Analysis of shear stress and hemodynamic factors in a model of coronary artery stenosis and thrombosis. *Am J Physiol* 1993;265(5 Pt 2):H1787-96.
69. Guyton AC *Textbook of Medical Physiology*, 7th ed. Philadelphia: W.B. Saunders Company, 1986.
70. Wisse E, Braet F, Luo D, De Zanger R, Jans D, Crabbe E, et al. Structure and function of sinusoidal lining cells in the liver. *Toxicol Pathol* 1996;24(1):100-11.
71. Nagura H, Koshikawa T, Fukuda Y, Asai J. Hepatic vascular endothelial cells heterogenously express surface antigens associated with monocytes, macrophages and T lymphocytes. *Virchows Arch A Pathol Anat Histopathol* 1986;409(4):407-16.
72. Friedman SL. Molecular regulation of hepatic fibrosis, an integrated cellular response to tissue injury. *J Biol Chem* 2000;275(4):2247-50.
73. Martinez-Hernandez A, Amenta PS. The extracellular matrix in hepatic regeneration. *Faseb J* 1995;9(14):1401-10.
74. Selden C, Khalil M, Hodgson HJ. What keeps hepatocytes on the straight and narrow? Maintaining differentiated function in the liver. *Gut* 1999;44(4):443-6.
75. Rappaport AM. The microcirculatory hepatic unit. *Microvasc Res* 1973;6(2):212-28.
76. Jungermann K, Kietzmann T. Zonation of parenchymal and nonparenchymal metabolism in liver. *Annu Rev Nutr* 1996;16:179-203.

References

77. Jungermann K, Kietzmann T. Oxygen: modulator of metabolic zonation and disease of the liver. *Hepatology* 2000;31(2):255-60.
78. Jungermann K, Thurman RG. Hepatocyte heterogeneity in the metabolism of carbohydrates. *Enzyme* 1992;46(1-3):33-58.
79. Lindros KO. Zonation of cytochrome P450 expression, drug metabolism and toxicity in liver. *Gen Pharmacol* 1997;28(2):191-6.
80. Benhamouche S, Decaens T, Godard C, Chambrey R, Rickman DS, Moinard C, *et al.* Apc tumor suppressor gene is the "zonation-keeper" of mouse liver. *Dev Cell* 2006;10(6):759-70.
81. McCuskey RS, Reilly FD, McCuskey PA, Dimlich RV. In vivo microscopy of the hepatic microvascular system. *Bibl Anat* 1979;(18):73-6.
82. Fausto N, Webber EM. Liver regeneration. In: Arias IM, eds. *The Liver: Biology and Pathobiology*, 3rd ed. New York: Raven Press, 1994;1059.
83. Steer CJ. Liver regeneration. *Faseb J* 1995;9(14):1396-400.
84. Fernandez-Seara J, Prieto J, Quiroga J, Zozaya JM, Cobos MA, Rodriguez-Eire JL, *et al.* Systemic and regional hemodynamics in patients with liver cirrhosis and ascites with and without functional renal failure. *Gastroenterology* 1989;97(5):1304-12.
85. Gitlin N, Lewis DC, Hinkley L. The diagnosis and prevalence of subclinical hepatic encephalopathy in apparently healthy, ambulant, non-shunted patients with cirrhosis. *J Hepatol* 1986;3(1):75-82.
86. Davis GL, Albright JE, Cook SF, Rosenberg DM. Projecting future complications of chronic hepatitis C in the United States. *Liver Transpl* 2003;9(4):331-8.
87. Rozga J. Liver support technology--an update. *Xenotransplantation* 2006;13(5):380-9.
88. Starzl TE, Marchioro TL, Vonkaulla KN, Hermann G, Brittain RS, Waddell WR. Homotransplantation of the Liver in Humans. *Surg Gynecol Obstet* 1963;117:659-76.
89. Kamath PS, Kim WR. The model for end-stage liver disease (MELD). *Hepatology* 2007;45(3):797-805.
90. Silberhumer GR, Hetz H, Rasoul-Rockenschaub S, Peck-Radosavljevic M, Soliman T, Steininger R, *et al.* Is MELD score sufficient to predict not only death on waiting list, but also post-transplant survival? *Transpl Int* 2006;19(4):275-81.
91. Habib S, Berk B, Chang CC, Demetris AJ, Fontes P, Dvorchik I, *et al.* MELD and prediction of post-liver transplantation survival. *Liver Transpl* 2006;12(3):440-7.

-
92. Yoo HY, Thuluvath PJ. Short-term postliver transplant survival after the introduction of MELD scores for organ allocation in the United States. *Liver Int* 2005;25(3):536-41.
93. Bernuau J, Rueff B, Benhamou JP. Fulminant and subfulminant liver failure: definitions and causes. *Semin Liver Dis* 1986;6(2):97-106.
94. Knell AJ, Dukes DC. Dialysis procedures in acute liver coma. *Lancet* 1976;2(7982):402-3.
95. Agarwal R, Farber MO. Is continuous veno-venous hemofiltration for acetaminophen-induced acute liver and renal failure worthwhile? *Clin Nephrol* 2002;57(2):167-70.
96. Bellomo R, Ronco C. Continuous haemofiltration in the intensive care unit. *Crit Care* 2000;4(6):339-45.
97. Mori T, Eguchi Y, Shimizu T, Endo Y, Yoshioka T, Hanasawa K, *et al.* A case of acute hepatic insufficiency treated with novel plasmapheresis plasma diafiltration for bridge use until liver transplantation. *Ther Apher* 2002;6(6):463-6.
98. Sadamori H, Yagi T, Inagaki M, Shima Y, Matsuda H, Tanaka N, *et al.* High-flow-rate haemodiafiltration as a brain-support therapy proceeding to liver transplantation for hyperacute fulminant hepatic failure. *Eur J Gastroenterol Hepatol* 2002;14(4):435-9.
99. Flendrig LM (1998). Development of a novel bioartificial liver. Amsterdam, University of Amsterdam. **PhD**: 149.
100. Rahman TM, Hodgson HJ. Review article: liver support systems in acute hepatic failure. *Aliment Pharmacol Ther* 1999;13(10):1255-72.
101. Ash SR, Sullivan TA, Carr DJ. Sorbent suspensions vs. sorbent columns for extracorporeal detoxification in hepatic failure. *Ther Apher Dial* 2006;10(2):145-53.
102. Falkenhagen D, Brandl M, Hartmann J, Kellner KH, Posniecek T, Weber V. Fluidized bed adsorbent systems for extracorporeal liver support. *Ther Apher Dial* 2006;10(2):154-9.
103. Yarmush ML, Dunn JC, Tompkins RG. Assessment of artificial liver support technology. *Cell Transplant* 1992;1(5):323-41.
104. Mitzner S, Klammt S, Stange J, Schmidt R. Albumin regeneration in liver support-comparison of different methods. *Ther Apher Dial* 2006;10(2):108-17.
105. Hughes R, Ton HY, Langley P, Davies M, Hanid MA, Mellon P, *et al.* Albumin-coated Amberlite XAD-7 resin for hemoperfusion in acute liver failure. Part II: in vivo evaluation. *Artif Organs* 1979;3(1):23-6.
106. Kapoor D. Molecular adsorbent recirculating system: Albumin dialysis-based extracorporeal liver assist device. *J Gastroenterol Hepatol* 2002;17 Suppl 3:S280-S286.

References

107. Heemann U, Treichel U, Look J, Philipp T, Gerken G, Malago M, *et al.* Albumin dialysis in cirrhosis with superimposed acute liver injury: a prospective, controlled study. *Hepatology* 2002;36(4 Pt 1):949-58.
108. Onodera K, Sakata H, Yonekawa M, Kawamura A. Artificial liver support at present and in the future. *J Artif Organs* 2006;9(1):17-28.
109. Stange J, Hassanein TI, Mehta R, Mitzner SR, Bartlett RH. The molecular adsorbents recycling system as a liver support system based on albumin dialysis: a summary of preclinical investigations, prospective, randomized, controlled clinical trial, and clinical experience from 19 centers. *Artif Organs* 2002;26(2):103-10.
110. Falkenhagen D, Strobl W, Vogt G, Schrefl A, Linsberger I, Gerner FJ, *et al.* Fractionated plasma separation and adsorption system: a novel system for blood purification to remove albumin bound substances. *Artif Organs* 1999;23(1):81-6.
111. Krause A. Prometheus- a new extracorporeal liver support therapy. In: Arroyo V, Forns X, Garcia-Pagan JC, Rodés J, eds. *Progress in the Treatment of Liver Diseases*, Barcelona: Ars Medica, 2003;437-443.
112. Rifai K, Manns MP. Review article: clinical experience with Prometheus. *Ther Apher Dial* 2006;10(2):132-7.
113. Laleman W, Wilmer A, Evenepoel P, Elst IV, Zeegers M, Zaman Z, *et al.* Effect of the molecular adsorbent recirculating system and Prometheus devices on systemic haemodynamics and vasoactive agents in patients with acute-on-chronic alcoholic liver failure. *Crit Care* 2006;10(4):R108.
114. Sauer IM, Goetz M, Steffen I, Walter G, Kehr DC, Schwartlander R, *et al.* In vitro comparison of the molecular adsorbent recirculation system (MARS) and single-pass albumin dialysis (SPAD). *Hepatology* 2004;39(5):1408-14.
115. Rozga J, Umehara Y, Trofimenko A, Sadahiro T, Demetriou AA. A novel plasma filtration therapy for hepatic failure: preclinical studies. *Ther Apher Dial* 2006;10(2):138-44.
116. Falkenhagen D, Strobl W, Hartmann J, Schrefl A, Linsberger I, Kellner KH, *et al.* Patient safety technology for microadsorbent systems in extracorporeal blood purification. *Artif Organs* 2002;26(2):84-90.
117. Ash SR, Carr DJ, Sullivan TA. Sorbent suspension reactor for extracorporeal detoxification in hepatic failure or drug overdose. *Asaio J* 2004;50(6):lviii-lxv.
118. Ash SR, Steczko J, Knab WR, Blake DE, Carr DJ, Harker KD, *et al.* Push-pull sorbent-based pheresis and hemodiabsorption in the treatment of hepatic failure: preliminary results of a clinical trial with the BioLogic-DTPF System. *Ther Apher* 2000;4(3):218-28.
119. Schwanzner-Pfeiffer D, Mitteregger R, Rossmann E, Falkenhagen D. Comparison of specific adsorbents for tumor necrosis factor-alpha and therapeutic anti-tumor necrosis factor-alpha antibodies: an in vitro sepsis model. *Int J Artif Organs* 2006;29(12):1140-7.

-
120. Zieve L. Metabolic abnormalities in hepatic coma and potential toxins to be removed. In: Williams R, Murray-Lyon IM, eds. *Artificial Liver Support*, Londen: Pitman, 1975.
121. Kawazoe Y, Eguchi S, Sugiyama N, Kamohara Y, Fujioka H, Kanematsu T. Comparison between bioartificial and artificial liver for the treatment of acute liver failure in pigs. *World J Gastroenterol* 2006;12(46):7503-7.
122. Van de Kerkhove MP, Hoekstra R, Chamuleau RA, van Gulik TM. Clinical application of bioartificial liver support systems. *Ann Surg* 2004;240(2):216-30.
123. Sorrentino F. Prime ricerche per la realizzazione di un fegato artificiale. *Chir & Patol Sperim* 1956;4:1401-1404.
124. Kimoto S, Sugiura M, Sakamoto K, Hori M, Miura T, Kojima Y. The artificial liver. *Arch De Vecchi Anat Patol* 1960;31:229-39.
125. Nose Y, Mikami J, Kasai N. An experimental artificial liver utilizing extracorporeal metabolism with sliced or granulated canine liver. *ASAIO Trans.* 1963;9:358.
126. Burnell JM, Dawborn JK, Epstein RB, Gutman RA, Leinbach GE, Thomas ED, *et al.* Acute hepatic coma treated by cross-circulation or exchange transfusion. *N Engl J Med* 1967;276(17):935-43.
127. Eiseman B, Liem DS, Raffucci F. Heterologous liver perfusion in treatment of hepatic failure. *Ann Surg* 1965;162(3):329-45.
128. Stockmann HB, Hiemstra CA, Marquet RL, JN IJ. Extracorporeal perfusion for the treatment of acute liver failure. *Ann Surg* 2000;231(4):460-70.
129. Munoz SJ, Ballas SK, Moritz MJ, Martinez J, Friedman LS, Jarrell BE, *et al.* Perioperative management of fulminant and subfulminant hepatic failure with therapeutic plasmapheresis. *Transplant Proc* 1989;21(3):3535-6.
130. Brunner G, Losgen H. Benefits and dangers of plasma exchange in patients with fulminant hepatic failure. In: Oda T, Shikawa Y, Inoue N, eds. *Therapeutic Plasmapheresis VI*, Cleveland, OH: ISAO Press, 1987.
131. Strom S, Fisher R. Hepatocyte transplantation: new possibilities for therapy. *Gastroenterology* 2003;124(2):568-71.
132. Morsiani E, Brogli M, Galavotti D, Pazzi P, Puviani AC, Azzena GF. Biologic liver support: optimal cell source and mass. *Int J Artif Organs* 2002;25(10):985-93.
133. Chamuleau RA, Poyck PP, van de Kerkhove MP. Bioartificial liver: its pros and cons. *Ther Apher Dial* 2006;10(2):168-74.

References

134. Jauregui HO, Chowdhury NR, Chowdhury JR. Use of mammalian liver cells for artificial liver support. *Cell Transplant* 1996;5(3):353-67.
135. Mitry RR, Hughes RD, Aw MM, Terry C, Mieli-Vergani G, Girlanda R, *et al.* Human hepatocyte isolation and relationship of cell viability to early graft function. *Cell Transplant* 2003;12(1):69-74.
136. Sauer IM, Zeilinger K, Obermayer N, Pless G, Grunwald A, Pascher A, *et al.* Primary human liver cells as source for modular extracorporeal liver support--a preliminary report. *Int J Artif Organs* 2002;25(10):1001-5.
137. Allen JW, Hassanein T, Bhatia SN. Advances in bioartificial liver devices. *Hepatology* 2001;34(3):447-55.
138. Mitaka T. The current status of primary hepatocyte culture. *Int J Exp Pathol* 1998;79(6):393-409.
139. Tateno C, Takai-Kajihara K, Yamasaki C, Sato H, Yoshizato K. Heterogeneity of growth potential of adult rat hepatocytes in vitro. *Hepatology* 2000;31(1):65-74.
140. Lawley TJ, Bielory L, Gascon P, Yancey KB, Young NS, Frank MM. A prospective clinical and immunologic analysis of patients with serum sickness. *N Engl J Med* 1984;311(22):1407-13.
141. te Velde AA, Flendrig LM, Ladiges NC, Chamuleau RA. Immunological consequences of the use of xenogeneic hepatocytes in a bioartificial liver for acute liver failure. *Int J Artif Organs* 1997;20(4):229-33.
142. Gislason GT, Lobdell DD, Kelly JH, Sussman NL. A treatment system for implementing an extracorporeal liver assist device. *Artif Organs* 1994;18(5):385-9.
143. Chamuleau RA, Deurholt T, Hoekstra R. Which are the right cells to be used in a bioartificial liver? *Metab Brain Dis* 2005;20(4):327-35.
144. Holt SE, Shay JW. Role of telomerase in cellular proliferation and cancer. *J Cell Physiol* 1999;180(1):10-8.
145. Lundberg AS, Hahn WC, Gupta P, Weinberg RA. Genes involved in senescence and immortalization. *Curr Opin Cell Biol* 2000;12(6):705-9.
146. Hoekstra R, Chamuleau RA. Recent developments on human cell lines for the bioartificial liver. *Int J Artif Organs* 2002;25(3):182-91.
147. Gruppuso PA, Bienieki TC, Faris RA. The relationship between differentiation and proliferation in late gestation fetal rat hepatocytes. *Pediatr Res* 1999;46(1):14-9.
148. Lilja H, Blanc P, Demetriou AA, Rozga J. Response of cultured fetal and adult rat hepatocytes to growth factors and cyclosporine. *Cell Transplant* 1998;7(3):257-66.

149. Werner A, Duvar S, Muthing J, Buntmeyer H, Lunsdorf H, Strauss M, *et al.* Cultivation of immortalized human hepatocytes HepZ on macroporous Cultispher G microcarriers. *Biotechnol Bioeng* 2000;68(1):59-70.
150. Petersen BE, Bowen WC, Patrene KD, Mars WM, Sullivan AK, Murase N, *et al.* Bone marrow as a potential source of hepatic oval cells. *Science* 1999;284(5417):1168-70.
151. Schuldiner M, Yanuka O, Itskovitz-Eldor J, Melton DA, Benvenisty N. Effects of eight growth factors on the differentiation of cells derived from human embryonic stem cells. *Proc Natl Acad Sci U S A* 2000;97(21):11307-12.
152. Strain AJ, Crosby HA. Hepatic stem cells. *Gut* 2000;46(6):743-5.
153. Catapano G. Mass transfer limitations to the performance of membrane bioartificial liver support devices. *Int J Artif Organs* 1996;19(1):18-35.
154. Nyberg SL, Shatford RA, Hu WS, Payne WD, Cerra FB. Hepatocyte culture systems for artificial liver support: implications for critical care medicine (bioartificial liver support). *Crit Care Med* 1992;20(8):1157-68.
155. Ohashi K, Kay MA, Kuge H, Yokoyama T, Kanehiro H, Hisanaga M, *et al.* Heterotopically transplanted hepatocyte survival depends on extracellular matrix components. *Transplant Proc* 2005;37(10):4587-8.
156. Tong JZ, Sarrazin S, Cassio D, Gauthier F, Alvarez F. Application of spheroid culture to human hepatocytes and maintenance of their differentiation. *Biol Cell* 1994;81(1):77-81.
157. Tilles AW, Baskaran H, Roy P, Yarmush ML, Toner M. Effects of oxygenation and flow on the viability and function of rat hepatocytes cocultured in a microchannel flat-plate bioreactor. *Biotechnol Bioeng* 2001;73(5):379-89.
158. Gerlach JC. Development of a hybrid liver support system: a review. *Int J Artif Organs* 1996;19(11):645-54.
159. Qiang S, Yaoting Y, Hongyin L, Klinkmann H. Comparative evaluation of different membranes for the construction of an artificial liver support system. *Int J Artif Organs* 1997;20(2):119-24.
160. Catapano G, Di Lorenzo MC, Della Volpe C, De Bartolo L, Migliaresi C. Polymeric membranes for hybrid liver support devices: the effect of membrane surface wettability on hepatocyte viability and functions. *J Biomater Sci Polym Ed* 1996;7(11):1017-27.
161. De Bartolo L, Catapano G, Della Volpe C, Drioli E. The effect of surface roughness of microporous membranes on the kinetics of oxygen consumption and ammonia elimination by adherent hepatocytes. *J Biomater Sci Polym Ed* 1999;10(6):641-55.
162. Gerlach J, Stoll P, Schnoy N, Bucherl ES. Membranes as substrates for hepatocyte adhesion in liver support bioreactors. *Int J Artif Organs* 1990;13(7):436-41.

References

163. Gerlach JC, Schnoy N, Vienken J, Smith M, Neuhaus P. Comparison of hollow fibre membranes for hepatocyte immobilisation in bioreactors. *Int J Artif Organs* 1996;19(10):610-6.
164. Jozwiak A, Karlik W, Wiechetek M, Werynski A. Attachment and metabolic activity of hepatocytes cultivated on selected polymeric membranes. *Int J Artif Organs* 1998;21(8):460-6.
165. Legallais C, David B, Doré E. Bioartificial livers (BAL): current technological aspects and future developments. *Journal of Membrane Science* 2001;181:81-95.
166. Auth MK, Okamoto M, Ishida Y, Keogh A, Auth SH, Gerlach J, *et al.* Maintained function of primary human hepatocytes by cellular interactions in coculture: implications for liver support systems. *Transpl Int* 1998;11 Suppl 1:S439-43.
167. Clement B, Guguen-Guillouzo C, Campion JP, Glaise D, Bourel M, Guillouzo A. Long-term cocultures of adult human hepatocytes with rat liver epithelial cells: modulation of albumin secretion and accumulation of extracellular material. *Hepatology* 1984;4(3):373-80.
168. Bhatia SN, Balis UJ, Yarmush ML, Toner M. Effect of cell-cell interactions in preservation of cellular phenotype: cocultivation of hepatocytes and nonparenchymal cells. *Faseb J* 1999;13(14):1883-900.
169. Planchamp C, Vu TL, Mayer JM, Reist M, Testa B. Hepatocyte hollow-fibre bioreactors: design, set-up, validation and applications. *J Pharm Pharmacol* 2003;55(9):1181-98.
170. Tarentino AL, Galivan J. Membrane characteristics of adult rat liver parenchymal cells in primary monolayer culture. *In Vitro* 1980;16(10):833-46.
171. Selden C, Roberts E, Stamp G, Parker K, Winlove P, Ryder T, *et al.* Comparison of three solid phase supports for promoting three-dimensional growth and function of human liver cell lines. *Artif Organs* 1998;22(4):308-19.
172. Glacken MW, Fleischaker RJ, Sinskey AJ. Large-scale production of mammalian cells and their products: engineering principles and barriers to scale-up. *Ann NY Acad Sci* 1983;413:355-72.
173. Diekmann S, Bader A, Schmitmeier S. Present and future developments in hepatic tissue engineering for liver support systems. *Cytotechnology* 2006;50:163-179.
174. De Bartolo L, Salerno S, Morelli S, Giorno L, Rende M, Memoli B, *et al.* Long-term maintenance of human hepatocytes in oxygen-permeable membrane bioreactor. *Biomaterials* 2006;27(27):4794-803.
175. Dunn JC, Tompkins RG, Yarmush ML. Long-term in vitro function of adult hepatocytes in a collagen sandwich configuration. *Biotechnol Prog* 1991;7(3):237-45.
176. Dunn JC, Tompkins RG, Yarmush ML. Hepatocytes in collagen sandwich: evidence for transcriptional and translational regulation. *J Cell Biol* 1992;116(4):1043-53.

177. Chan C, Berthiaume F, Nath BD, Tilles AW, Toner M, Yarmush ML. Hepatic tissue engineering for adjunct and temporary liver support: critical technologies. *Liver Transpl* 2004;10(11):1331-42.
178. Naka S, Takeshita K, Yamamoto T, Tani T, Kodama M. Bioartificial liver support system using porcine hepatocytes entrapped in a three-dimensional hollow fiber module with collagen gel: An evaluation in the swine acute liver failure model. *Artif Organs* 1999;23(9):822-8.
179. Ellis AJ, Hughes RD, Wendon JA, Dunne J, Langley PG, Kelly JH, *et al.* Pilot-controlled trial of the extracorporeal liver assist device in acute liver failure. *Hepatology* 1996;24(6):1446-51.
180. Kamohara Y, Rozga J, Demetriou AA. Artificial liver: review and Cedars-Sinai experience. *J Hepatobiliary Pancreat Surg* 1998;5(3):273-85.
181. Watanabe FD, Mullon CJ, Hewitt WR, Arkadopoulos N, Kahaku E, Eguchi S, *et al.* Clinical experience with a bioartificial liver in the treatment of severe liver failure. A phase I clinical trial. *Ann Surg* 1997;225(5):484-91; discussion 491-4.
182. Tzanakakis ES, Hess DJ, Sielaff TD, Hu WS. Extracorporeal tissue engineered liver-assist devices. *Annu Rev Biomed Eng* 2000;2:607-32.
183. Mullon C, Pitkin Z. The HepatAssist bioartificial liver support system: clinical study and pig hepatocyte process. *Expert Opin Investig Drugs* 1999;8(3):229-35.
184. Baquerizo A, Mhoyan A, Kearns-Jonker M, Arnaout WS, Shackleton C, Busuttill RW, *et al.* Characterization of human xenoreactive antibodies in liver failure patients exposed to pig hepatocytes after bioartificial liver treatment: an ex vivo model of pig to human xenotransplantation. *Transplantation* 1999;67(1):5-18.
185. Jauregui HO, Naik S, Santangini H, Pan J, Trenkler D, Mullon C. Primary cultures of rat hepatocytes in hollow fiber chambers. *In Vitro Cell Dev Biol Anim* 1994;30A(1):23-9.
186. Sussman NL, Kelly JH. Improved liver function following treatment with an extracorporeal liver assist device. *Artif Organs* 1993;17(1):27-30.
187. Dixit V, Gitnick G. The bioartificial liver: state-of-the-art. *Eur J Surg Suppl* 1998;(582):71-6.
188. Busse B, Gerlach JC. Bioreactors for hybrid liver support: historical aspects and novel designs. *Ann NY Acad Sci* 1999;875:326-39.
189. Fremond B, Malandain C, Guyomard C, Chesne C, Guillouzo A, Campion JP. Correction of bilirubin conjugation in the Gunn rat using hepatocytes immobilized in alginate gel beads as an extracorporeal bioartificial liver. *Cell Transplant* 1993;2(6):453-60.
190. Dore E, Legallais C. A new concept of bioartificial liver based on a fluidized bed bioreactor. *Ther Apher* 1999;3(3):264-7.

References

191. David B, Dore E, Jaffrin MY, Legallais C. Mass transfers in a fluidized bed bioreactor using alginate beads for a future bioartificial liver. *Int J Artif Organs* 2004;27(4):284-93.
192. David B, Barbe L, Barthes-Biesel D, Legallais C. Mechanical properties of alginate beads hosting hepatocytes in a fluidized bed bioreactor. *Int J Artif Organs* 2006;29(8):756-63.
193. Koebe HG, Dahnhardt C, Muller-Hocker J, Wagner H, Schildberg FW. Cryopreservation of porcine hepatocyte cultures. *Cryobiology* 1996;33(1):127-41.
194. van de Kerkhove MP, Hoekstra R, van Nooijen FC, Spoelstra FO, Doorschodt BM, van Wijk AC, et al. Subnormothermic preservation maintains viability and function in a porcine hepatocyte culture model simulating bioreactor transport. *Cell Transplant* 2006;15(2):161-8.
195. Cheng YB, Wang YJ, Zhang SC, Liu J, Chen Z, Li JJ. Response of porcine hepatocytes in primary culture to plasma from severe viral hepatitis patients. *World J Gastroenterol* 2005;11(48):7585-90.
196. Shi Q, Gaylor JD, Cousins R, Plevris J, Hayes PC, Grant MH. The effects of serum from patients with acute liver failure on the growth and metabolism of Hep G2 cells. *Artif Organs* 1998;22(12):1023-30.
197. De Bartolo L, Jarosch-Von Schweder G, Haverich A, Bader A. A novel full-scale flat membrane bioreactor utilizing porcine hepatocytes: cell viability and tissue-specific functions. *Biotechnol Prog* 2000;16(1):102-8.
198. Fruhauf NR, Oldhafer KJ, Holtje M, Kaiser GM, Fruhauf JH, Stavrou GA, et al. A bioartificial liver support system using primary hepatocytes: a preclinical study in a new porcine hepatectomy model. *Surgery* 2004;136(1):47-56.
199. Shito M, Kim NH, Baskaran H, Tilles AW, Tompkins RG, Yarmush ML, et al. In vitro and in vivo evaluation of albumin synthesis rate of porcine hepatocytes in a flat-plate bioreactor. *Artif Organs* 2001;25(7):571-8.
200. Hu WS, Friend JR, Wu FJ, Sielaff TD, Peshwa M, Lazer A, et al. Development of a bioartificial liver employing xenogenic hepatocytes. *Cytotechnology* 1997;23:29-38.
201. Nyberg SL, Shatford RA, Payne WD, Hu WS, Cerra FB. Primary culture of rat hepatocytes entrapped in cylindrical collagen gels: an in vitro system with application to the bioartificial liver. Rat hepatocytes cultured in cylindrical collagen gels. *Cytotechnology* 1992;10(3):205-15.
202. Park JK, Lee DH. Bioartificial liver systems: current status and future perspective. *J Biosci Bioeng* 2005;99(4):311-9.
203. Mizumoto H, Funatsu K. Liver regeneration using a hybrid artificial liver support system. *Artif Organs* 2004;28(1):53-7.
204. Ijima H, Nakazawa K, Mizumoto H, Matsushita T, Funatsu K. Formation of a spherical multicellular aggregate (spheroid) of animal cells in the pores of polyurethane foam as a cell culture substratum and its application to a hybrid artificial liver. *J Biomater Sci Polym Ed* 1998;9(7):765-78.

205. Gion T, Shimada M, Shirabe K, Nakazawa K, Ijima H, Matsushita T, *et al.* Evaluation of a hybrid artificial liver using a polyurethane foam packed-Bed culture system in dogs. *J Surg Res* 1999;82(2):131-6.
206. Nakazawa K, Ijima H, Fukuda J, Sakiyama R, Yamashita Y, Shimada M, *et al.* Development of a hybrid artificial liver using polyurethane foam/hepatocyte spheroid culture in a preclinical pig experiment. *Int J Artif Organs* 2002;25(1):51-60.
207. Jasmund I, Langsch A, Simmoteit R, Bader A. Cultivation of primary porcine hepatocytes in an OXY-HFB for use as a bioartificial liver device. *Biotechnol Prog* 2002;18(4):839-46.
208. Millis JM, Cronin DC, Johnson R, Conjeevaram H, Conlin C, Trevino S, *et al.* Initial experience with the modified extracorporeal liver-assist device for patients with fulminant hepatic failure: system modifications and clinical impact. *Transplantation* 2002;74(12):1735-46.
209. Sussman NL, Gislason GT, Conlin CA, Kelly JH. The Hepatix extracorporeal liver assist device: initial clinical experience. *Artif Organs* 1994;18(5):390-6.
210. Demetriou AA, Rozga J, Podesta L, Lepage E, Morsiani E, Moscioni AD, *et al.* Early clinical experience with a hybrid bioartificial liver. *Scand J Gastroenterol Suppl* 1995;208:111-7.
211. Demetriou AA, Brown RS, Jr., Busuttill RW, Fair J, McGuire BM, Rosenthal P, *et al.* Prospective, randomized, multicenter, controlled trial of a bioartificial liver in treating acute liver failure. *Ann Surg* 2004;239(5):660-7; discussion 667-70.
212. Qian Y, Lanjuan L, Jianrong H, Jun L, Hongcui C, Suzhen F, *et al.* Study of severe hepatitis treated with a hybrid artificial liver support system. *Int J Artif Organs* 2003;26(6):507-13.
213. Xue YL, Zhao SF, Luo Y, Li XJ, Duan ZP, Chen XP, *et al.* TECA hybrid artificial liver support system in treatment of acute liver failure. *World J Gastroenterol* 2001;7(6):826-9.
214. Patzer JF, 2nd, Mazariegos GV, Lopez R. Preclinical evaluation of the Excorp Medical, Inc, Bioartificial Liver Support System. *J Am Coll Surg* 2002;195(3):299-310.
215. Mazariegos GV, Kramer DJ, Lopez RC, Shakil AO, Rosenbloom AJ, DeVera M, *et al.* Safety observations in phase I clinical evaluation of the Excorp Medical Bioartificial Liver Support System after the first four patients. *Asaio J* 2001;47(5):471-5.
216. Ding YT, Qiu YD, Chen Z, Xu QX, Zhang HY, Tang Q, *et al.* The development of a new bioartificial liver and its application in 12 acute liver failure patients. *World J Gastroenterol* 2003;9(4):829-32.
217. Sauer IM, Obermeyer N, Kardassis D, Theruvath T, Gerlach JC. Development of a hybrid liver support system. *Ann N Y Acad Sci* 2001;944:308-19.
218. Mundt A, Puhl G, Muller A, Sauer I, Muller C, Richard R, *et al.* A method to assess biochemical activity of liver cells during clinical application of extracorporeal hybrid liver support. *Int J Artif Organs* 2002;25(6):542-8.

References

219. Poyck PP, Pless G, Hoekstra R, Roth S, van Wijk AC, Schwartlander R, *et al.* In vitro comparison of two bioartificial liver support systems: MELS CellModule and AMC-BAL. *Int J Artif Organs* 2007;(in press).
220. Sauer IM, Gerlach JC. Modular extracorporeal liver support. *Artif Organs* 2002;26(8):703-6.
221. Morsiani E, Brogli M, Galavotti D, Bellini T, Ricci D, Pazzi P, *et al.* Long-term expression of highly differentiated functions by isolated porcine hepatocytes perfused in a radial-flow bioreactor. *Artif Organs* 2001;25(9):740-8.
222. Morsiani E, Pazzi P, Puviani AC, Brogli M, Valieri L, Gorini P, *et al.* Early experiences with a porcine hepatocyte-based bioartificial liver in acute hepatic failure patients. *Int J Artif Organs* 2002;25(3):192-202.
223. Van de Kerkhove MP, Di Florio E, Scuderi V, Mancini A, Belli A, Bracco A, *et al.* Phase I clinical trial with the AMC-bioartificial liver. *Int J Artif Organs* 2002;25(10):950-9.
224. van de Kerkhove MP, Poyck PP, Deurholt T, Hoekstra R, Chamuleau RA, van Gulik TM. Liver support therapy: an overview of the AMC-bioartificial liver research. *Dig Surg* 2005;22(4):254-64.
225. McClelland RE, MacDonald JM, Coger RN. Modeling O₂ transport within engineered hepatic devices. *Biotechnol Bioeng* 2003;82(1):12-27.
226. Sumaru K, Kanamori T. Optimal design of bio-hybrid systems with a hollow fiber scaffold: model analysis of oxygen diffusion/consumption. *Biochemical Engineering Journal* 2004;20:127-136.
227. Moussy Y. Convective flow through a hollow fiber bioartificial liver. *Artif Organs* 2003;27(11):1041-9.
228. Ledezma GA, Folch A, Bhatia SN, Balis UJ, Yarmush ML, Toner M. Numerical model of fluid flow and oxygen transport in a radial-flow microchannel containing hepatocytes. *J Biomech Eng* 1999;121(1):58-64.
229. Hay PD, Veitch AR, Smith MD, Cousins RB, Gaylor JD. Oxygen transfer in a diffusion-limited hollow fiber bioartificial liver. *Artif Organs* 2000;24(4):278-88.
230. Hay PD, Veitch AR, Gaylor JD. Oxygen transfer in a convection-enhanced hollow fiber bioartificial liver. *Artif Organs* 2001;25(2):119-30.
231. Roy P, Baskaran H, Tilles AW, Yarmush ML, Toner M. Analysis of oxygen transport to hepatocytes in a flat-plate microchannel bioreactor. *Ann Biomed Eng* 2001;29(11):947-55.
232. Patzer JF, 2nd. Oxygen consumption in a hollow fiber bioartificial liver--revisited. *Artif Organs* 2004;28(1):83-98.

233. Nyberg SL, Hibbs JR, Hardin JA, Germer JJ, Persing DH. Transfer of porcine endogenous retrovirus across hollow fiber membranes: significance to a bioartificial liver. *Transplantation* 1999;67(9):1251-5.
234. De Rave S, Tilanus HW, Van der Linden J, De Man RA, Van der Berg B, Hop WC, *et al.* The importance of orthotopic liver transplantation in acute hepatic failure. *Transpl Int* 2002;15(1):29-33.
235. Flendrig LM, Calise F, Di Florio E, Mancini A, Ceriello A, Santaniello W, *et al.* Significantly improved survival time in pigs with complete liver ischemia treated with a novel bioartificial liver. *Int J Artif Organs* 1999;22(10):701-9.
236. Glicklis R, Merchuk JC, Cohen S. Modeling mass transfer in hepatocyte spheroids via cell viability, spheroid size, and hepatocellular functions. *Biotechnol Bioeng* 2004;86(6):672-80.
237. Monkos K. Viscosity of bovine serum albumin aqueous solutions as a function of temperature and concentration. *Int J Biol Macromol* 1996;18(1-2):61-8.
238. Pearson D, Holden M. A clinical evaluation of the performance characteristics of one membrane and five bubble oxygenators: gas transfer and gaseous microemboli production. *Perfusion* 1986;1:15-26.
239. Bird RB, Stewart WE, Lightfoot EN *Transport Phenomena*, New York: John Wiley and Sons, 1960.
240. Goldstick TK, Ciuryla VT, Zuckerman L. Diffusion of oxygen in plasma and blood. *Adv Exp Med Biol* 1976;75:183-90.
241. Perry RH, Green DW *Perry's Chemical Engineers' Handbook*, 6th ed. New York: McGraw-Hill, 1984.
242. Zander R. Oxygen solubility in normal human blood. In: Kovach AGB, Dora E, eds. *Adv Physiol Sci: Oxygen transport to tissue*, Oxford: Pergamon Press, 1981;331-332.
243. Balis UJ, Behnia K, Dwarakanath B, Bhatia SN, Sullivan SJ, Yarmush ML, *et al.* Oxygen consumption characteristics of porcine hepatocytes. *Metab Eng* 1999;1(1):49-62.
244. Catapano G, De Bartolo L. Technique for the kinetic characterization of the metabolic reactions of hepatocytes in adhesion culture. *Biotechnol Prog* 1998;14(3):500-7.
245. Flendrig LM, la Soe JW, Jorning GG, Steenbeek A, Karlsten OT, Bovee WM, *et al.* In vitro evaluation of a novel bioreactor based on an integral oxygenator and a spirally wound nonwoven polyester matrix for hepatocyte culture as small aggregates. *J Hepatol* 1997;26(6):1379-92.
246. Funatsu K, Ijima H, Nakazawa K, Yamashita Y, Shimada M, Sugimachi K. Hybrid artificial liver using hepatocyte organoid culture. *Artif Organs* 2001;25(3):194-200.

References

247. Custer L, Mullon CJ. Oxygen delivery to and use by primary porcine hepatocytes in the HepatAssist 2000 system for extracorporeal treatment of patients in end-stage liver failure. *Adv Exp Med Biol* 1998;454:261-71.
248. Sielaff TD, Nyberg SL, Rollins MD, Hu MY, Amiot B, Lee A, *et al.* Characterization of the three-compartment gel-entrapment porcine hepatocyte bioartificial liver. *Cell Biol Toxicol* 1997;13(4-5):357-64.
249. Nilsson L, Stenström S. Gas diffusion through sheets of fibrous porous media. *Chemical Engineering Science* 1995;50(3):361-371.
250. Perrins WT, McKenzie DR, McPhedran RC. Transport properties of regular arrays of cylinders. *Proc. R. Soc.* 1979;A369:207-225.
251. Rayleigh L. On the influence of obstacles arranged in rectangular order upon the properties of a medium. *Phil. Mag.* 1892;34:481-502.
252. Riley MR, Buettner HM, Muzzio FJ, Reyes SC. Monte Carlo simulation of diffusion and reaction in two-dimensional cell structures. *Biophys J* 1995;68(5):1716-26.
253. Jones DP. Effect of mitochondrial clustering on O₂ supply in hepatocytes. *Am J Physiol* 1984;247(1 Pt 1):C83-9.
254. Darr TB, Hubel A. Freezing characteristics of isolated pig and human hepatocytes. *Cell Transplant* 1997;6(2):173-83.
255. Colton CK. Implantable biohybrid artificial organs. *Cell Transplant* 1995;4(4):415-36.
256. Yarmush ML, Toner M, Dunn JC, Rotem A, Hubel A, Tompkins RG. Hepatic tissue engineering. Development of critical technologies. *Ann NY Acad Sci* 1992;665:238-52.
257. Grote J, Susskind R, Vaupel P. Oxygen diffusivity in tumor tissue (DS-carcinosarcoma) under temperature conditions within the range of 20--40 degrees C. *Pflugers Arch* 1977;372(1):37-42.
258. Vaupel P, Hutten H, Thews G. Critical diffusion ranges for oxygen and glucose in tumor tissue considering Michaelis-Menten kinetics. *Bibl Anat* 1975;13:313-4.
259. Catapano G, Hornscheidt R, Wodetzki A, Baurmeister U. Turbulent flow technique for the estimation of oxygen diffusive permeability of membranes for the oxygenation of blood and other cell suspension. *J Membrane Sci* 2004;230:131-139.
260. Crawford AR, Lin XZ, Crawford JM. The normal adult human liver biopsy: a quantitative reference standard. *Hepatology* 1998;28(2):323-31.
261. Nakata K, Leong GF, Brauer RW. Direct measurement of blood pressures in minute vessels of the liver. *Am J Physiol* 1960;199:1181-8.

262. MacPhee PJ, Schmidt EE, Groom AC. Intermittence of blood flow in liver sinusoids, studied by high-resolution in vivo microscopy. *Am J Physiol* 1995;269(5 Pt 1):G692-8.
263. Wanless IR. Physioanatomic considerations. In: Schiff ER, Sorrell MF, Maddrey WC, eds. *Diseases of the liver*, Philadelphia: Lippincott Williams and Wilkins, 1999;3-38.
264. De Groot H, Littauer A, Noll T. Metabolic and pathological aspects of hypoxia in liver cells. In: Acker H, eds. *Oxygen sensing in tissue*, New York: Springer-Verlag, 1988;49-64.
265. Semenza GL. Regulation of mammalian O₂ homeostasis by hypoxia-inducible factor 1. *Annu Rev Cell Dev Biol* 1999;15:551-578.
266. Fariss MW. Oxygen toxicity: unique cytoprotective properties of vitamin E succinate in hepatocytes. *Free Radic Biol Med* 1990;9(4):333-43.
267. Dutta A, Popel AS. A theoretical analysis of intracellular oxygen diffusion. *J Theor Biol* 1995;176(4):433-45.
268. Foy BD, Rotem A, Toner M, Tompkins RG, Yarmush ML. A device to measure the oxygen uptake rate of attached cells: importance in bioartificial organ design. *Cell Transplant* 1994;3(6):515-27.
269. Nyberg SL, Rimmel RP, Mann HJ, Peshwa MV, Hu WS, Cerra FB. Primary hepatocytes outperform Hep G2 cells as the source of biotransformation functions in a bioartificial liver. *Ann Surg* 1994;220(1):59-67.
270. Poyck PP, Hoekstra R, van Wijk AC, Attanasio C, Calise F, Chamuleau RA. Functional and morphological comparison of three primary liver cell types cultured in the AMC bioartificial liver. *Liver Transpl* 2007;(in press).
271. Shatford RA, Nyberg SL, Meier SJ, White JG, Payne WD, Hu WS, *et al.* Hepatocyte function in a hollow fiber bioreactor: a potential bioartificial liver. *J Surg Res* 1992;53(6):549-57.
272. Smith MD, Smirthwaite AD, Cairns DE, Cousins RB, Gaylor JD. Techniques for measurement of oxygen consumption rates of hepatocytes during attachment and post-attachment. *Int J Artif Organs* 1996;19(1):36-44.
273. Van de Kerkhove MP, Poyck PP, Van Wijk AC, Galavotti D, Hoekstra R, Van Gulik TM, *et al.* Assessment and improvement of liver specific function of the AMC-bioartificial liver. *Int J Artif Organs* 2005;28(6):617-30.
274. Abrahamse SL, van de Kerkhove MP, Sosef MN, Hartman R, Chamuleau RA, van Gulik TM. Treatment of acute liver failure in pigs reduces hepatocyte function in a bioartificial liver support system. *Int J Artif Organs* 2002;25(10):966-74.
275. Flendrig LM, Chamuleau RA, Maas MA, Daalhuisen J, Hasset B, Kilty CG, *et al.* Evaluation of a novel bioartificial liver in rats with complete liver ischemia: treatment efficacy and species-specific alpha-GST detection to monitor hepatocyte viability. *J Hepatol* 1999;30(2):311-20.

References

276. Sosef MN, Abrahamse LS, van de Kerkhove MP, Hartman R, Chamuleau RA, van Gulik TM. Assessment of the AMC-bioartificial liver in the anhepatic pig. *Transplantation* 2002;73(2):204-9.
277. Poyck PP, Hoekstra R, Chhatta AA, Ten Bloemendaal L, Van Wijk AC, Galavotti D, *et al.* Time-related analysis of metabolic liver functions, cellular morphology and gene expression of hepatocytes cultured in a bioartificial liver. *Tissue Eng* 2007;(in press).
278. Mareels G, Poyck PP, Eloot S, Chamuleau RA, Verdonck PR. Three-dimensional numerical modeling and computational fluid dynamics simulations to analyze and improve oxygen availability in the AMC bioartificial liver. *Ann Biomed Eng* 2006;34(11):1729-44.
279. Seglen PO. Preparation of rat liver cells. 3. Enzymatic requirements for tissue dispersion. *Exp Cell Res* 1973;82(2):391-8.
280. Hoekstra R, Deurholt T, Poyck PP, ten Bloemendaal L, Chhatta AA. Increased reproducibility of quantitative reverse transcriptase-PCR. *Anal Biochem* 2005;340(2):376-9.
281. Nishikawa M, Uchino J, Matsushita M, Takahashi M, Taguchi K, Koike M, *et al.* Optimal oxygen tension conditions for functioning cultured hepatocytes in vitro. *Artif Organs* 1996;20(2):169-77.
282. Suleiman SA, Stevens JB. The effect of oxygen tension on rat hepatocytes in short-term culture. *In Vitro Cell Dev Biol* 1987;23(5):332-8.
283. Bader A, Fruhauf N, Tiedge M, Drinkgern M, De Bartolo L, Borlak JT, *et al.* Enhanced oxygen delivery reverses anaerobic metabolic states in prolonged sandwich rat hepatocyte culture. *Exp Cell Res* 1999;246(1):221-32.
284. Toutain HJ, Moronville-Halley V, Sarsat JP, Chelin C, Hoet D, Leroy D. Morphological and functional integrity of precision-cut rat liver slices in rotating organ culture and multiwell plate culture: effects of oxygen tension. *Cell Biol Toxicol* 1998;14(3):175-90.
285. Yanagi K, Miyoshi H, Ohshima N. Improvement of metabolic performance of hepatocytes cultured in vitro in a packed-bed reactor for use as a bioartificial liver. *Asaio J* 1998;44(5):M436-40.
286. Yanagi K, Ohshima N. Improvement of metabolic performance of cultured hepatocytes by high oxygen tension in the atmosphere. *Artif Organs* 2001;25(1):1-6.
287. Brand MD, Affourtit C, Esteves TC, Green K, Lambert AJ, Miwa S, *et al.* Mitochondrial superoxide: production, biological effects, and activation of uncoupling proteins. *Free Radic Biol Med* 2004;37(6):755-67.
288. Hayes JD, Flanagan JU, Jowsey IR. Glutathione transferases. *Annu Rev Pharmacol Toxicol* 2005;45:51-88.
289. Krauss S, Zhang CY, Lowell BB. The mitochondrial uncoupling-protein homologues. *Nat Rev Mol Cell Biol* 2005;6(3):248-61.

290. Negre-Salvayre A, Hirtz C, Carrera G, Cazenave R, Troly M, Salvayre R, *et al.* A role for uncoupling protein-2 as a regulator of mitochondrial hydrogen peroxide generation. *FASEB J* 1997;11(10):809-15.
291. Rotem A, Toner M, Bhatia S, Foy BD, Tompkins RG, Yarmush ML. Oxygen is a factor determining in-vitro tissue assembly - Effects on attachment and spreading of hepatocytes. *Biotechnol Bioeng* 1994;43:654-660.
292. Chan C, Berthiaume F, Lee K, Yarmush ML. Metabolic flux analysis of cultured hepatocytes exposed to plasma. *Biotechnol Bioeng* 2003;81(1):33-49.
293. Poyck PP, Mareels G, Hoekstra R, van Wijk AC, Van der Hoeven T, van Gulik TM, *et al.* Enhanced oxygen availability improves liver-specific functions of the AMC bioartificial liver. *Artif Organs* 2007;(submitted).
294. Farmer DG, Anselmo DM, Ghobrial RM, Yersiz H, McDiarmid SV, Cao C, *et al.* Liver transplantation for fulminant hepatic failure: experience with more than 200 patients over a 17-year period. *Ann Surg* 2003;237(5):666-75; discussion 675-6.
295. Nyberg SL, Shirabe K, Peshwa MV, Sielaff TD, Crotty PL, Mann HJ, *et al.* Extracorporeal application of a gel-entrapment, bioartificial liver: demonstration of drug metabolism and other biochemical functions. *Cell Transplant* 1993;2(6):441-52.
296. Dierickx PW, De Wachter D, Verdonck PR. Blood flow around hollow fibers. *Int J Artif Organs* 2000;23(9):610-7.
297. van Pelt JF, Severi T, Crabbe T, Eetveldt AV, Verslype C, Roskams T, *et al.* Expression of hepatitis C virus core protein impairs DNA repair in human hepatoma cells. *Cancer Lett* 2004;209(2):197-205.
298. Chevrollier A, Loiseau D, Gautier F, Malthiery Y, Stepien G. ANT2 expression under hypoxic conditions produces opposite cell-cycle behavior in 143B and HepG2 cancer cells. *Mol Carcinog* 2005;42(1):1-8.
299. Kelly JH, Darlington GJ. Modulation of the liver specific phenotype in the human hepatoblastoma line Hep G2. *In Vitro Cell Dev Biol* 1989;25(2):217-22.
300. Galban CJ, Locke BR. Analysis of cell growth kinetics and substrate diffusion in a polymer scaffold. *Biotechnol Bioeng* 1999;65(2):121-32.
301. Stein AM, Demuth T, Mobley D, Berens M, Sander LM. A mathematical model of glioblastoma tumor spheroid invasion in a three-dimensional in vitro experiment. *Biophys J* 2007;92(1):356-65.
302. Washizu J, Chan C, Berthiaume F, Tompkins RG, Toner M, Yarmush ML. Amino acid supplementation improves cell-specific functions of the rat hepatocytes exposed to human plasma. *Tissue Eng* 2000;6(5):497-504.

References

303. Gombert AK, Nielsen J. Mathematical modelling of metabolism. *Curr Opin Biotechnol* 2000;11(2):180-6.
304. Sharma NS, Ierapetritou MG, Yarmush ML. Novel quantitative tools for engineering analysis of hepatocyte cultures in bioartificial liver systems. *Biotechnol Bioeng* 2005;92(3):321-35.
305. Uygun K, Matthew HW, Huang Y. Investigation of metabolic objectives in cultured hepatocytes. *Biotechnol Bioeng* 2007;97(3):622-37.
306. Kuchel PW, Roberts DV, Nichol LW. The simulation of the urea cycle: correlation of effects due to inborn errors in the catalytic properties of the enzymes with clinical-biochemical observations. *Aust J Exp Biol Med Sci* 1977;55(3):309-26.
307. Venkatasubramanian R, Henson MA, Forbes NS. Incorporating energy metabolism into a growth model of multicellular tumor spheroids. *J Theor Biol* 2006;242(2):440-53.